

Stony Brook University



OFFICIAL COPY

The official electronic file of this thesis or dissertation is maintained by the University Libraries on behalf of The Graduate School at Stony Brook University.

© All Rights Reserved by Author.

**SINGLE PHOTON COUNTING FOR ULTRA-WEAK
FLUORESCENCE DETECTION: SYSTEM DESIGN,
CHARACTERIZATION AND APPLICATION TO
DNA-SEQUENCING**

A Dissertation Presented

by

Vinit H. Dhulla

to

The Graduate School

in Partial Fulfillment of the

Requirements

for the Degree of

Doctor of Philosophy

in

Electrical Engineering

Stony Brook University

December 2007

Stony Brook University

The Graduate School

Vinit H. Dhulla

We, the dissertation committee for the above candidate for the
Ph.D. in Electrical Engineering, hereby recommend acceptance of this
dissertation.

Vera Gorfinkel – Dissertation Advisor
Associate Professor, Department of Electrical and Computer Engineering

Hang-Sheng Tuan – Chairperson of Defense
Professor, Department of Electrical and Computer Engineering

Dmitri Donetski
Assistant Professor, Department of Electrical and Computer Engineering

Andriy Tsupryk
**Senior Research Scientist, Department of Electrical and Computer
Engineering**

Clark McGrew
Assistant Professor, Department of Physics and Astronomy

This dissertation is accepted by the Graduate School

Lawrence Martin
Dean of the Graduate School

Abstract of the Dissertation

**Single Photon Counting For Ultra-weak Fluorescence
Detection: System Design, Characterization and
Application to DNA Sequencing**

by

Vinit H. Dhulla

Doctor of Philosophy

in

Electrical Engineering

Stony Brook University

2007

The objective of the proposed research is to design and characterize single photon counting systems (SPCSs) for detecting ultra-weak fluorescent signals in various biomedical applications, our application being DNA-sequencing. This thesis investigates the feasibility of designing cost-effective, SPCSs to perform fast, high performance DNA-sequencing at low cost.

This thesis presents design, development and characterization of unique single-channel and multi-channel (16 and 32 channel) SPCSs based on a large-area single photon avalanche diode (SPAD) having 0.5mm diameter (model C30902S-DTC from Perkin Elmer Optoelectronics). A novel logic circuit for generating precise quench and reset delays in the quenching circuit is presented. Further, the developed SPCSs are integrated into DNA-sequencing instruments. Excellent DNA sequencing results, demonstrating single fluorescent molecule

sensitivity is presented. Thus, for the first time, experimental evidence of the application of large-area SPAD for highly sensitive detection of DNA-sequences is demonstrated.

Recently solid-state alternative to the traditional photomultiplier tube (PMT) called silicon photomultiplier (SiPM) became commercially available. SiPMs are analog detectors (output signal proportional to number of input photons) that are primarily used in applications in fields such as nuclear physics, nuclear medicine etc., where the incoming photons usually arrive simultaneously in few numbers. SiPM is designed using standard CMOS technology and offer exciting advantages, but it is not used in photon counting applications as digital detectors, mainly due to their high dark count rate (DCR). This thesis investigates the photon counting properties of SiPM and demonstrates, for the first time, their use for detecting very weak fluorescence signals. SiPMs have high level of noise such as cross-talk and after-pulsing. This thesis investigates the noise of SiPM when used as a photon counter. Furthermore, this work demonstrates, for the first time, DNA-sequencing with SiPM, opening up a new application area, and potentially more, for this device. Multi-channel photon counting systems based on large-area SPAD (>200 μ m diameter) are needed in some applications, for e.g. multi-lane DNA-sequencing, but are unavailable. SiPM arrays are relatively easy to design and fabricate (CMOS), facilitating design of multi-channel photon counting systems and hence high-throughput and highly sensitive DNA-sequencing at low-cost.

TABLE OF CONTENTS

LIST OF FIGURES	VIII
LIST OF TABLES	XVI
ACKNOWLEDGEMENTS	XVII
PUBLICATIONS	XX
INTRODUCTION: MOTIVATION, FOCUS OF THIS THESIS, CONTRIBUTIONS AND ORGANIZATION.....	1
CHAPTER 1	10
ANALYSIS OF DNA-SEQUENCING INSTRUMENTS BASED ON SOLID- STATE SINGLE PHOTON DETECTORS	10
1.1 ROLE OF FLUORESCENCE DETECTION IN DNA-SEQUENCING	10
1.2 UNDERSTANDING DNA-SEQUENCING RESULTS	11
1.3 CHARACTERIZATION OF CE-BASED SEQUENCING SYSTEMS.....	15
1.4 DETECTOR REQUIREMENTS FOR DNA-SEQUENCING APPLICATION.....	19
1.5 SOLID-STATE SINGLE PHOTON DETECTORS AS DETECTORS FOR DNA-SEQUENCING	21
1.6 SUMMARY	23
CHAPTER 2.....	25
SINGLE PHOTON AVALANCHE DIODE, SILICON PHOTOMULTIPLIER AND QUENCHING CIRCUITS	25
2.1 TRENDS IN PHOTON DETECTION TECHNIQUES	26
2.2 SPAD VERSUS SiPM.....	29
2.3 PRINCIPLE OF OPERATION OF SPAD AND SiPM.....	30
2.4 REVIEW OF IMPORTANT PERFORMANCE PARAMETERS.....	39
2.5 PROGRESS AND COMMERCIAL AVAILABILITY OF LARGE-AREA SPADS AND SiPMs	47
2.6 CHOICE OF SPAD AND SiPM FOR DNA-SEQUENCING APPLICATION	50
2.7 FIBERIZATION OF SPAD MODEL C30902S-DTC.....	53
2.8 REVIEW OF QUENCHING CIRCUITS (QCs)	55
CHAPTER 3	64
SINGLE-CHANNEL SINGLE PHOTON COUNTING MODULE (S-SPCM): DESIGN, IMPLEMENTATION AND CHARACTERIZATION	64
3.1 STAND-ALONE PHOTON-COUNTING MODULE.....	65
3.2 DESIGN OF HIGH-SPEED MIXED-SIGNAL QUENCHING CIRCUIT	67
3.2.1 <i>Results and Discussion</i>	76
3.2.2 <i>Improved Timing and Logic Circuit</i>	84
3.2.3 <i>Summary</i>	86
3.3 DESIGN AND TESTING OF TEMPERATURE CONTROLLER.....	87
3.4 DESIGN AND TESTING OF POWER SUPPLY MODULE	92

3.5 COMPLETE SINGLE-CHANNEL PHOTON COUNTING MODULE (S-SPCM).....	94
3.6 EXPERIMENTAL RESULTS AND DISCUSSION	96
3.6 SUMMARY	113
CHAPTER 4.....	116
MULTI-CHANNEL SINGLE PHOTON COUNTING MODULE (M-SPCM): DESIGN, IMPLEMENTATION AND CHARACTERIZATION	116
4.1 SPAD MODEL C30902S: EXPERIMENTAL RESULTS AND DISCUSSION.....	118
4.2. DESIGN OF 16 AND 32-CHANNEL PHOTON COUNTING MODULES	121
4.3 FEATURES AND SHORTCOMINGS OF THE DESIGNED M-SPCMS	126
4.4 EXPERIMENTAL RESULTS AND DISCUSSION	129
4.5 APPLICATION OF 32-CHANNEL MODULE TO SPECTROGRAPHY	135
4.6 SUMMARY	139
CHAPTER 5.....	141
INVESTIGATION OF SILICON PHOTOMULTIPLIERS AS HIGH-SPEED PHOTON CENTERS AND THEIR APPLICATION TO DNA-SEQUENCING..	141
5.1 INTRODUCTION.....	141
5.1.1 <i>Why SiPM can be used as Detectors in Certain High-speed Photon Counting Applications</i>	143
5.1.2 <i>Advantages of using SiPM as Detector for Photon Counting Applications as Compared to Large-area SPAD</i>	145
5.1.3 <i>Feasibility of Using SiPM as Detector for DNA-sequencing</i>	146
5.1.4 <i>Summary</i>	148
5.2 COOLED SiPM: EXPERIMENTAL RESULTS AND DISCUSSION	149
5.2.1 <i>The Device</i>	149
5.2.2 <i>Temperature Control & Biasing Circuit</i>	150
5.2.3 <i>Experimental Set-up</i>	154
5.2.4 <i>Electrical Characterization</i>	156
5.3 HAMAMATSU MPPCs: EXPERIMENTAL RESULTS AND DISCUSSION.....	172
5.3.1 <i>Experimental Set-up</i>	172
5.3.2 <i>Electrical Characterization</i>	174
5.4. AFTER-PULSING AND CROSS-TALK IN SiPM (NOISE ANALYSIS)	188
5.4.1 <i>Cross-talk Mechanism and its Effect on Photon Counting Performance of SiPM</i>	196
5.5 SUMMARY	198
CHAPTER 6.....	201
DNA SEQUENCING WITH SOLID-STATE SINGLE PHOTON DETECTORS	201
6.1 EXPERIMENTAL SET-UP.....	201
6.2 INTEGRATION OF DETECTOR MODULES INTO SINGLE-LANE DNA-SEQUENCER	202
6.4 SEQUENCING RESULTS	206
6.4.1 <i>Sequencing with individual detectors (S-SPCM and SiPMs)</i>	206
6.4.2 <i>Multi-lane DNA-sequencing</i>	212
6.5 SUMMARY	213

CHAPTER 7	215
CONCLUSION AND FUTURE WORK	215
7.1 CONCLUSIONS	216
7.2 RECOMMENDATIONS FOR FUTURE WORK	219
BIBILOGRAPHY.....	221
LIST OF ABBREVIATIONS	234
APPENDIX A.....	236
DETAILED CIRCUIT DIAGRAM AND LAYOUT FILES OF THE DESIGNED PCB.....	236

LIST OF FIGURES

Figure 1.1 Single-lane DNA-sequencer. (A) General view (1 - High voltage supply with a built-in voltmeter and current-meter; 2 - polymer replacement system; 3 - temperature control system; 4 - tube-changer carousel; 5 – fiberized precision optical system), (B) Schematics showing principle of operation. 11	11
Figure 1.2 Typical DNA-sequencing trace; beginning (top) and end (bottom) of sequencing run..... 12	12
Figure 1.3 (a) Typical sequencing trace obtained in large scale sequencing with standard dye, (b) Variation of SNR with signal. 13	13
Figure 1.4 Quality Factor graph for DNA-sequence detection 14	14
Figure 2.1 Photon Number Counting (SPAD) Vs Photon Number Resolving (SiPM). 30	30
Figure 2.2 Principle of operation of a reverse biased p-n junction. 31	31
Figure 2.3 Impact ionization (left) and avalanche multiplication (right) in APD. . 32	32
Figure 2.4 Avalanche multiplication in the geiger mode (multiplication faster than extraction) (left) and operating regime of SPAD (right)..... 34	34
Figure 2.5 (a) Microphotograph of a typical SiPM pixel [84], (b) topology of a SiPM [84] and (c) matrix of independent pixels arranged on a common substrate and connected to a common output load resistor [38]. 35	35
Figure 2.6 SiPM equivalent circuit 35	35
Figure 2.7 SPAD model C30902S fiberization system; (a) graphical representation of the problem; (b) FC/PC connector and mount ring; (c) CAD design; (d) photo of implementation. 54	54
Figure 2.8 Principle of operation of quenching circuit. 56	56

Figure 2.9 Typical passive quenching circuit (PQC)	56
Figure 2.10 Active quenching circuit [39]	60
Figure 3.1 Block diagram of a stand-alone photon counting system.....	66
Figure 3.2 Circuit diagram of the quenching circuit. For more detailed circuit diagram see Figure A.1.	68
Figure 3.3 Timing and logic circuit; case 1: when no photon is detected.	73
Figure 3.4 Timing and logic circuit; case 2: when a photon is detected.	74
Figure 3.5 First prototype of the designed QC.	77
Figure 3.6 Output pulse from the quenching circuit sent to the counter.....	78
Figure 3.7 Quenching pulse. Measured using 10X probe.....	78
Figure 3.8 Quench (a) and reset (b) delay pulse (precisely matched).	79
Figure 3.9 Quenching circuit output pulse (a), Quench delay pulse (b) and reset delay pulse (c).	83
Figure 3.10 Circuit diagram of the improved quenching circuit. For detailed circuit diagram refer to Figure A.5.....	85
Figure 3.11 Circuit diagram of the implemented temperature controller.	89
Figure 3.12 First prototype of the temperature controller circuit (front and back).	89
Figure 3.13 Variation of the thermistor resistance on C30902S-DTC.....	90
Figure 3.14 Bridge circuit formed in Figure 3.12 used to calculate the voltages to set different temperatures on SPAD.....	91

Figure 3.15 Calculated voltage values to set different temperature on SPAD. ...	92
Figure 3.16 Circuit diagram of the designed power supply module	93
Figure 3.17 Designed PCB; front side (left) and reverse side with mounted fiberized SPAD (right).....	95
Figure 3.18 Implemented S-SPCM; (a) closed module showing fiberized SPAD, (b) open module shown mounting PCB and (c) with power supply module. 95	
Figure 3.19 S-SPCM: Block diagram of the experimental set-up used for characterization.	96
Figure 3.20 S-SPCM: Photo of the experimental set-up.	97
Figure 3.21 S-SPCM: Variation of V_{BR} with temperature.	98
Figure 3.22 S-SPCM: Variation of PCR with comparator threshold (V_{TH}).	100
Figure 3.23 S-SPCM: Stability.	101
Figure 3.24 S-SPCM: Variation of DCR with V_{OV} at -20°C (top) and $+22^{\circ}\text{C}$ (bottom).....	103
Figure 3.25 S-SPCM: Variation of DCR with temperature at three different V_{OV}	104
Figure 3.26 S-SPCM: Histogram of photo count distribution at the detector output as compared to Poisson distribution.....	105
Figure 3.27 S-SPCM: Experimental set-up for characterizing sensitivity.	107
Figure 3.28 S-SPCM: Attenuation versus PCR at different V_{OV}	108
Figure 3.29 Attenuation versus PCR of S-SPCM at different V_{OV} plotted against attenuation versus PCR of PKI SPCM.	109
Figure 3.30 S-SPCM: Attenuation versus PCR after changing the value of the power supply resistor to $10\text{k}\Omega$ (R_3 in Figure A.1).	110

Figure 3.31 S-SPCM: Signal-to-Noise ratio.	111
Figure 3.32 Comparison of linearity and DR of the designed S-SPCM at $10V_{OV}$ with PKI SPCM.	113
Figure 4.1 Testing of un-cooled SPAD model C30902S.	118
Figure 4.2 C30902S: Variation of DCR with over-voltage.	119
Figure 4.3 Sensitivity and linearity of SPAD model C30902S.	121
Figure 4.4 Block diagram of the 16-channel single-photon counting module... ..	122
Figure 4.5 Photos of the implemented 16-channel module; (A) front view of photon detection module and optical detection module for light collection, (B) 16 PCBs with output of each connected to 16-channel counter, (C) Top view.	125
Figure 4.6 32-channel module; (A) Block diagram, (B) photo (C) photo of 1-channel PCB.	126
Figure 4.7 Comparison of DCR of 50 SPADs ($T = -20^{\circ}C$, $V_{OV}=10V$).	130
Figure 4.8 Output count rates of each channel of the 16-channel module.	131
Figure 4.9 Output count rates of each channel of the 32-channel module.	132
Figure 4.10 Linearity of the 16-channel module.	133
Figure 4.11 Linearity of the 32-channel module.	133
Figure 4.12 Noise of the designed M-SPCM.	134
Figure 4.13 Application of the designed 32-channel photon counting module to spectrography.	136
Figure 4.14 System color matrix.	138

Figure 4.15 DNA sequencing traces obtained with the spectrometer	138
Figure 4.16 Base calling quality scores obtained with the spectrometer.....	139
Figure 5.1 Typical system configuration for photon counting with SiPM.	144
Figure 5.2 Photos of the cooled SiPM (a, b). TEC is clearly visible in (b).	150
Figure 5.3 Cooled SiPM: Variation of thermistor resistance with temperature.	151
Figure 5.4 Bridge circuit formed in Figure 3.11 used to calculate the voltages to set different temperatures on SiPM.	152
Figure 5.5 Cooled SiPM: Biasing circuit.....	153
Figure 5.6 Cooled SiPM: Optical set-up used for characterization.....	155
Figure 5.7 Photo of the experimental set-up used for characterizing all SiPMs.	155
Figure 5.8 Cooled SiPM: Variation of V_{BR} with temperature.	156
Figure 5.9 Cooled SiPM output pulses; (a) Low V_{OV} (b) High V_{OV} (~8V).....	157
Figure 5.10 Cooled SiPM: Variation of DCR with V_{OV} at +25°C.....	158
Figure 5.11 Cooled SiPM: Variation of DCR with V_{OV} at -20°C (linear scale) ..	159
Figure 5.12 Cooled SiPM: Variation of DCR with V_{ov} at -20°C (log scale)	159
Figure 5.13 Variation of DCR with comparator threshold at $T=-20^{\circ}\text{C}$	160
Figure 5.14 Cooled SiPM: Block diagram of the experimental set-up for sensitivity measurement.	164
Figure 5.15 Cooled SiPM: Attenuation versus PCR at different V_{OV}	164

Figure 5.16 Attenuation versus PCR of PKI SPCM versus Cooled SiPM for increasing V_{OV} .	165
Figure 5.17 Cooled SiPM: Signal-to-Noise ratio.	166
Figure 5.18 Comparison of cooled SiPM at 10Vov with PKI SPCM.	167
Figure 5.19 Comparison of linearity of cooled SiPM at 10Vov with PKI SPCM.	168
Figure 5.20 Cooled SiPM: Block diagram of the experimental for measuring sensitivity to different wavelengths.	169
Figure 5.21 Cooled SiPM: Sensitivity at four different wavelengths.	170
Figure 5.22 Optical set-up for characterizing 100-pixel and 1600-pixel MPPCs.	173
Figure 5.23 Fiberized connecter used for focusing light on MPPCs.	174
Figure 5.24 Output pulses, (a, b) 100-pixel device, (c, d) 1600-pixel device at low (left) and high (right) V_{OV} . Note: (c) was recorded in the averaging mode.	176
Figure 5.25 Variation of DCR with V_{Bias} for 100-pixel and 1600-pixel device.	178
Figure 5.26 Variation of DCR with comparator threshold for 100-pixel and 1600-pixel device ($V_{Bias} = V_{OP}$).	180
Figure 5.27 100-pixel device: Variation of DCR and PCR with comparator threshold ($V_{Bias}=V_{OP}$).	180
Figure 5.28 1600-pixel device: Variation of DCR and PCR with comparator threshold at $V_{Bias} =V_{OP}$ and $V_{OP}+1V$.	181
Figure 5.29 100-pixel device: Sensitivity, DR and linearity.	182
Figure 5.30 1600-pixel device: Sensitivity, DR and linearity.	183

Figure 5.31 Comparison of sensitivity, DR and linearity for 100-pixel and 1600-pixel device.....	184
Figure 5.32 100-pixel device: Signal-to-Noise ratio.	186
Figure 5.33 1600-pixel device: Signal-to-Noise ratio.	186
Figure 5.34 Recording of counts for noise analysis (integration time is 10ms).	190
Figure 5.35 Histogram of the recorded counts shown in Figure 5.32.....	190
Figure 5.36 Cooled SiPM: Variation of mean and variance with V_{OV} and V_{TH}	191
Figure 5.37 100-pixel device: Variation of Mean and Variance with V_{OV} and V_{TH}	191
Figure 5.38 1600-pixel device: Variation of Mean and Variance with V_{OV} and V_{TH}	192
Figure 5.39 Mean and variance of 100-pixel device in dark and light.	195
Figure 5.40 Mean and variance of 1600-pixel device in dark and light.	195
Figure 5.41 Effect of cross-talk on photon counting performance of SiPM.	197
Figure 6.1 Typical set-up for DNA-sequencing experiment.....	202
Figure 6.2 Electrical set-up for performing DNA sequencing with SiPMs.	204
Figure 6.3 Output pulse from the 32-channel amplifier circuit.....	204
Figure 6.4 Block diagram of the complete DNA-sequencing set-up used for SiPMs.....	205
Figure 6.5 Photo of the complete DNA-sequencing set-up used for SiPMs.....	205
Figure 6.6 S-SPCM (C30902S-DTC): DNA-Sequencing traces (Laser power = 18mW).....	207

Figure 6.7 Cooled SiPM: DNA-sequencing traces (Laser power = 17mW).....	208
Figure 6.8 Hamamatsu MPPCs: Typical sequencing traces (Laser power = 17mW).....	209
Figure 6.9 Quality factor curves for all four SiPMs obtained using universal Phred software; (a) S-SPCM (SPAD), (b) 100-pixel SiPM, (c) 400-pixel SiPM,(d) 1600-pixel SiPM.	210
Figure 6.10 Fragment of the sequencing trace between 600 and 700 bases obtained with the 16-channel photon counting module. BigDye™ Sequencing Standard (ABI, CA, USA) diluted to 1: 64 in formamide.	212
Figure A.1 Detailed circuit diagram of the quenching circuit shown in Figure 3.2. S-SPCM and 16-channel M-SPCM are based on this circuit.....	236
Figure A.2 Detailed circuit diagram of the temperature controller circuit for SPAD model C30902S-DTC.	237
Figure A.3 Layout of the implemented circuits. PCB consists of quenching circuit and temperature controller circuit. The thick blue and red tracks are for supporting the high current switching in temperature controller circuit. Photo of fabricated PCB is shown in Figure 3.17.....	238
Figure A.4 Layout view showing component placements	239
Figure A.5 Detailed circuit diagram of the Improved quenching circuit shown in Figure 3.10; 32-channel M-SPCM is based on this circuit.....	239
Figure A.6 PCB layout consisting of improved quenching circuit and temperature controller.....	240
Figure A.7 Photo of fabricated PCB. 32-channel photon detection module is based on this PCB.....	240

LIST OF TABLES

Table 1.1 Comparison of PMT with a solid-state single photon detector.....	22
Table 1.2 Effects of DCR and PDE on SNR of DNA-sequencer.	23
Table 2.1 Typical detector materials and their detection wavelength range.....	39
Table 2.2 Typical specifications of APD series C30902S from PKI [4].	51
Table 3.1 Summary of important performance parameters of the designed S- SPCM and comparison with PKI SPCM.	115
Table 5.1 Specifications of the cooled SiPM at +25°C.	149
Table 5.2 Comparison of TEC specifications of SPAD model C30902S-DTC and Cooled SiPM.	151
Table 5.3 Calculated values of V_{TP4} to set different temperatures on the cooled SiPM.....	152
Table 5.4 Specifications of the characterized Hamamatsu MPPCs [6].	172
Table 5.5 Comparison and summary of important performance parameters of all the three characterized SiPMs.	199

ACKNOWLEDGEMENTS

Life at Stony Brook would not have been the same without the guidance, support, encouragement, friendship and love of many wonderful people. I would like to take this opportunity to express my gratitude to most of them.

First of all, this research would not have culminated into this dissertation without the help and support of my academic advisor Dr. Vera Gorfinkel. I am extremely grateful to her for providing me with this wonderful and exciting opportunity. Her enthusiasm and acute acumen for research and her humble, considerate, kind and caring nature is very infectious. I am immensely proud to have been associated with her and her Florescence Detection Lab. I would like to express my gratitude to Professor Hang-Sheng Tuan, Professor Dmitri Donetski, Dr. Andriy Tsupryk and Professor Clark McGrew for serving as members of my Defense Examination Committee. I would also like to thank the staff in the Electrical Engineering Dept. for their assistance, especially Deborah Kloppenburg.

Many people in the fluorescence detection lab have contributed to this work. Thanks to all members of this lab for assistance at various stages: Tatyana, Andrey, Andriy, Ivan, Lu, Anatoly, Gregory, Olga, Dmitri, Marina and Georgiy. Special thanks go to George Gudkov for answering hundreds of my questions with amazing patience. He made me a much better engineer.

I have made some friends for life at the university in Prashant, Prachi, Gaurav, Mandeep, RajjiBhabhi, Keyur, Navin, Sumeet, Dhaval, Manu and Zankhana with whom I share great memories and who have been great friends in good and bad times. Their support, encouragement and friendship kept me going. They are my family in this country. Special thanks to Prashant for help during my qualifiers, Prachi for honest criticism and encouragement, Mandy for valuable suggestions, RajjiBhabhi for great food (especially during her stay at F2088), Navin for great deals and useful discussions, Keyur for wonderful trips and Manu for the cricket and the coffee breaks while I was writing this dissertation. Also, visit to Mandeep's place felt like home away from home and those moments with Ansh are invaluable. I would also like to thank my ex-boss and now a good friend Mr. Dave Jagsarran who made my experience on the campus a unique and memorable one. His selfless support and encouragement has been invaluable. Special thanks go to my long-time pals Chirag Desai for those everyday calls that lightened me up and the west-coast trip, Dr. Amit Bavisi, Amit Sheth, Vishal Shah and Divyang Patel for their selfless inspiration, friendship and valuable suggestions. Finally, I would like to all my friends that I made during the last five years at Stony Brook with whom I share good memories: Parag, Chhavi, Ritwij, Priya, Ravi, Somnath, Siddharth, Navani, Jha, Gajju, Samrat, Bhaskar, Santosh, Vamsi, Jaggi, Gisselle, Amber and Ivan.

Finally, it's time to mention the people who matter the most and have showered unconditional love, support and sacrifice, my parents, Mr. Hemendra Dhulla and Mrs. Usha Dhulla, my loving brother Tejas and my sister Rachana. I am really thankful to my dad for allowing me to always pursue what I wanted and my little brother for believing and supporting me in whatever I did. Special thanks to the Asher family for their love,

support and encouragement and my favorite, Yunali (Manu). Finally, I feel from the bottom of my heart that I would not be what I am today without the support of Nutan, a friend, philosopher and guide. She made me believe in myself and forced me to keep studying. Her long inspiring talks and unconditional love and support through good times and bad are something that I will cherish for life. I know she is the happiest and proudest today.

PUBLICATIONS

So far, following publications have been the outcome of this research.

[1] **V. Dhulla**, G. Gudkov, D. Gavrilov, A. Stepukhovich, A. Tsupryk, O. Kosobokova, A. Borodin, B. Gorbovitski and V. Gorfinkel, "Single Photon Counting Module Based on Large-area APD and Novel Logic Circuit for Quench and Reset Pulse Generation," IEEE J. Select. Topics Quantum. Electron., Vol. 13, no. 4, pp. 926-933, , July/August 2007.

[2] G. Gudkov, **V. Dhulla**, A. Borodin, D. Gavrilov, A. Stepukhovich, A. Tsupryk, B. Gorbovitski, V. Gorfinkel, "32-channel single-photon counting module for ultra-sensitive detection of DNA sequences", conference on Advanced Photon Counting Techniques, Proc.of SPIE vol.6372, 63720C, Boston, Massachusetts, USA Oct 1-4, 2006.

[3] **V. Dhulla**, G. Gudkov, A. Stepukhovich, A. Tsupryk, O. Kosobokova, D. Gavrilov, V. Gorfinkel, "Single photon detection module for multi-channel detection of weak fluorescence signals", conference on Smart Medical and Biomedical Sensor Technology III, Proc.of SPIE Vol.6007 600719-1, pp. 1-9, 2005.

INTRODUCTION: Motivation, Focus of this Thesis, Contributions and Organization

Motivation

One of the major goals of human genome project (HGP) [1], which begun formally in 1990, is to determine the sequences of the 3 billion base pairs that make up human DNA. The mapping of human genes is an important step in the development of medicines and other aspects of health care. As a consequence of the HGP, there will be a more thorough understanding of the genetic bases of human biology and of many diseases. This, in turn, will lead to better therapies and, perhaps more importantly, prevention strategies for many of those diseases. Similarly, as the technology developed by the HGP is applied to understanding the biology of other organisms, many other human activities will be affected including agriculture, environmental management, and biologically-based industrial processes [2]. At current technology state, the cost of mammalian size genome is of the order of 1-10 million USD and the desired goal is to bring down the cost of sequencing such a genome to 1000 USD. Therefore, 3-4 orders of magnitude reduction of the DNA sequencing cost is one of the major goals in the development of the sequencing technology and instrumentation. All DNA-sequencing instruments use some kind of photon detection systems. One method of reducing the over-all cost of DNA-sequencing is to either increase the sensitivity or reduce the cost of these photon detection systems or both. This is the major motivation behind conducting this research.

Currently cost of single-lane DNA-sequencers makes them practically unaffordable by the university research labs for performing day to day research. Hence, there is a strong need for low-cost DNA-sequencers affordable by the university labs. One way of reducing the cost of DNA-sequencers is to reduce the cost of photon detection systems.

Finally, new applications are still being realized that required detection of ultra-weak fluorescent signals of the order of femto watts. Hence, there is an increasing need for highly sensitive photon detection systems.

Focus of this thesis and accomplished research

The total cost of genome sequencing is constituted by several factors. Among them, most important are the cost of consumables and the cost of equipment, cost of consumable being higher than the equipment cost. The amount of consumables used can be significantly decreased by increasing the sensitivity of DNA-sequencing instruments, thus facilitating significant reduction of the total cost per sequenced base pair. The equipment related cost mainly depends on the throughput of the DNA sequencing machines. By increasing the throughput of existing instruments we can read more base pairs in the same time, therefore reducing the equipment cost. This thesis investigates solid-state single photon detectors to improve sensitivity and cost of sequencing.

DNA-sequencing instruments use photon detection systems (mostly PMT) for detecting the fluorescence emitted by the DNA molecule. These photon detection systems determine the sensitivity of DNA-sequencing. Although, PMT can detect low light levels, they suffer from problems such as low photon detection efficiency (PDE) (7-10% for a

typical PMT), high noise, and requirement of power supply in KV range etc. to name a few. Recently, highly sensitive solid-state detectors namely Single Photon Avalanche Diodes (SPADs) (in the late 90's) and Silicon Photomultipliers (SiPM) (in early 2007) became commercially available. SPAD is a digital detector suitable for photon counting applications such as DNA-sequencing whereas SiPM is an analog detector primarily designed for resolving photon numbers and hence not the ideal detector for counting photons in DNA-sequencing application. Both the detectors have numerous advantages as compared to a PMT. Although single photon detection based on SPAD is the most sensitive method of detecting weak fluorescence signals, it is not used in DNA-sequencing due to the complexity of the involved optics. To our knowledge, use of SiPM in photon counting applications has not yet been investigated.

The focus of this thesis is to investigate these solid-state detectors (SPAD and SiPM) for ultra-weak fluorescence detection and design cost-effective, highly sensitive single and multi-channel single photon counting systems (SPCSs) based on these detectors to achieve the goal of performing highly sensitive, high through-put DNA-sequencing at low-cost. In this regard the accomplished research is listed as follows:

1. **Investigation of the feasibility of using SPAD as detector for highly sensitive DNA-sequencing.**

Current DNA-sequencers either use PMT or a charged couple device (CCD) as photon detectors for detection of weak fluorescence signals. Recently, highly sensitive solid-state detectors called SPADs became commercially available. It is known that DNA-sequencing can be performed with a SPAD, but it is still not used due to the complexity of the involved optics. To perform high-speed photon detection and counting,

SPADs need to be used in conjunction with special circuit called quenching circuit (QC). A high-performance, highly sensitive single-channel single photon counting module (S-SPCM) was designed based on commercially available large-area SPAD having 0.5mm (500 μ m) diameter; model C30902S-DTC from Perkin Elmer Optoelectronics (PKI) (Chapter 3). The S-SPCM was designed keeping in mind its application to four color fluorescence detection. Following sub-tasks were accomplished in the design of the whole module:

- Design and characterization of high-speed quenching circuit. A novel, completely digital timing and logic circuit was designed to generate precisely matched, accurate quench and reset delay pulses in the quenching circuit.
- Highly stable ($\pm 0.001^\circ\text{C}$) temperature controller based on temperature controller IC Max1978 was designed and tested.
- Stand-alone power supply module for all the sub-modules.

All performance aspects of the designed S-SPCM were characterized. Further, the designed S-SPCM was integrated into a single-lane DNA-sequencer and DNA-sequencing was successfully carried out, *thus providing, for the first time, experimental demonstration of the application of large-area SPAD to DNA-sequencing.*

High performance single photon counting modules (SPCMs) based on large-area SPAD (200-400 μ m diameter) are commercially available [3], but they are not a feasible option for two main reasons, (i) they cannot be customized for our application-specific needs and (ii) they are highly priced (~USD 4500 per channel). Our future goal was to design multi-channel photon counting systems; hence commercially available SPCM was not a feasible option. This led us to investigate and design our own systems.

2. **Design, development and characterization of multi-channel single photon counting modules (M-SPCM) based on large area SPAD.**

As discussed earlier, high throughput DNA sequencing is possible by performing multi-lane DNA-sequencing in parallel. Such sequencers require multi-channel photon detection systems. Arrays of high-performance large-area SPADs would be the ideal choice of detector for such a system, both cost wise and size wise. But, such arrays were not available commercially when this research was conducted and are still not available. Hence there was no choice, but to design multi-channel systems based on individual SPADs. 16-channel and 32-channel M-SPCMs based on the same SPAD model (C30902S-DTC from PKI) have been designed, tested and integrated into multi-lane DNA-sequencing instruments. Further, spectroscopy was performed in our lab with the designed 32-channel system, demonstrating adaptability of the designed systems to different applications (chapter 4).

3. **Investigation of silicon photomultipliers (SiPMs) as detector for high-speed photon counting applications & their application to DNA-sequencing**

SiPM is an analog detector primarily designed and used in photon number resolving applications as linear detector. It has not been reported to have been used in photon counting applications (digital detection) due to its rather high dark count rate (DCR). Although it suffers from high DCR, it is an exciting detector mainly because of its compatibility with the CMOS technology; hence low cost and prospects of availability of arrays of SiPMs. Three commercial SiPMs have been characterized as high-speed photon counters and their feasibility to be used as detectors for DNA-sequencing has been demonstrated (chapter 5). DNA-sequencing has been successfully carried out with

all the three characterized SiPMs (chapter 6). This basically opens *s up a new application for SiPM and vice-versa, i.e. range of new, highly sensitive, low-cost detectors can be used for DNA-sequencing as compared to only couple of choices available until now.*

Contributions

In summary, following research contributions are the outcome of this dissertation:

1. Characterization of SiPM as photon counter, optimal conditions for SiPM for DNA-sequencing application and first demonstration of the application of SiPM to DNA-sequencing.
2. First study of the effect of noise of SiPM on its photon counting performance.
3. Novel, fully digital timing and logic circuit for generating precisely matched accurate quench and reset delay pulses.
4. First experimental proof of the application of large area SPAD to DNA-sequencing.

Significance to the DNA-sequencing field

1. *Increased choice of detectors for DNA-sequencing.* So far, only two detectors were used for DNA-sequencing viz. PMT and CCD, but in this thesis DNA-sequencing was performed with 5 commercially available detectors and the results show that both SPAD and SiPM can be used for DNA-sequencing. Hence a wide range of detectors can now be used for this application. *Further, DNA-sequencing is a new field of application for SiPM.*

2. Cost of consumables is the highest in DNA-sequencing. Significant improvement in DNA-sequencing sensitivity (~ 10 fold) was observed with these detectors. Therefore, either more base pairs can now be resolved with the same amount of DNA-material or more diluted DNA-samples can be used with these detectors, both resulting in significant cost-reduction.
3. Large-area (up to $500\mu\text{m}$ diameter) SPAD arrays are needed in some applications (for e.g. multi-lane DNA-sequencing), but are unavailable. Since SiPM can be used as detector for DNA-sequencing, arrays of SiPM can be designed. Since SiPM is based on standard CMOS technology, SiPM arrays are relatively easy to design and fabricate at much lower cost, facilitating design of multi-channel photon detection system and hence high-throughput DNA-sequencing at low-cost. This will also facilitate the design of low-cost DNA-sequencers that can be affordable by the university research labs for day-to-day research.

Organization of this thesis

The remainder of the dissertation is organized as follows:

Chapter 1 discusses the role of photon detection in DNA-sequencing and introduces various parameters that are used to characterize a DNA-sequencer. It then explains the understanding of DNA-sequencing results mainly from photon detection point of view. Based on this understanding, important performance parameters that a detector for DNA-sequencing applications must have are formulated. Chapter concludes by discussing the advantages of using solid-state single photon detectors as detectors for DNA-sequencing.

This thesis focuses on the design of photon-counting systems based on two completely different types of solid-state single photon detectors viz. SPAD and SiPM. **Chapter 2** discusses the principle of operation of these two types of detectors, principle difference between them, their important performance parameters and their commercial availability. Then the selection of detector for our application and SPAD fiberization is discussed. Finally, since SPADs cannot be used as high-speed photon counters unless they are used with quenching circuits (QC), the chapter concludes with the principle of operation and review of different types of QCs.

Chapter 3 presents the design, implementation and characterization of a single-channel single photon counting module (S-SPCM) based on large area SPAD model C30209S-DTC from PKI. Development of S-SPCM required the design and characterization of important sub-modules is presented.

Chapter 4 presents the design, development and results of two (16 and 32-channel) unique multi-channel photon counting modules (M-SPCMs) for multi-lane DNA-sequencing. Shortcomings and features of the designed systems are discussed. Finally, the easy adaptability of the designed M-SPCMs to another application (spectrography) is experimentally demonstrated.

Chapter 5 presents in detail the electrical characterization of three selected SiPMs viz. the MAPD model VIC-FFK (referred to as cooled SiPM) from Voxel-Inc [5], the MPPC model S10362-11-100U and S10362-11-25U (referred to as 100 and 1600-pixel device respectively) from Hamamatsu Photonics [6] as high speed photon counters and studies their feasibility as detectors for DNA-sequencing application. Effect of noise on the use of SiPM as photon counters is studied in detail and optimum parameters for

best photon counting results are presented. DNA-sequencing is performed with these devices, the results of which are presented in chapter 6.

Chapter 6 discusses the integration of the designed S-SPCM and the SiPM based photon counting system into the single-lane DNA-sequencing set-up. Results of DNA-sequencing with each detector are presented and discussed.

Chapter 7 concludes the dissertation and recommends future work.

CHAPTER 1

ANALYSIS OF DNA-SEQUENCING INSTRUMENTS BASED ON SOLID-STATE SINGLE PHOTON DETECTORS

1.1 Role of Fluorescence Detection in DNA-sequencing

Figure 1.1A shows the photo of a single-lane DNA-sequencer that is used for characterizing the designed photon counting modules and Figure 1.1B shows a typical scenario in which a DNA-sample is passing through a capillary (50-150 μm diameter) and is irradiated by a laser. A labeled DNA sample undergoes separation in a single-capillary fiberized separation/reading module. The separated zones arriving at the detection window in the capillary are illuminated by a laser light delivered from a miniature fiberized laser source. The fluorescence from labeled DNA fragments is collected by a fiber receiver and delivered to the optical system (5 in Figure 1.1A). After appropriate filtering the fluorescence is focused on the photon detector (photon counting system) that produces an output pulse corresponding to each detected photon. These pulses are then transferred to a computer for recording, processing and graphical presentation. During the separation sequencing traces are displayed in real time on the computer screen. For detailed description and analysis of the DNA-sequencers based on single photon detection techniques refer to [7].

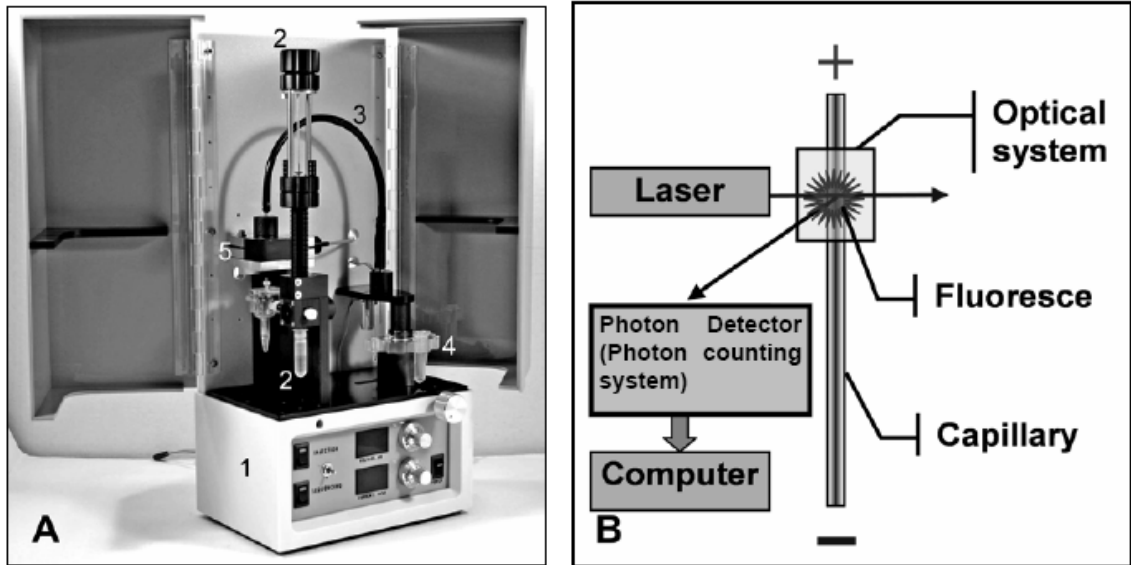


Figure 1.1 Single-lane DNA-sequencer. (A) General view (1 - High voltage supply with a built-in voltmeter and current-meter; 2 - polymer replacement system; 3 - temperature control system; 4 - tube-changer carousel; 5 – fiberized precision optical system), (B) Schematics showing principle of operation.

1.2 Understanding DNA-sequencing Results

Figure 1.2 shows the typical sequencing traces obtained from the sequencer at the start (top) and end (bottom) of a typical DNA-sequencing run. The X-axis represents the base pair number (read length) and Y-axis shows the background subtracted photon count rate (PCR) and it can be seen that the average PCR is in the range of $\sim 10,00,000$ Counts/s (1 MHz). A typical DNA-sequencing run takes about 60-90 minutes and the peaks start becoming visible after about 20-30 minutes. It can be seen that the pulses are narrow with much higher PCR and clearly separated at the beginning of the sequencing run (top frame) as compared to the end of the sequencing run where the pulses become smaller

(low PCR) and broader and hence difficult to resolve. At one point, the amplitude of the pulse becomes so low that they are difficult to detect. Pulse broadening happens because the small DNA-strands travel first and faster inside the capillary as compared to the longer strands. Since the longer strands travel slowly, they spend longer time inside the capillary which has the effect of pulse broadening and hence decrease in peak amplitude. The amplitude of the pulses depends on the laser power that irradiates the capillary and the sensitivity of the photon detector and the pulse separation depends on the quality of the separation medium and the polymer.

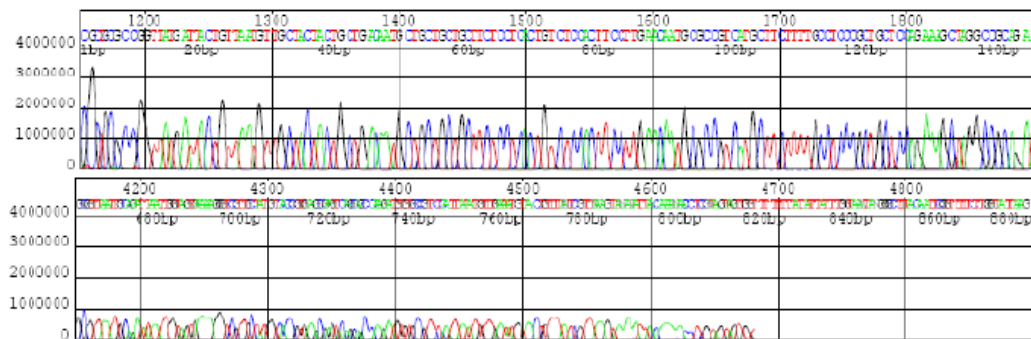


Figure 1.2 Typical DNA-sequencing trace; beginning (top) and end (bottom) of sequencing run.

Typically, DNA-sequencing traces to be detected can be divided into two types, viz. the traces obtained in large scale sequencing with standard dyes (Figure 1.2 and 1.3a (left)) and in cases when it is necessary to detect mutations in forensics and medicine where it may be necessary to detect two colored peaks in the same time as shown in Figure 1.3a (right). In the later case, quality of the DNA is unknown and can be very weak. Figure 1.3b shows the typical curve of variation of the SNR with signal and from

the aforementioned discussion it can be seen that for DNA-sequencing it is required to detect very weak signal. Since there is a strict requirement on the SNR to detect a particular base with high accuracy, it is very important that the associated electronics such as amplifiers, counters etc. add minimum noise. Hence single photon detectors are the best choice of detectors for such an application since they have the best sensitivity and add minimum noise apart from the fundamental noise of the photon flux. Further, apart from high sensitivity in order to detect wide range of signals and to detect two peaks with high accuracy, it is required that the photon detector have wide dynamic range and linearity.

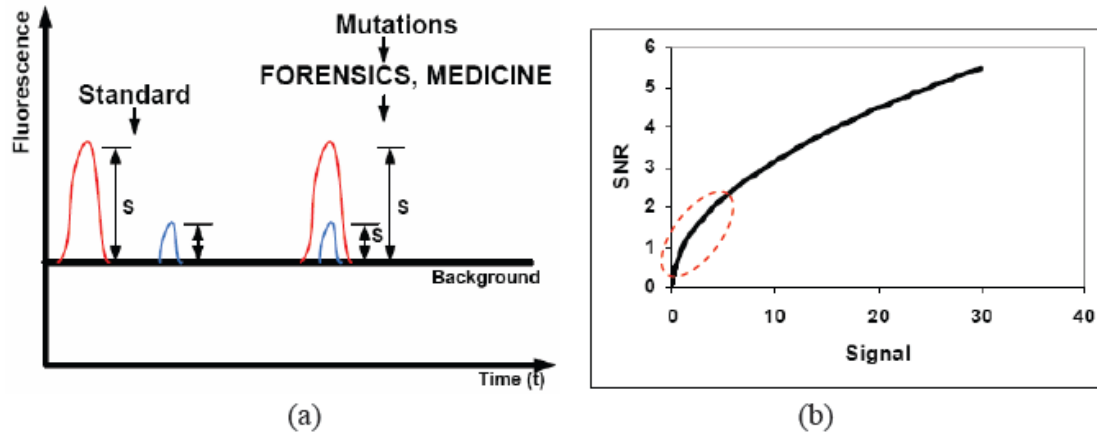


Figure 1.3 (a) Typical sequencing trace obtained in large scale sequencing with standard dye, (b) Variation of SNR with signal.

Finally the obtained traces (Figure 1.2) are processed using the standard Phred software. Phred is a base-calling program for DNA sequence traces. Phred reads DNA sequence chromatogram files (Figure 1.2) and analyzes the peaks to call bases, assigning quality scores ("Phred scores") to each base call [37]. Quality scores range from 4 to

about 60, with higher values corresponding to higher quality. Phred can read input files in two formats viz. (a) SCF ("Standard Chromatogram Format") files which is the universal format for trace sequence files that is supported by many different programs and manufacturers and (b) Applied Biosystems (ABI) chromatogram files. As per the sequencing standard, a quality score (quality factor, QF) of 20 or more is required to call the base with 99% accuracy. Figure 1.4 shows a typical QF graph. The number of base-pairs with $QF \geq 20$ determines the read-length of sequencing and hence the higher the read length the better the quality of sequencing. It can be seen that as the pulses in Figure 1.2 become smaller and wider towards the end of sequencing, the QF starts decreasing and at one point it goes below 20. Hence, if the photon detector has higher sensitivity, it will be able to detect the smaller peaks with high accuracy, this increasing the resolved base pairs. This would facilitate the use of either less consumables or more diluted DNA material, thus lowering the cost of DNA-sequencing. It must be mentioned that the cost of DNA-sequencing is dominated by the cost of consumables.

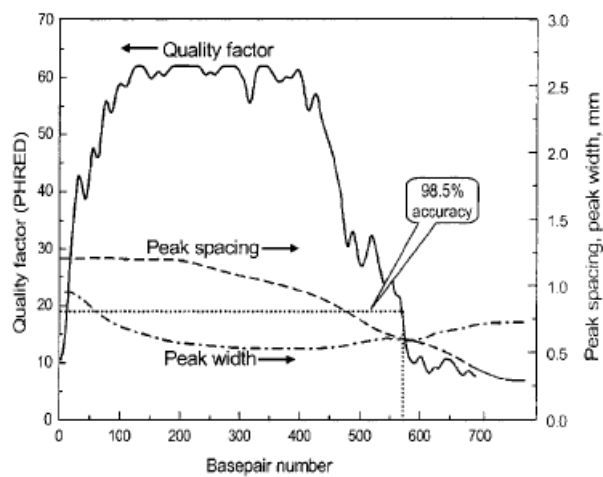


Figure 1.4 Quality Factor graph for DNA-sequence detection

1.3 Characterization of CE-based Sequencing Systems

This section presents theoretically the important parameters described in last section that are used to characterize CE based DNA-sequencer based on single photon detection technique.

Sensitivity and read length (theory)

Sensitivity of a DNA sequencing system is defined as the minimum (threshold) concentration of labeled DNA fragments $n_{DET,TH}$ needed for the detection of the separated bands of DNA fragments with a signal-to-noise ratio SNR greater than SNR_{TH} . This implies that the signal detected at the peak maximum must be:

$$A_{DET} > SNR_{TH} \times Noise \quad (1.1)$$

It has been experimentally determined that our base calling software requires resolution $SNR_{TH} \geq 4$ in order to achieve the quality score of 20, which is considered as a minimum successful base calling score. In order to characterize the sensitivity of DNA sequencer, we need to measure the noise of the sequencing system and determine a signal Φ (Equation 1.6) detected by the system from a single DNA fragment per 1mW of the excitation power P_{Laser} . Using the obtained Φ we can calculate the threshold concentration of labeled DNA fragments $n_{DET,TH}$ at the maximum of the separated band needed for a successful detection of the band:

$$n_{DET, TH} = \frac{A_{DET, TH}}{\Phi \times P_{Laser} \times V_{DET}} \geq \frac{SNR_{TH} \times Noise}{\Phi \times P_{Laser} \times V_{DET}} \quad (1.2)$$

where V_{DET} is the detection volume in the separated band.

Sensitivity of the DNA sequencer based on single photon detection

Generally, in single photon detection systems the major noise component is the stochastic noise of the detected photon flux [8]. Other noise components are associated with the dark count of the photon detector and the background of the sequencer. Therefore the signal-to-noise ratio (SNR) of the sequencer is represented by:

$$SNR = \frac{Signal}{Noise} = \frac{S \times T_{INT}}{\sqrt{(S + B + DC) \times T_{INT}}} \quad (1.3)$$

where S is the registered photo count rate (PCR) induced by useful fluorescence, B is the PCR due to the background radiation, DC is the dark count of the photon detector and T_{INT} is the integration time. The background radiation in our sequencer is mainly produced by the fluorescence of the separation polymer. Unfortunately, commercial separation polymers (POP-5, POP-6, POP-7, ABI, CA, USA [9]) fluoresce in the same spectral range as the most popular fluorescent markers (BigDye kits, ABI, CA, USA [9]), which makes the background an unavoidable part of the measured fluorescence. The fluorescence detected in the system depends on several factors, such as spectrum and power of the illumination source $P_{Laser(\lambda)}$, collection efficiency of the fluorescence radiation, and detection efficiency $\varepsilon_{DET}(\Delta\lambda)$ of the photodetector in the spectral range $\Delta\lambda$ in which the signal is detected. Since the peak height decreases by the end of a typical sequencing run, the background fluorescence becomes the main source of the system

noise. Thus, for the estimation of the minimum detectable peaks we can assume that $S \ll B$ and from Equations 1.1 and 1.3 obtain:

$$a_{DET, TH} = SNR_{TH} \times \sqrt{\frac{(b\Delta\lambda)}{(T_{INT} \times P_{Laser})}} \quad (1.4)$$

where a and b are the useful and background signals detected by the sequencer per 1mW of the illumination power and DC is neglected since \sqrt{DC} is very small. From equations 1.1, 1.2 and 1.4 we can find the threshold concentration of DNA fragments at the maximum of the detected band:

$$n_{DET, TH} = SNR_{TH} \frac{1}{\phi V_{DET}} \sqrt{\frac{\beta(\Delta\lambda)}{\epsilon_{DET} \times P_{Laser} \times T_{INT}}} \quad (1.5)$$

where, β is the signal emitted by the separation polymer per 1mW of excitation power and delivered to the photodetector. Φ is the signal emitted by a single DNA fragment per 1mW of excitation power P_{Laser} and delivered to the photodetector (Equation 1.6) and b is represented by Equation 1.7.

$$\phi = \varphi(\Delta\lambda) \times \epsilon_{DET}(\Delta\lambda) \quad (1.6)$$

$$b = \beta(\Delta\lambda) \times \epsilon_{DET}(\Delta\lambda) \quad (1.7)$$

Equation 1.5 shows that in single photon detection systems the threshold concentration of DNA fragments needed for the detection of fluorescent bands with SNR_{TH} decreases as square root of the illumination power, integration time and the detection efficiency.

Resolution of the DNA sequencer based on CE separation

Measure of the sequence resolution is estimated by the ratio of the peak spacing ΔX and the peak width W [10]-[11] by the following equation:

$$R = \frac{2 \times \Delta X}{W_1 + W_2} = \frac{t \Delta v}{W} \quad (1.8)$$

where ΔX is the distance between two adjacent bands and W_1 and W_2 are peak widths measured at half maximum, Δv is the difference in the velocity of fragments in two subsequent bands, t is the elution time and W is the peak width. The elution time is defined as $t = L_{DET}/v$, where L_{DET} is the capillary length to the detection window. The peak width W is introduced assuming that $W_1 \approx W_2$ for two subsequent bands. The selectivity of the system $\Delta v/v$ is determined by fragment migration mechanisms [12]. It was found experimentally that in order to achieve the quality score 20, our base-calling software requires that the resolution $R_{TH} \geq 0.75$.

Read length of the DNA sequencing system

We define the *read length* as a molecular size of DNA fragments K that can be: (i) resolved by the DNA sequencing system with resolution R higher than the certain threshold value R_{TH} , and (ii) detected by the sequence detection system with SNR greater than SNR_{TH} .

$$\begin{cases} R_K \geq R_{TH} \\ A_{DET, k, TH} \geq SNR_{TH} \times Noise \end{cases} \quad (1.9)$$

In order to estimate the read length achievable in a specific DNA sequencing system from Equation 1.9, we have to determine SNR_{TH} and R_{TH} required for a successful base calling, estimate or measure the system noise, to introduce a model for evolution of the peak width, peak spacing and peak amplitude during the period of time from the electro-kinetic injection to the detection of the peak, and relate the resolution R_K and the amplitude $A_{DET, K}$ of the detected peaks to characteristics of the separation medium, parameters of the electro-kinetic injection, and the sequence detection system (Equations 1.4 and 1.5).

1.4 Detector Requirements for DNA-sequencing Application

Based on the discussion so far, a detector suitable for high-performance DNA-sequencing must have following important features:

(a) High Sensitivity (High SNR): In the last section it was shown that as DNA-sequencing progresses, the peaks start becoming small and wider (see Figure 1.2). Sensitivity of a detector can be defined as the ability to detect these small peaks with a quality score ≥ 20 . This means that for a particular DNA-sample, a detector with higher sensitivity will be able to resolve more base pairs (higher read length) as compared to a

detector with low sensitivity. Therefore high sensitivity of the detector provides two very important advantages viz. (i) more resolved base pairs for the same DNA-sample and (ii) facilitates the use of more diluted samples, hence reducing the cost of consumables and hence DNA-sequencing.

(b) Low noise: DCR of the detector and the associated electronics adds to the noise of the DNA-sequencer as shown in Equation 1.3. Noise of the system varies a square root of the sum of all the noise components. In cases where the DCR of the detector is much lower than the background count rate, the DCR does not add much to the over-all noise of the system. Even if the DCR is higher than the background count rate, since the noise increases as the square root, the higher DCR does not affect the SNR much. Hence, unlike most of the other applications, high DCR of the detector is not a big issue for this application. But, it must be noted that a detector with high DCR puts a lower limit on the minimum detectable signal (MDS) from the noise.

(c) Wide dynamic range and linearity: To make a base call, the peaks are identified by the proportion of their colors. Also, depending on the wavelength of the laser that is used to shine the capillary, one base color (there are four, one for each acid of the DNA) will provide better response (will fluoresce more) than the others. Further the background fluoresces in the same wavelength spectrum as the signal and is unavoidable. This background noise is subtracted from the photo counts obtained due to each of the four colors. If the subtraction of this background is not accurate, it will influence the counts due to weaker peaks (low counts) much more than the counts due to the strong peak (high counts), i.e. the ratio of peaks may change much more after the subtraction of the background noise. In order to accurately measure both the peaks, the detector must

satisfy two important requirements (i) have wide dynamic range such that it can measure the highest and the lowest of the peaks and (ii) wide linear range such that both the peaks possibly fall in the linear range of the detector so that the difference is accurately known, enabling high accuracy in base calling.

(d) High resolution: As it was seen in the Figure 1.2, two pulses of different color overlap and hence consist of mixture of two colors. Therefore in order to detect the correct base, it is required that the detector has good resolution, which means that it must have sufficient difference between the count rates in the four different wavelengths of interest such that it can easily resolve peaks of different colors from one another in case they over-lap.

(e) Large active area: It has been experimentally determined in our lab that best light collection efficiency is obtained using a fiber with core diameter of 400 μ m. Hence detectors with active area diameter in this range are ideal for this application. If the detector has much lower diameter than the diameter of the fiber core, it will decrease the light collection efficiency (hence sensitivity) and also increase the complexity of the associated optics.

1.5 Solid-state Single Photon Detectors as Detectors for DNA-sequencing

From the aforementioned discussion it was established that a detector with single photon sensitivity having wide dynamic and linear range, large active area, low noise and

good resolution is required for best sequencing results. Until recently PMTs were the only choice of detectors that matched these requirements. Recently solid-state photon detectors that offer advantages over the PMT became commercially available, but are still not used in many applications because of the complexity of the involved optics. Table 1.1 shows the comparison of a typical single channel PMT with a typical solid-state detector having single photon sensitivity (SPAD).

Table 1.1 shows that all the parameters of the solid-state detector are better or comparable with the PMT, especially the PDE. High PDE means increased photo counts for the same amount of light, hence increased sensitivity. Sensitivity of the DNA-sequencer (SNR) was defined by Equation 1.3. Taking into account a PDE of 10% (maximum) for the PMT and 25% (minimum) for the solid-state detector, for the same output light power, the solid-state detector will measure 3 times more counts than the PMT. Table 1.2 shows the comparison of SNR for two different values of dark count considering typical value of back ground count rate B as 200 KHz.

Table 1.1 Comparison of PMT with a solid-state single photon detector

Factor	PMT (single channel)	Solid-state
PDE	Low (7-10%)	High (25-60%)
Voltage	KV	Few hundred
Receiving area	Too Large	Sufficient or small
Dynamic range	1 MHz	>10 MHz
Linearity	~ 1MHz	>1MHz

Table 1.2 Effects of DCR and PDE on SNR of DNA-sequencer.

Device	PDE (%)	T_{INT} (Sec)	B	S per molecule (S)	SNR (DCR = 1KHz)	SNR (DCR = 100KHz)
PMT	10	1	200000	10000	22	18
Solid-state detector	30	1	200000	30000	62	52

It can be seen that (i) SNR can be improved significantly (almost proportional to increase in PDE) by using a detector with high PDE and (ii) SNR does not depend much on the dark count of the detector, because while the signal increases linearly, DCR increases as the square root. Therefore it can be concluded that a solid-state detector with high PDE will provide a significant improvement in DNA-sequencing performance as compared to the PMT.

1.6 Summary

This chapter introduced the performance parameters of the single-lane DNA-sequencer developed in our lab. It was discussed in the introduction section that the cost of DNA-sequencing can be significantly reduced by lowering the cost of consumables. Amount of consumables used can be significantly decreased by increasing sensitivity of DNA sequencing instruments which would result in a significant reduction of the total

cost per sequenced base pair (highly diluted DNA-samples can be used). Single photon detectors have much higher PDE as compared to PMTs and hence much higher sensitivity can be achieved with such detectors. Generally most of the applications that use single photon detectors have a strict requirement on the DCR of the detector, but it was shown that high dark count is not a major problem if the detector has high PDE. Since, in DNA-sequencing application wide range of signals need to be measured, high sensitivity of the detector must be accompanied by wide dynamic range, good linearity and resolution. Further, due to the size of the capillary that emits fluorescence and the associated optics; large-area ($\sim 500\mu\text{m}$ diameter) detectors are required for this application. The large area of a detector would facilitate the use of large diameter fibers to collect and easily focus light onto the active area of the device with maximum efficiency. Two solid-state detectors having single photon sensitivity (SPAD and SiPM) are discussed in detail in the next chapter.

CHAPTER 2

SINGLE PHOTON AVALANCHE DIODE, SILICON PHOTOMULTIPLIER and QUENCHING CIRCUITS

In quantum physics, the photon is the quantum of the electromagnetic field (light). That is to say, an electromagnetic field is made up of many photons. In some respects a photon acts as a particle, for instance when registered by the light sensitive device in a camera. In other respects, a photon acts like a wave, as when passing through the optics in a camera. According to the so-called wave-particle duality in quantum physics, it is natural for the photon to display either aspects of its nature, according to the circumstances. Normally, light is formed from a large number of photons, with the intensity proportional to the number of them. That is the intensity of light can be measured by counting the number of photons. In the recent past, there has been growing number of applications in variegated fields that require the detection of very low-intensity light levels, for e.g. DNA-sequencing [7], single molecule detection (SMD) [13][14], astronomy [15], cryptography [16], optical fiber testing in communication [17]-[19], sensor applications [20], laser ranging in space applications and in telemetry [21] [22], non-invasive testing of VLSI circuits [23] to name a few and new applications are still being realized. Solid-state detectors such as PIN and avalanche photodiode (APD) are sensitive detectors of light, but they cannot be used to measure extremely weak light levels (few tens-few hundred photons) because they have higher noise levels. For such low intensity, extremely sensitive detectors are required that can distinguish the light

from the noise. Two different types of solid-state detectors that can detect extremely weak light levels [24] have recently become available and are called Single Photon Avalanche Diode (SPADs) and Silicon Photomultiplier (SiPM). These detectors have the ability to detect even a single photon and technologies developed using these detectors to count photons is termed as Single Photon Counting Technology (SPCT). SPCT is relatively new and growing technology since it has found numerous applications in wide range of fields and still new applications are being realized. This aim of this chapter is to introduce and discuss these solid-state single photo detectors.

2.1 Trends in Photon Detection Techniques

This section provides a brief introduction to different types of photon detectors, their advantages and dis-advantages in the order of their evolution or commercialization.

Photomultiplier Tube (PMT)

PMTs have been available commercially for almost 70 years now and are still the detectors of choice in applications that require detection of very low light. In these years they progresses remarkably, especially in sensitivity, gain, size, cost, speed and effective sensitive area. But they possess certain inherent dis-advantages such as sensitivity to magnetic fields, low (25% typical) quantum efficiency and hence low (7-10%) photon detection efficiency (PDE), requirement of bias voltage in KV range and still big in size

for certain applications. Until the early 90's these were the only choices of detectors for ultra sensitive photon detection because of their high internal gain.

PIN photodiode and Avalanche Photodiode (APD)

Later, solid state detectors of light such as PIN photodiode and avalanche photodiode (APD) became available. PIN has no internal gain and APD has very limited gain (typically 1000) and high noise, hence both of them cannot be used to detect low light levels. In principle, an APD can be made sensitive to detect weak signals by biasing it above breakdown (geiger mode). But at such high bias, it suffers from such high noise levels that it becomes practically unusable.

Single Photon Avalanche Diode (SPAD)

In the early 1990s, single photon detection became possible with the commercialization of other type of large area detectors called SPADs [4] [25]. SPADs can be widely categorized into two types viz. thin junction (small area) and thick junction (large area) depending on the width of their depletion layers [26] [40]. But since the interest of this thesis is only in large-area detectors, only large-area devices are considered. SPAD is a specifically designed category of APD working with a reverse bias voltage well above the breakdown voltage (V_{BR}). When biased above V_{BR} , the electric field (F) is such that even a single photon absorbed in the active area of the device generates large output current (~few mA) that is detectable even without an output amplifier [25]. Although they don't have large active area (typically 500 μ m diameter) as compared to PMT, they offer numerous advantages such as high quantum efficiency

(QE) in the visible spectrum (50-80%), much higher PDE (40-60%), small size, low bias-voltage requirements (couple of hundred volts) and negligible DCR. SPADs are considered to be the most sensitive detectors of light and are replacing PMTs in many applications. It must be noted that a SPAD is a digital device, which means that the output signal is not proportional to the number of input photons.

Silicon Photomultiplier (SiPM)

As the name indicates, SiPM is the real solid-state alternative to a PMT. SiPM is an analog detector whose output is proportional to the number of input photons. SiPMs are referred to in literature with various names such as micro-pixel/channel avalanche photodiodes (MAPDs), geiger mode APD (GAPD or GM-APD), metal-resistive layer-semiconductor APD (MRS APD), solid-state photomultiplier (SSPM), silicon PMT (SiPMT), multi pixel photon counter (MPPC), pixilated photon counter etc; *in this thesis it is referred to as SiPM*. SiPM is a matrix of individual detectors or pixels or micro-cells (*is referred to as pixel*) that are connected together in parallel. Each pixel works independently as a photon counter (like SPAD), but the output signal is the sum of all the individual pixels, which makes it an analog detector. Some of the notable advantages of SiPM are very low-cost since they are based on standard CMOS technology, insensitivity to magnetic fields, compact and low bias voltage (~25-75V) that is ~30 to 60 times lower than the voltage required by traditional PMTs and 3-4 times lower than large area SPADs. Although the concept of SiPM was realized way back in the 1970s, they suffered from a number of problems and only became commercially available only in the past one year or so [5], [6], [27], [28].

2.2 SPAD versus SiPM

Figure 2.1 shows the basic difference in the principle of operation between SPAD and a SiPM. In a SPAD, the output signal does not depend on the number of input photons, i.e. an output pulse with same amplitude is obtained irrespective of the number of input photons. Therefore SPAD is strictly a photon counting detector and is preferred in applications where one expects to receive mostly single photons that are spaced out in time [13]-[23]. If two or more photons arrive simultaneously, only one will be detected, introducing non-linearity in photon counting. On the other hand, the output signal amplitude of a SiPM is proportional to the number of input photons. Therefore, SiPM is the choice of detector, but not limited to applications where the input photons come simultaneously in large numbers [29] [30]. One of the goals of this thesis is to investigate the feasibility of using SiPM for high-speed photon-counting applications similar to a SPAD.

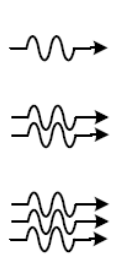
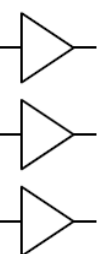
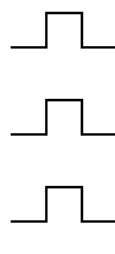
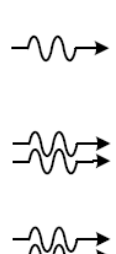
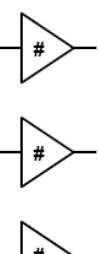
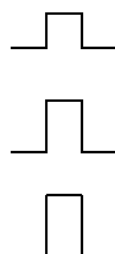
Optical Input	Detector	Output	Technology
			<p>SPAD Photon Counting [Output signal same for any number of input photons]</p>
			<p>SiPM Photon Number Resolving [Output Signal Proportional to the Number of input Photons]</p>

Figure 2.1 Photon Number Counting (SPAD) Vs Photon Number Resolving (SiPM).

2.3 Principle of Operation of SPAD and SiPM

Principle of operation of all the semiconductor devices can be explained starting with the principle of a basic p-n junction. A p-n junction is formed by combining a P-type and N-type semiconductor together in very close contact. The term junction refers to the region where the two types of semiconductor meet. Depending on the application requirement, the junction is either forward biased, zero biased or reverse biased. To detect photons, a junction can either be zero biased or reverse biased, but a reversed-biased junction is more sensitive to light since it has the effect of widening the depletion

layer (therefore expanding the reaction volume) and hence strengthening the photocurrent. Also a reverse biased junction tends to have lower capacitance, which improves the speed of their time response. The principle of operation is explained below in logical fashion starting with the principle of a reverse biased p-n junction. For general reference on semiconductor device physics and optoelectronic devices refer to [31]-[33].

Reverse biased p-n junction

When a semiconductor p-n junction is reversed biased, high F exists in the vicinity that helps in keeping electrons confined to the n-side and holes confined to the p-side of the junction. When an incident photon of sufficient energy (depending on material, for e.g. $>1.1\text{eV}$ for Silicon (Si)) is absorbed in the region where the field exists, an electron-hole pair is generated and under the influence of this F , the electron drifts to the n-side, resulting in the flow of electrons and hence photocurrent in the external circuit. Figure 2.2 illustrates the concept in space-time diagram. A photodiode is usually a p-n junction or a p-i-n structure. PIN diodes are much faster and more sensitive than ordinary p-n junction diodes, and hence are often used for optical communications and in lighting regulation.

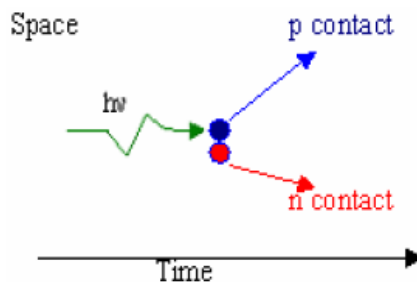


Figure 2.2 Principle of operation of a reverse biased p-n junction.

Avalanche photodiode (APD)

An APD is basically a variation of the p-n junction photodiode. It detects the light by using the same principle as an ordinary photodiode, except; it is designed to support higher F than an ordinary p-n junction. When a photon is absorbed in the depletion region, an electron-hole (e-h) pair is generated. One of the carriers (mostly electron) accelerates and gains sufficient energy from the F to collide with the crystal lattice and generate another e-h pair, losing some of its kinetic energy in the process. This process is known as impact ionization [33] (Figure 2.3, left). This electron or hole can accelerate again, as can the secondary electron or the hole, and create more e-h pairs, hence the term “avalanche”. After a few transit times, a competition develops between the rate at which e-h pairs are being generated by impact ionization and the rate at which they exit the high-field region and are collected. If the magnitude of the reverse-bias voltage is below the V_{BR} , collection wins the competition, causing the population of electronics and holes to decline. Figure 2.3 (right) illustrates the avalanche multiplication process in a space-time diagram.

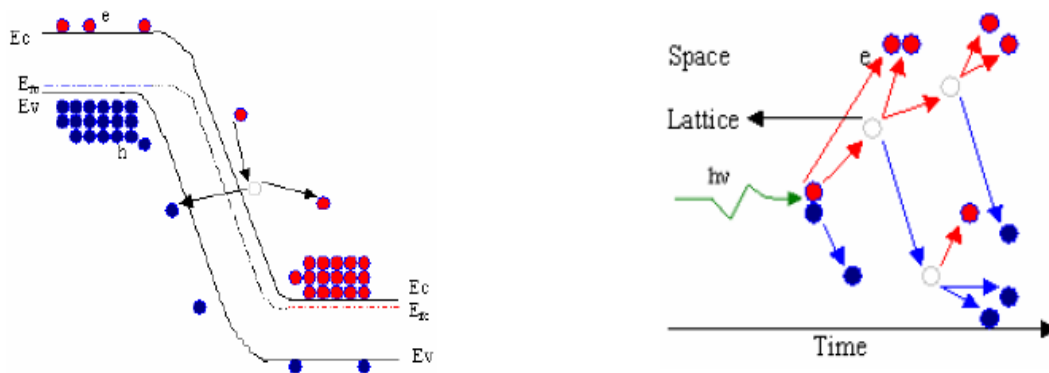


Figure 2.3 Impact ionization (left) and avalanche multiplication (right) in APD.

Each absorbed photon creates on average a finite number M of electron-hole pairs and this internal gain M is typically in the range of tens or hundreds [34]. Since the average photocurrent is proportional to the incident optical flux, this mode of operation is called the *linear mode*, which is the most common mode of operation. Since APDs are selected as solid-state alternatives to PMTs, they are somewhat similar, but with a basic difference: we see an intrinsic positive feedback when there is amplification taking place due to the avalanche process. This positive feedback loop strongly enhances the statistical fluctuations of the multiplication process, which increases much more than proportionally to the gain. Hence, whereas PMTs provide a gain with a mean value around 10^6 and moderate fluctuations, the mean value of the gain obtainable in APDs with acceptable fluctuations is lower than 1000 in the best cases. APDs operated in linear mode can detect single photons only in the most favorable cases and their performance as single photon detectors is not very satisfactory. It must be noted that an APD is biased close to but below V_{BR} . Properties of APD are discussed in [35] and for practical APD users guide refer to [36]

Single photon avalanche diode (SPAD)

SPAD deliberately exploits the intrinsic positive feedback that represents a significant drawback for APDs. Consider an APD that is biased at a voltage that is higher than V_{BR} with a power supply that can source unlimited current. At this bias, the F is so high ($>3 \times 10^5 \text{V/cm}$) that a single charge carrier injected in the depletion layer can trigger a self-sustaining avalanche. When a photon is absorbed in the depletion region of such a device, the electrons and holes will multiply faster (on average) by impact ionization then

they can be extracted. The space-time diagram in Figure 2.4 (left) illustrates this concept. The population of electronics and holes in the high-field region and the associated photocurrent grow exponentially in time. The more above breakdown the SPAD is biased, the faster is the growth of time constant. Hence, basically p-n junction devices that can work when biased above the V_{BR} and generate macroscopic current pulses in response to single-photons are called SPADs. This mode of operation is called *Geiger mode (GM)*, derived from the Geiger-Muller counter due to the similarity in their operation and hence sometimes SPAD is also referred to as GM-APD. Figure 2.4 (right) shows the operating regime of SPAD; V_{BR} is the breakdown voltage, V_{Bias} is the applied bias voltage and V_{OV} is the over-voltage, which is the voltage above breakdown the SPAD is biased i.e. $V_{OV} = (V_{Bias} - V_{BR})$.

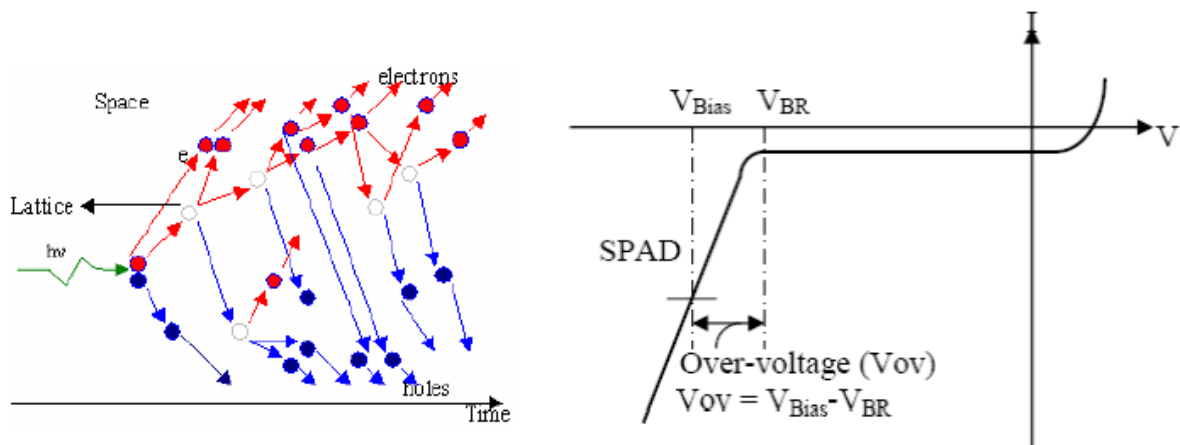


Figure 2.4 Avalanche multiplication in the geiger mode (multiplication faster than extraction) (left) and operating regime of SPAD (right).

Silicon photomultiplier (SiPM)

SiPM is basically a number of SPADs connected together on a common silicon substrate through individual quenching resistors (Figure 2.5c). Figure 2.5a and Figure

2.5b show the microphotograph and structure of individual pixel respectively. Figure 2.6 shows the electrical equivalent circuit. SiPM, like SPAD is biased above breakdown and is operated in the geiger mode. Under normal conditions, the applied bias voltage is the same across all the pixels, hence a high F exists across each pixel and each pixel is ready to detect an incoming photon.

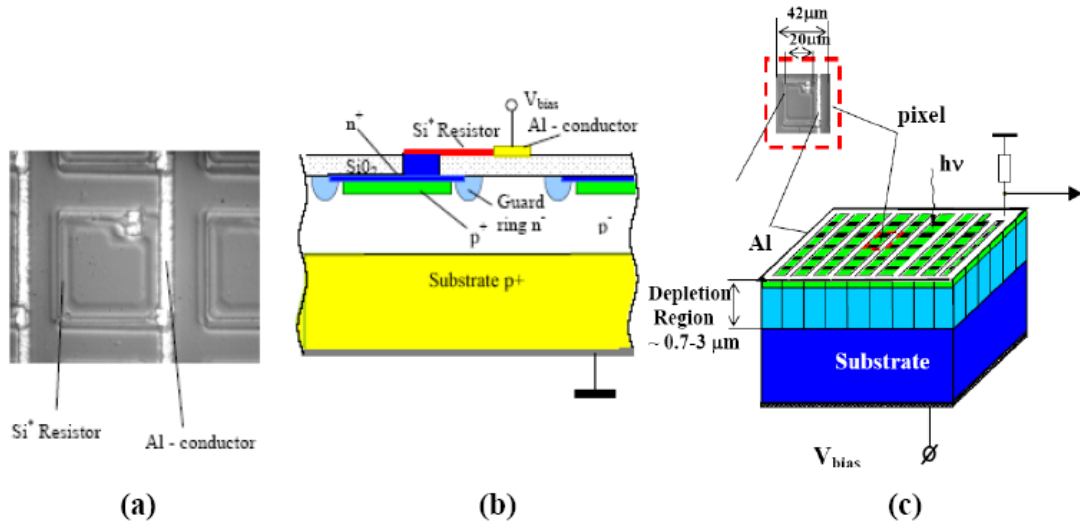


Figure 2.5 (a) Microphotograph of a typical SiPM pixel [84], (b) topology of a SiPM [84] and (c) matrix of independent pixels arranged on a common substrate and connected to a common output load resistor [38].

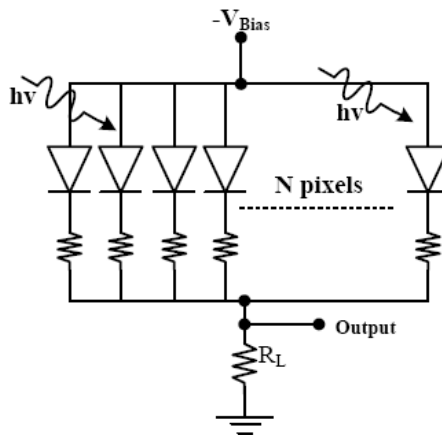


Figure 2.6 SiPM equivalent circuit

When an incoming photon is absorbed in the active region of the SiPM, an avalanche is initiated in the pixel that received the photon. This avalanche current is passively quenched (momentarily shut off) by the quenching resistor connected to that particular pixel. The speed of quenching the avalanche depends on the value of this quenching resistor, i.e. the lower the resistance the faster the quenching. But, the value of this resistor must be high enough to quench the avalanche current below a certain value called the latching current. Depending on the RC time constant (R is the SiPM internal resistance and C is the pixel capacitance), the pixel charges back to the actual bias voltage and ready to detect another photon. For detailed information on passive quenching (PQ) and passive quenching circuits refer to section 1.8 and [39]. The amplitude of the output pulse in this case will correspond to one photon and the width of the output pulse will be approximately equal to the RC time constant. The RC time constant depends on the size of the pixel and will be small for smaller pixels since device capacitance is proportional to the device active area. During this time, the SiPM will be insensitive to incoming photons and hence this time is defined as the *dead time* of the SiPM. If two photons are simultaneously detected by two different pixels, two pixels will fire and since the output current flowing through the load resistor (R_L in Figure 2.6) will be higher, the amplitude of the output signal in this case will be higher than the amplitude due to one photon. That is the SiPM as a whole integrates over all the pixels and the final output from SiPM is the summation of the output charge from all the pixels. It must be noted that more pixels (than number of received photons) can fire due to non-linear noise effects such as afterpulsing and cross-talk and are discussed in section 1.4. Passive

quenching resistors are made from polysilicon and also help in decoupling one pixel from another to minimize cross-talk.

Since the SiPM output signal does not depend on the number of primary carriers (because of geiger mode), each pixel detects the carriers created due to photon (or ionization particle or thermal generation) with the same response signal, i.e. the output charge from one or single pixel (Q_{pix}) is independent of the number of produced photoelectrons within the pixel, and can be written as:

$$Q_{pix} = C_{pix}(V_{Bias} - V_{BR}) \quad (2.1)$$

where, C_{pix} is the pixel capacitance. Since all the pixels are connected in parallel, if the response of each pixel is well uniform, the total charge from SiPM (Q_{SiPM}) can be quantized to multiples of Q_{pix} and proportional to the number of fired pixels (N_{fired}) i.e.

$$Q_{SiPM} = N_{fired} \times Q_{pix} \quad (2.2)$$

The number of pixels that can fire simultaneously is equal to the total number of pixels in a SiPM, which is defined as the *dynamic range* of the SiPM.

Since SiPM is internally quenched by individual quenching resistors (PQ) it does not require any external QC whereas SPADs normally require an external QC. It is important to note that it is possible to integrate passive quenching resistors with SPADs, but it is feasible option only for small area SPADs (< 50 μm diameter) since passively quenched large area SPADs are practically un-usable in most applications (maximum frequency is 200-400 KHz). In summary, small pixel size combined with small width of

depletion region (typically 0.7-3 μm), extremely high F (2-3 $\times 10^5\text{V/cm}$) and carrier drift velocity of $\sim 10^7$ cm/s make the geiger discharge extremely short, intrinsically making the SiPM very fast.

SPAD as high-speed single photon counter (quenching circuit)

A single charge carrier injected in the depletion layer of a SPAD can trigger a self-sustaining avalanche. The current rises swiftly to a macroscopic steady level (few tens of mA) and continues to flow until the avalanche is quenched by lowering V_{Bias} below V_{BR} . This lowers the F such that it is not able to accelerate the carriers to impact-ionize with lattice atoms, therefore current ceases. In order to be able to detect another photon, the bias voltage must be raised again above V_{BR} . These operations require a suitable circuit, which has to perform the following functions; (i) sense the leading edge of the avalanche current, (ii) quench the avalanche by lowering V_{Bias} below V_{BR} and at the same time generate a standard output pulse synchronous with the avalanche build-up and (iii) restore the voltage across the SPAD back to V_{Bias} . The circuit that performs this task is aptly termed as the quenching circuit (QC). QC is an integral part of a SPAD based single photon counting system and the performance of such a system equally depends on the performance of both SPAD and QC. Types of QCs and their advantages and dis-advantages are discussed in section 1.8 and [39].

2.4 Review of Important Performance Parameters

The aim of this section is to introduce important performance parameters of SPAD and SiPM. It must be noted that most of the parameters of SPAD and SiPM are common and mean the same, but some parameters have different meaning and are discussed accordingly. Also, it is important to note that SiPM is primarily designed for resolving photon numbers as opposed to photon counting (Section 1.2), but the aim of this thesis is to investigate their use as photon counters.

Detector material

Only photons with sufficient energy to excite electrons across the material's bandgap will produce significant photocurrents, therefore the material used to make a detector is critical to defining its properties. Commonly used materials and their wavelength range are summarized in Table 2.1.

Table 2.1 Typical detector materials and their detection wavelength range.

Material	Wavelength range (nm)
Silicon (Si)	190–1100
Germanium (Ge)	400–1700
Indium Gallium Arsenide (InGaAs)	800–2600

Because of their greater bandgap, silicon-based photodiodes generate less noise than germanium-based photodiodes, but germanium photodiodes must be used for wavelengths longer than approximately 1 μ m. Since the focus of this thesis is to design

photon counters for visible light, only silicon detectors are discussed. Hence, unless otherwise mentioned, it should be assumed that all discussion, results etc. are based on a silicon device.

Dark count rate (DCR)

As the name indicates, DCR represent the counts in the absence of light. It is one of the most important performance measures as the poissonian fluctuation of DCR represents the internal noise of the detector. The square root of the variance of the DCR determines the minimum detectable signal (MDS) of the detector. The total DCR is the combination of primary and secondary dark counts [41] [42]. Primary dark counts are due to thermally generated carriers in the junction and they increase with temperature and over-voltage. Operating the device at lower temperatures can significantly lower this type of DCR. Secondary dark counts are a result of after-pulsing, which is discussed in detail in the next sub-topic. DCR depends on a lot of factors viz. over-voltage, temperature, detector active area, and cleanliness of the fabrication. It is important to note that the DCR does not scale linearly with the active area of the device, especially when the active area diameter is increased beyond $25\mu\text{m}$ [43]. This non-linear increase in DCR has been attributed to two main factors in [43], (i) afterpulsing associated with trapping effects due to defects in the silicon and (ii) the gettering mechanism for the removal of defects and impurities is not sufficient to remove the defects outside the active area in larger diameter detectors. The reason for high DCR is usually attributed to the poor quality of the silicon (low-cost) and technology related problems [44]. Large-area SPADs with low DCRs are available, but are relatively costlier [4]. SiPMs have the highest DCR (typically $1\text{MHz}/\text{mm}^2$) due to the nature of the fabrication technology and use of low-cost silicon.

SiPMs with lower DCR that most probably use better quality silicon became recently available [6]. It is expected that DCRs will improve as the technology progresses.

After-pulsing

During an avalanche, large numbers of carriers cross the depletion region of the device. Due to material defects, some of these carriers are captured at deep levels inside the junction and are later released with a statistically fluctuating delay, correlated with the actual event and whose release times depends on how deep inside the released carrier was trapped and also the junction temperature [41] [42]. The number of carriers captured depends on the total number of carriers crossing the junction, which depends on the total charge of the avalanche pulse generated. Therefore, after-pulsing depends on the time required to quench the avalanche (T_A in Section 3.2.1) since it was initiated and the current intensity, both of which are a feature of the associated quenching circuitry. The current intensity also depends on the over-voltage, which is influenced by the required PDE. Afterpulsing also depends on the quality of the silicon and cleanliness of the fabrication process.

In SPADs, one method of minimizing after-pulsing is to increase the hold-off time [39, 42], which is the time the SPAD is held below bias after quenching. If sufficient time is provided, all the carriers will be swept across the junction, which can reduce after-pulsing significantly, but at the same time it increases the total dead time of the circuit, resulting in increased non-linearity and decreased speed.

In a SiPM, output amplitude is proportional to the number of input photons (section 1.2). Based on the physical mechanism of generation of afterpulsing, it can be

assumed that high percentage of output pulses produced as a result of after-pulsing will have amplitude similar or smaller than those produced by 1p.e. (photoelectron) pulse and the probability of 2p.e after-pulses will be very small and almost negligible at the level of 3p.e. Therefore, one solution would be to set the threshold of the read-out electronics such that most of the after-pulses are bypassed. Other solution would be bias the detector at low over-voltage. But increasing the threshold or lowering the over-voltage has the effect of lowering the sensitivity (PDE) of the detector, hence, depending on the requirement and tolerance of the application, a trade-off needs to be established.

Capacitance

Capacitance of a detector increases with the active area of the device and it is required that it be minimum [31]. The capacitance of the detector along with the internal series resistance determine the time required to charge or discharge the voltage across the detector, hence it puts a limit on the maximum speed at which a detector can operate.

Dynamic Range (DR) and Linearity

DR is the difference between the maximum and minimum measurable useful signal and is defined differently for SPAD and SiPM. For SPAD, DR is defined as the maximum saturation photo-count rate (DCR) minus the DCR at a particular bias voltage. Hence, depending on the quenching circuit, typical values range from few MHz-few tens of MHz.

DR for SiPM is defined as the maximum number of photons that it can resolve simultaneously, which is equal to the number of pixels. Hence, when used as photon resolver, the DR of a SiPM ranges from 100 Hz- few KHz.

For a SPAD the maximum achievable DR is determined by the speed of the SPAD (capacitance) and quenching circuit whereas for SiPM the DR is determined by the number of pixels. Since, the aim of this thesis is to use the SiPM as photon counter, the photon counting DR of a SiPM will be different and can be defined as the number of times a particular pixel of the SiPM can fire or the maximum count rate that can be obtained from the SiPM. As the input of both of these devices approaches the DR limit, the output becomes more and more non-linear. Therefore, linearity or linear range for both SPAD and SiPM is defined as the range of values within the total DR when the output signal is proportional or increases linearly with the input signal.

Quantum efficiency (QE)

All the photons that are absorbed by the detector may not necessarily be absorbed in the active region and only the photons absorbed in the active region will go on to create an avalanche. QE is the probability that a photon will be absorbed in the active region of the device. Ideally, it should be unity, i.e. all the photons absorbed, should be absorbed in the active region. QE efficiency depends on antireflection (AR) coating on the diode window and the SPAD structure. We know that absorption coefficient is very high ($10^5/\text{cm}$) for smaller wavelengths ($<400\text{nm}$) and low for larger wavelengths ($>850\text{nm}$). Hence, smaller wavelength photon is immediately absorbed within very short distance inside the surface and as a result many e-h pairs will recombine at the surface,

while longer wavelength photon might go unabsorbed through the active portion of the depletion layer. Since SiPM has dead area around each pixel, QE of SiPM is typically lower than that of SPAD. Typical values of QE for SPAD range from 40-80%.

Photoelectron detection probability (P_{de})

Ideally, when a photon is absorbed in the active region it will generate e-h pairs, which will continue to produce a chain of impact ionizations until the diode is completely discharged. But this is not the case for all the absorbed photons, because in certain cases, the avalanche terminates prematurely, i.e. it is not self-sustaining and terminates before completely discharging the diode. In this case the event goes undetected. Hence, P_{de} is the probability that an incident photon will produce a detection event. P_{de} increases with V_{OV} due to increase in avalanche triggering probability [45].

Photon detection efficiency (PDE)

PDE is essentially the photoelectron detection probability times the QE and increases with V_{OV} [25] [45] [46]. PDE for SiPM and SPAD cannot be determined using the same formula. The dead-space between pixels effectively reduces the PDE of SiPM and need to be taken into account. PDE is wavelength dependent and is represented by Equations 2.3 and 2.4 for SPAD and SiPM respectively.

$$PDE_{(SPAD)} = QE \times P_{de} \quad (2.3)$$

$$PDE_{(SiPM)} = QE \times P_{de} \times \mathcal{E}_{geom} \quad (2.4)$$

where, ϵ_{geom} is the geometrical efficiency of the SiPM and is defined as the fraction of total SiPM area occupied by active cell areas, also referred to as fill factor represented Equation 2.5. ϵ_{geom} is limited by the dead area around each cell and depends on the design of the pixel. PDE of both the detectors can be increased by increasing V_{OV} .

$$\epsilon_{geom} = \frac{Total \cdot Detector \cdot Activearea}{Total \cdot SiPM Area} \quad (2.5)$$

Gain

When an avalanche is generated in the SPAD, current continues to flow through the junction (assuming ideal power supply) until the avalanche is quenched or the junction is damaged due to over-heating. Hence gain cannot be defined for a SPAD alone, i.e. without a quenching circuit or it can be speculated that SPAD alone has infinite gain.

Since the SiPM is intrinsically passively quenched, gain can be defined for a SiPM. As discussed before, the output charge Q_{pix} from a single pixel is independent of the number of produced photoelectrons within the pixel, and is represented by Equation 2.1. Therefore gain of the pixel is given by:

$$Gain = \frac{Q_{pix}}{e} \quad (2.5)$$

where, e is the charge on one electron. If we assume the typical value of C to be ~ 100 fF and the typical value of $(V_{Bias} - V_{BR})$ to be one volt, then Q_{pix} will be in the range of hundreds of femto farads and gain will typically range from $10^6 - 10^7$.

Cross-talk

Cross-talk does not exist in SPADs, but it is intrinsic to SiPMs due to the nature of the detector. The high gain and close packing of the structures on the surface of the SiPM make cross-talk between adjacent cells an important subject in this evaluation. There are two types of cross-talk viz. inter-pixel and optical. Inter-pixel cross-talk happens when a single detected photon results in the discharge of more than one cell and optical-cross talk happens as a result of the photons that are created due to the geiger discharge at the rate $\sim 10^{-5}$ Photons per electron [52]. Careful design of quenching resistor (also facilitates decoupling) can help minimize the inter-pixel cross-talk, whereas increasing the $\varepsilon_{\text{geom}}$ or dead-space between pixels can lower the probability of both types of cross-talk. It can be assumed that the probability of cross-talk at the level of 1p.e. pulses will be more as compared to 2p.e or 3p.e pulses or more, hence, similar to after-pulsing, cross-talk can be significantly reduced by increasing the threshold of the read-out electronics to beyond 1p.e. But again, this has the dis-advantage of reduced sensitivity.

2.5 Progress and Commercial Availability of Large-area SPADs and SiPMs

Since our lab is not involved in the research and development of the design and fabrication of SPADs or SiPMs, we rely on the commercial availability of these detectors for this research. Therefore, the design, development and progress related issues of these detectors are not discussed in detail in this thesis. Review on the development and progress of SPADs can be found in [44] and SiPM can be found in [49] [50]. In chapter 1, it was discussed that large-area of the detector is important for DNA-sequencing application. Some other applications of large-area SPAD include fluorescence correlation spectroscopy (FCS) [47], fluorescence lifetime imaging (FLIM) [48]. In this thesis, devices with active-area diameter of more than 200 μm are considered as large-area devices.

SPAD

First SPADs were developed at the Shockley laboratory in the 60's [41, 51]. With their diodes they observed macroscopic voltage pulses triggered by the absorption of single optical photons. Thanks to the work of this group, a basic understanding of this phenomenon was gained. In the 70's, fundamental contributions to the understanding of the avalanche mechanism and of its statistical properties were given by R.J. McIntyre [34]. Since then, significant progress has been reported in all aspects of the development of SPADs and SPAD arrays (SPADA) and can be referred to in [25], [44], [53]-[69].

When this research was started in 2004, to our knowledge, there was just one commercial provider of large area SPADs and that was Perkin Elmer Optoelectronics (PKI), Canada [4]. In fact, as far as we knew, they were probably the only commercial providers of any type of SPADs. The SPADs were advertised as large area APDs that had limited capability to operate beyond breakdown (geiger mode). Most of the available SPADs from PKI (then and now) have a typical photosensitive diameter of 0.5mm (500 μ m). Although these device claimed to offer excellent PDE under suitable biasing conditions and very low DCR (~ few hundred Hz), high cost of these devices was and is a know problem. The reason for high cost is that they are fabricated with a sophisticated process based on special ultra-pure ultra-high resistivity silicon wafers and a proprietary nonplanar technology, which inherently has low fabrication yield. Moreover, the fabrication technology is unsuitable for monolithic integration of detectors and circuits. Over the last few years, significant research has been done on SPADs that can be fabricated with standard fabrication technologies [44], [105], [53]-[56], [112]-[113] to lower the cost and number of breakthroughs has been reported. Number of sources of commercial silicon SPADs other than PKI have increased since 2004, but are still very few [70]-[73]. Further to our knowledge *most* of them only provide SPADs with active area diameter of up to 100 μ m, some of which are available only with photo counting modules, for e.g. photon counting and timing systems [73] and photo counting detector module [114].

In summary, it seems still a number of problems need to be solved before the large area (>200 μ m) SPADs will become available at low cost. One of the problems with large area SPADs is high DCR. But it must be mentioned that for some applications,

such as ours, high DCRs of few hundred KHz are acceptable (section 1.5). Hence if SPADs having high DCR become available they could be used in some applications provided they have high sensitivity in the wavelength range of interest accompanied by wide dynamic and linear range.

SiPM

SiPMs were first developed in Russia in the mid-1980s after the study of the stationary avalanche multiplication of photocurrent in metal-conducting dielectric-semiconductor structures. The first actual photodetectors based upon this structure were produced in late 80's. Early references of SiPMs can be found in [75]-[77]. Since then, there have been few developers of SiPM and the literature available on SiPMs has increased considerably. Design and development aspects of SiPMs can be referred to in [84], [49], [50], [78]-[91] and [11-15] report detailed characterization of different devices. Most of the applications of SiPMs reported so far have been in high-energy physics [84].

To our knowledge, SiPMs, if at all available, were only available for evaluation purposes. Only recently, in the beginning of 2007, they became commercially available from few companies [6], [72]-[74]. The standard or typical active area of SiPMs is 1mm^2 ; hence large area is not a problem with SiPMs. SiPMs from Hamamatsu Photonics have much lower DCR [6] at high gain and room temperature as compared to other available SiPMs probably due to the use of purer silicon.

2.6 Choice of SPAD and SiPM for DNA-Sequencing Application

This section introduces the SPAD and the SiPM that were selected for this research.

SPAD

As mentioned in the last section, PKI is the only provider of large-area detectors. Further there is a small range of detectors to choose from a list of available detectors [4]. Based on the requirements discussed in section 1.2 and 1.4, SPAD model C30902S-DTC was selected. There are two other diodes in this series viz. C30902S and C30902S-STC. All the detectors have an active area diameter of 500 μ m, but the difference between them is that in C30902S-DTC the detector is mounted on a 2-stage thermoelectric cooler (TEC), C30902S-STC has a one stage TEC and C30902S has no TEC. The reasons for selecting this particular model are as follows:

1. C30902S is known to have heating problems [25].
2. To achieve best sensitivity results since sensitivity can be increased by increasing V_{OV} . But increasing V_{OV} results in increased DCR. DCR can be lowered by cooling the detector. The detector with one-stage peltier (C30902S-STC) can be cooled to minimum of 0°C , whereas C30902S-DTC can be cooled to -20°C, hence to be able to achieve highest possible sensitivity and lowest possible DCR, detector with 2-stage TEC cooler was a better choice.
3. Wide dynamic range (10 MHz) [3].
4. Since the whole detector along with the TE-cooler is hermetically sealed in a small package, it would be easier to cool the diode as compared to external

cooling and further it would facilitate design of compact single photon-counting modules. Figure 2.7 shows the photo of the selected diode.

5. It is designed for ultra-low light level applications ($< 1\text{pW}$).

Table 2.2 summarizes the typical specifications of the selected SPAD series. PKI SPCM module [3] has a special connectorization/fiberization system that allows focusing of light onto the active area of the device with maximum efficiency. The selected SPAD model is not available with such a fiberization system; hence a special fiberization was designed in our lab for this device and is described in section 1.7.

Table 2.2 Typical specifications of APD series C30902S from PKI [4].

Performance parameter	Typical value
Spectral response range	400 to 1000 nm
Photosensitive diameter	0.5mm
Dark count rate at 5% detection probability	15,000 c/s (+22°C), 350 c/s (-25 °C)
Max saturated count rate	Up to 12 MHz
Linear range	~ 2 MHz
Typical gain	250
Time response	0.5ns
Operating temperature range	-40°C to +70°C
Capacitance	2 pF
Temperature coefficient of V_R (reverse bias voltage) for constant gain	0.7V/°C
Breakdown voltage range	180-250V

SiPM

The selection criteria for SiPM are similar to that of SPAD. As mentioned earlier, SiPM started becoming commercially very recently (beginning to 2007) and there are not many choices of detectors. Three detectors that were chosen are as follows:

1. Multi-Pixel Avalanche Photodiode (MAPD) from Voxel-Inc [72] and is referred to as *cooled SiPM*¹ in this thesis.
2. MPPC model S10362-11-100U from Hamamatsu Photonics [6].
3. MMPPC model S10362-11-25U from Hamamatsu Photonics [6].

The details of the first device (MAPD) are provided in section 5.2.1. The detectors 2 and 3 from Hamamatsu Photonics only became commercially available very recently (mid 2007). Both these models have an active area of 1mm^2 . The difference between the two devices is that the model S10362-11-100U has 100 pixels and width of each pixel is $100\mu\text{m}$, whereas model S10362-11-25U has 1600 pixels and width of each pixel is $25\mu\text{m}$. These devices are not mounted on a TE cooler; hence they cannot be easily cooled. From here device model S10362-11-100U will be referred to as *100-pixel device* and S10362-11-25U as *1600-pixel device*. Hamamatsu has one more variation of this model, which is a 400-pixel device with $50\mu\text{m}$ pixel width, but only two extreme versions of devices were selected to get the characteristic spread. For detailed information on the Hamamatsu SiPMs, refer to the data-sheet [6].

¹ In this thesis, detector that has the facility to be cooled is referred to as cooled detector. SPAD model C30902S-DTC and MPAD from Voxel-Inc are sometimes referred to as cooled SPAD and cooled SiPM respectively.

2.7 Fiberization of SPAD Model C30902S-DTC

The goal of designing the fiberization system is to focus maximum light onto the active area of the detector. The problem is represented by the picture shown in Figure 2.7a. The core diameter has to satisfy two conditions: the size of image of the fiber core (D_F) must be smaller than the diameter of the diode receiving area D_{APD} and the spot of the beam from the fiber must be smaller than the active area of the GRIN lens. Two main constraints faced were (a) a rather large distance L_2 (2.4mm) between the diode crystal and the glass window which covers the diode case and (b) position of diode crystal inside the diode case varies from diode to diode by ± 0.1 mm. The important part of the design was to determine an optimum size of the GRIN lens Z that would allow the use of the fiber with maximum core diameter. Since the size of the focused spot must be smaller than the receiving area of the diode, we have to choose different GRIN lenses for fibers with different core diameter. We carried out calculations for SLW-1.8 GRIN lens (NSG, Japan) which fits the FC/PC format and found that for the lens of 1.8 mm diameter (SLW-1.8, NSG America) the optimum length Z is 4.26mm. A two-part fiberization system was selected for design and consists of the SPAD mount ring and the FC/PC connector with inserted GRIN lens (Figure 2.7b). The design of the fixture allows both lateral alignment of the GRIN lens to the diode crystal and vertical alignment of the GRIN lens enabling sharp focusing of the fluorescence delivered by the fiber onto the receiving surface of the diode. The designed fiberization system allows efficient coupling (80%) of the radiation from high numerical aperture fibers (up to 400 μ m diameter) onto

the receiving surface of the SPAD. For detailed description and results of the designed fiberization system, refer to [40]; Figure 2.7d shows the implementation.

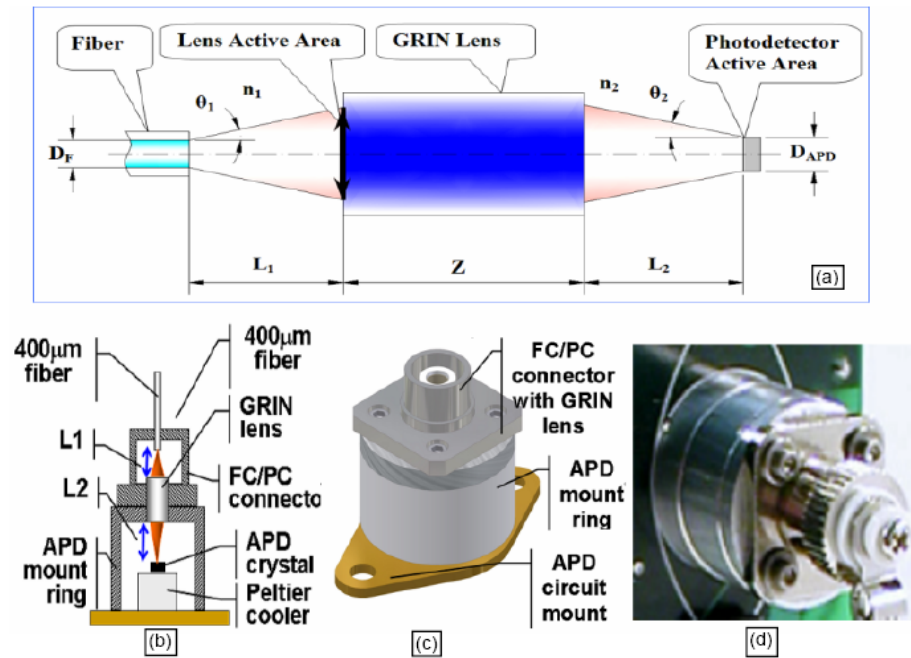


Figure 2.7 SPAD model C30902S fiberization system; (a) graphical representation of the problem; (b) FC/PC connector and mount ring; (c) CAD design; (d) photo of implementation.

2.8 Review of Quenching Circuits (QCs)

QC was introduced in section 1.3. Figure 2.8 explains the quenching principle with the help of a diode's reverse bias I-V characteristics. In normal conditions, SPAD is biased in geiger mode ($V_{\text{Bias}} > V_{\text{BR}}$) (point 1) and it continues to remain in this state until a photon is absorbed. An avalanche will be initiated even if a single photon is absorbed in this region, which reflects single photon sensitivity of the device. When a photon is absorbed, avalanche occurs, the junction breaks down and a macroscopic current flows through the device in a very short time (point 1 to 2). The task of the associated circuit is to detect this rise in current as soon as possible and immediately quench (terminate) it (point 2 to 3). It remains in this state for a predetermined time so that the device gets back to its normal state and then switched back (point 3 to 1) to V_{ex} (Note $V_{\text{ex}} = V_{\text{Bias}}$ from Figure 2.4). Now the SPAD is again ready to detect another photon.

It is clear that the QC is a critical piece of circuitry in a photon counting system since it serves a large number of roles and is a major design challenge. More importantly, the performance of a photon counting system is not only dependent on the quality of the SPAD, but it is also largely dependent on the performance of the QC, especially speed. QCs can be classified into three different types, viz., passive quenching circuit (PQC), active quenching circuit (AQC) and Mixed or Hybrid quenching circuit (MQC) which is a mixture of the first two types. The aim of this section is to review different types of QCs and discuss their advantages and dis-advantages.

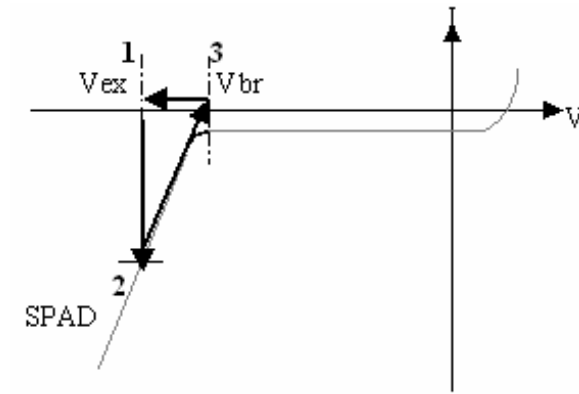


Figure 2.8 Principle of operation of quenching circuit.

Passive quenching circuit (POC)

Passive quenching or self-quenching is the first and simple method of quenching an avalanche. All later quenching circuits were developed starting with the principle of this one.

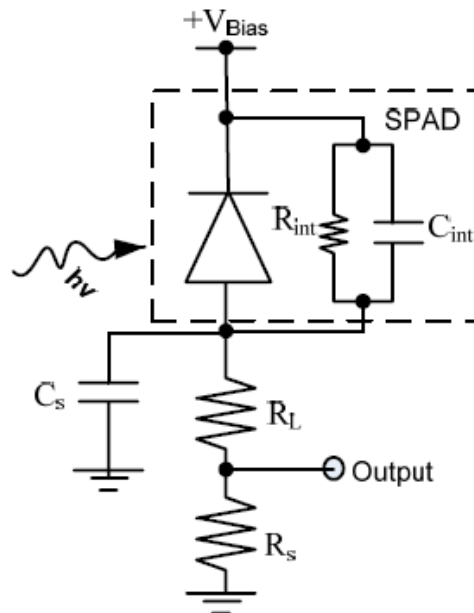


Figure 2.9 Typical passive quenching circuit (PQC)

Figure 2.9 shows a typical PQC where each component represents the following:

C_{int} is the internal capacitance of the diode. It depends on the active area of the diode and varies proportionally with it.

- R_{int} is the internal resistance of the diode, generally in the range of ~ 500 Ohms for large area SPADs.
- C_s is the stray capacitance or the wiring capacitance due to the circuit design and layout.
- R_L is the high value load resistor (quenching resistor).
- R_s is a small value series resistor in order to get a voltage pulse at the output.

Here, C_{int} and R_s are fixed and cannot be changed, but C_s can be lowered by careful circuit design and layout. The total capacitance to be charged is $C = C_{int} + C_s$. In the event of an avalanche, a macroscopic current flows through the diode. Voltage drop across the large value ballast resistor (R_L) quenches the avalanche by limiting the current below a latching current value. The latching current depends on the device and varies typically from few ten's of microamperes to few hundred microamperes [25]. After the avalanche is completely quenched, the diode recharges back with a time constant $R_{int} * C$. The diode is not sensitive to detect another photon from the time the avalanche is initiated to the time it completely recharges; hence this period is called the dead time of the diode.

As can be seen, in this mode of operation, the photon-counting rate is limited by the RC time constant, which can vary from few hundred nanoseconds to few microseconds. Minimizing the RC time constant can increase the photon-counting rate a little, but, the value of R should be selected such that it is high enough to maintain the current below the latching current value and it should not be very high, in which case it

will increase the recharge time of the diode and hence the maximum photon-counting rate. For different configurations and detailed study of POCs, refer to [39].

Drawbacks of passive quenching

- Large RC ($R_{\text{int}} * C$) time constant prevents the bias voltage from dropping rapidly. This results in the delay of quenching the avalanche and hence inaccuracy in the detection of the arrival of photon at the same time increased power loss, which results in the increase in SPAD temperature.
- Large current flows across the junction during the avalanche and carriers can get trapped in the SPAD junction. The number of trapped carrier increases as the time the SPAD is left unquenched increases. Once V_{Bias} drops below V_{BR} , these carriers can spontaneously re-emit. If V_{Bias} is reset too early, then these re-emitted carriers can falsely re-trigger the avalanche. This problem can be overcome only by holding the bias voltage low for a certain amount to allow these carriers to be completely swept out of the junction without retriggering an avalanche.
- Large value of RC limits the maximum operating frequency to few hundred KHz with large area devices, making it practically un-usable in most applications.

To summarize, POC is an easy to implement and an effective method of quenching for small area (less than $50\mu\text{m}$) devices since they have very low capacitance (capacitance scales with area) and hence higher speeds is possible with PQ. They can also be used with large area devices where high counting rates is not a requirement (\sim few-few hundred KHz). Since, the selected SPAD for our application is a large area device that is expected to count photons at high-speed ($\geq 1\text{MHz}$), PQ is not a feasible

option. In order to over-come the above-mentioned drawbacks, faster quenching method known as active quenching is used.

Active quenching circuit (AQC)

This method forces back on the SPAD to drop the bias voltage much quicker enabling significant speed improvements over the PQ method; however, it is no simple task to design an effective AQC. Due to the time constraints involved there is a significant amount of component integration to reduce propagation delays as well as stray capacitances. The concept of AQC, pioneered by Dr. Sergio Cova, was demonstrated for the first time in 1954 [58] and its application to photon timing in [59]. Various AQCs have since been reported, with size decreasing from nuclear instrumentation modules to compact boards and to monolithic active quenching circuits [39], [93]-[97]. Figure 2.10 illustrates the principle of active quenching. For simpler explanation, it can be loosely broken down into further sub-circuits as follows.

(a) Comparator: The first task of the active quenching circuit is to act as a comparator. Comparator is one of the important components of the AQC and it performs the following tasks (a) detect the sharply rising avalanche current caused by an incoming photon or the thermal generation and avoid causing any false detection caused by any fluctuation in the dark current background; (b) generate an useable signal output which is representative of the current pulse generated by the SPAD. Generally, a line driver is used at the output of the comparator to shape the output pulse and further boost the amplitude of this pulse before sending it to appropriate circuitry for registering the photon. The output of the comparator is mainly used for two purposes, (i) to provide a

reference which can be used by external counting devices to record the number of avalanche events which occur and (ii) to initiate the voltage pulse (quenching action) that is used to reduce the SPAD bias voltage below breakdown, i.e. basically to initiate the quenching action. Since all the above mentioned tasks affect performance of the quenching circuit as well as some photon detection performance parameters (as discussed in the drawbacks of the PQC), a very high-speed comparator must be used.

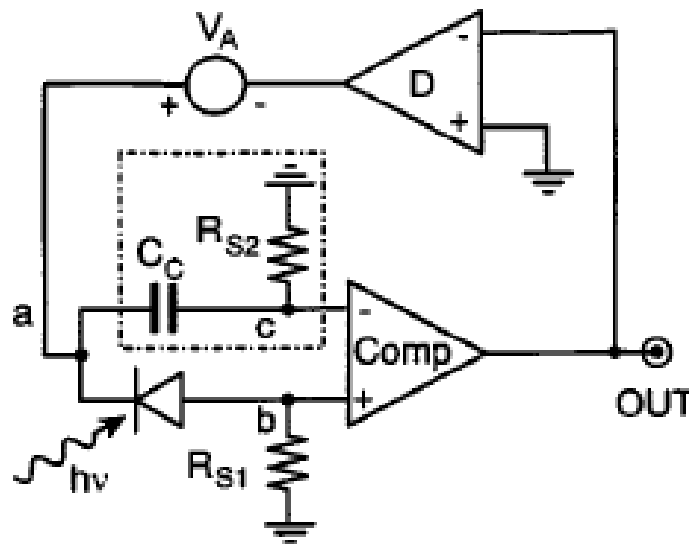


Figure 2.10 Active quenching circuit [39]

(b) Voltage Driver: A voltage driver, represented by “D” in Figure 2.10 is required to enable the large voltage quenching pulses (\sim few tens of volts) to be generated. This pulse is required to force back onto the SPAD and reduce the bias voltage such that the avalanche current is quenched and the SPAD is insensitive to later arriving photons. The reason for such high voltage of this pulse is due to the biasing arrangement that is

employed for SPADs (usually biased 5-10% above the breakdown voltage for achieving high sensitivity). Once the quenching action is initiated, the high voltage pulse must be applied as soon as possible to minimize heating and after-pulsing effects and hence it must have a fast rise time. For detailed explanation refer to [39].

(c) **Timing Circuitry:** Timing circuit controls the dead time of the AQC. The dead time is composed of two different time viz., the quench time and the reset time. During quench time, the SPAD bias is held below breakdown and reset time allows the SPAD capacitance to recharge back to the actual bias voltage. Important delay times of the quenching circuit are explained in detail in section 3.2.1. Although, these time itself are very critical, but it is required for the generated quench and reset times to be precise and also end of the quench time should be precisely matched with the start of the reset time. Further, it is important that all this be done without adding unnecessary capacitances to the design.

Advantages and dis-advantages of AOC

- Fastest possible method of quenching an avalanche.
- High accuracy in photon timing.
- Small delay in quenching the avalanche resulting in fewer carriers crossing the junction and hence low false re-triggering of avalanche. This also results in lower power loss and hence less heating of the SPAD.
- Dead time of the circuit does not depend on the component values and can be accurately controlled. Hence determination of precise dead time is possible for satisfactory circuit operation.
- Stringent circuit requirements.

In summary, although AQC is an attractive method of quenching the avalanche, it is not the most preferred method because of the involved complexity and stringent circuit requirements. In order to relax the circuit design requirements, a hybrid approach is usually employed and is discussed next.

Mixed quenching circuit (MQC)

As the name indicates, this method is the combination of passive and active quenching methods described above. Mostly, passive quenching is employed as the first stage to limit the avalanche current to a low value, followed by the application of quench pulse during the quench delay time and the reset action that recharges the SPAD back to the bias voltage that is greater than the breakdown voltage. The value of the load resistor that provides the initial passive quenching action can be lower as compared to pure PQ since the actual quenching is done by active method. Overall, this method enables a simpler design to be used, while still allowing some control over the dead time and the use of a voltage pulse to speed up quenching. However the time constant caused by the combination of SPAD capacitances and the PQ resistances means that the quenching speed is limited. It does however out-perform a straight passive circuit, at the cost of complexity and designer effort. In MQC, performance limitations are heavily dependent on switching delays which are directly related to the capacitance of the circuit. For detailed review and design, refer to [39] [96].

In summary, PQC is suitable for SPADs having small RC time constants since it can be operated at higher speed and MQC is preferred over AQC due to the eased circuit

requirements and simpler design. For detailed analysis and comparison of different circuit, refer to [39] [96].

CHAPTER 3

SINGLE-CHANNEL SINGLE PHOTON COUNTING MODULE (S-SPCM): DESIGN, IMPLEMENTATION AND CHARACTERIZATION

The goal of this chapter is to design high-performance S-SPCM based on the selected large-area SPAD model C30902S-DTC from PKI (see section 2.6) to investigate their feasibility for high-performance DNA-sequencing. This chapter presents, design, implementation and characterization of a high-speed (~10MHz) MQC, a highly stable ($\pm 0.001^{\circ}\text{C}$) temperature controller and a stand-alone power supply unit. A novel timing and logic circuit for generating precisely matched accurate quench and reset delay time is designed for the QC. Important performance parameters of the QC are characterized and optimum quench and reset delay times needed for the selected SPAD are studied. The designed QC and the temperature controller circuit are fabricated on a single PCB and mounted in a metal box to form a compact, stand-alone S-SPCM. The required voltages for this module are provided by the stand-alone power supply unit making the whole S-SPCM stand-alone in nature. The SPAD is fiberized using the fiberization system discussed in section 2.7, making the designed S-SPCM general purpose in nature since it can be easily integrated into any application having similar photon counting requirements. The complete S-SPCM is then characterized and best possible results with the selected SPAD are demonstrated.

3.1 Stand-alone Photon-counting Module

In this thesis, the difference between a photon counting module and a photon counting system is as follows: a photon counting system consists of a detector, a QC to quench the avalanche and generate output pulses, a counter circuit that can count these pulses and a power supply unit to supply the required power to all these units (Figure 3.1). But since there are commercially available photon counters that can be used for counting the output pulses (for e.g. SR 400 from Stanford Research Systems), it is not absolutely necessary to design a counter circuit (depends on the need of the application). Hence such a unit without the counter circuit is classified as a photon counting module.

Figure 3.1 shows the block diagram and interconnection of various sub-modules of the photon counting system. The APD in the block diagram represents the selected SPAD model C30902S-DTC. The aim is to design a general purpose, robust, stable and a compact photon counting module that could be easily integrated into our DNA-sequencing machine as well as other applications, if required. The designed sub-circuits to make the complete S-SPCM are listed as follows:

1. High-speed MQC. It must be noted that the reset circuit, high-speed comparator, line driver and the threshold adjustment block shown in Figure 3.1 are all important sub-circuits of the designed QC (Section 3.2).
2. High precision, highly stable ($\pm 0.001^\circ\text{C}$) temperature controller to cool the detector chip to lower temperatures and control its temperature (Section 3.3).
3. A power supply unit (Section 3.4).

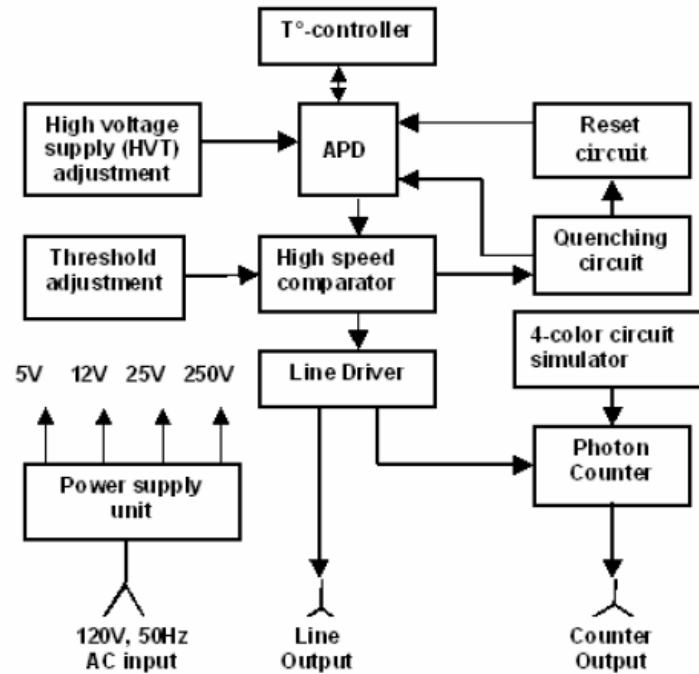


Figure 3.1 Block diagram of a stand-alone photon counting system

We already have two high-speed photon counters in our lab, one is the Stanford counter SR400 and other is a designed FPGA based high-speed counter circuit. This counter circuit can be connected to a PC via parallel port and is specifically designed to work with our data recording software facilitating easy data recording and storage. Stanford counter was used for initial tests and then the S-SPCM was characterized with our counter circuit.

3.2 Design of High-speed Mixed-signal Quenching Circuit

MQC is the optimum configuration of QC [39]. A good QC must have the following features or must be able to perform the following tasks efficiently:

1. Sense the onset of an avalanche as soon as possible (detect).
2. Lower the bias voltage across the SPAD below V_{BR} as fast as possible (quench).
3. Restore the bias across the SPAD to above V_{BR} as quickly as possible (reset).
4. Some parameters of a QC such as V_{BR} , quench delay time and reset delay time are SPAD dependent. Further, these parameters are device independent that is two exact same devices (same structure, fabrication batch etc.) can have different V_{BR} and different requirements for quench and reset times. Therefore a good quenching circuit must have provision to adjust these parameters.
5. To achieve high sensitivity, a SPAD needs to be biased at a voltage that is sufficiently higher (5-10%) than the V_{BR} [4] [98]. Hence the circuit must have two important features:
 - Provision to apply V_{Bias} above V_{BR} , i.e. 10-20% V_{OV}
 - The quench voltage (V_Q) must be large enough to adequately quench the device to a voltage below V_{BR} , i.e. $V_Q > V_{OV}$.

Since V_{BR} for this specific SPAD ranges from 180-220V (at -20°C), V_{Bias} must range from ~ 170 -250V and V_Q must range from 5-30V. This is taken into account while selecting the components for the quenching circuit.

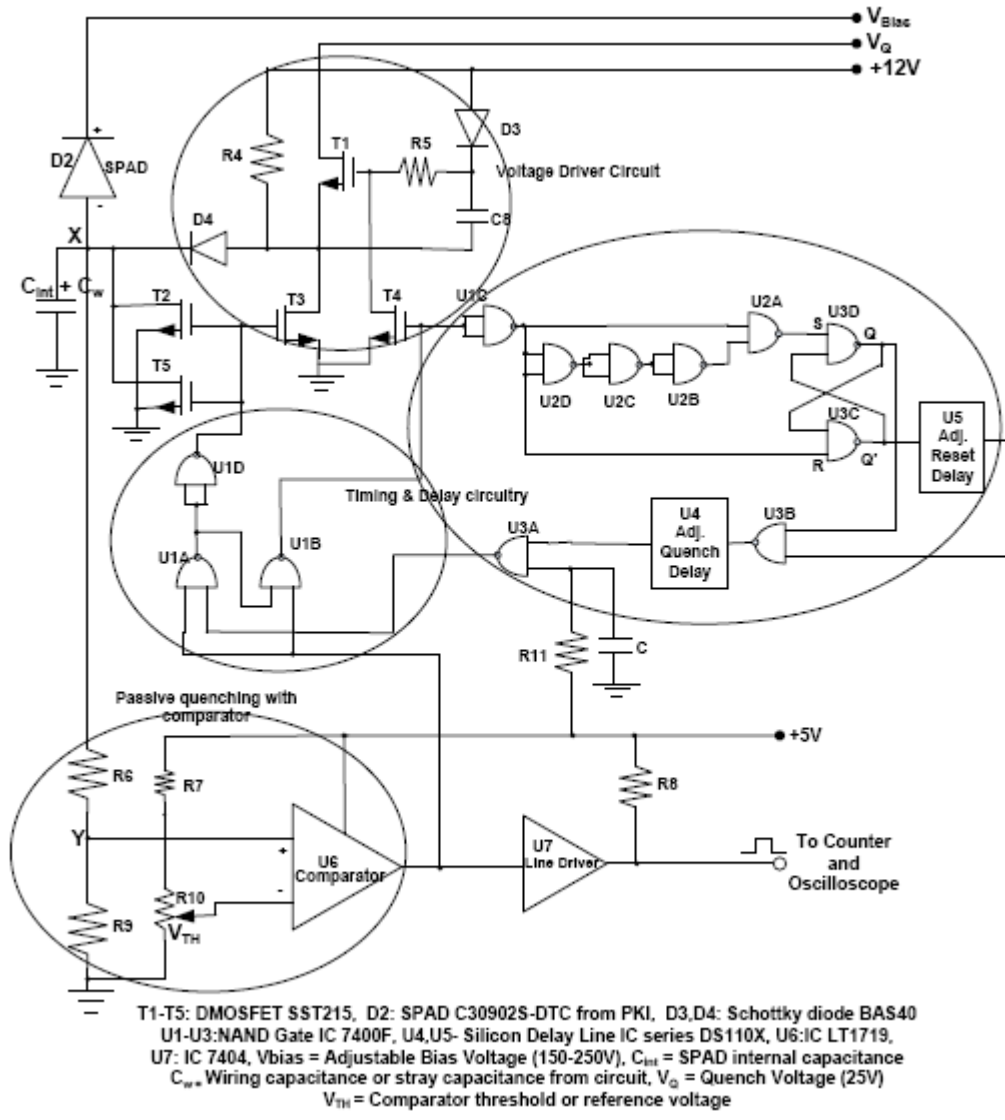


Figure 3.2 Circuit diagram of the quenching circuit. For more detailed circuit diagram see Figure A.1.

Generally a MQC consists of a PQC followed by an AQC which consists of the comparator, voltage driver and the timing circuitry. Some of the reported QCs can be found in [25] [39] [95] [98] [104]. One of the common methods of generating quench and reset delay times is to use mono-stable multi-vibrator for timing purposes, whose timing is set by a RC. Hence, each time the delay needs to be changed, the RC has to be

changed. Our future goal was to design multi-channel systems based on the same quenching circuit. Since different SPADs may need different timing, tuning multi-channel system for optimum delays would be very inefficient with mono-stable based timing circuit. To solve this problem, a completely digital timing and logic circuit was designed that allows easy tuning of delay times. The circuit is designed using only 12 nand gates and delay line ICs and has certain advantages as compared to the mono-stable approach and will be discussed below. Figure 3.2 shows the circuit diagram of the complete MQC. Details of all the important components are shown in the figure. The circuit explanation is simplified by breaking it down into three important sub-circuits, viz. passive quenching and comparator, voltage driver circuit and timing and delay circuit. Each sub-circuit is marked with a circle in the figure and is explained below. Also, it should be noted the nand gates are implemented using TTL IC 74F00, but are shown as individual gates for explanation purposes. More detailed or the actual implemented circuit along with the layouts are provided in appendix A.

Passive quenching (PQ) and comparator

PQ is provided by load resistor R6 (50K Ω) and R9 (50 Ω) helps to create a voltage pulse at node Y. As soon as the voltage at node Y crosses the reference or the comparator threshold voltage (V_{TH}) (set using R9), the comparator triggers and generates a fast positive going edge at the output that triggers the timing and the voltage driver circuit. The comparator output goes low when the input at node Y goes below V_{TH} . It is important to note that in a pure PQC the value of the quenching resistor is usually in the range of few hundred k Ω , but in MQC, since the actual quenching is done by the voltage driver circuitry, a much lower value of R6 can be selected. A lower value of R6 helps in

detecting the avalanche much faster since the time it takes for node Y to cross V_{TH} will be shorter. Ultimately, this helps in minimizing the charge that crosses the junction and hence afterpulsing.

Voltage driver circuit

In Figure 3.2, voltage driver circuit mainly consists of transistors (T1-T5), diodes (D3, D4), resistors (R4, R5), capacitor (C8) and voltages (V_Q , +12V). T1-T5 are implemented with n-channel DMOSFET model SST-215, since it has low turn-on time (1ns), low reverse capacitance (0.2pF) and low on-resistance between drain and source ($r_{DS ON}$) [99]. The task of the voltage driver circuitry is to momentarily lower the bias across the SPAD to below breakdown in order to quench the avalanche. This is done by applying voltage V_Q to the anode (node X) of the SPAD; momentarily decreasing the effective bias across SPAD to $V_{Bias}-V_Q$ (i.e. below V_{BR}). Maximum value of supply V_Q is limited by the drain to source breakdown voltage of the T1, (typical value 35 V), but is sufficiently high for the selected SPAD. V_Q is provided by an adjustable power-supply to accommodate different devices if needed. A bootstrap configuration, with positive feedback provided by the capacitor C8 is employed. This configuration has the major advantage of driving the transistor T1 well into the ohmic region, thus providing a low resistance path between V_Q and the anode (point X) of the SPAD. This ensures a very fast active quenching transition. Gate of transistor T4 is biased at a quiescent high level (TTL) in the linear region (ohmic region) with very low drain to source voltage drop, hence whenever the quenching pulse appears at the gate of this transistor, it goes into cutoff region and the gate voltage of T1 starts increasing. T1 is configured as a source follower, so that the source voltage rises until it is clamped at the supply voltage V_Q by

T4 entering the ohmic region. During the transient, the blocking diode D3 is switched off, enabling the capacitor C8 (that essentially behaves like a battery, providing a constant voltage ($V_{C8} = 11 \text{ V}$) to further increase (bootstrap) the gate voltage of T1. For detailed analysis of the bootstrap configuration and the voltage driver circuit refer to [98].

To summarize, in the quiescent state, the biasing is such that T1, T2, T3 and T5 are off and T4 is on. They continue to remain in this state until an avalanche is initiated and the comparator output goes high (logic '1'), which triggers the logic circuitry that in turn triggers the voltage driver circuitry that performs the following tasks:

1. T2, T3 and T5 continue to remain off. T4 is turned off, hence T1 turns on.
2. When T1 turns on, it creates a low resistance path between the supply V_Q and node X (SPAD anode); hence V_Q is applied to node X (SPAD anode), quenching the SPAD. It should be noted that this action essentially charges the capacitance ($C_{int} + C_w$) at node X to V_Q . The time for which the SPAD is kept in the quenched state is determined by the quench delay generated by IC U4 plus loop delay (section 3.2.1). This time is defined as the *quench delay* time (T_{QD}) of the circuit and is variable.
3. After the quench time is over, the logic circuit turns on T4, which turns T1 on and at the same time T2 and T5 are also turned on.
4. Turning on T2 and T5 creates a low resistance path between node X and ground, essentially discharging V_Q on $C_{int} + C_w$ to ground. Two transistors are used in parallel to speed up the discharge process. The time for which the two transistors are on is determined by the reset delay IC U5 and is termed as the *reset delay time* (T_{RD}) (section 3.2.1). This process is essentially resetting the device back to V_{Bias}

after which T2 and T5 are turned off and the circuit goes back to quiescent state until another avalanche is initiated.

The above action is repeated each time an avalanche is initiated and the comparator is triggered. It must be noted that besides generating the quench and reset delay; it is also required to send appropriate signals to transistors T1-T5 to turn off or on. Also, it must be noticed that the reset action has to begin as soon as the quench action is completed. These tasks are performed by the timing circuit which is described below.

Timing and delay circuit

In order to simplify the explanation of the logic and timing circuit, consider the simplified version of the previous circuit shown in Figures 3.3 and 3.4 below for two cases (no photon is detected and photon is detected). In this circuit, the quenching and reset transistors are replaced with switches S1 and S2, which act as quench and reset switch respectively. Also, assume that S1 is a p-channel transistor, hence it turns on when logic '0' is applied and S2 is n-channel transistor that turns on when logic '1' is applied. As mentioned earlier all the nand gates are implemented with TTL nand-gate IC 74F00 and the delays (U4 and U5) are implemented with silicon tap delay line IC series DS110X [43]. There are only two possible cases of operation, viz. when there is no photon detected and when a photon is detected (avalanche can be initiated by actual photon or thermally). Each case is explained below.

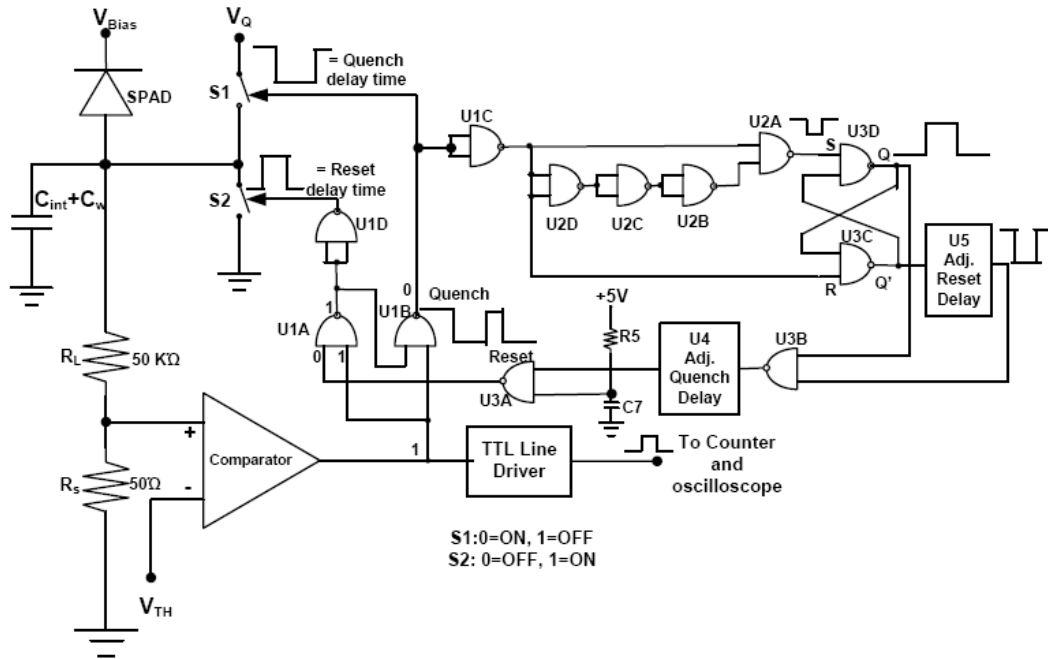


Figure 3.4 Timing and logic circuit; case 2: when a photon is detected.

Case 2: Photon is detected

When an avalanche is initiated (either due to a detected photon or thermal generation) and the comparator is triggered, the output of the comparator switches to logic high ('1') initiating the logic circuit. The logic circuit performs the action in following sequence to generate precisely timed quench and reset delays:

- Logic '1' at the output of the comparator continues to keep S2 off while turning on S1 as shown in Figure 3.4. As soon as S1 turns on, V_Q is connected to SPAD anode, immediately quenching the avalanche. It must be noted that once the comparator output goes high, there are just 2 gate delays and one transistor turn on time before the avalanche is quenched.

- The output of U1B is also applied to the input of U1C at the same time as S1, initiating the loop consisting of U2, U3, U5 and U4.
- The idea behind using 3 nand gates in series (U2D, U2C and U2B) is to generate a short negative pulse at the ‘S’ input of the nand latch formed by U3C and U3D. When the comparator output was ‘0’, the state of the nand latch input was SR= 10 and output QQ’=01. This negative pulse momentarily changes the state of the latch to form the pulses as shown at QQ’ outputs.
- The pulse at Q is passed through the adjustable delay IC U4 and the Q’ output is passed through the delay ICs U5 and U4. Therefore, first pulse is precisely delayed by the delay time set by IC U4 and the second pulse is precisely delayed by the sum of the delays set by ICs U5 and U4 and the pulses obtained at the output of U3A as shown in Figure 3.4.
- S1 and S2 continue to remain in the same state until positive going edge of the quench pulse. That is the output of U3A=0, output of U1A=1 and hence output of U1D = 0, i.e. S2=0, keeping it in off state and output of U1B and hence S1=0, keeping it on.
- As soon as the quench pulse ends and the reset pulse starts (positive going edge), the output of U3A=1, U1A=0 and hence U1B = 1, turning off S1 (S1=1) and at the same time U1A=0 also makes U1D=1, turning on S2 (S2=1). This point marks the end of quench time and the start of the reset time. By turning off S1, the low resistance path between V_Q and the SPAD anode is shut off. Also, turning on S2 provides a low resistance path for the capacitor ($C_{int} + C_W$) to discharge through the ground, effectively restoring the SPAD bias.

- The decreasing voltage also makes the output of the comparator go low, which turns off S1 and S2; bringing the circuit to the quiescent state until another the next avalanche is detected.

The above described action takes place each time an avalanche is initiated.

3.2.1 Results and Discussion

Figure 3.5 shows the prototype (front and back) of the designed circuit. A common metal ground plane was created to keep the noise to minimum as shown in Figure 3.5(left). In order to get an estimate of the spread of different delay times required for this SPAD, ~5-6 SPADs were measured. During the measurements it was found that since the SPAD was not mounted on a heat-sink the count rates started decreasing (heating effects) with time and also there was no temperature control. Hence only limited measurements were done to verify the operation of the designed QC with the SPAD. Complete characterization of SPAD and the QC is presented in section 3.6.

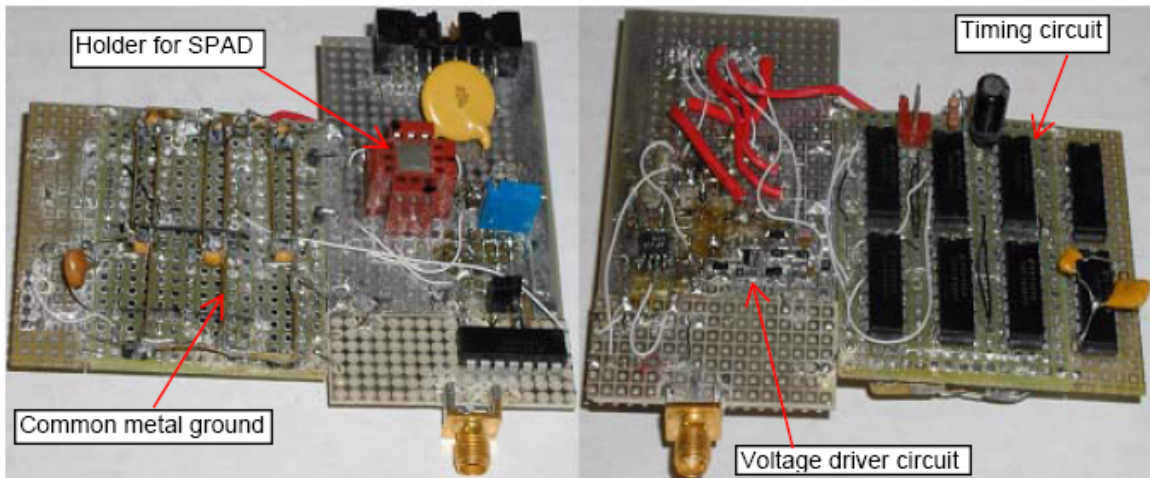


Figure 3.5 First prototype of the designed QC.

Figure 3.6 shows the final output pulse from the line driver IC that is generated each time an avalanche is triggered (either due to photon or thermal). This output pulse is sent to a high-speed counter to register the count. Figure 3.7 shows the high-voltage quench pulse that is applied for the period of the quench delay pulse (Figure 3.8a). Falling edge¹ of the quench pulse represents the reset action i.e. restoring of the SPAD bias. The time for which the reset action takes place is determined by the reset delay pulse (Figure 3.8b). The width of quench, reset and output pulses depends on the SPAD and may vary from device to device. Each of these times and other important parameters of the quenching circuit are discussed in detail.

¹ It must be noted that the quench pulse is a negative pulse and the leading edge (going downward) of this pulse is referred to as rising edge and the positive going edge is referred to as the falling edge.

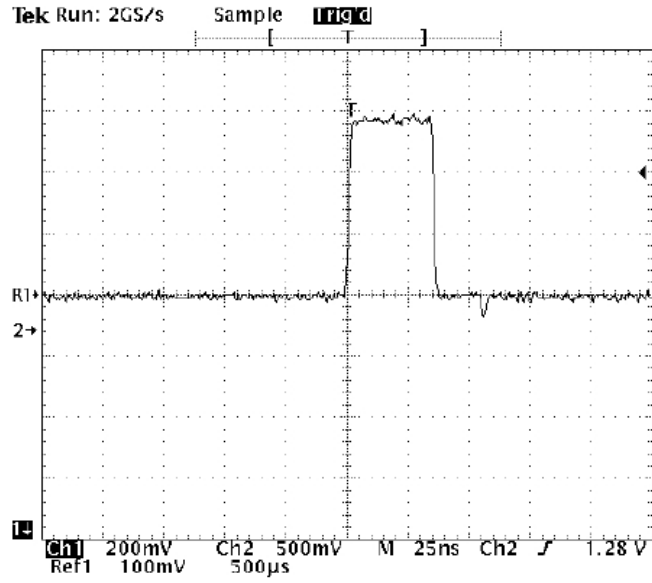


Figure 3.6 Output pulse from the quenching circuit sent to the counter.

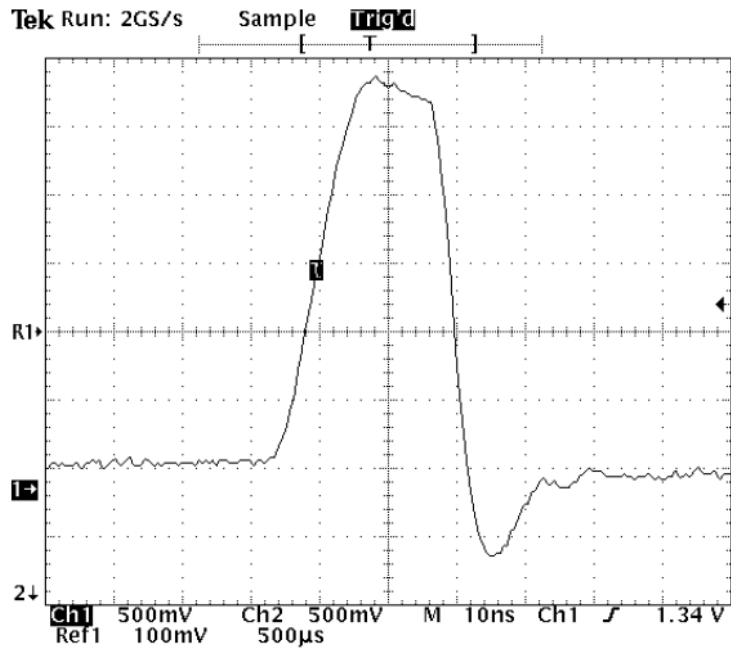


Figure 3.7 Quenching pulse. Measured using 10X probe.

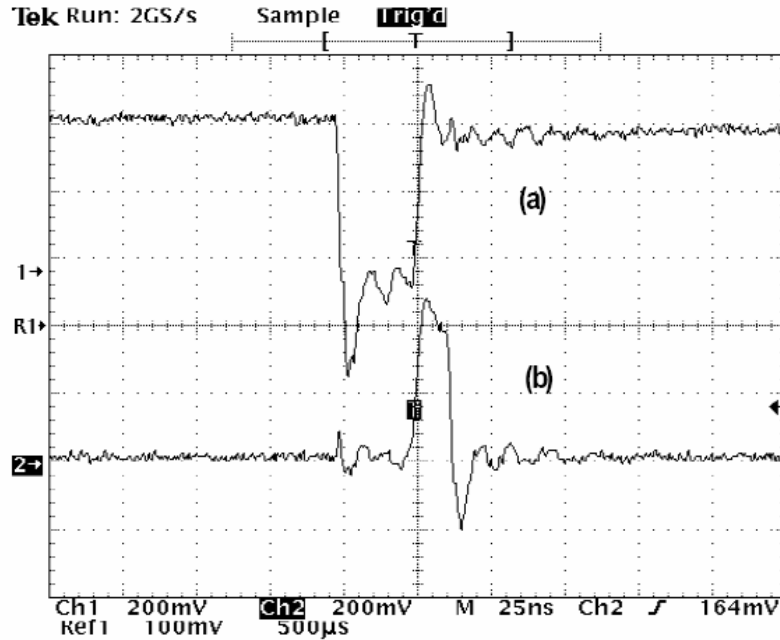


Figure 3.8 Quench (a) and reset (b) delay pulse (precisely matched).

Time to quench an avalanche (T_A)

Once an avalanche is initiated, current starts flowing through the depletion region of the device and a large number of carriers cross the junction. It is intended that the number of carriers crossing the junction should be as small as possible for the reasons discussed in section 2.4 (see afterpulsing). There is a certain amount of time needed to quench the avalanche and it is determined by the combination of SPAD and QC parameters and hence it is different for different combination of SPADs and QCs. In the designed circuit, it is the sum of time required for the SPAD to start conducting current once a photon is detected, time it takes the comparator input to cross V_{TH} , comparator delay to produce the output, one nand gate delay ($U1B$), one transistor turn off time and one transistor turn on time represented by the equation 3.1.

$$T_A = T_{APD} + T_{TH} + T_{CD} + T_{ND} + T_{ON} + T_{OFF} \tag{3.1}$$

where,

T_A = Time to quench an avalanche

T_{APD} = Time required for the SPAD to begin conducting current.

T_{TH} = Time required for the comparator input (Node Y) to cross V_{TH} .

T_{CD} = Comparator LT1719 propagation delay ($\sim 4.5\text{ns}$)

T_{ND} = One nand delay of IC 74F00 (measured to be $\sim 1.5\text{ns}$)

T_{ON} = Turn on time of DMOSFET SST215 ($\sim 1\text{ns}$)

T_{OFF} = Turn on time of DMOSFET SST215 ($\sim 1\text{ns}$)

In the above equation only T_{APD} is SPAD dependent and will vary from device to device whereas all the other times are QC dependent. Most of the QC dependent delays can be determined fairly accurately either by measurement or component datasheets. Based on component delays, T_A for this circuit is approximated to be 10-12ns.

Quench delay time (T_{QD})

Carriers crossing the junction during an avalanche can be trapped in the depletion region of the device. When the quench pulse (Figure 3.7) is applied (SPAD is shut off), these carriers are swept out of the junction. Hence, sufficient time must be provided for the carriers to move out or to be swept out of the depletion region. This time depends on the number of carriers that crossed the junction and the intensity of the current generated that in turn depends on V_{OV} . If T_{QD} is too short, some carriers will remain trapped inside the junction initiating a false avalanche (after-pulsing) and if it is too long, the SPAD off time will increase, introducing non-linearity in photon counting and also limiting the frequency of operation. Hence, T_{QD} is usually determined by establishing a trade-off

between the acceptable after-pulsing, speed and the required PDE i.e. V_{OV} for a particular application. For example if the application does not require high-speed photon counting, T_{QD} can be long, reducing or may be completely eliminating the possibility of afterpulsing. In this circuit, T_{QD} can be easily changed digitally on the quench delay IC U4 which is an advantage of this circuit as compared to the mono-stable based approach. It is very important to note that the total quench delay is not only determined by the delay set on quench delay IC U4 (T_{U5}). The rising edge of the quench delay pulse starts with the rising edge of the comparator and goes through the loop of nand gates, which also introduces delays. This loop delay (T_{LD}) is measured to be 10ns. So, for setting a quench delay time of 35ns, the delay IC U5 is set to 25ns and 10ns is added by the loop. In this thesis, this total time of 35ns is referred to as T_{QD} and is given by equation 3.2.

$$T_{QD} = T_{LD} + T_{U4} \quad (3.2)$$

where, T_{LD} is the loop delay and T_{U4} is the delay set on the quench delay IC U4. As mentioned earlier, behavior of SPAD for different values of T_{QD} was studied for 5-6 SPADs and a range of 25ns-35ns was found to be sufficient. Figure 3.8 and Figure 3.9 shows the pulses for the two lowest and highest observed T_{QD} respectively. Usually only one pulse was seen in the dark at low V_{OV} , but when T_{QD} was set to less than 25ns, more pulses were seen together quite frequently, which suggested that there was afterpulsing. In the designed QC T_{QD} is adjustable from 10 to 60ns, which is sufficient for the selected SPAD.

Reset or recharge delay time (T_{RD})

During reset time, basically the capacitance between SPAD anode and ground ($(C_{int} + C_{wire})$ in Figure 3.4) is discharged through switch S2 to ground, essentially restoring the SPAD bias to make it ready to detect another photon. Therefore, it must be large enough to allow the complete discharge of this capacitance and ensure that the SPAD bias is completely restored in order to avoid retriggering of the comparator, and hence, oscillations. On the contrary, reset time should not be very large as it increases the total dead time of the circuit and hence photon loss. Further, the SPAD is slowly recovering to its normal bias during this time meaning it is half-ready to detect photons. Therefore, if the reset time is too long, the probability that SPAD will detect another photon during this time will increase, not allowing the SPAD to completely quench itself for a long time, leading to diode heating.

T_{RD} of 10-15ns was found to be sufficient for the measured device. Most of the devices worked well with 10ns (Figure 3.8b), but 1-2 required 15ns (Figure 3.9c). When T_{QD} was set to less than 10ns, (i.e. 5ns¹) a train of output pulse was seen at the output (oscillations) suggesting that the SPAD did not have sufficient time to restore the bias completely and the comparator kept retriggering. In the designed circuit, reset delay is adjustable from 5 to 25ns by reset delay IC U5 ($T_{RD} = T_{U5}$).

Output pulse

Figure 3.9 (a) and 3.6 show the output pulse for two different SPAD at the output of line driver IC that is sent to the counter and oscilloscope. The rising edge of the output pulse is formed as soon as the comparator triggers, which initiates the quenching action.

¹ Delays can be adjusted in steps of 5ns in the used delay line ICs.

The output pulse ends when the voltage at the positive input of the comparator is pulled below threshold by the discharging SPAD anode during reset. Therefore the width of the output pulse for this circuit is approximately equal to the sum of quench and reset delay pulses ($T_{QD} + T_{RD}$) as shown in Figure 3.9a.

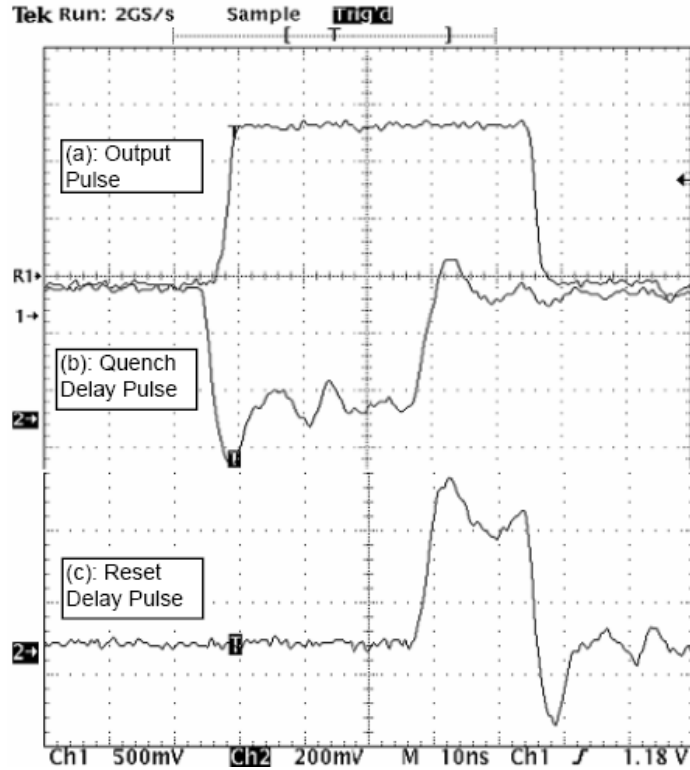


Figure 3.9 Quenching circuit output pulse (a), Quench delay pulse (b) and reset delay pulse (c).

Dead time (T_{DT})

As the name indicates, the time for which SPAD is insensitive to incoming photons is called the dead time (T_{DT}). T_{DT} effectively represents photon loss, hence it is desired that it be as short as possible since it influences the speed and linearity of the circuit and its effects are noticeable, especially at high-count rates. Since, in most MQCs,

T_{DT} is fairly accurately known or can be determined experimentally, photon loss can be taken into account while evaluating the actual photon count rate [100], [101]. Beginning of the T_{DT} can be considered to be the time when the SPAD starts generating an avalanche and the ending time can be considered when the SPAD bias is restored. Therefore for this circuit the dead time is approximately equal to the sum of three times viz. T_A , T_{QD} and T_{RD} , i.e. as soon as the output pulse goes low, the detector must be able to see another photon.

$$T_{DT} = T_A + T_{QD} + T_{RD} \quad (3.3)$$

Speed

Speed of the QC is limited by the associated capacitances (SPAD internal capacitance and Wiring capacitance) and mainly by the speed of the components such as comparator, transistors and diodes. Nothing can be done to reduce the internal capacitance of the SPAD, but the wiring capacitance can be reduced by careful design of the layout.

3.2.2 Improved Timing and Logic Circuit

Few modifications were made to the designed timing and logic circuitry. The modified circuit is as shown in Figure 3.10. For detailed circuit diagram, layout and implementation see Figures A.5, A.6 and A.7 respectively. Modifications do not alter the functioning as compared to the previous circuit (Figure 3.2) described in section 3.2 , but

this circuit required four less nand gates as compared to previous version and hence one less nand gate IC 74F00. The only difference is that the loop delay for the new circuit reduced by $\sim 5\text{ns}$, hence the quench delay on the delay IC needs to be set accordingly. It should be noted that component designations are different in this circuit as compared to the previous one. The circuit is explained below for two cases and can also be referred from [102].

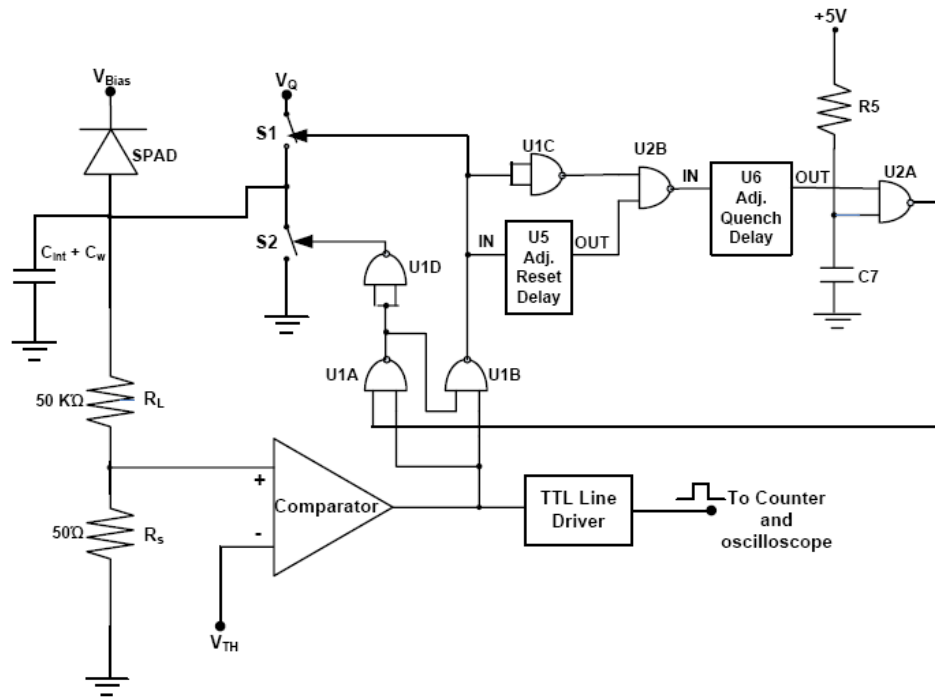


Figure 3.10 Circuit diagram of the improved quenching circuit. For detailed circuit diagram refer to Figure A.5.

Case 1: No photon is detected

When no photon is detected, the comparator output remains zero, the outputs of U1A, U1B and U1D are 1, 1 & 0 respectively, and hence S1 and S2 both are off. The

circuit continues to remain in this state until a photon is absorbed in the active region of the device and an avalanche is initiated.

Case 2: Photon is detected and an avalanche is initiated

When a photon is detected and an avalanche is initiated, large current flows through the SPAD. The large value resistor R_L initially limits this current. When the voltage at positive input of the comparator crosses V_{TH} , the output of the comparator goes high. Output of U1A and hence U1D remains same, hence S2 continues to remain off. At the same time U1B output goes low, hence S1 is turned on and hence V_Q is applied to the anode of the SPAD, thus quenching the avalanche. The output of U1B is also applied to U1C and the reset delay IC U5. The output from U1C propagates further through U2B, quench delay IC U6, U2A, U1A and finally generating a '1' at the output of U1D, thus turning on switch S2, initiating the reset action. At the same time, output from U1A goes to U1B, which generates a '1' to turn off switch S1. The reset action is terminated after about the time determined by the reset delay IC U5 when the '0' at the input of reset delay IC U5 propagates through the same loop and turns off S2. Now, the SPAD is ready to detect another photon. This loop action takes place each time the SPAD fires and the current is large enough to trigger the comparator.

3.2.3 Summary

This section presented the design of a high-speed quenching circuit; a critical component of a SPAD-based photon counter. A novel logic circuit based on standard

TTL components that generates precisely matched, accurate quench and reset delays was designed and analyzed. The designed logic circuit uses only 6 TTL nand gates and 2 delay ICs, making it a much simpler design that requires very few basic components. Further, since the designed timing circuit is digital, the generated timing can be expected to be precise, which is not the case with RC timing used in mono-stable. Also, timing based on RC circuit can change with time and temperature. Moreover, the digital nature of the designed circuit and ease of changing delays will make the tuning of a multi-channel system much easier. Time to quench the avalanche (T_A) is an important parameter used to determine the quality of a QC. It must be noted that it takes for the SPAD to start the avalanche (T_{APD}) depends on the SPAD and is different for different SPADs and cannot be controlled (is unknown). For the designed circuit, this time (T_A) is ~10-12 ns, which comparable with most of the reported QCs that have been used with large area devices [95], [96], [98].

3.3 Design and Testing of Temperature Controller

SPAD parameters such as DCR, V_{BR} and afterpulsing varies with temperature, hence temperature stability is a must. For initial testing, a temperature controller module (model 5C7-362) from Oven industries Inc was used. This model can be connected to the serial port on the computer and the temperature can be controlled using the software provided. It provides accurate temperature control and is very easy to use. But, to build

compact, stand alone single photon counting module, it was necessary to design a controller of our own which is compact and provides accurate temperature control. A controller based on IC Max 1978 [103] was designed. The controller IC gives excellent performance and controls temperature with a stability of $\pm 0.001^{\circ}\text{C}$. It is available in a 48pin QFN package (7mm x 7mm) that occupies very small space on the printed circuit board (PCB) and provides an excellent low cost solution. Minor modifications were made in the circuit configuration provided in [104] to suit the TEC specifications of the SPAD provided in the passport that comes with the SPAD. Figure 3.11 shows the circuit diagram and Figure 3.12 shows the first prototype. Since this IC was relatively new and comes in a QFN (Quad flat no lead) package, for the prototype, they were soldered at Schmartboard, Sunnyvale, CA [105] on their patented Schmartboard (Figure 3.12).

Instructions for testing the controller can be found in [103] [104]. The temperature is set by adjusting the voltage on the variable resistor R25 at the input of FB+ and FB-, for e.g. 0.75V represents 25°C , 1V approximately represents 10°C and the slope is approximately $-14\text{mV}/^{\circ}\text{C}$ [103]. Resistance of the thermistor inside the SPAD varies with temperature as shown in Figure 3.13.

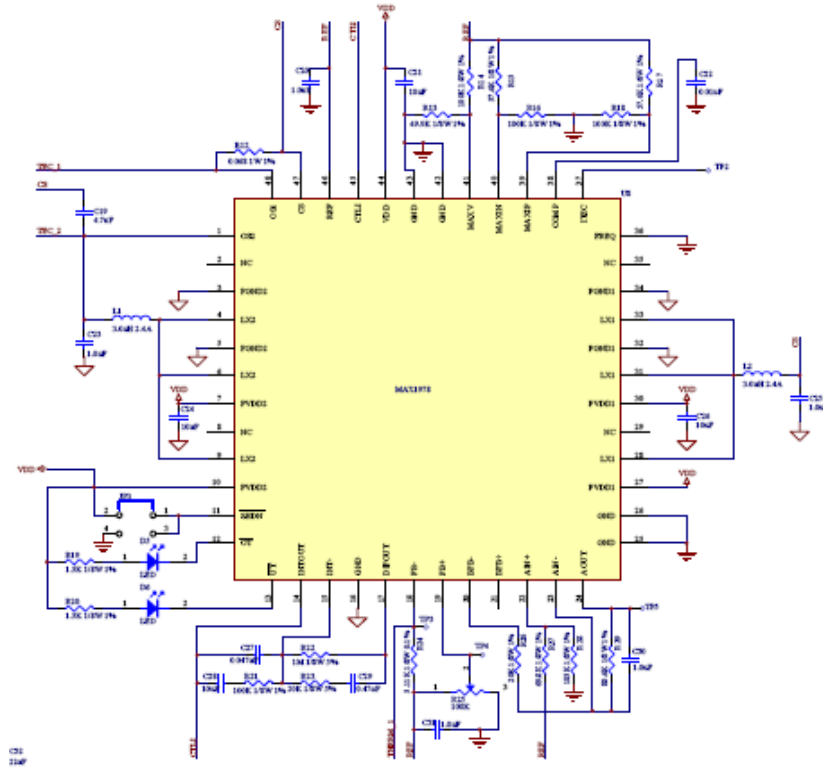


Figure 3.11 Circuit diagram of the implemented temperature controller.

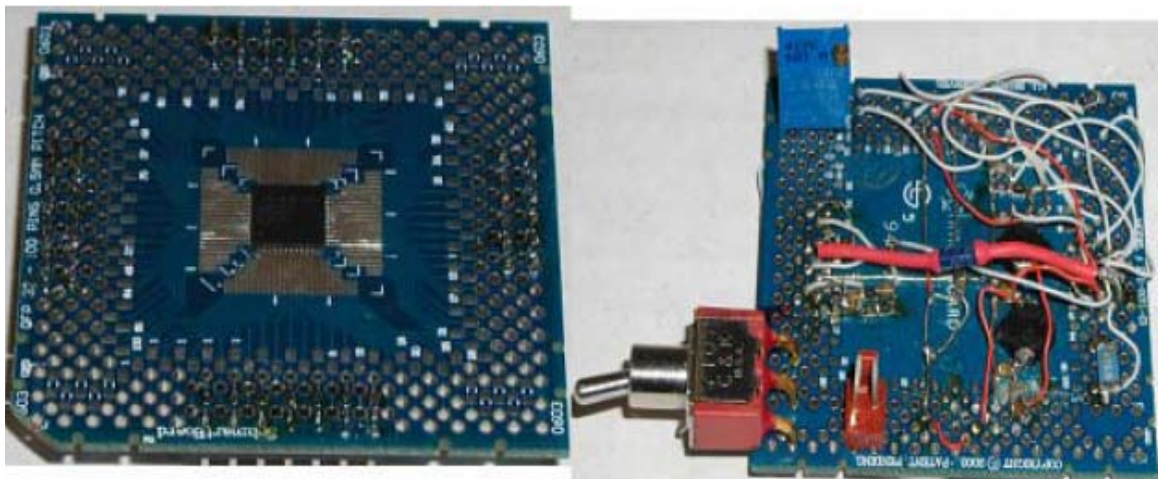


Figure 3.12 First prototype of the temperature controller circuit (front and back).

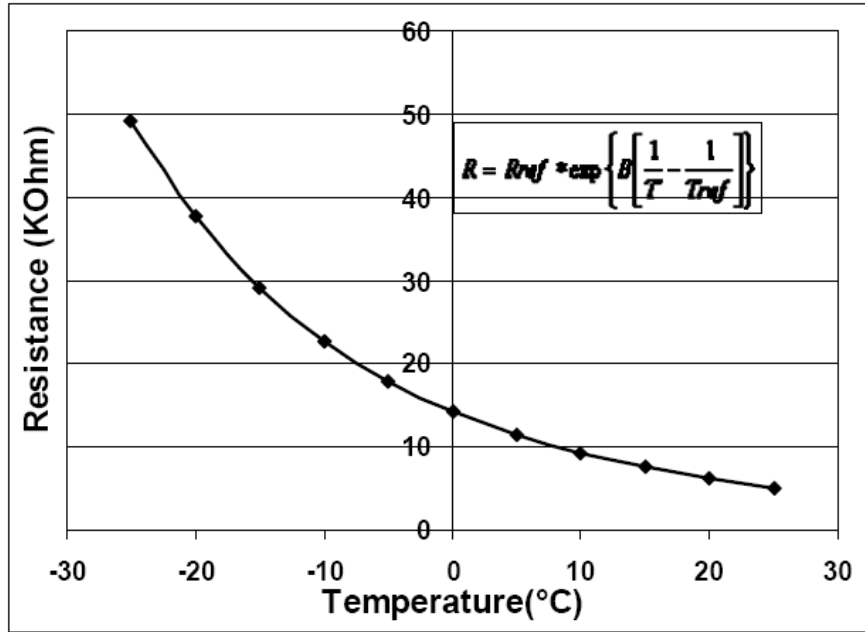


Figure 3.13 Variation of the thermistor resistance on C30902S-DTC.

Based on the resistance values shown in Figure 3.13, the voltage that needs to be set in order to get the required temperature on the TEC was calculated. Figure 3.14 shows only the bridge formed in temperature controller circuit (Figure 3.11, Figure A.2), where TP4 (Pin FB+ of IC Max 1978) is the set voltage and TP3 (Pin FB- of IC Max 1978) is the voltage on the peltier. TP3 and TP4 are just the test points on the circuit and can be seen in Figure A.4. When the voltage on TP3 is equal to the voltage on TP4 ($V_{TP3}=V_{TP4}$), the bridge is balanced and the actual temperature on the peltier is equal to the set temperature. The voltage to be set on TP4 to get the required temperature can be calculated using only one side of the bridge using the simple voltage divider equation 3.4, where, $R(t)$ for different temperatures can be obtained from Figure 3.13 and $V_{ref}=1.5V$ [101]. Voltage on TP4 is set using the 100K potentiometer R25. Figure 3.15 shows the values as suggested by the datasheet and the values that were experimentally measured. It

was found experimentally that for higher temperatures the slope is $\sim -14\text{mV}/^\circ\text{C}$, but as we go to lower temperatures (less than -10°C), the slope decreases and becomes as low as $-8\text{mV}/^\circ\text{C}$.

$$V_{TP3} = \frac{V_{ref} \times R(t)}{1200 \times R(t)} \quad (3.4)$$

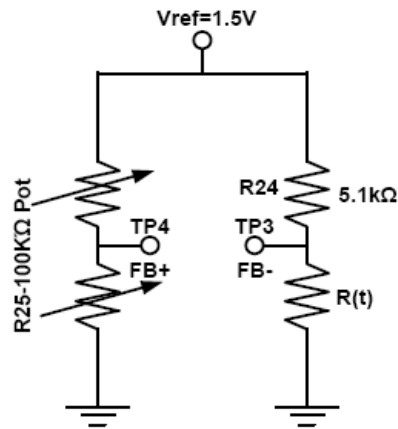


Figure 3.14 Bridge circuit formed in Figure 3.12 used to calculate the voltages to set different temperatures on SPAD.

It is very important to test the operation of the temperature controller circuit before using it with actual diode as it involves switching of high currents and a wrong connection can damage the peltier. Hence, a simple test circuit was designed to test the controller. This circuit basically emulates the thermistor and the peltier inside the diode. When the set voltage was changed, the voltage across the peltier changed either in the positive or negative direction or it became zero. So just by measuring this voltage and by

checking if the correct over-voltage and under-voltage LED's glowed, it was verified if the temperature controller was able to sense the change in voltage and hence temperature.

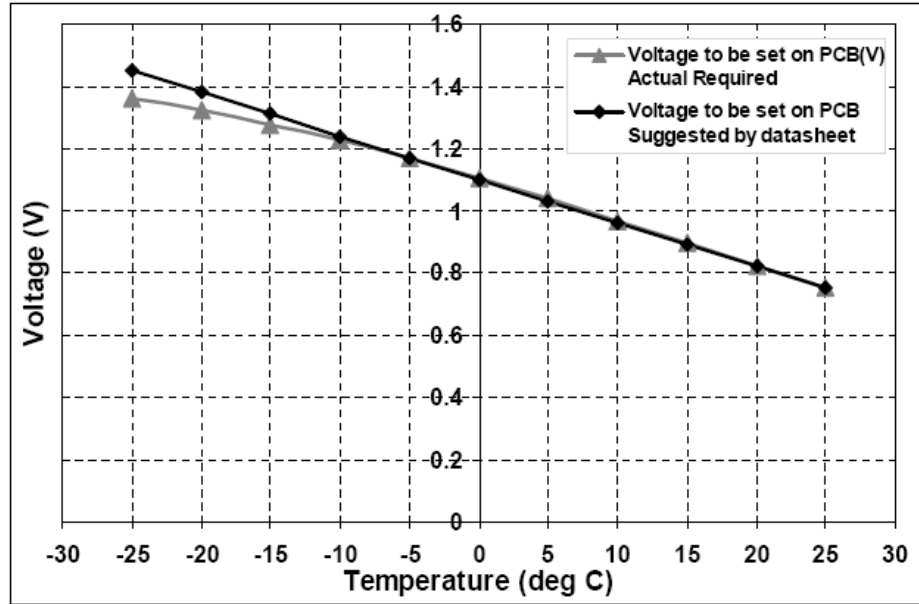


Figure 3.15 Calculated voltage values to set different temperature on SPAD.

3.4 Design and Testing of Power Supply Module

The SPAD, the designed QC and the temperature controller all together need four different voltage supplies viz. a variable 170-250V for SPAD bias (V_{Bias}), 25-35V for the quenching voltage (V_Q), 12V for bootstrap in QC and 5V for the logic ICs and temperature controller. Further, since the temperature controller switches currents of the

order of ± 2 amps (depending on required temperature), the +5V supply should have the capability to handle such currents. A power supply unit based on standard components was designed; Figure 3.16 shows the circuit diagram along with the component part numbers and values. Wherever required, the output voltage was made variable on the designed PCB (Figure 3.17).

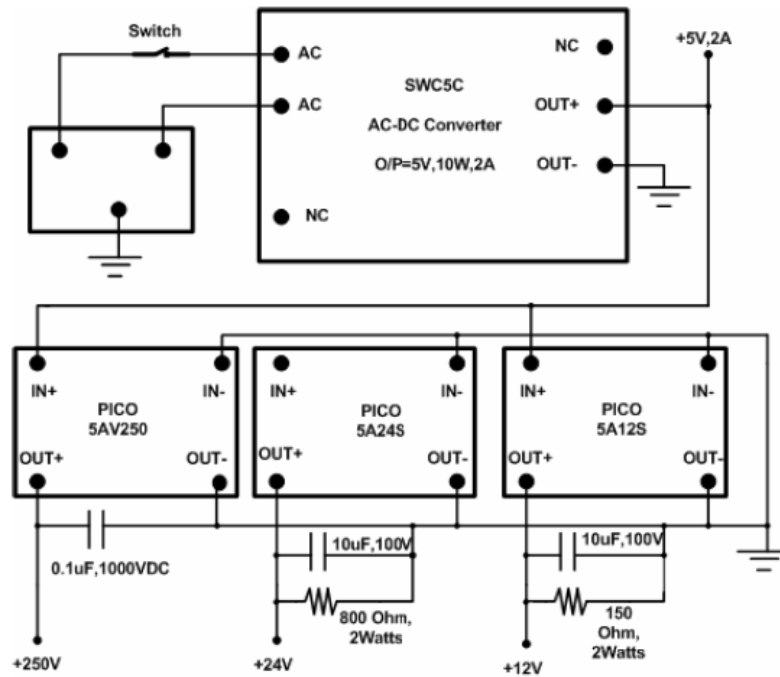


Figure 3.16 Circuit diagram of the designed power supply module

3.5 Complete Single-channel Photon Counting Module (S-SPCM)

The designed QC and the temperature controller circuit were laid out and fabricated on the PCB as shown in Figure 3.17 (see Appendix A for detailed circuits and layouts). The PCB along with the SPAD were mounted on a metal box to make a compact, stand-alone single photon counting system as shown in Figure 3.18. Since the SPAD operates with high voltages, it is expected to generate a lot of heat and power when it is operated for extended hours or when operated at high over-voltages with high light levels. Further, the temperature controller switches currents of the order of ± 2 amperes; hence it is expected to generate a lot of power too. The generated heat from device is dissipated through the bottom part (base) of the SPAD. Hence the device is purposefully mounted on a black metal box that serves two purposes viz. blocks external ambient light and serves as the heat sink. The module has an output co-axial connector that can be connected to oscilloscope or photon counter or both as required. All the required voltages are supplied to the module through the power supply module (Figure 3.18c), hence only connection required to the complete module is 120Vac power from the wall.

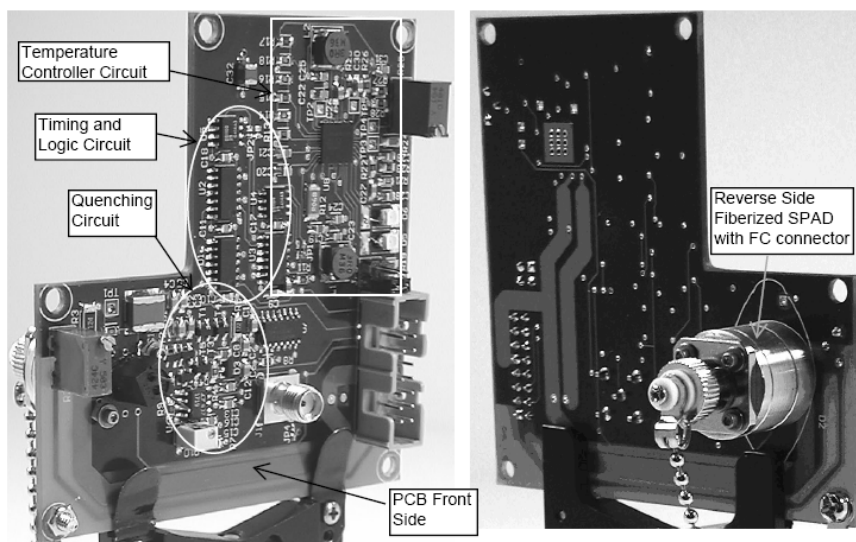


Figure 3.17 Designed PCB; front side (left) and reverse side with mounted fiberized SPAD (right).

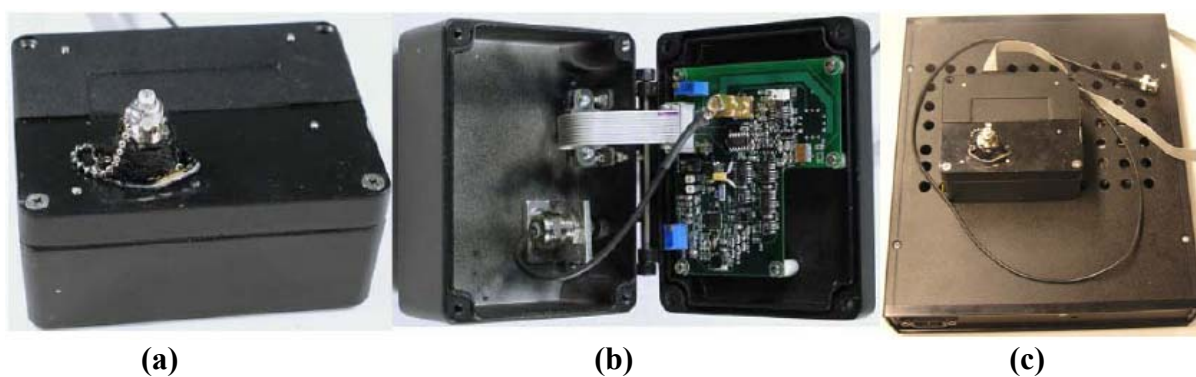


Figure 3.18 Implemented S-SPCM; (a) closed module showing fiberized SPAD, (b) open module shown mounting PCB and (c) with power supply module.

Performance of the SPAD, QC and the S-SPCM as a whole were characterized and are discussed in detail in the next section. Further DNA-sequencing was also performed with this module, the results of which are discussed in Chapter 6.

3.6 Experimental Results and Discussion

This section presents experimental characterization (electrical) of the designed photon counting module. These results reveal the photon counting capability of the selected SPAD model along with the designed QC and the temperature controller.

Experimental set-up

Figure 3.19 shows the block diagram of the experimental set-up. A white light lamp was used as the source of light for all experiments; it was turned off for dark count related experiments. The light from the lamp was passed onto an attenuator box using a fiber optic cable (FOC1). This attenuator box consists of 2 adjustable neutral density (ND) filter wheels for selecting filters with different optical density (OD). Each wheel has 6 filters and a range of 0-5 OD, therefore using a combination of these two wheels, different attenuation in the range of 0-10OD can be selected. For more attenuation, ND Edmund Optics filters were used. These extra filters were fitted into the space in front of the white lamp.

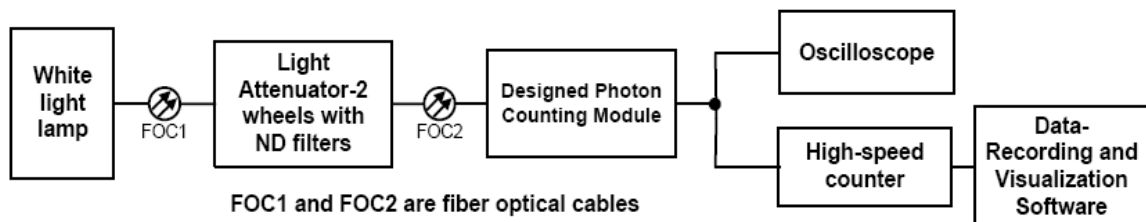


Figure 3.19 S-SPCM: Block diagram of the experimental set-up used for characterization.

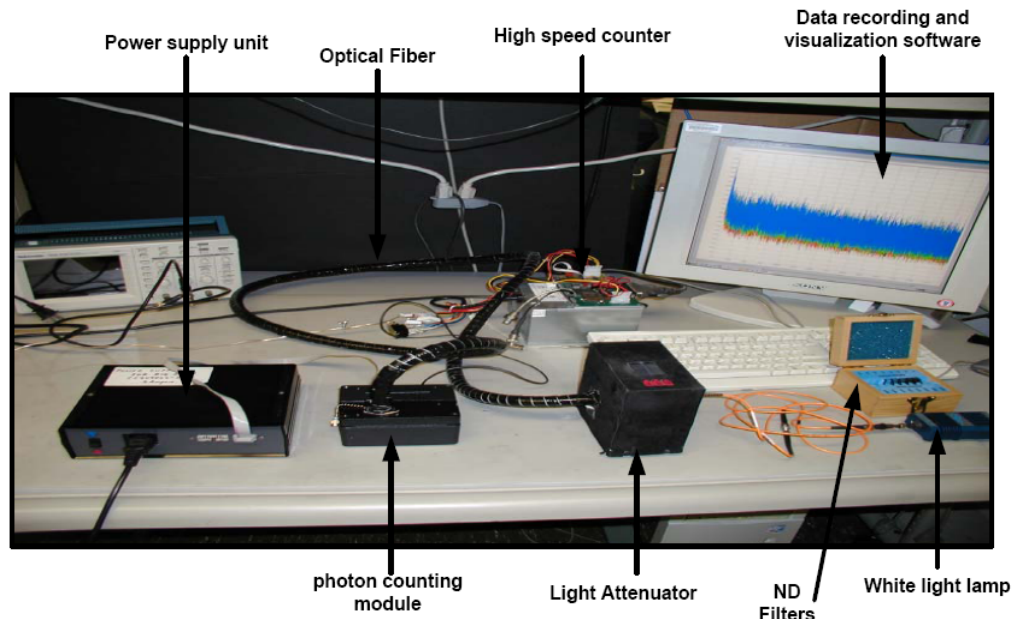


Figure 3.20 S-SPCM: Photo of the experimental set-up.

Breakdown Voltage (V_{BR})

V_{BR} varies for different SPADs of the same type and it depends on temperature. V_{BR} at two temperatures (+22°C and -20°C) is specified by the manufacturer along with each SPAD; hence the temperature coefficient can be easily determined. For the cooled diode this value ranges from 0.5 to 0.8 V/°C. Breakdown voltage was measured at different temperatures and is as shown in Figure 3.21. The calculated temperature coefficient for this particular diode is 0.6095V/°C and experimentally it was found to be 0.66V/°C. This experiment verifies the functioning and accuracy of our temperature controller with the SPAD. It must be noted that difference in the voltages to be set on the PCB was found at low temperatures (Figure 3.15) and is reflected in Figure 3.21. The reason for this can be (a) difference in ambient temperature and (b) there is a ceramic

piece between where the SPAD chip is placed and where the thermistor is placed, hence it takes a little longer time for the thermistor to reach the same temperature as the device. Since these measurements were made rather immediately after the temperature was changed, this difference at lower temperature can be due to experimental error. But, what is important is that once the temperature becomes stable, it should remain stable for long hours. If the diode gets heated and the temperature of the detector increases, it can increase the V_{BR} of the device which can result in decrease of effective V_{OV} and hence decrease in gain. Hence temperature and V_{BR} stability is very important.

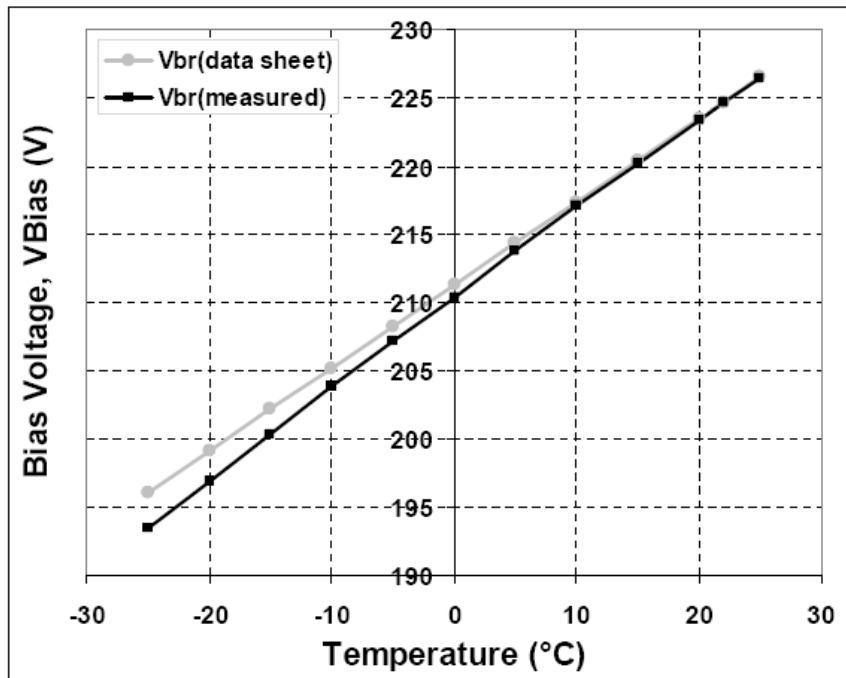


Figure 3.21 S-SPCM: Variation of V_{BR} with temperature.

Variation of Photocount Rate (PCR) with Comparator Threshold (V_{TH})

While performing the experiments it was found that the output count rates changed when the comparator threshold (V_{TH}) (R10 in Figure 3.2) was changed. Hence, in order to find an optimum threshold, behavior of the PCR with variation in V_{TH} was studied (Figure 3.22). It was observed that at very low thresholds ($< 3\text{mV}$), the comparator picked-up noise (Node Y in Figure 3.2) and the PCR increased abruptly. For such low thresholds, shape of the output pulse completely deformed and continuous train of pulse is seen on the oscilloscope and the difference from the regular pulse was clearly noticeable. It must be noted that the V_{TH} where the comparator starts picking up noise depends on the circuit layout and the wiring capacitance. Stable count rate was observed for a good range (3-11mV) of comparator thresholds, implying that all the photons that are received by the detector are counted for this threshold range. Further, the count rate abruptly drops to zero as V_{TH} is increased beyond 11mV. This is a strange behavior since it would be expected that the count rate would start dropping slowly rather than just going to zero. The QC is digital in nature and it quenches the avalanche as soon as it receives a signal from the comparator, which means that somehow the SPAD and the comparator input reach such a state that they cannot detect and trigger the comparator. The reason for this can be that as the V_{TH} is increased; the voltage required at Node Y (see Figure 3.2) also increases, effectively allowing the avalanche to develop for a longer period of time. As V_{TH} is increased further, at one point this time probably becomes comparable or greater than the average arrival time between two photons. This means that the incoming photos are not detected. Therefore the comparator threshold must be selected in the stable region and as low as possible such that it does not register counts

due to noise. For this particular combination of PCB and SPAD, V_{TH} is selected to be 4mV. Unless otherwise mentioned, V_{TH} is set to 4mV for this SPAD for all the experiments in this section.

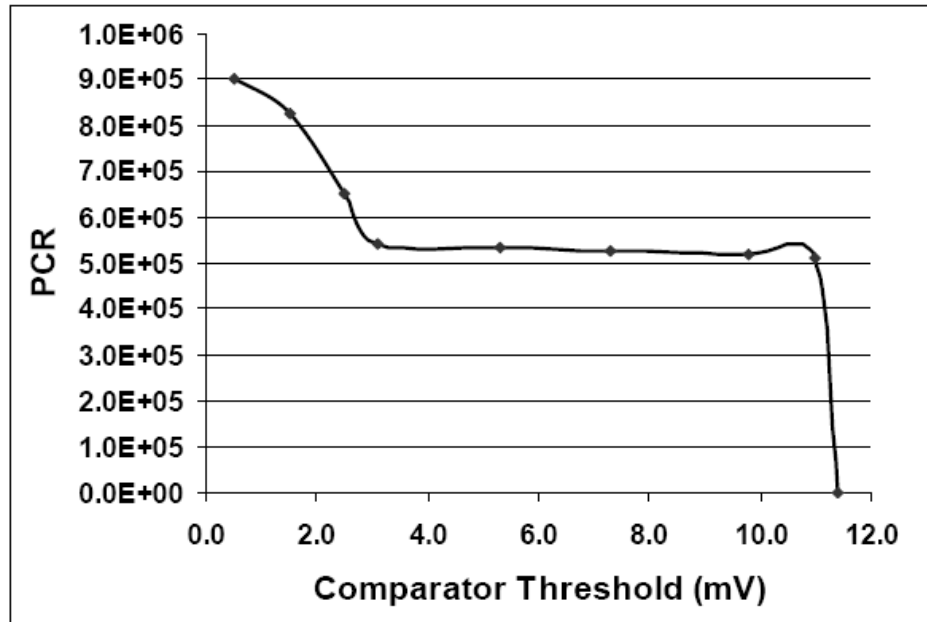


Figure 3.22 S-SPCM: Variation of PCR with comparator threshold (V_{TH}).

Stability

In order to check the stability of V_{BR} and the temperature controller, the device was tested for long hours at three different count rates. Also, typical DNA sequencing experiments last for one hour, hence, if the photon counter is illuminated with high light levels for long period of time, it may get over-heated. If adequate heat sink is not provided, device V_{BR} increases, effectively decreasing the V_{OV} , resulting in drop in count rate levels with time. To measure all these performance, the S-SPCM was illuminated

with a constant light and the PCR was recorded every hour for 6 hours at -20°C (Figure 3.23).

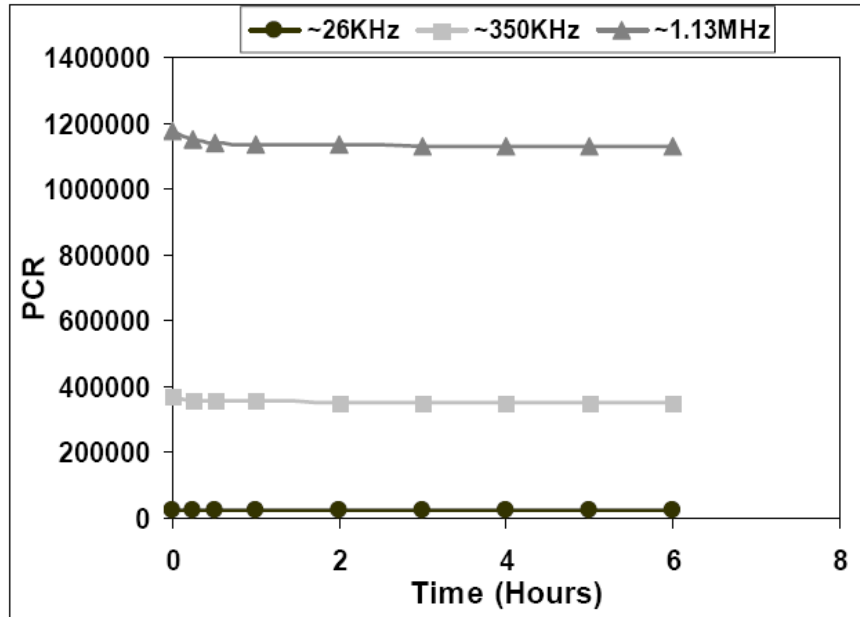


Figure 3.23 S-SPCM: Stability.

The experiment was repeated for three different light levels. For all three light levels it was observed that initially the PCR drops slowly between 0 to 30 minutes before settling to a stable value. As speculated earlier, the reason for this can be that once the diode is illuminated, the temperature on the diode chip starts increasing depending on the illumination level. Further, the diode is mounted on a crystal that is glued or rested on a 2-stage cascaded peltier element. The temperature-sensing resistor rests on the top of this 2-stage peltier element. So basically, there is a ceramic piece between the top of the peltier element and the diode. It takes some time for the heat to pass through this ceramic and raise the temperature of the sensor. Once the temperature of the sensor changes, it

adjusts the current on the peltier to accommodate for the diode heating and stabilize the temperature. Hence, it can be concluded that this initial drop is due to the property of the diode rather than circuit design. The initial drop in count rate varies between 3 to 4 % and once the count rate stabilizes, the maximum change in count rate is about 0.5%, suggesting that the designed S-SPCM is quite robust for performing long experiments and that the VBR and temperature controller are highly stable.

Dark Count Rate (DCR)

Quality of a SPAD can be judged by studying its behavior in the dark. Dark counts represent the internal noise of the detector and the square root of the variance of dark count essentially represents the minimum detectable signal (MDS). DCR depends on V_{OV} and temperature and dependence on both the parameters was studied. Figure 3.24 shows the variation of DCR with V_{OV} at two different temperatures, viz. -20°C and $+22^{\circ}\text{C}$. DCR has a linear dependence on the V_{OV} at both temperatures. When the temperature was changed from $+22^{\circ}\text{C}$ to -20°C , the DCR decreased by ~ 42 times and this difference is consistent at almost all V_{OV} , which clearly shows that DCR can be significantly reduced by operating the device at lower temperatures. For -20°C , the DCR does not increase much with V_{OV} and even at $10V_{OV}$ the DCR is just 500 Hz, which can result in tremendous improvement in SNR, sensitivity and MDS in many applications. From DNA-sequencing point of view this DCR (at -20°C) is negligible (refer to Section 1.5). Figure 3.25 shows the variation of DCR with temperature. DCR increases exponentially with increase in temperature for all three over-voltages and increases much faster as V_{OV} increases ($V_{BR}+10\text{V}$ curve). In summary, DCR of this device increases exponentially with increase in temperature and can be decreased significantly (~ 42 times)

by cooling the detector. Hence, unless otherwise mentioned, most of the experiments are performed at -20°C . Since this decrease in DCR due to temperature is a property of the silicon, similar decrease in DCRs can be expected for all silicon-based detectors.

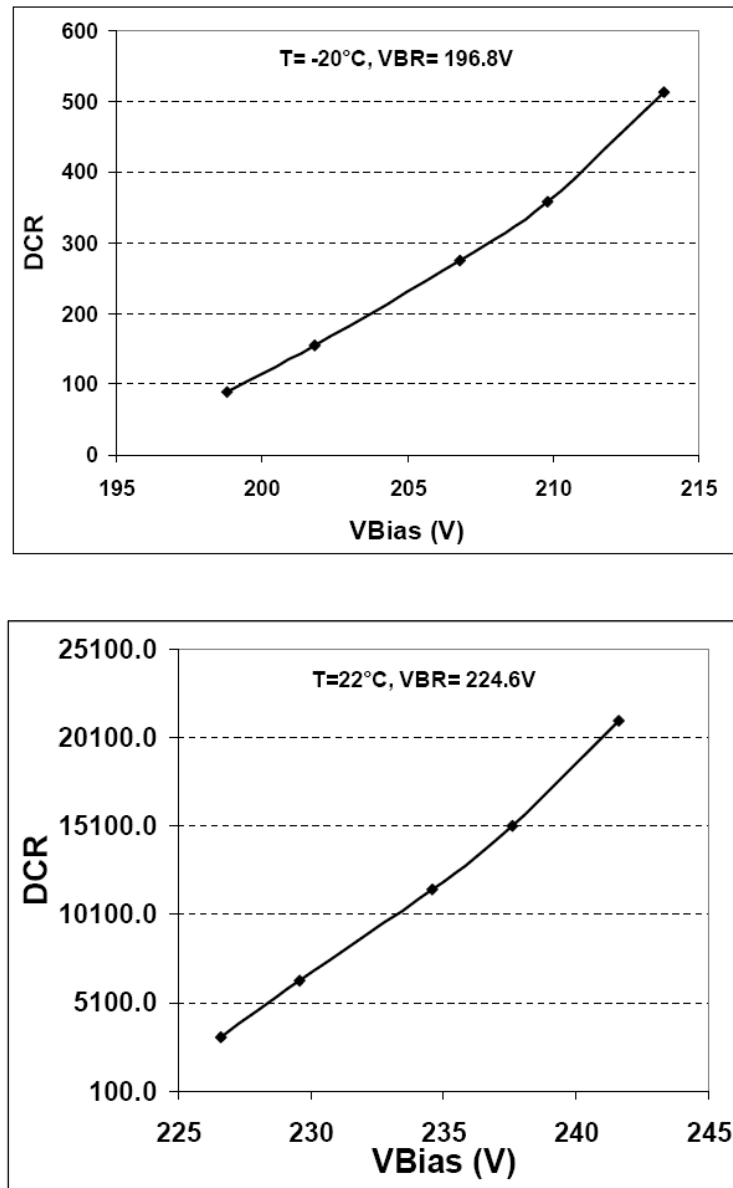


Figure 3.24 S-SPCM: Variation of DCR with V_{OV} at -20°C (top) and $+22^{\circ}\text{C}$ (bottom).

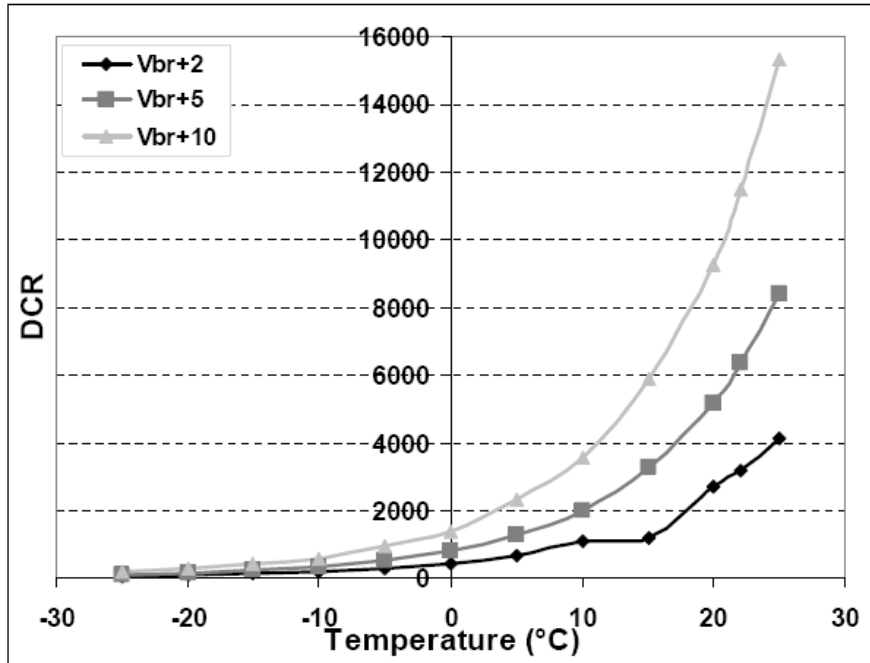


Figure 3.25 S-SPCM: Variation of DCR with temperature at three different V_{ov} .

Noise

Noise in a photon counting system is determined by the distribution of photo counts. A correctly operating photon counting system follows a Poisson distribution where the variance of the photo counts (the number of photons counted over the given time interval) is equal to its mean value. In this case, match between the measured photon count distribution and the Poisson distribution determines the quality of the counting circuit. Photo counts were accumulated over 0.1sec (integration time) and were recorded for ~30 minutes with our software. Figure 3.26 shows the histogram of the photo count distribution (experimental histogram, represented by bars) of the designed S-SPCM compared to the Poisson distribution function that best fits the measured distribution of photo counts (solid line), demonstrating a good match between the experimental and

theoretically predicted distributions. The mean of the recorded photo counts is equal to its variance and represented by equation 3.5. This basically indicates that the measured noise is only caused by the stochastic nature of the photon fluxes detected by the photon detector and that the detector itself does not produce any additional noise.

$$Mean = \frac{2(FWHM)^2}{\ln(2)} \quad (3.5)$$

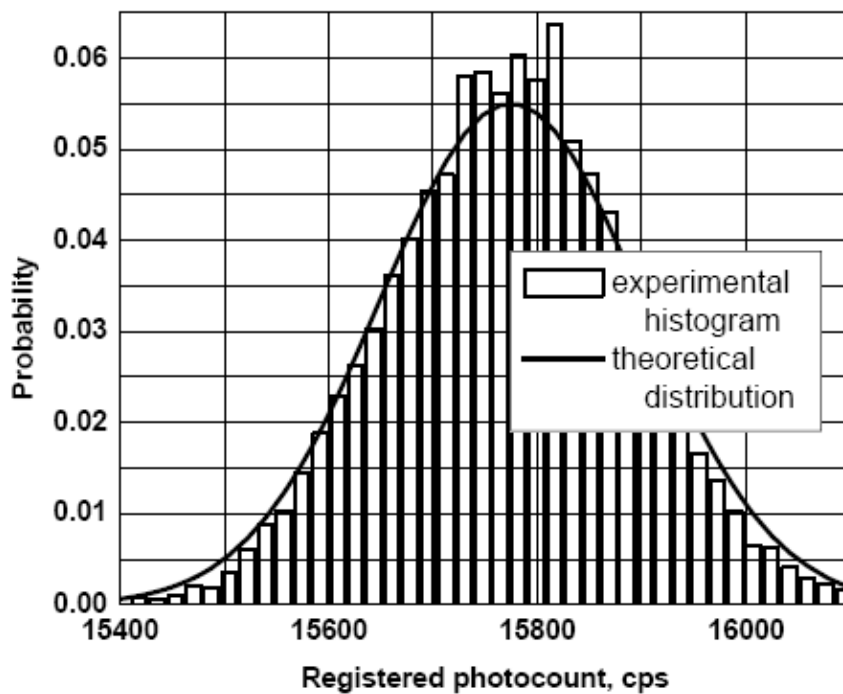


Figure 3.26 S-SPCM: Histogram of photo count distribution at the detector output as compared to Poisson distribution.

Sensitivity, optimum operating point and SNR

Sensitivity of a SPAD can be increased by increasing the V_{OV} since the avalanche triggering probability increases with V_{OV} [45]. But since increasing V_{OV} also has the effect of increasing the DCR and after-pulsing, operating at high V_{OV} is not feasible in many applications. Generally these are the applications that require very low DCR. But, DCR of this SPAD ($T=-20^{\circ}\text{C}$) is not a problem for DNA-sequencing applications even at high V_{OV} (see Figure 3.24) since the background counts of the sequencer itself are much higher (typically 200-400 KHz) than the DCR. The behavior of DCR with increasing V_{OV} (Figure 3.24) essentially represents the gain of the SPAD. Since the gain of a SPAD is same at each V_{OV} , (in dark or light) PCR should approximately follow the same pattern (increase by same factor) as the DCR. Hence, for a constant light level, one can expect to see an increase in count rates with increase in V_{OV} and the rate of increase would be similar to the rate of increase of DCR with V_{OV} . Further, assuming poisson statistics, the noise of the detector increases as the square root whereas the signal increases linearly, hence the effective SNR increases much faster with increase in V_{OV} and increase in SNR means increase in sensitivity.

The idea here is to first measure the attenuation versus PCR at low V_{OV} for the device under test. If both are plotted on a log-scale, the device would be linear if the curve goes under 45 degree from X and Y axis. If the plot is non-linear, the over-voltage is increased in small steps and same measurements are repeated until either the best linearity is obtained or if no increase in sensitivity is observed (Figure 3.28). Figure 3.28 shows that for the same light level (attenuation), the count rate increases with V_{OV} , suggesting that the S-SPCM becomes more sensitive. Finally, it reaches a point where no

improvement in sensitivity is observed. Since both the axes in Figure 3.28 are log scale, the device can be called linear if the obtained curve is 45 degrees from both axes, passing through origin. But no detector is ideal and further, light attenuation levels (X-axis in Figure 3.28) are not well calibrated. Sometimes for the same attenuation setting, two completely different count rates were observed.

In order to filter the experimental non-ideal effects, S-SPCM is compared with PKI SPCM¹. For each attenuation level and each over-voltage, the count rates are measured from the S-SPCM and PKI SPCM without changing the optical setting or moving the filters. Since, PKI SPCM is a known device, its count rates are set as the comparison standard. Same fiber is used for both the modules since both are fiberized and have FC connectors. This way it is ensured that exactly same light output power is focused on to both the detector. Figure 3.27 shows the block diagram of the experimental set-up.

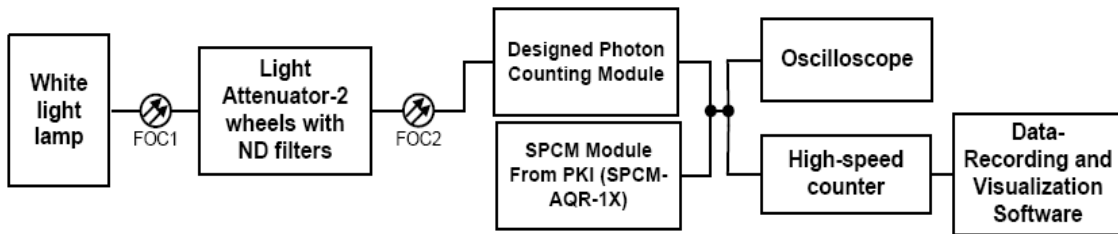


Figure 3.27 S-SPCM: Experimental set-up for characterizing sensitivity.

It must be noted that there is just one curve for PKI SPCM in Figure 3.28. This is because the PKI SPCM is tuned to best V_{OV} that cannot be changed. Finally the

¹ SPCM module SPCM-AQ-1X from Perkin Elmer Optoelectronics [3] is referred to as PKI SPCM in this thesis. This module uses the revolutionary SLIK diode that has a typical active area diameter of 180 μ m. This module has the best linear and dynamic range (~4MHz and 15MHz respectively) for a large-area SPAD.

attenuation versus photo count curve for each V_{OV} is plotted against the attenuation versus photo count curve of PKI SPCM (red (SPCM) curve in Figure 3.28) as shown in Figure 3.29. This basically means that for one attenuation setting, the count rate obtained with S-SPCM for each over-voltage are compared with the count rates obtained with PKI SPCM. Therefore any non-linearities are filtered out, since they affect both the modules in the same way. Hence, if both the device has similar count rates, a perfect linear curve will be obtained. Figure 3.29 shows that the sensitivity (count rates) of S-SPCM approach the count rates of PKI SPCM as V_{OV} is increased. These curves clearly show the DR and linearity of the designed module for each over-voltage. Further it must be noted that the DCR has been subtracted from the plotted values of PCR (it can be neglected, since DCR is 500 Counts/s for S-SPCM and is very small as compared to obtained PCR).

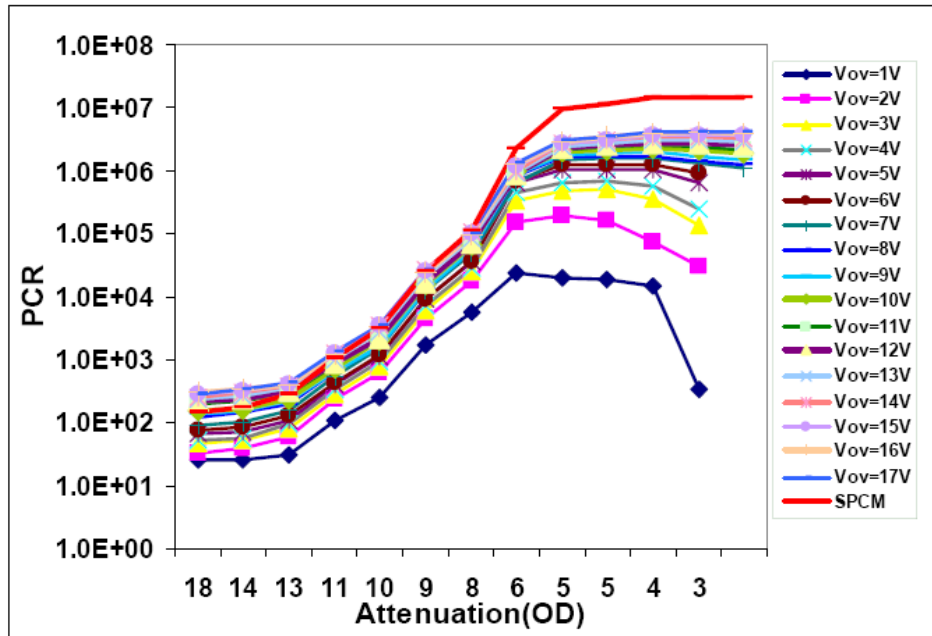


Figure 3.28 S-SPCM: Attenuation versus PCR at different V_{OV} .

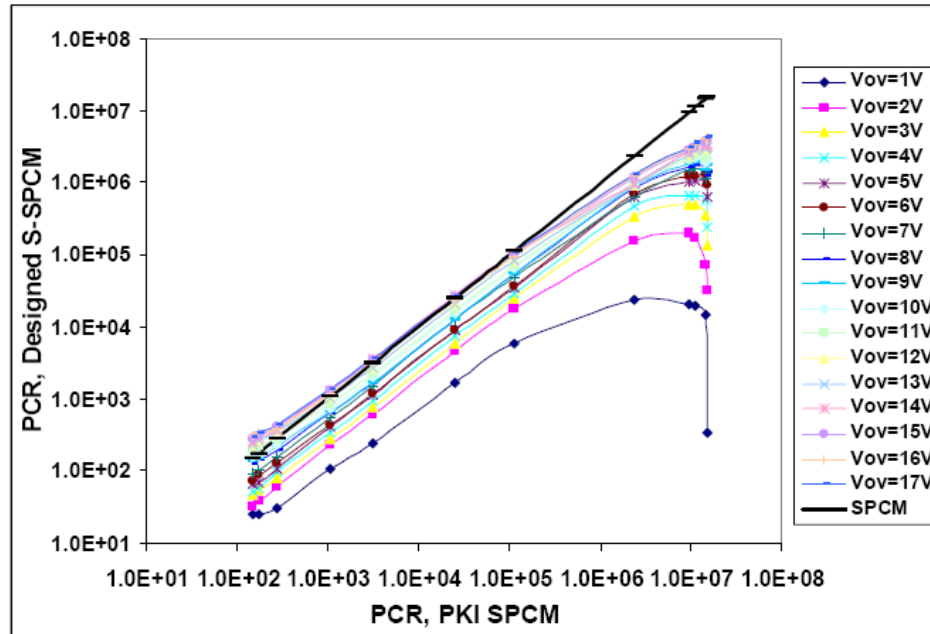


Figure 3.29 Attenuation versus PCR of S-SPCM at different V_{OV} plotted against attenuation versus PCR of PKI SPCM.

Based on the dead-time of the quenching circuit (50-60ns for this particular SPAD), theoretically a maximum saturation count rate of 16-20 MHz should be possible. But the maximum count rate was found to be ~ 4.3 MHz at $17V_{OV}$. This basically meant that either the SPAD was not capable of operating at high frequency or the quenching circuit was not capable of counting at high speeds. The problem was found to be with the QC. It was found that there was a large voltage drop across the high value resistor R3 ($100K\Omega$) connecting V_{Bias} to the SPAD cathode (see Figure A.1), hence the SPAD was not biased as it should be and further it was not receiving the required current. Changing the resistor to a lower value ($10K\Omega$) solved the problem. This resistor was made variable in the improved quenching circuit (R1 and R3 in Figure A.5). Although the shape and behavior of the curves did not change, much better PCR was observed for the same light levels at same V_{OV} (Figure 3.30). It was found that the PCR of the designed S-SPCM

were comparable with the PCR of PKI SPCM at much lower V_{OV} (~10V) after the resistance was changed as compared to ~17V before. DR and linearity up to $7V_{OV}$ is not comparable with SPCM, but became comparable at $10V_{OV}$. Further, not much improvement in sensitivity is observed as the V_{OV} is increased beyond 10V. This was confirmed by plotting the SNR curves at different V_{OV} as shown in Figure 3.31. The SNR was calculated using equation 3.6.

$$SNR = \left[\frac{(PCR - DCR)}{\sqrt{PCR + DCR}} \right] \quad (3.6)$$

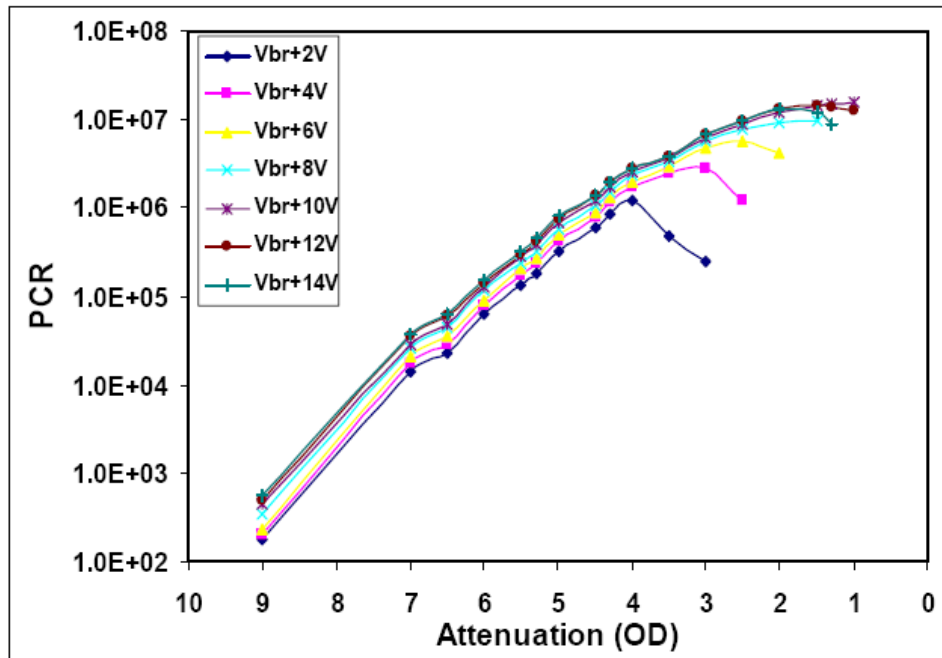


Figure 3.30 S-SPCM: Attenuation versus PCR after changing the value of the power supply resistor to 10k Ω (R3 in Figure A.1).

The curves show that $10V_{OV}$ has the best combination of SNR and dynamic range and it decreased when V_{OV} was increased beyond 10V. Based on the above results and discussion, optimum operating point for a particular application can be determined and it can be seen that $10V_{OV}$ with $4mV V_{TH}$ is the best operating point for DNA-sequencing application.

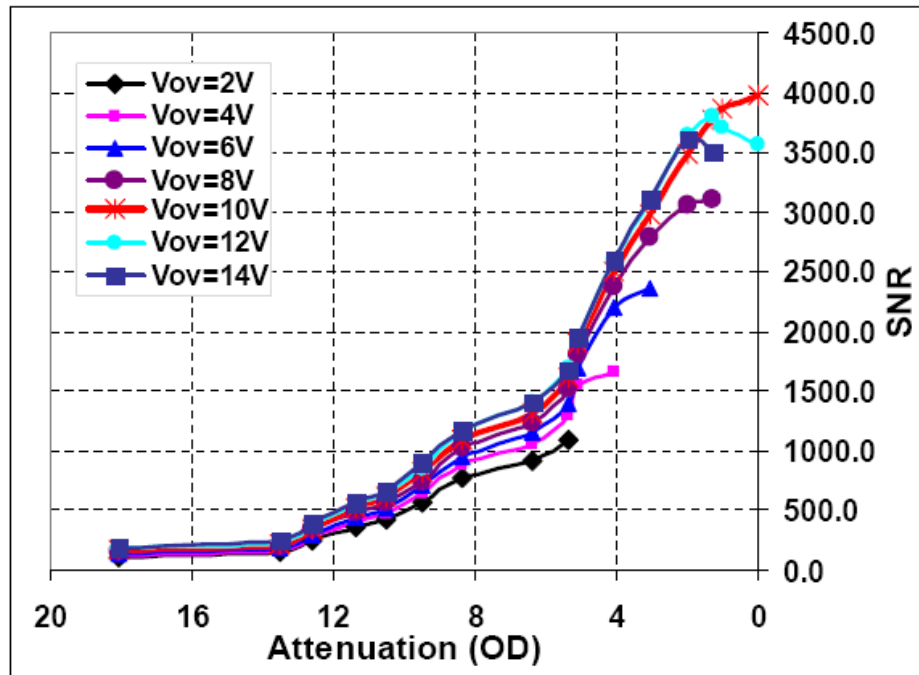


Figure 3.31 S-SPCM: Signal-to-Noise ratio.

Finally, it can be seen that behavior similar to Figure 3.22 (count rate dropping to zero) was observed in Figure 3.28 and 3.30, but is much more prominent in Figure 3.28. In Figure 3.28, for low V_{OV} , it would be expected that the PCR would keep increasing with increasing light levels at all V_{OV} ; but would be non-linear or the rate of increase would be slower at low V_{OV} and faster at high over-voltages. But, it can be seen that the SPAD count rate saturates at high light levels and then at one point the count rate

suddenly drops (almost to zero). Since in this case V_{TH} is constant as opposed to Figure 3.22, it probably suggests that the avalanche generation time (T_{APD}) changes significantly with V_{Bias} and at one point it becomes comparable or greater than the average arrival time between two photons. Therefore as V_{OV} increases, the saturation count rate limit increases.

Linearity and Dynamic Range (DR)

From the sensitivity and SNR results it was found that the S-SPCM has the best combination of linearity and DR at $10V_{OV}$. Figure 3.32 shows the comparison of attenuation versus PCR curves of the S-SPCM and PKI SPCM, both tuned to optimum parameters. Following conclusions can be made from these curves:

- The DR rate specified for this SPAD (C30902S series) is 10MHz [3] and it was also measured to be ~ 10 MHz which means that best possible performance has been achieved with the designed QC.
- The SPCM has a linear range of ~ 4 MHz and the designed module has a linear range of ~ 2 MHz. This can be attributed to the significant difference in active areas of the two SPADs. The PKI SPCM employs a SLIK device that has a typical active area of $0.023\mu m^2$ and S-SPCM employs a SPAD with active area of $0.196\mu m^2$, which is 8.52 times larger than the PKI SPCM. Since the capacitance of a silicon detector varies linearly with the active area, it is expected that the PKI SPCM will have better high frequency behavior. Therefore, it can be concluded that the best possible linearity has been achieved with the designed S-SPCM for

this SPAD. If needed, it is possible to increase the linear range of S-SPCM by applying various mathematical linearity correction models [101].

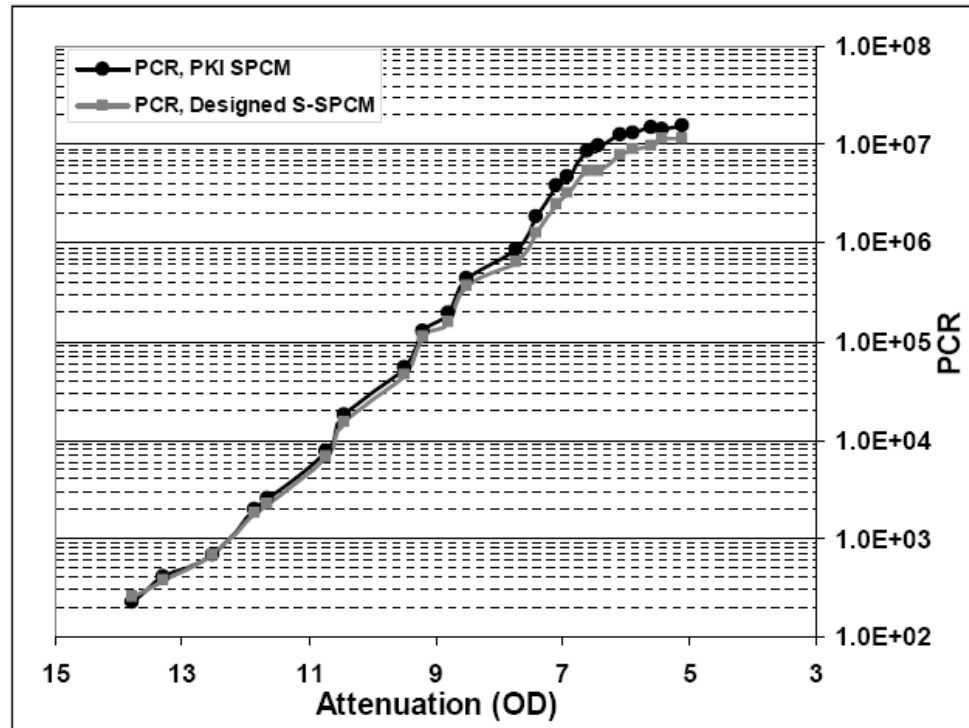


Figure 3.32 Comparison of linearity and DR of the designed S-SPCM at $10V_{OV}$ with PKI SPCM.

3.6 Summary

This chapter presented the design, implementation and characterization of a single channel single photon counting module that involved the design of various small modules, in particular the design of quenching circuit. A novel, digital circuit for generating precisely matched quench and reset delay was presented. This approach will

make the tuning of the designed multi-channel photon counting systems much easier. Moreover, it is a more stable approach as compared to the traditional mono-stable based approach. The time to quench the avalanche (T_A) is ~ 10 - 12 ns, which is equal or better than the best times reported.

Linearity and DR of a photon counting system is very important for good DNA-sequencing results and depends on the SPAD and the QC. The achieved DR is the best possible value achievable with this model of SPAD [3]. The difference in linearity is attributed to the 8.5 times smaller active area of the PKI SPCM that used SLIK device. A linear range of ~ 2 MHz has been achieved, which is ~ 2 times higher than the maximum PCR to be counted from the DNA-sequencer (typically 500 KHz to 1MHz) and hence is more than satisfactory for the intended application. One of the goals was to achieve highest possible sensitivity from this module and it was shown that to achieve highest sensitivity, the SPAD needs to be operated at sufficiently high V_{OV} ($\sim 5\%$ of V_{BR} for this SPAD). It was found that the optimum V_{OV} to obtain the best combination of sensitivity, SNR, dynamic range and linearity is 10V. This is best large area SPAD commercially available. Since the behavior of different SPADs of the same type should be more or less same, these results provides the user of this SPAD to select the optimum operating point for any particular application based on the acceptable DCR and required sensitivity and SNR. Fiberization of the S-SPCM facilitates integration of this module into any other application that requires detection of ultra-weak fluorescence signals. Table 3.1 provides the summary of important results of the designed S-SPCM with PKI SPCM.

Table 3.1 Summary of important performance parameters of the designed S-SPCM and comparison with PKI SPCM.

Specification	PKI SPCM	Designed S-SPCM	Unit
SPAD active area	0.023	0.196	μm^2
Time to quench the avalanche (T_A)	NA	~10-12	ns
Optimum V_{OV} for best sensitivity	NA	10	V
Linearity	~ 4MHz	~ 2 MHz	MHz
Temperature on SPAD	NA	-20	$^{\circ}\text{C}$
Sensitivity	Best	Comparable with PKI SPCM	
Stability of temperature control	NA	± 0.001	$^{\circ}\text{C}$
Temperature control range	NA	+30 to -25	$^{\circ}\text{C}$
Dynamic Range (DR)	15	~10	MHz
Dead time ^{*1}	40	50	50ns
Cost	~4500	Lower than 4500	USD
Fiberized	Yes	Yes	

***1:** Required dead time may vary for different device of the same type. This is the dead-time for the device mounted on the designed S-SPCM.

CHAPTER 4

MULTI-CHANNEL SINGLE PHOTON COUNTING MODULE (M-SPCM): DESIGN, IMPLEMENTATION AND CHARACTERIZATION

One of the approaches to increase the efficiency and hence cost of DNA-sequencing is to increase the throughput of the DNA-sequencer. Throughput can be increased by increasing the number of DNA-sequencing channels to perform DNA-sequencing in parallel. 16 and 32-channel multi-lane DNA-sequencers have been designed in our lab that requires M-SPCMs. 10-fold increase in sensitivity of DNA-sequencing was obtained with the designed S-SPCM based on the SPAD model C30902S-DTC; hence array of large-SPAD with similar performance would be the ideal choice for designing a M-SPCM, both cost and area-wise. Such arrays were not available then and are still not available commercially. To our knowledge there is commercial source of SPAD array, [106] but it is based on small area SPAD (40x40 μm). Hence, there was no choice but to design M-SPCMs based on individual SPADs. Research on all types of SPAD arrays can be found in [56] [64]-[67] [69] [105]-[107].

Cheaper, un-cooled version (C30902S) of the same SPAD model was tested since it has the exact same detector chip (active area) as the cooled version, except that the detector chip is not mounted on a TEC. Hence, although it will have high DCR (5-10 KHz), it is expected that it would have the same levels of sensitivity and linearity. This level of DCR would not increase the over-all noise of the DNA-sequencer. But, it is

known that diode heating is a major limitation with this model since it was designed initially for low-power operation in the linear mode [25]. In the packaging of this device, the detector chip is mounted upon the end of a central contact pin and heat is conducted to the outside world through this pin. This is a problem of the heat sink and not of the diode itself; the same diode, mounted upon a temperature-regulated heat sink may perform better [25]. Keeping in mind all the above problems, this device was tested (section 4.1). Although device exhibited similar sensitivity and linearity as the cooled version, heating effects were found to be a major problem. It was concluded that this device could not be used for our application. Since single fluorescent molecule sensitivity and excellent DNA sequencing results were obtained with our designed S-SPCM based on the cooled version, (Chapter 3). M-SPCMs were designed with the same SPAD model as S-SPCM.

This chapter presents the design, implementation and characterization of two (16 and 32-channel) M-SPCMs for our 16 and 32-lane DNA-sequencers respectively. Once again the goal was to design general purpose systems that can be integrated into any other application having similar photon counting requirements. The designed M-SPCMs [108] [109] are unique and had never been reported in literature before. Besides DNA-sequencing, spectrography was performed in our lab with the designed 32-channel module, thus demonstrating its general purpose nature and its adaptability to other applications.

4.1 SPAD Model C30902S: Experimental Results and Discussion

The device was tested with the designed PCB (Section 3.5). The temperature controller on the PCB was not utilized. To minimize heating problems, the device was mounted on a large, thick metal plate (Figure 4.1) to provide sufficient heat-sink. The device is mounted on the back side, hence is not visible.

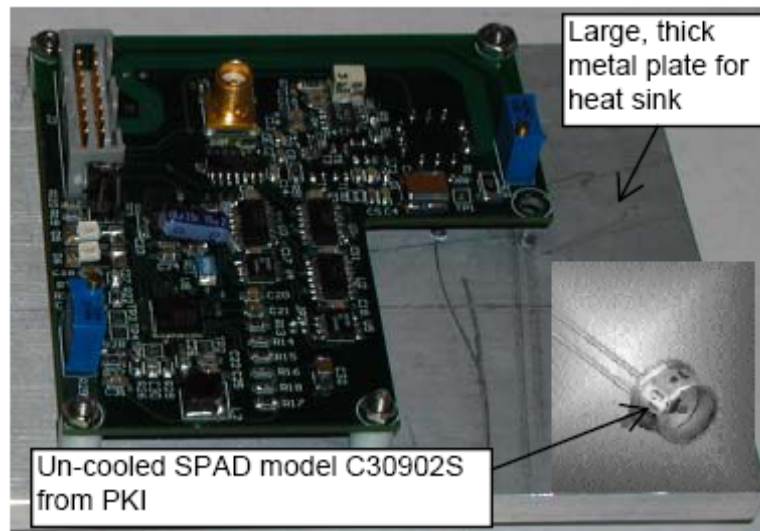


Figure 4.1 Testing of un-cooled SPAD model C30902S.

Dark Count Rate (DCR)

Figure 4.2 shows the variation of DCR with V_{OV} . Similar to the cooled SPAD, it varies linearly. The DCR range is 20 KHz to 36 KHz for a V_{OV} range of 8-14V. Since this DCR does not add much to the high background count rate (200-400 KHz) of the DNA-sequencer, the total increase in noise is negligible (Equation 1.3). But, while

performing this experiment it was found that although the device was mounted on a sufficiently large heat-sink, the DCR was not constant and decreased with time. The reason for this drift should be due to the decrease in V_{Bias} with time because of diode heating.

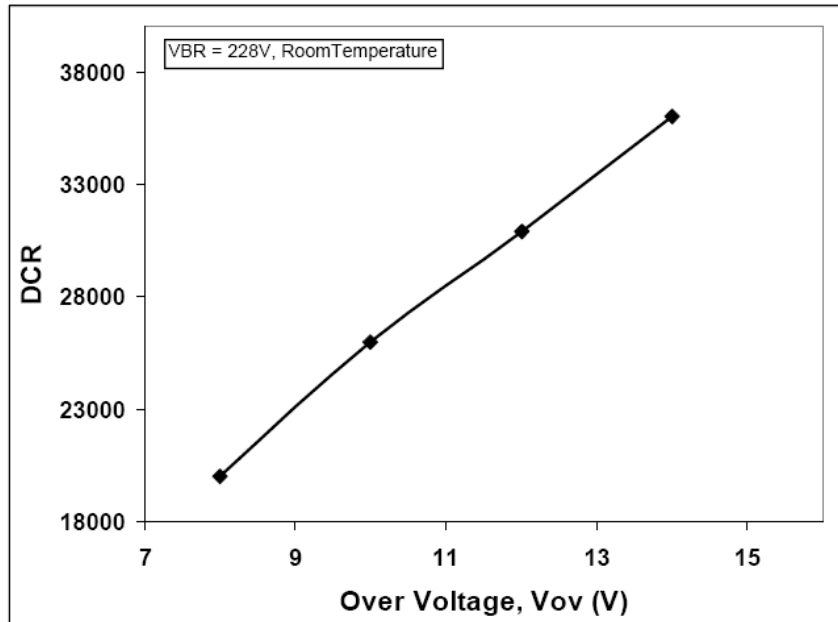


Figure 4.2 C30902S: Variation of DCR with over-voltage.

Sensitivity, Linearity and DR

These parameters were measured in the same way as described in section 3.6 and the results are shown in Figure 4.3. To filter out experimental non-linearities, all the curves are plotted against PKI SPCM (see experimental set-up sub-topic in section 3.6 and Figure 3.29 explanation). Although the results show similar sensitivity and linearity performance as compared to that obtained with the cooled SiPM, following problems were faced:

- It was observed that even with such a large heat-sink, the count rates were not stable, especially as V_{OV} was increased. The reason for this is that this device is not mounted on a ceramic and is just connected to the 2 pins (anode and cathode) that come out of the device and conduct heat to the heat-sink. This is not sufficient for such a large device that conducts large current (few mA).
- Significant drop in V_{Bias} was observed as the V_{OV} was increased ($\sim 4-6V$ for $V_{OV} \geq 8V$). This means that the gain of the device decreased a lot. While performing this experiment, the SPAD was turned off after each reading and once the device was turned on the PCR were quickly recorded before the count rate started dropping. Three different SPADs were tested and similar results were obtained.
- The above problem could be solved by monitoring the change in V_{BR} and compensating each time it drifted. This would be a feasible task for a single channel system, but not for a multi-channel system since the change in V_{BR} may not be the same for each device and hence each device would require its own V_{BR} compensation circuit. This would mean increase in cost and size of the module, but no significant increase in performance.

It was concluded that this device may be a good choice of detector for applications requiring gated mode operation where the device is biased in geiger mode for short times. For DNA-sequencing applications, it is required to operate the device in free-running mode for few hours; hence this device cannot be used.

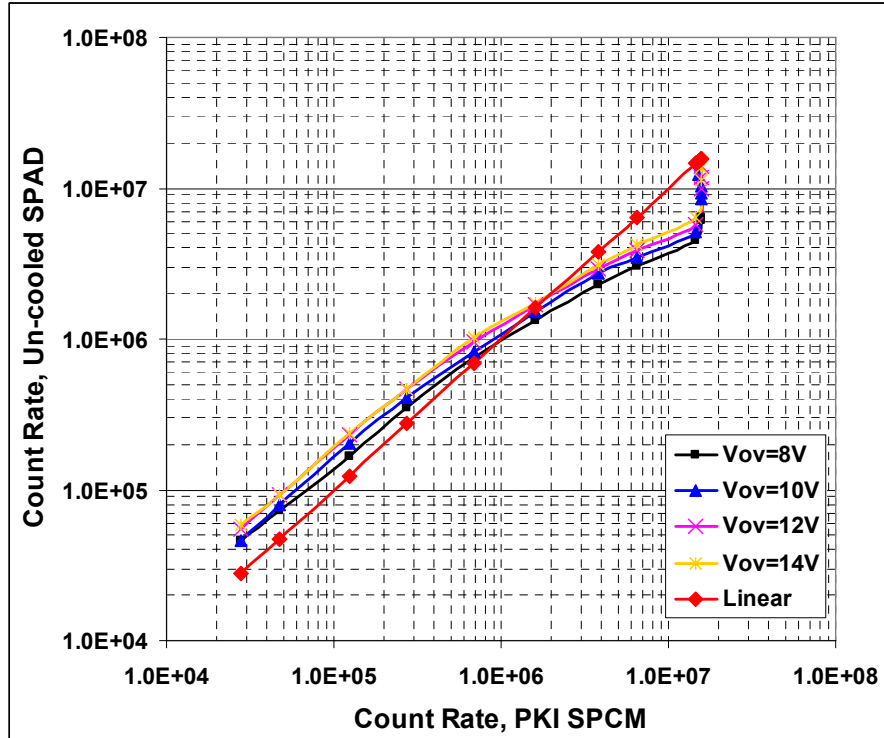


Figure 4.3 Sensitivity and linearity of SPAD model C30902S.

4.2. Design of 16 and 32-channel Photon Counting Modules

Two different photon counting modules viz. 16 and 32-channel were designed for a 16-lane and a 32-lane DNA sequencer respectively. Some drawbacks were found in the design of 16-channel module and were eliminated in the design of 32-channel system. Further some new features were added to the 32-channel module.

System description

Figure 4.4 shows the block diagram of the designed 16-channel photon counting module combined with the optical detection module, Figure 4.5 shows the implementation of the 16-channel module and Figure 4.6 shows the block diagram and photo of implementation of the 32-channel module. Both the modules are designed keeping in mind its application to four-color fluorescence detection.

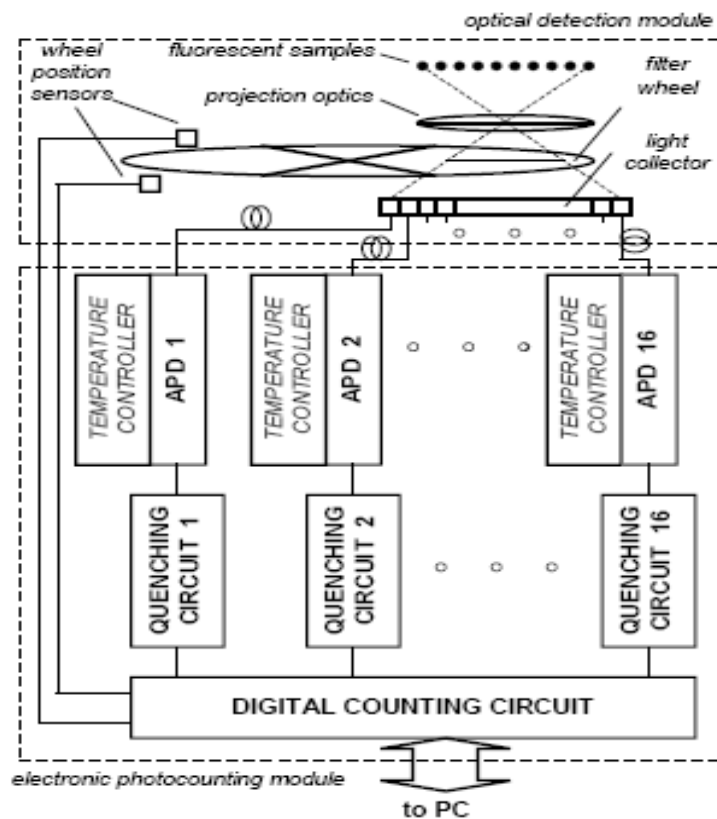


Figure 4.4 Block diagram of the 16-channel single-photon counting module.

The optical detection module uses four band-pass filters attached to a constantly rotating filter wheel. The beam of the collected fluorescence passes through the sequence of filters. During each revolution of the wheel, the detector performs measurement of the

fluorescence light intensity that passed through each filter, producing four measurements per revolution, which allows estimation of concentration of each of four fluorescent markers in the sample, given the knowledge of the transmittance of the filters.

The 16 and 32 channels of the M-SPCMs comprise of 16 and 32 SPADs (C30902S-DTC) respectively, each connected to individual PCB that consist of QC and temperature controller which keeps the SPAD temperature at -20°C and five power supplies. The PCB in the 16-channel system was based on first design of the QC (Figure 3.2 and 3.17). A new PCB (Figure A.7) was designed for the 32-channel system and is based on the improved timing and logic circuit described in section 3.2.2. The size of the new PCB is much smaller since the timing circuit has 2 less nand gate ICs and uses smallest size of the available SMD components (Figure 4.6c). Five supply voltages required are the same as described in section 3.4. For the 16-channel system one power supply was used to supply power to all the channels. Appropriate commercially available power supplies with high current ratings were selected. Two +5V supplies were used; one with low current rating for the logic ICs and one with high current rating for the temperature controller circuit. For the 32-channel system two power supplies were used, each powering 16-channels.

The output signal obtained from the PCB is a TTL level signal and has sufficient amplitude for further processing without any additional electronics. A high-speed FPGA based N-channel (16 or 32 depending on module) counter designed in our lab counts the pulses from the comparator. The counter has N identical TTL-compatible counting inputs and is controlled by signals from two sensors. The two sensors form encoding signals using a 2-bit Gray code to identify the band-pass filters in the filter

wheel. The change of the code word at the sensor output indicates the change of the filter in alignment. The counter uses this filter code to assign the photo count to individual filters. The counting of the input photon pulses in each channel is performed by summation of pulses arriving to the channel input during the time intervals when a particular band-pass filter is in alignment with the photo detector.

In the 16-channel system data collected by the counter is transferred directly to a PC using standard IEEE 1284 Parallel Port Interface. The 32-channel system consists of a dedicated micro-computer (PC-104) that collects and processes the data from the 32-channel counter. Further it consists of an ethernet port facilitating data access from any computer on the network. The data is transferred in samples using a binary format. One data sample is collected during one full revolution of the filter wheel. The frame consists of count values obtained in four fluorescence detection bands (four color filters) for each detection channels. The frames are sent in order of their generation, determined by the filter code on the wheel and the direction of its rotation. Each frame starts with a 6-byte header, which includes the following fields: 1-byte counter type, 2-byte frame number, 1-byte color code (filter number) and a 2-byte counting period length. The frame number contains the number of the current frame. The number is incremented by 1 for each following frame thus forming a rising sequence with overflow. The frame numbers serve as synchronization marks and are used by the data processing software to find data frames in a continuous data stream. Frame numbers are also used for verification of data integrity and for finding errors introduced by interference in the transmission line. The duration of the counting period is measured in milliseconds and is represented by a two-byte value. The time duration when the filter is “on” is measured separately for each filter

and is used by processing software to calculate the photon count rate. During the normal operation of the system the filter wheel performs 10 revolutions per second resulting in data transfer rate of 10 frames per second. Figure 4.5 and Figure 4.6 show implementation of 16-channel and 32-channel module respectively.

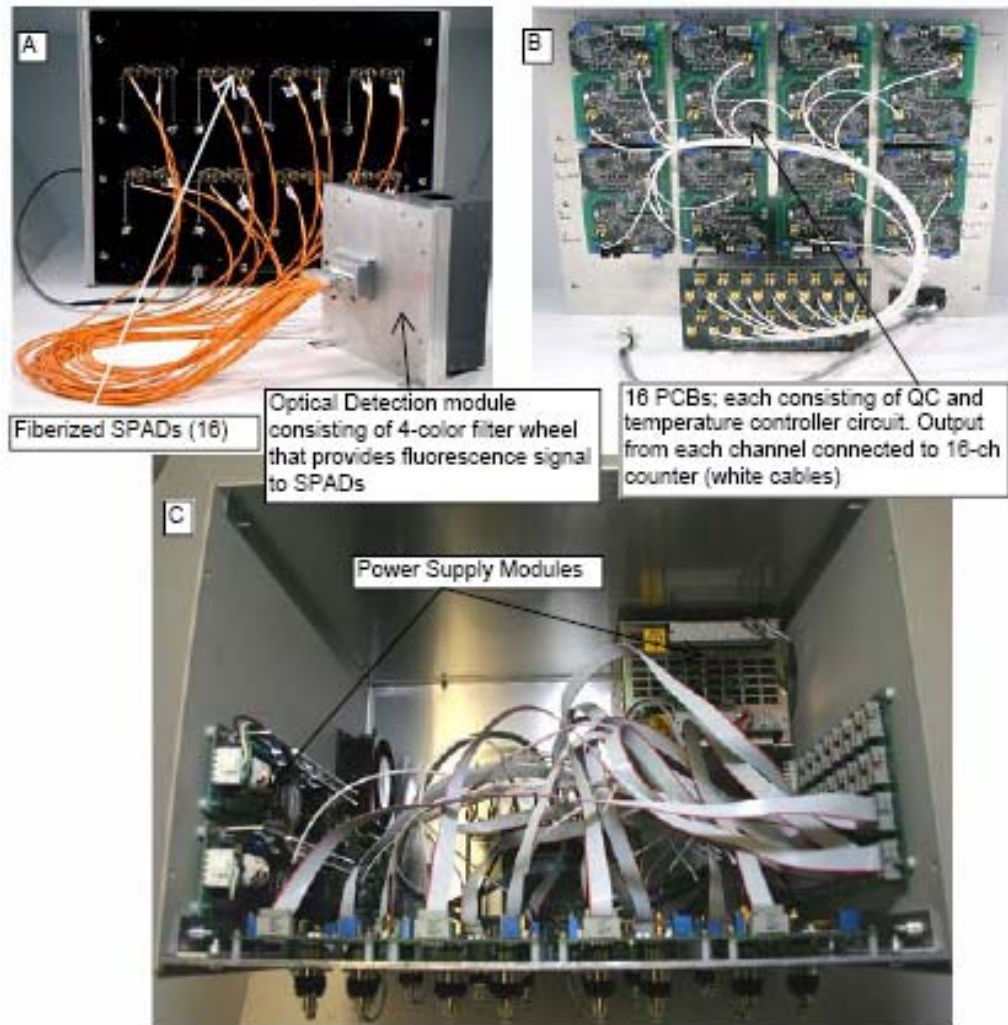


Figure 4.5 Photos of the implemented 16-channel module; (A) front view of photon detection module and optical detection module for light collection, (B) 16 PCBs with output of each connected to 16-channel counter, (C) Top view.

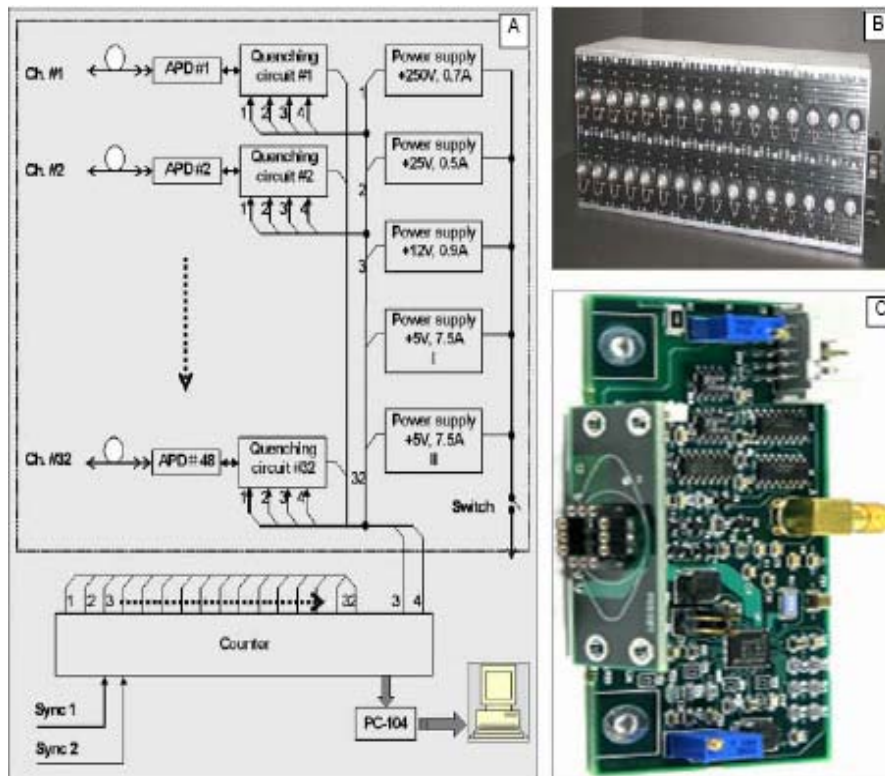


Figure 4.6 32-channel module; (A) Block diagram, (B) photo (C) photo of 1-channel PCB.

4.3 Features and Shortcomings of the Designed M-SPCMs

Common features of 16-channel and 32-channel module

- The designed modules are compact, general purpose, easily portable, robust and unique since such a system has never been reported in literature before.
- All the required voltages are generated inside the module and it requires only 120Vac for its operation.

- Fiberization of the SPAD facilitates use of the designed modules in any other application requiring multi-channel photon detection. For example, the 32-channel module was used to perform spectrography (see section 4.5).
- Fiberization of each channel (SPAD) of the module allowed to couple light with maximum efficiency and facilitated easy integration into multi-lane DNA-sequencing set-up.

Shortcoming of 16-channel module

Couple of shortcomings was identified while working with the 16-channel module and are discussed below:

- The structural architecture of this module is not very efficient. All the 16-channel PCBs and SPADs in the designed system are mounted on a common big metal plate (coated with black color) that also acts as the heat sink (Figure 4.5A). Therefore, in order to adjust or change a particular parameter or component the whole plate had to be removed. Further, it is not easy to remove or mount the PCB.
- The system generates lot of heat and power because of the number of power supplies and huge currents required. The designed fan system was not enough to efficiently fan out the heat. Hence a bigger and more efficient fan out system was needed. This system was later added to the module.

Improvements and new features in the 32-channel module

The above described short-comings of the 16-channel system were eliminated by making the following changes:

- The PCB in the 16-channel system was based on first design of the QC (Figure 3.2 and 3.17). A new PCB was designed for this system and is based on the improved QC (section 3.2.2). The size of the new PCB is much smaller since the timing circuit has 2 less nand gates chip and smallest size of the available SMD components (Figure 4.6C)
- Each of the 32 channels has its own heat sink as compared to a common big metal plate in the 16-channel system. Hence, each channel can be easily removed from the system for testing or tuning purposes (Figure 4.6C).
- Much better fan out system for the power generated inside the module.
- In the 16-channel system data collected by the counter is transferred directly to a PC using standard IEEE 1284 Parallel Port Interface, whereas the 32-channel module consists of a dedicated micro-computer (PC-104) and an ethernet port. The micro-computer (PC-104) collects and stores the data from the 32-channel counter. This data is then transferred to the database and the data bank through ethernet, facilitating data access and control from any computer on the network.

4.4 Experimental Results and Discussion

Designed M-SPCMs were characterized in the same way as S-SPCM. For consistent DNA-sequencing results, it was important to obtain consistent performance from each channel of M-SPCM; requiring individual tuning of each channel. These module were characterized using the same experimental set-up that was used to characterize the S-SPCM (section 3.6) was used.

Comparator threshold (V_{TH})

Each channel was first tested individually to verify its operation. It was found that all the QCs did not operate satisfactorily for the same comparator threshold voltage; hence it had to be determined and set individually for each channel. A batch of PCBs was hand soldered and hence one of the reasons for such behavior was thought to be difference in wiring capacitances at node Y in Figure 3.2.

Quench and reset delay times

Based on the results obtained from the characterization of the designed S-SPCM, the quench and reset delay times were set to 35ns and 10ns respectively. It should be noted that the 35ns quench includes the loop delay (T_{LD}) and part of the time to quench the avalanche (T_{ND} , T_{ON} and T_{OFF} in total T_A) (section 3.2.1). It was found that most of the SPADs performed satisfactorily with these settings. For ~8-10 channels after-pulses were observed at very low count rates, which suggested that the quench or reset delay time or both were not enough. The problem was solved by appropriately increasing the

quench and reset delay times. The designed timing and logic circuit allowed easy changing of delay times as required. It must be noted that a RC based timing circuit would have been really difficult to tune for such multi-channel systems.

Dark count rate (DCR)

A total of 50 SPADs of the same type (C30902S-DTC) were measured during the design and development of S-SPCM and M-SPCM. Figure 4.7 shows the DCR for all the SPADs at $10V_{OV}$. The average DCR for 48 devices was ~ 700 Hz, but two devices have a DCR of ~ 10 KHz. Since these are one of the very few large-area SPADs available, they are used in many applications, hence this data may be useful for some users.

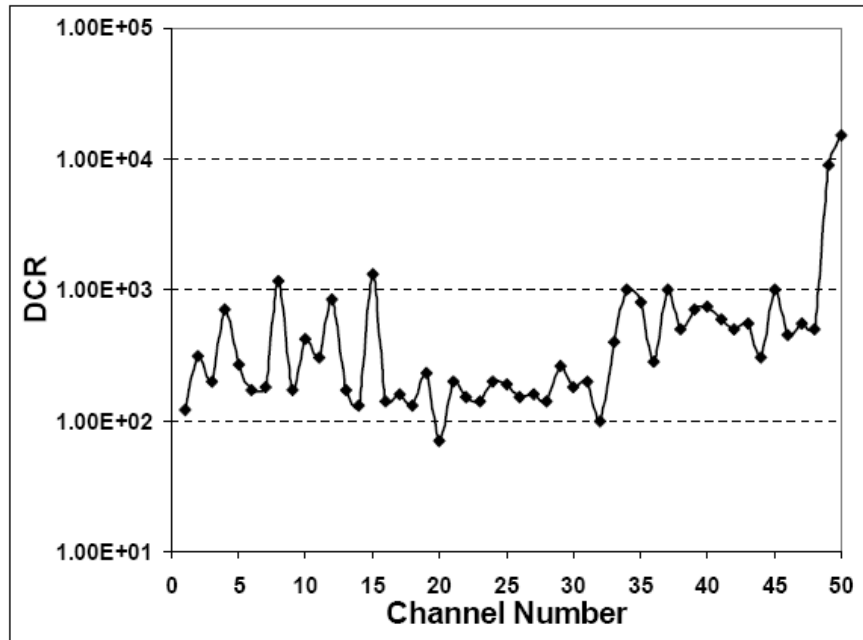


Figure 4.7 Comparison of DCR of 50 SPADs ($T = -20^{\circ}\text{C}$, $V_{OV}=10\text{V}$).

Tuning for consistent performance

To obtain consistent DNA-sequencing results from all the channels, it is required to tune each channel to the same performance level. This means that for a constant light level, each channel must output approximately same output counts. Since the best operating point from our application point of view was found to be 10VOV, VOV on all the channels was set to 10V. It was observed that at 10VOV, some channels had less and some had more output count rate for the same light level. This mismatch can be attributed to minor misalignments in fiberization system, minor temperature and VBR differences on the SPAD. The easiest way to match the count rate for each channel was to increase or decrease the VBR on the required channels to match the count rates of all the channels. Figure 4.8 and Figure 4.9 shows the results after this alignment was done for 16-channel and 32-channel module respectively. It shows the count rates at the output of each channel in dark and at different light levels and they are similar.

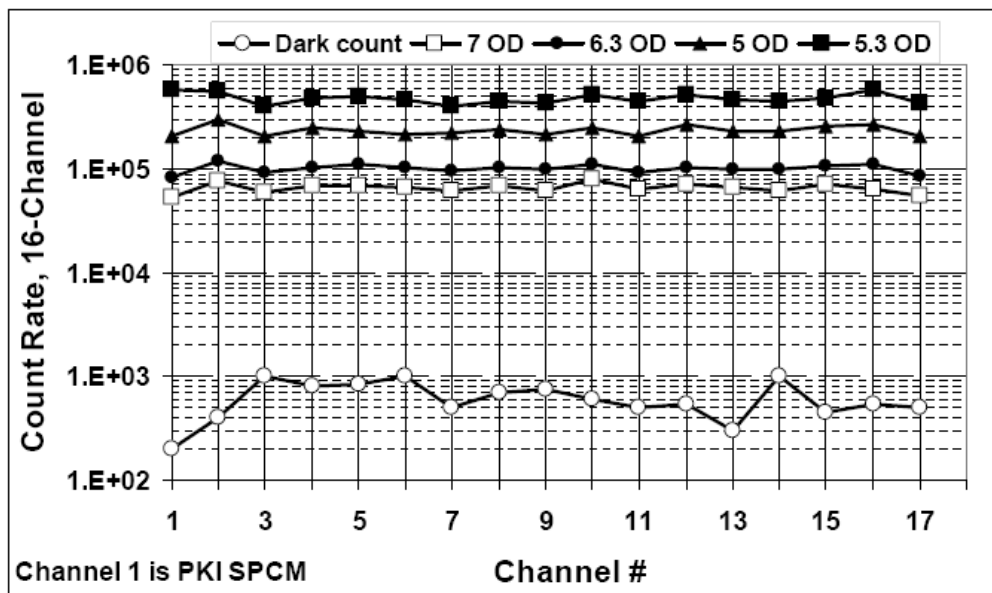


Figure 4.8 Output count rates of each channel of the 16-channel module.

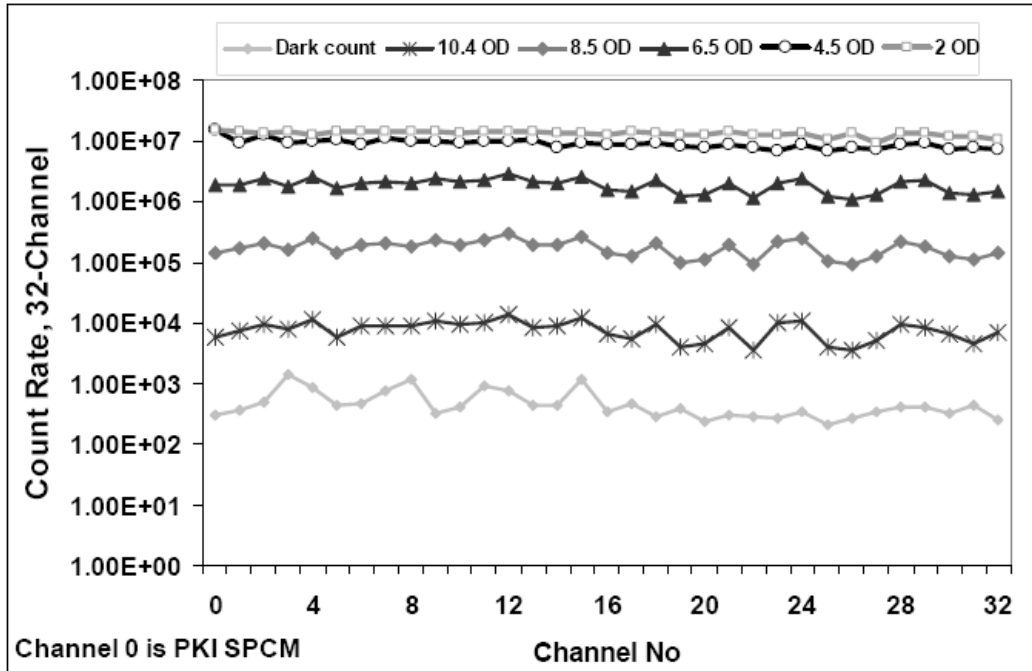


Figure 4.9 Output count rates of each channel of the 32-channel module.

Linearity and DR

The linearity of both the modules was measured in the same way as the S-SPCM (section 3.6). Each channel was measured with the same fiber by switching the fiber to each channel and finally to PKI SPCM to ensure that same output light was focused on each detector. Figure 4.10 and Figure 4.11 show the linearity of each channel plotted against PKI SPCM for 16-channel and 32-channel module respectively. Uniform results were obtained from all the 48-channels.

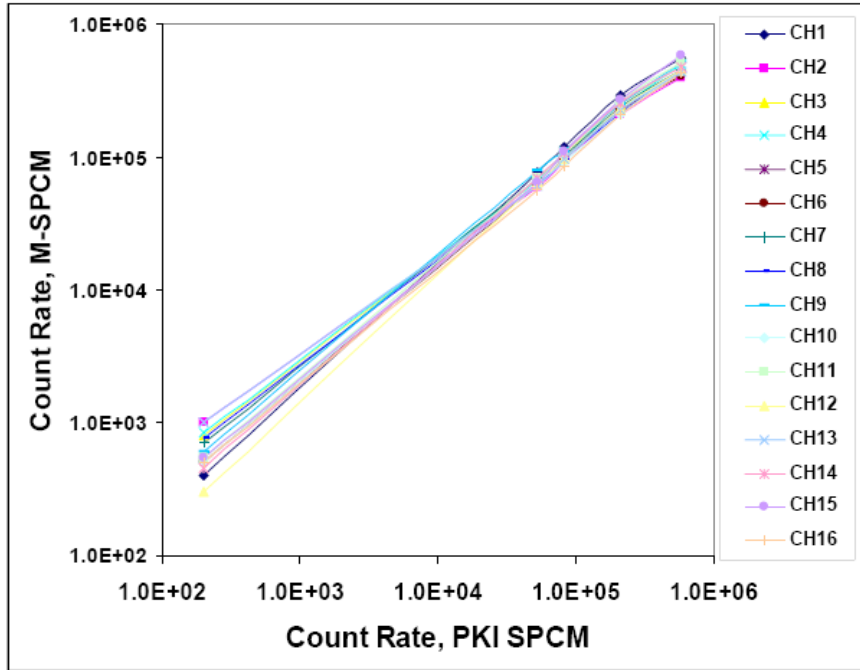


Figure 4.10 Linearity of the 16-channel module.

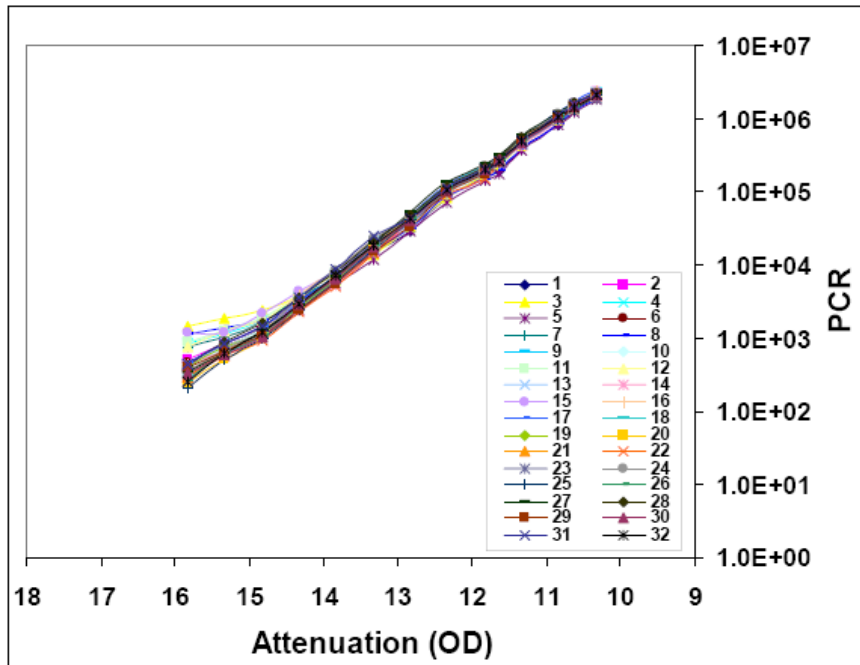


Figure 4.11 Linearity of the 32-channel module.

Noise

The noise was measured in the same way as described in section 3.6 for almost all the 48 channels of the designed M-SPCMs. The carried out noise analysis showed practically ideal fit of the measured distribution of photo-counts (blue bars) and Poisson curve (red solid line) for both the SPCM and all channels of the designed M-SPCM. Figure 4.12A shows the distribution at the output of the PKI SPCM and Figure 4.12B shows a typical distribution observed at all channels of both the M-SPCMs. This means that the only noise present in the system is due to the stochastic nature of the photon fluxes detected by the photon detectors.

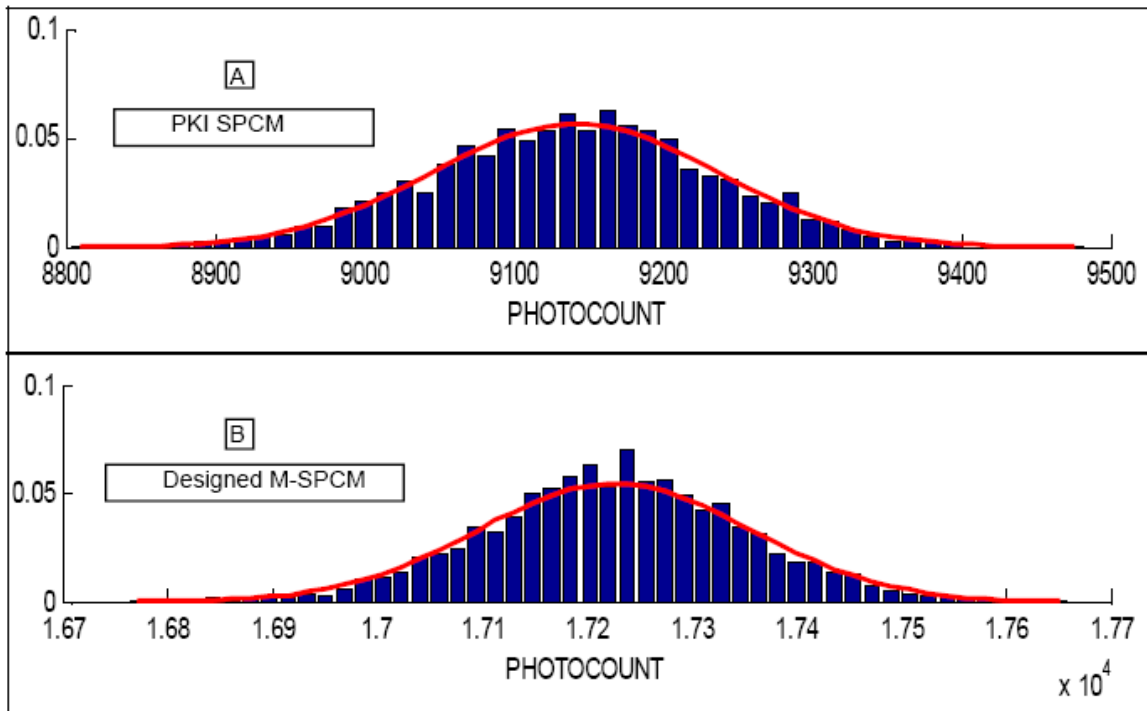


Figure 4.12 Noise of the designed M-SPCM.

4.5 Application of 32-channel Module to Spectrography

In the last decade several experiments have clearly demonstrated that, once illuminated, all biological systems emit for some time a very weak flux of photons, called Delayed Luminescence (DL) [110]. All these experimental findings highlight the importance of building devices with single photon detection capability, in order to measure DL up to ~ 1000 nm [110]. Arrays of high-performance SPADs are needed for such applications [110] [111]. It is speculated that such devices should be able to resolve the few detected photons both in time and in wavelength, and possibly obtain a matrix for imaging purpose. The resulting devices are called Single Photon Spectrographs. The above discussed requirements make the designed M-SPCMs an excellent contender for such an application because of its high sensitivity and very low DCR. Further the fiberization system facilitates easy integration into any other application. Spectrography was performed in our lab with the designed 32-channel module; Figure 4.13 shows block diagram (top) along with the photo (bottom) of the actual experimental set-up.

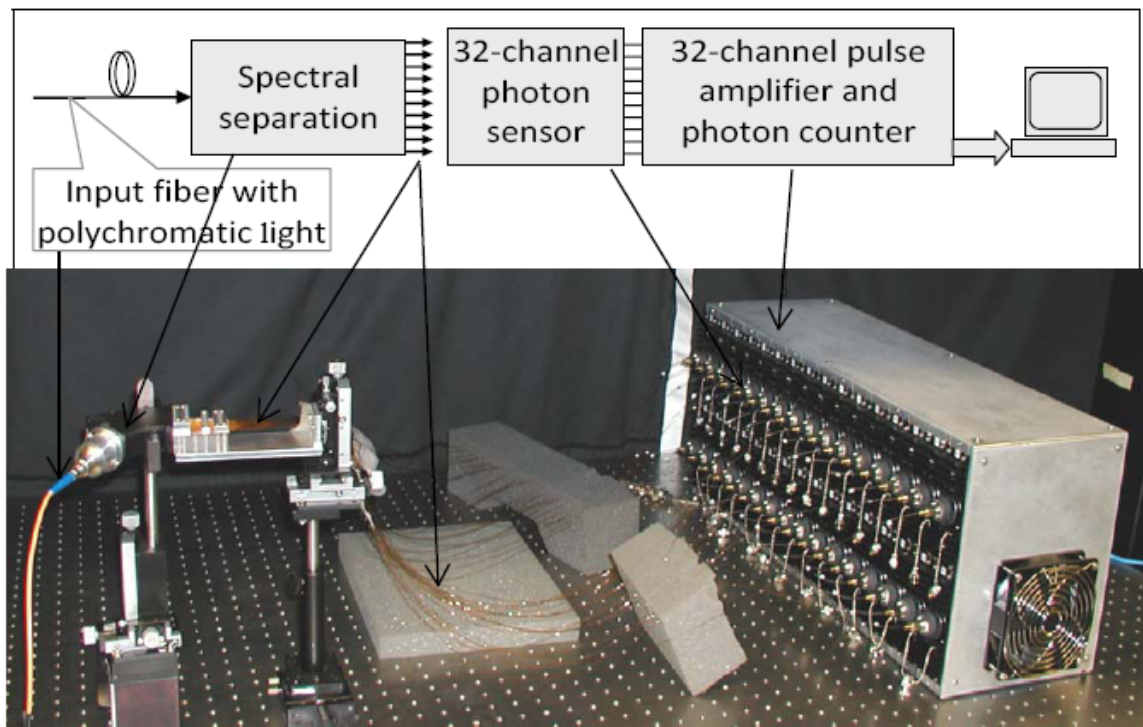


Figure 4.13 Application of the designed 32-channel photon counting module to spectrography.

The sensor system is developed to measure, with single photon sensitivity, radiation emitted by mixtures of minute amounts of multiple fluorescence dyes and to determine very accurately the content of individual dyes in the dye mixture. In Figure 4.13, the fluorescence comes to the spectrometer through the input fiber coupled to the collimator (F810SMA-543, Thorlabs Inc, NJ, USA) which produces a parallel polychromatic beam of ~10mm diameter. The polychromatic fluorescence collected by the input fiber passes through the spectral separation module that performs the separation and the measurement of fluorescence in the range of wavelengths from 480nm to 630nm. The parallel beam passes through laser rejection filters and undergoes separation on the diffraction grating (GR13-1850, Thorlabs Inc, NJ, USA) into constituent wavelength components. The separated monochromatic beams are focused onto channels of the 32-

channel photon counting module. The obtained photo-counts are transferred to computer for recording and data processing.

DNA-sequencing was performed with the developed sensor based on spectrograph. For the decomposition of the entire measured spectrum, the spectral components which describe individual dyes must be obtained experimentally by measuring fluorescence emitted by each dye separately and by normalizing the measured vector of photocount rates. The determination of concentrations of individual dyes in the mixture is performed for each time frame. The obtained sequence of dye concentrations forms four sequencing traces, which are further used for base calling. The obtained four sequencing traces undergo standard processing [7] that includes noise filtering (smoothing), baseline subtraction, crosstalk removal, mobility shift correction, peak height and spacing equalization. After re-sampling to 7-15 points per peak the traces are stored in .SCF format and processed by standard base calling PHRED software. The result of the processing is returned as a sequence of base-calls with their positions and quality scores. Figure 4.14 shows the system color matrix, Figure 4.15 shows the DNA sequencing traces and Figure 4.16 shows the base calling quality scores obtained with the spectrometer. For understanding DNA-sequencing results refer to section 1.2.

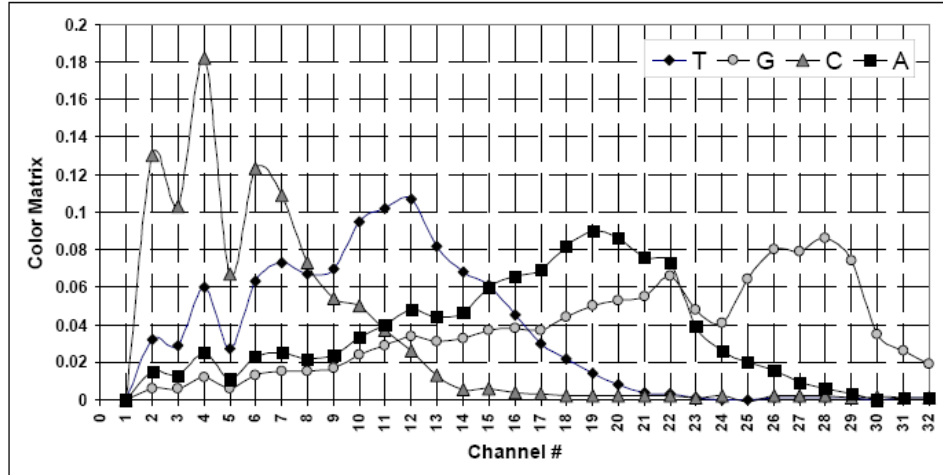


Figure 4.14 System color matrix

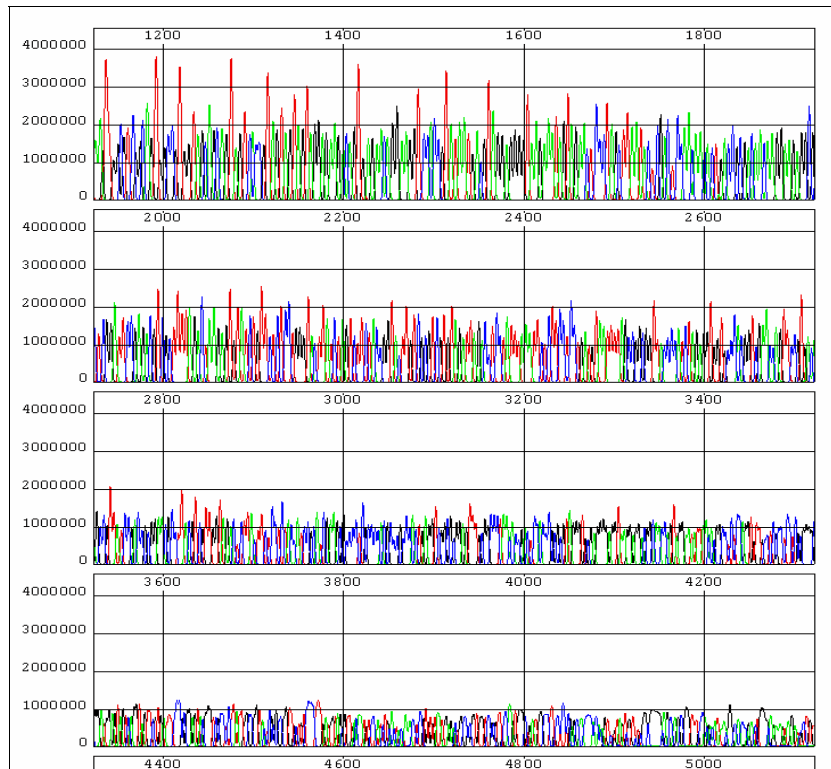


Figure 4.15 DNA sequencing traces obtained with the spectrometer

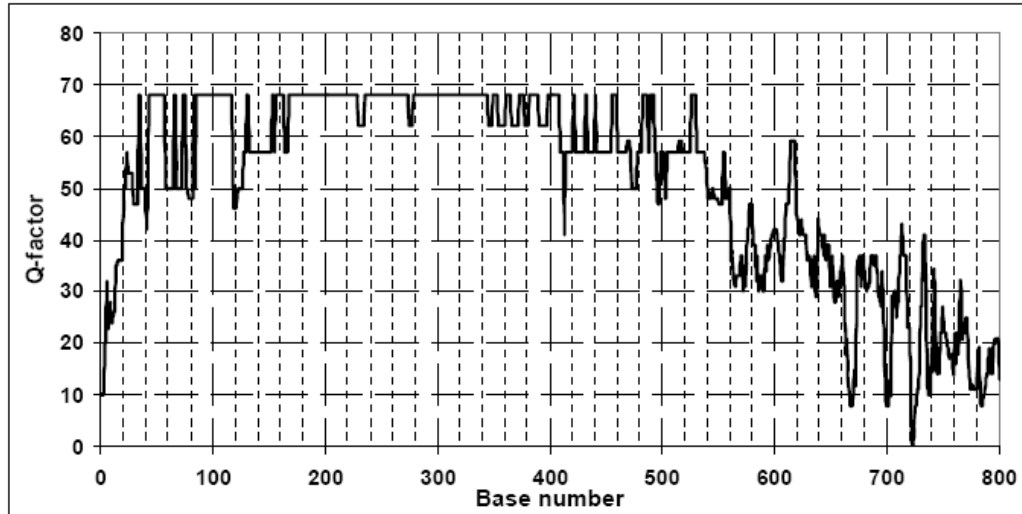


Figure 4.16 Base calling quality scores obtained with the spectrometer.

4.6 Summary

This chapter presented the design, development and characterization of two different M-SPCMs (16 and 32-channel) based on SPAD model C30902S-DTC. The designed systems are unique, robust, general purpose, easily portable and require just 120Vac for their operation. These modules can be easily integrated into any other application with similar photon counting requirements. Spectrography was performed in our lab with the designed 32-channel photon counting module demonstrating its adaptability to different applications. We believe that due to extremely high sensitivity in conjunction with broad detection dynamic range, the developed spectrometer may be very useful for various applications which require a highly accurate analysis of biological

samples labeled with multiple fluorescent markers. Fiberized optical input of the spectrometer allows an easy and efficient coupling to any measurement system based on fiber collection of the analyzed fluorescence. The DNA sequencing experiments carried out with the spectrometer demonstrated an applicability of the spectrometer to highly accurate sequence detection.

CHAPTER 5

INVESTIGATION OF SILICON PHOTOMULTIPLIERS AS HIGH-SPEED PHOTON CENTERS AND THEIR APPLICATION TO DNA-SEQUENCING

5.1 Introduction

The concept of solid-state SiPM has been known for over 30 years, but due to number of problems their progress was relatively slow. Probably the reasons were technology related. It was known that few years back, SiPM suffered from very high DCR. But, the SiPMs progressed with technology and have started to become commercially available only in the past one year or so from very few selected companies [6], [72]-[74]. They still suffer from high DCR, but in their current state, they have become usable in many applications. Further they have relatively low PDE (25-40%) as compared to SPAD, but 2-4 times better than PMT. Although they have some disadvantages, they have certain unique advantages that make them an attractive choice of detector for a large number of applications and are listed below.

Features of SiPM

1. Low operating voltage (20-70V) as compared to PMT and even large area SPAD and hence low power consumption.
2. High gain ($\sim 10^5$ - 10^7)

3. SiPMs are fabricated using standard CMOS processes which offer several advantages such as possibility to integrate the driving and read-out electronic circuit on the same chip, low-cost of fabrication, reproducibility of the dark current and gain characteristics. Further arrays of SiPM are relatively easy to design and fabricate (CMOS).
4. Relatively low cost (low resistivity Si, relatively simple technology)
5. Compact and rugged
6. Insensitivity to magnetic fields
7. Excellent photon resolving capability
8. Very low charge particle sensitivity (negligible nuclear counting effect)
9. Very good timing (≤ 100 ps)
10. Small recovery time
11. Good temperature and voltage stability
12. Simple requirement of associated electronics (no need for QC).

Being analog in nature, they have mainly been used in applications in which the signals are rare and where a bunch of photons are expected to be received simultaneously i.e. photon number resolving applications. But given the nature of the device combined with the above mentioned features, although few, they can be used as detectors in certain high-speed photon counting applications and these conditions are discussed in the next section.

5.1.1 Why SiPM can be used as Detectors in Certain High-speed Photon Counting Applications

It is known that high-speed photon counting is possible with a SPAD. The principle difference between a SPAD and a SiPM is that a SPAD is a digital device and SiPM is an analog device. Further SiPM is a matrix of small area pixels connected in parallel where each pixel is basically acts as an independent photon counter i.e. each pixel is basically a small area SPAD.

SPAD is a digital device and hence can only resolve one photon at a time. This implies that SPAD can only be used in applications where it is expected that the probability of receiving two or more simultaneous photons is negligible. Now, since SiPM is essentially a matrix of SPADs, it implies that if a SiPM is used with the same source where the probability of receiving two or more photons is negligible it will essentially behave as a SPAD. In this case SiPM can be imagined as one big SPAD and if the comparator threshold of the counter at the output of SiPM is set below the amplitude of the pulse due to 1p.e. then irrespective of whether one or more simultaneous photons are received at the input, only one photon will be registered at the output. Figure 5.1 shows such a set-up.

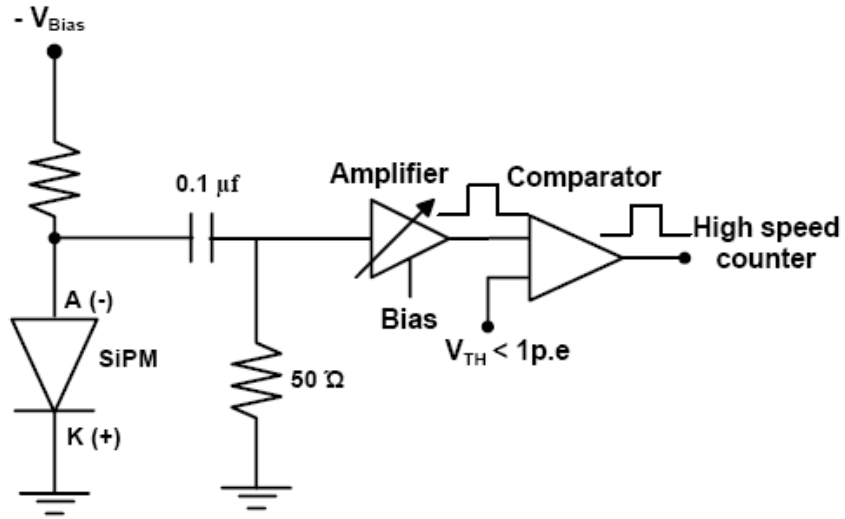


Figure 5.1 Typical system configuration for photon counting with SiPM.

Some of the problems of using SiPM as high-speed photon counter can be thought as (i) it was shown that high sensitivity can be achieved by operating a detector at high V_{OV} . Since SiPMs have already high DCR, increasing the V_{OV} further may significantly increase the DCR (up to few MHz). In this case, although SiPM have high gain, it is possible that SiPM may not be able to detect real light above the DCR because of the limit imposed by the dynamic range of the detector; (ii) the response of SiPM to light may not be highly non-linear due to the same problem discussed above and (iii) high level of non-linearities (noise) due to cross-talk and afterpulsing effects.

Therefore it can be concluded that in principle, SiPM can be used as a photon counter if the above mentioned parameters such as sensitivity, dynamic range, linearity, noise and DCR are within acceptable levels for a particular application.

5.1.2 Advantages of using SiPM as Detector for Photon Counting Applications as Compared to Large-area SPAD

First, it is very important to note that SiPMs come into consideration only for applications that require large area devices since the standard or rather smallest size of currently available SiPMs is 1mm^2 . Further very low DCRs have been achieved with small area SPADs and they are available commercially at low-cost from a few companies [70]-[73], but non-availability of good, large-area SPADs is a known problem. Advantages of using SiPM as detector in photon counting applications as compared to large area SPADs are as follows:

1. *SiPM offers the combined advantages of both, small-area and large-area SPADs:*

Speed of a photon-counter depends on the speed of the quenching circuit. A large-area SPAD cannot be used without an active quenching circuit since with passive quenching it can achieve count rates of up to only few hundred KHz. Further, design of an active quenching circuit is not an easy task. A small area SPAD can achieve count rates of up to few MHz with passive quenching because of low RC time constants. *Since SiPM consists of many small area pixels combined to make a large active area, it can provide high speed operation with a large active area without the need for a quenching circuit.* Although, a SiPM will require an output amplifier, but range of amplifiers are easily available commercially, which is not the case with QCs.

2. Large area SPADs based on standard technologies suffer from high DCR because of problems with un-efficient gettering mechanisms as well as technology related

problems [44]. SiPMs use small area devices which have efficient gettering mechanism, but the high DCR is mostly due to the use of low-cost silicon as well as technology related problems. Hence, low DCR has currently been achieved in SiPMs at room temperature with the use of purer silicon [6]. Further DCRs can be significantly reduced by cooling the detector. Also, DCRs will further decrease as the technology progresses.

3. Arrays of large-area SPADs are currently needed for some applications [7], [110]-[111], but are un-available. Multi-channel photon counting systems based on individual large-area devices have been designed [108]-[109], but are high in cost. Hence, if SiPMs can replace SPADs for such applications, they have the potential to significantly reduce the cost of photon detection.
4. Current unavailability of low-cost large area SPADs and the current low-cost of SiPMs.

5.1.3 Feasibility of Using SiPM as Detector for DNA-sequencing

Based on the requirements of a detector for DNA-sequencing discussed in section 1.4, the feasibility of using SiPM for this application is analyzed as follows:

- Large active area: The typical active area of a standard SiPM is 1mm^2 . The SPAD that were used in the design of S-SPCM and M-SPCM have an active area diameter of 0.5mm. Therefore the active area of SiPM is ~ 5 times larger than the area of a large area SPAD. This means the active-area is sufficient for this application and moreover larger area can facilitate the use of a large diameter

fiber for collecting light from the capillary, increasing the light collection efficiency of the optical system.

- Dark Count Rate: It was shown in section 1.5 that the SNR of the DNA-sequencer does not degrade much with increase in DCR, but it does affect the minimum detectable signal. But SiPM should have a very wide dynamic range such that it can detect actual photon due to the signal above the DCR with good linearity.
- High Gain: The gain is comparable with that of a large area SPAD and hence it can be expected that same sensitivity levels can be achieved with SiPM as long as the dynamic range does not pose an upper limit.
- Speed and Dynamic Range (DR): Maximum frequency of photons emitted from the capillary (photon source) in our (and most other) DNA-sequencing instruments range from 500 KHz to 1.5 MHz. Because of the small size of the pixel, it is expected that SiPM will have small capacitance and hence sufficient DR for this application.
- Linearity: For good sequencing results, it is extremely important that the SiPM be linear. If the SiPM has sufficiently wide DR, then it can be expected to be linear.

Most of the above parameters needs to be investigated and are investigated in this thesis in the following sections.

5.1.4 Summary

Based on aforementioned discussion it is clear that SiPMs have the potential to count photons and used in certain fluorescence detection applications where high DCR is not a problem, DNA-sequencing is one such application. *For DNA-sequencing, although SiPM satisfies the criterion of large active-area, some key parameters such as sensitivity, DCR, linearity and dynamic range need to be thoroughly investigated.* In order to answer some of the above questions, this chapter investigates the use of SiPM as high-speed photon counters in general and the feasibility of using them as detectors for DNA-sequencing.

Three different SiPMs from two different manufacturers were selected (introduced in section 1.6). Following sections present the characterization of the selected SiPMs. Although the behavior and specifications of SiPMs from both the manufacturers is completely different, the results show that under certain conditions all the three SiPMs can be used as high-speed, highly sensitive photon counters and can be used for weak fluorescence measurements. Finally the SiPM based photon counting set-up was integrated into our single-lane DNA-sequencing set-up and excellent DNA-sequencing results were obtained (chapter 6).

5.2 Cooled SiPM: Experimental Results and Discussion

5.2.1 The Device

Voxtel-Inc in Beaverton, Oregon [72] provided us with this unique SiPM for evaluation purposes and is referred to as *cooled SiPM* since this SiPM is mounted on a 3-stage TE cooler and can be cooled to lower temperatures. Figure 5.2a and 5.2b show the photo of the SiPM and Table 5.1 summarizes important specifications of this device; more details can be obtained in [72]. The six output pins of the detector are anode, cathode, TEC (+), TEC (-) and two pins for the thermistor. The anode and cathode leads are used to bias the detector and the rest of the four leads are used for temperature control. The method of temperature control is described in the next section.

Table 5.1 Specifications of the cooled SiPM at +25°C.

Specification	Value
Chip Size (mm ²)	1.1
No of pixels/mm ²	1024
Operating Voltage (V)	40-46V
Gain (M)	1E+6

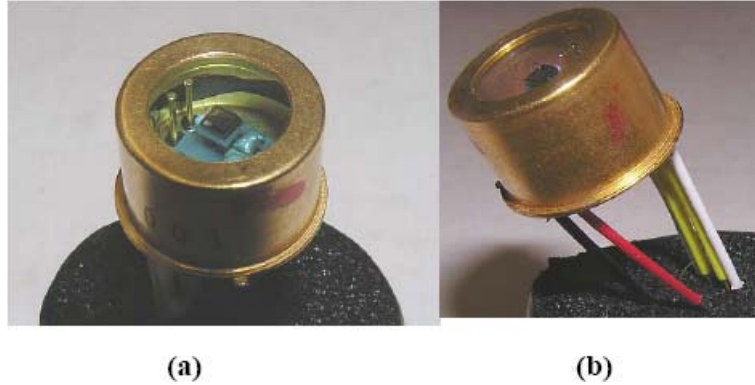


Figure 5.2 Photos of the cooled SiPM (a, b). TEC is clearly visible in (b).

5.2.2 Temperature Control & Biasing Circuit

Temperature Controller

The resistance of the peltier element (TEC) and the thermistor are $\sim 1\Omega$ and $1.2k\Omega$ respectively at room temperature ($+25^\circ\text{C}$). Figure 5.3 shows variation of the thermistor¹ resistance with temperature. A temperature controller was designed for the SPAD and is described in detail in section 3.3. Since both the TEC had similar ratings as shown in Table 5.2, same temperature controller could be used for controlling the temperature on the SiPM with minor modification. The value of the thermistor in SPAD model C30902S-DTC and cooled SiPM are $5.1k\Omega$ and $1.2k\Omega$ respectively; therefore in order to balance the bridge shown in Figure 3.14, the value of the high precision resistor (see R21 in Figure 3.11 and A.2) was changed from $5.1k\Omega$ to $1.2k\Omega$.

¹ Thermistor sits on the peltier element inside the hermetically sealed cooled SiPM. It senses the temperature on the peltier and sends feedback to the temperature controller circuit that takes appropriate action. SPAD model C30902S-DTC from PKI has the same arrangement.

Table 5.2 Comparison of TEC specifications of SPAD model C30902S-DTC and Cooled SiPM.

Specification	C30902S-DTC	Cooled SiPM
ΔT_{Max}	83°C	110°C
I_{max}	1.4A	1.4A
V_{max}	2V	1.9V
Q_{max}	0.92W	0.4W

The values of the voltage required to set different temperature were calculated using the bridge circuit shown in Figure 5.4 by using the values of $R(t)$ from Figure 5.3 (refer to section 3.3 for more details). Table 5.3 shows the calculated values of voltage that need to be set on TP4 (FB+) in order to set a particular temperature on the peltier.

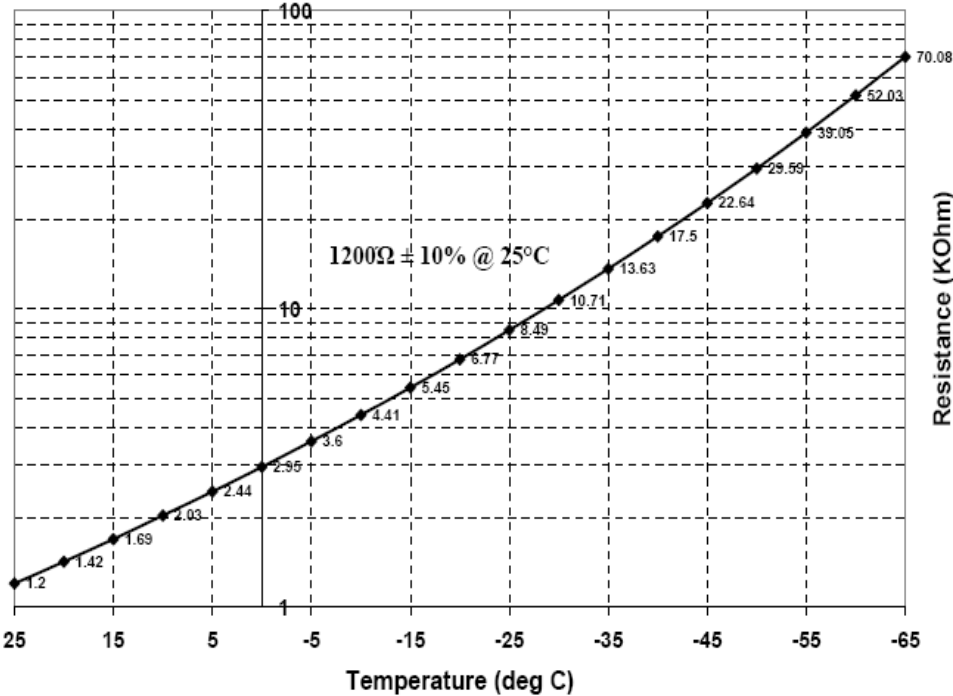


Figure 5.3 Cooled SiPM: Variation of thermistor resistance with temperature

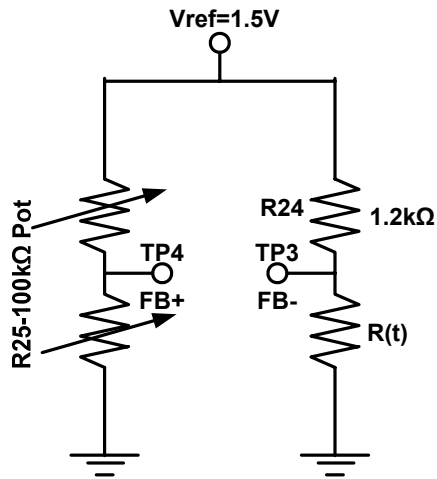


Figure 5.4 Bridge circuit formed in Figure 3.11 used to calculate the voltages to set different temperatures on SiPM.

Table 5.3 Calculated values of V_{TP4} to set different temperatures on the cooled SiPM.

Required Temperature on peltier (°C)	Resistance on thermistor, $R(t)$ (kΩ)	Voltage to be set on TP4 (V)
25	1.2	0.75
20	1.42	0.813
15	1.69	0.877
10	2.03	0.943
5	2.44	1.005
0	2.95	1.066
-5	3.60	1.125
-10	4.41	1.179
-15	5.45	1.229
-20	6.77	1.274
-25	8.49	1.314

The designed PCB for S-SPCM (see Figure 3.17) consisted of quenching circuit and the temperature controller circuit on the same board. Instead of designing a new controller especially for this purpose, only the temperature controller from one of those

boards was utilized and it was connected as shown in Figure 5.5 and 5.6 (photo). The thermistor (pins 10, 11) and TEC (pins 1, 4) leads from the cooled SiPM were connected to the respective pins on the PCB. These four pins are shown in Figure A.1. To obtain desired results, the board was connected as close as possible to the SiPM with smallest possible wires as shown in Figure 5.6.

Biasing circuit

The detector is biased using the circuit shown in Figure 5.5. Since the device is already passively quenched internally, it does not require any external quenching circuitry.

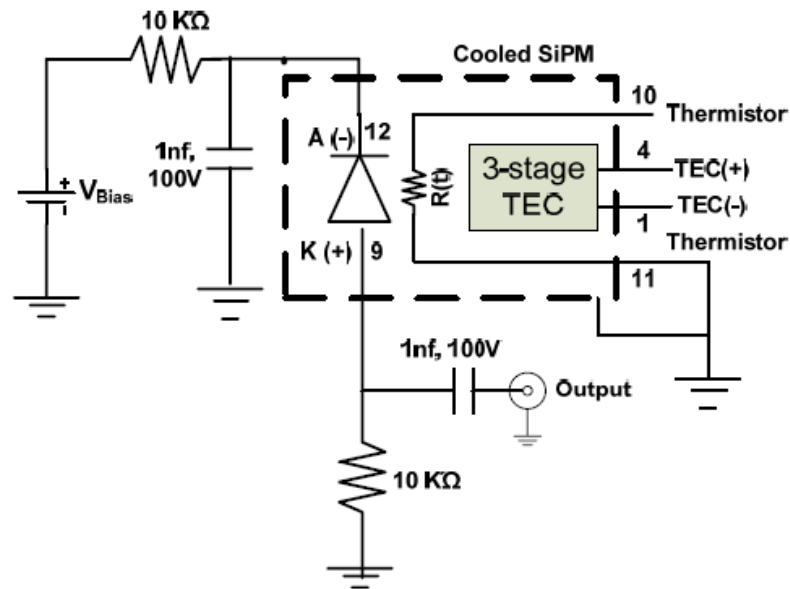


Figure 5.5 Cooled SiPM: Biasing circuit

5.2.3 Experimental Set-up

While testing the cooled SiPM, three optical set-ups were built at various stages for performing different experiments. Figure 5.6 shows photo of the final optical set-up that was used for electrical characterization of the detector, except that instead of the fiberization system as shown in the picture, a grin lens system was used. The photo of the grin lens is shown separately on the bottom of Figure 5.6. The fiberization system was built for performing DNA-sequencing experiments after performing the electrical characterization with the GRIN lens based system (photo not available). The GRIN lens on the left was adjusted to focus light onto the maximum active area of the detector. The SiPM is mounted right in front of the GRIN lens on a thick metal plate that acts as the heat sink and is connected to the biasing circuit and the temperature controller circuit described in the previous section. The output from the detector is a low amplitude signal and is connected to a fast preamplifier (model VT120C from EG&G Ortec) that has a gain of 20. The amplifier is connected as close as possible to the detector and the output from the amplifier is connected simultaneously to oscilloscope and high speed photon counter (Stanford photon-counter SR 400). It should be noted that unless otherwise mentioned, all the output counts were recorded with this counter. To isolate the device from the ambient light, the optical set-up was placed in a specially designed black-box. Figure 5.7 shows a photo that gives a general idea of the experimental set-up. It should be noted that that photo shows one of the three built optical set-ups placed inside the black-box and not the described optical set-up (photo not available); the optical set-up used for characterization was placed in the same box.

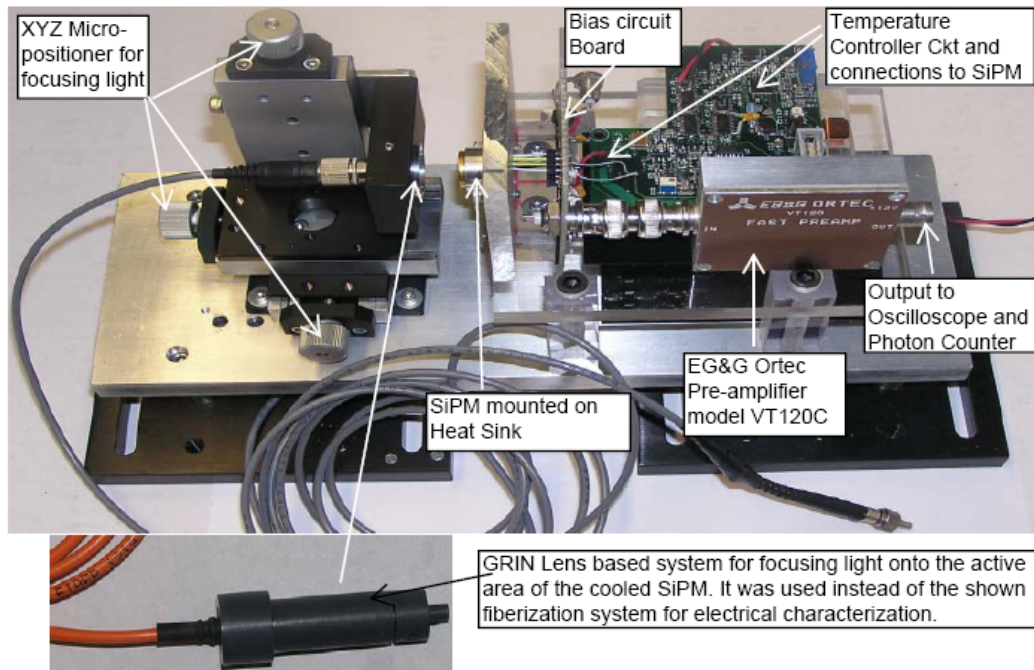


Figure 5.6 Cooled SiPM: Optical set-up used for characterization.

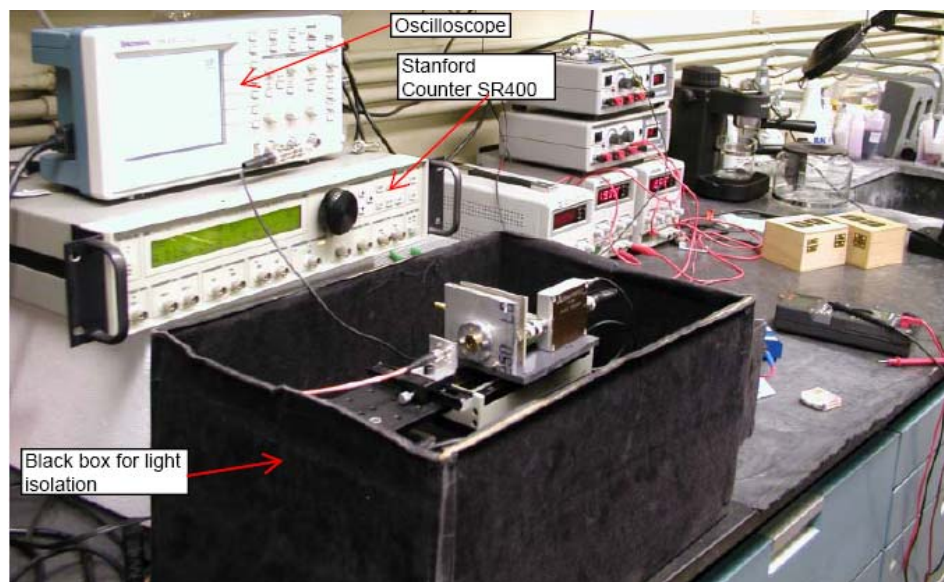


Figure 5.7 Photo of the experimental set-up used for characterizing all SiPMs.

5.2.4 Electrical Characterization

This section presents detailed electrical characterization and analysis of the obtained experimental results. Block diagrams of the experimental set-ups with important parameters are presented in the respective sections, if necessary.

Breakdown Voltage (V_{BR})

Figure 5.8 shows the variation of the breakdown voltage with temperature. The voltages required to set different temperatures are shown in table 5.3. The V_{BR} of this device varies by $107\text{mV}/^\circ\text{C}$ and V_{BR} at -20°C is $\sim -37.57\text{V}$.

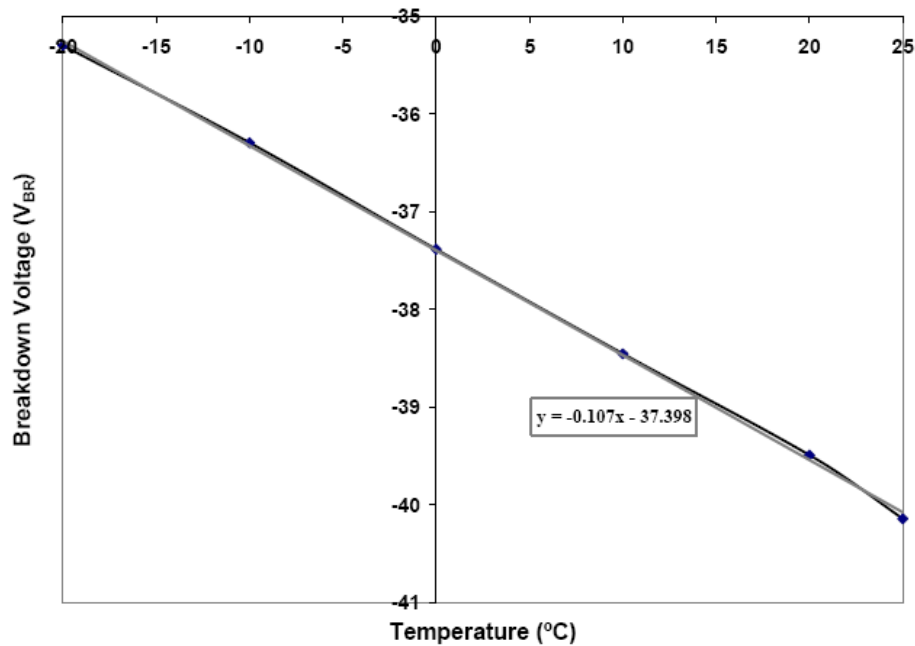


Figure 5.8 cooled SiPM: Variation of V_{BR} with temperature.

Dead Time

Dead time of a passively quenched detector can be determined by the associated RC time constant (refer to section 1.8) and approximately equal to the width of the output pulse. Figure 5.9a and 5.9b shows output pulses at the output of the amplifier at low and high V_{OV} respectively. The amplifier itself has a fast rise time of $\sim 1\text{ns}$ [115]. The pulses shown in Figure 5.9 have a FWHM of $\sim 20\text{-}25\text{ns}$. At higher V_{OV} (right), non-linearities such as after-pulsing and cross-talk are clearly visible and are discussed separately in section 5.4. It can be seen that the amplitude of the pulse increases at high over-voltage, but the pulse-width remains almost the same. Hence, theoretically, the maximum achievable count rate with this device should be $\sim 40\text{ MHz}$ (Deadtime^{-1}). Even if the largest width of the pulse is considered ($\sim 35\text{-}37\text{ns}$), theoretically, it should be able to count up to a maximum frequency of $\sim 27\text{MHz}$.

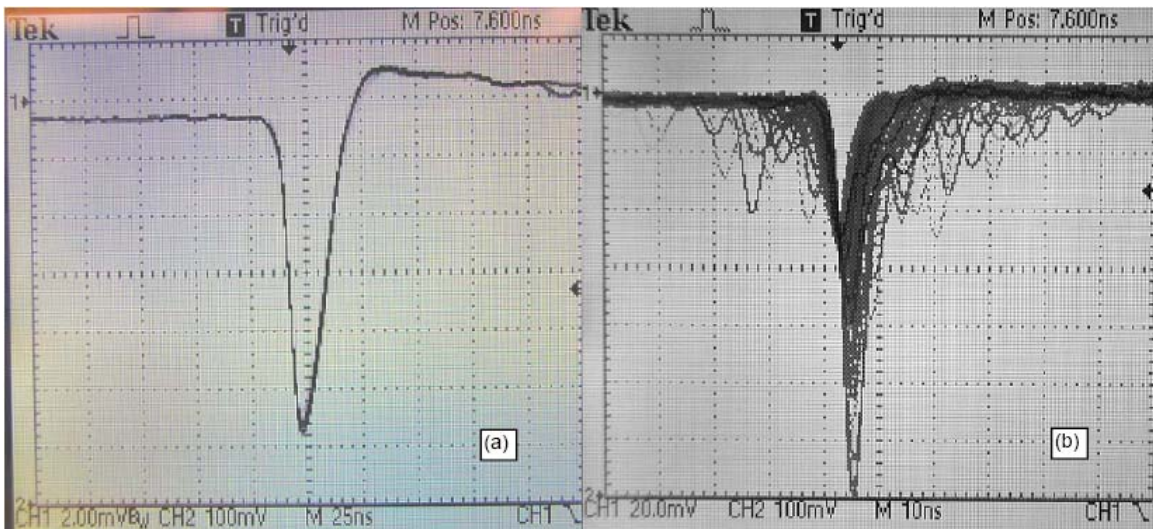


Figure 5.9 Cooled SiPM output pulses; (a) Low V_{OV} (b) High V_{OV} ($\sim 8\text{V}$).

Dark Count Rate (DCR)

(a) Variation of DCR with V_{OV} at different temperatures

Quality of a detector can be judged by studying its behavior in the dark. Variation of DCR with V_{OV} at +25°C and -20°C is shown in Figure 5.10 and Figure 5.11 respectively. Comparator threshold (V_{TH}) was set to -4mV which is ~0.5 photo electron level (p.e) in order to count all the incoming photons (photon counting mode) and can be seen in Figure 5.13. For -20°C, the DCR shoots from ~200 KHz at 10 Vov to ~3MHz at 11Vov; hence, to accommodate this sudden change it is also plotted on a log scale as shown in Figure 5.12. This sudden rise in DCR was not observed at +25°C. Similar to the DCR of SPAD (see Figure 3.24) significant decrease in DCR was observed when the detector was cooled to -20°C. The DCR dropped by ~50 times for 5V to 10V over-voltage range when the temperature was changed from +25°C to -20°C.

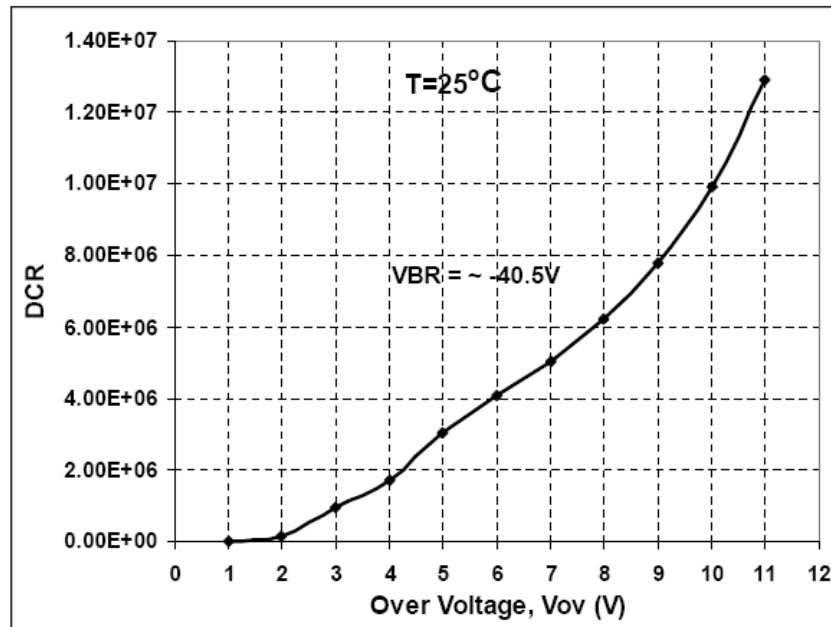


Figure 5.10 Cooled SiPM: Variation of DCR with V_{OV} at +25°C.

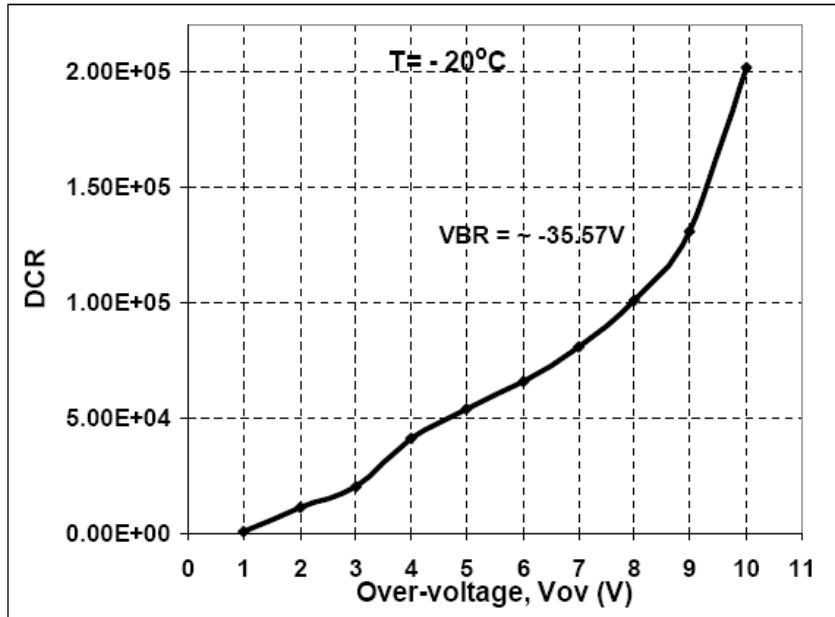


Figure 5.11 Cooled SiPM: Variation of DCR with V_{ov} at -20°C (linear scale)

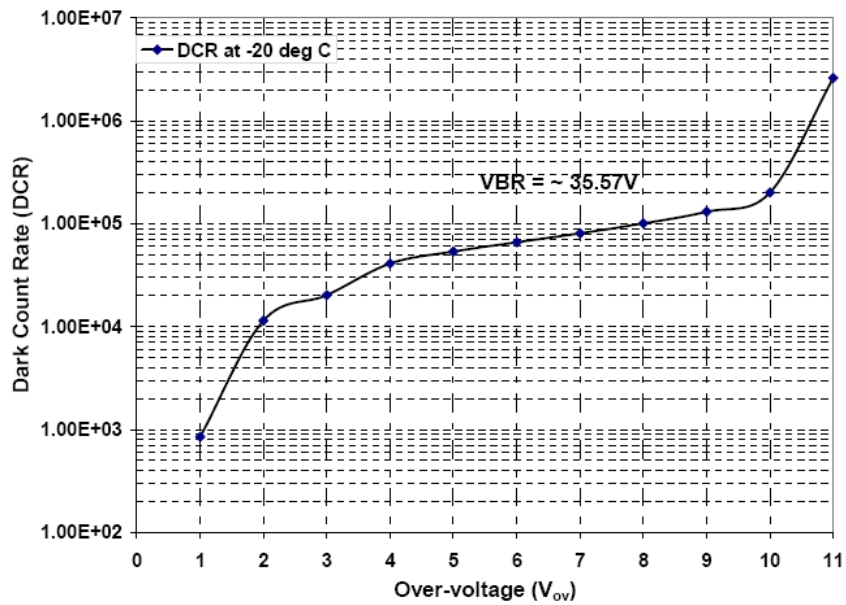


Figure 5.12 Cooled SiPM: Variation of DCR with V_{ov} at -20°C (log scale)

(b) Variation of DCR with comparator threshold (V_{TH})

Next, the variation of DCR with the comparator threshold was studied at $T=-20^{\circ}\text{C}$ for five different over-voltages and the results are shown in Figure 5.13.

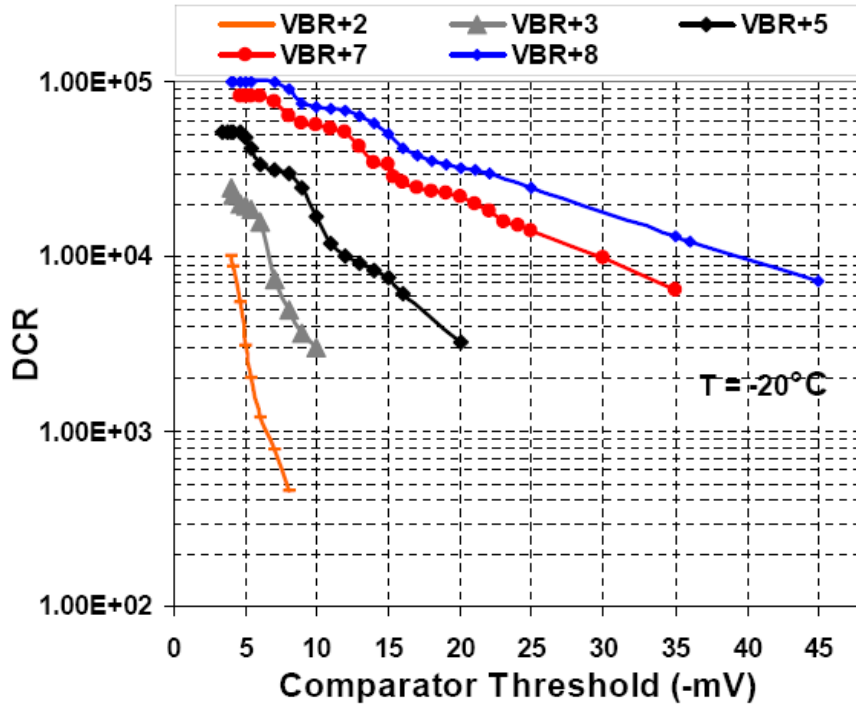


Figure 5.13 Variation of DCR with comparator threshold at $T=-20^{\circ}\text{C}$.

It can be seen that the count rate decreases as the comparator threshold¹ is increased. Further a step like behavior is observed as reported in few literatures [89] [116]. In this device, steps started becoming clearly visible only at $V_{BR}+5$ volts. This step like behavior is explained as follows:

- Each step represents the pulses due to number of photos. Since the threshold at the first step is small, it means that it counts all the incoming pulse amplitudes.

¹ Stanford counter SR400 was used as the photon counter to characterize all the SiPMs; hence the comparator threshold in this chapter refers to the threshold set on this counter. For characterizing S-SPCM (chapter 3), this threshold was set on the comparator IC U6 shown in Figure 3.2.

For SiPM, the output pulse due to one photon, 2 photons and so on are referred to as 1p.e, 2p.e pulses etc. and so on. Therefore, the first step represents counts due to all the output pulse amplitudes (1p.e, 2p.e, 3p.e and so on), the second step represents counts due to all the pulses except the pulses due to 1p.e, the third step represents counts due to all the pulses except the pulses due to 1p.e and 2p.e and so on.

- Above point implies that count rates due to 1p.e pulses can be estimated by subtracting the counts at second step from the first and similarly 2p.e. pulses can be estimated by subtracting counts at third step from the second and so on.
- If the steps are distinct and clear as in [89] [116], it would imply that each pixel generates same output charge corresponding to number of detected photons, suggesting that the device has uniform gain across the active-area of the device. This is not exactly the case with this device.
- It would be expected that pulses at the level of 1p.e or at the max 2p.e would be observed in the dark, but Figure 5.13 and [89] [116] show that pulses at the level of up to 6-7p.e. are observed in the dark. Such high numbers of pulses (steps) in the dark were observed with the other two SiPMs characterized in this thesis and are discussed in section 5.3.2 (see sub-topic variation of DCR with comparator threshold). The reason for this is high level of non-linearities such as after-pulsing and cross-talk that are present in SiPMs and is well-known [50]. After-pulsing and cross-talk phenomena were introduced in section 1.4. Due to the nature of physical phenomena responsible for generation of after-pulsing, it can be speculated that after-pulsing at the level of 1p.e is the maximum and the

probability of after-pulsing decreases significantly at the level of 2p.e and almost becomes negligible at the level of 3p.e. and higher. On the other hand, cross-talk happens due to inter-pixel currents and optical photons [52]. Optical photons are more likely to generate high amplitude pulses ($>2\text{-}3\text{p.e}$) and hence it can be speculated that steps due to 3p.e, 4p.e, 5p.e are mainly due to cross-talk. It must be noted that since this thesis investigates the photon counting properties of SiPM, the threshold is set to less than 1p.e. in order to count all the photons. Therefore pulses with all the amplitude i.e. 1p.e, 2p.e, 3p.e. etc. are counted as one pulse. Hence, the effect of cross-talk on photon counting performance of SiPM will be different and is investigated in section 5.4. *It must be noted that DCR is referred to as noise in some literatures [84], [49], [83], but since DCR is known and can be easily subtracted from the obtained PCR, in this thesis DCR is classified as back ground and only above mentioned non-linearities (after-pulsing and cross-talk) are classified as noise. Therefore, from now on, after-pulsing and cross-talk are referred to as noise of the SiPM in this thesis.*

- It can be noticed that the drop in count rate from setp1 to setp2 and step2 to step 3 is higher at $V_{BR}+5\text{V}$ and smaller at $V_{BR} +7$ and $V_{BR} +8$ volts. This means that (i) noise increases with increase in V_{OV} and (ii) noise decreases much faster at low V_{OV} as compared to high V_{OV} . Hence, noise can be decreased significantly by operating at low V_{OV} and high comparator thresholds. But in photon-counting mode it is required to operate at minimum threshold and highest feasible over-voltage.

- The comparator threshold that needs to be set in order to operate this device in photon counting mode is ~ -4 to -7 mV depending on V_{OV} (< 1 p.e threshold).

Sensitivity, operating point and SNR

Sensitivity of this SiPM was characterized using the same method described in detail in section 3.6 (refer to sub-topic Sensitivity, optimum operating point and SNR). The main difference between this experimental set-up and the experimental set-up in Figure 3.27 that was used to characterize S-SPCM is that the cooled SiPM is not fiberized. The light was adjusted using the XYZ positioner such that maximum light was focused onto the active area of the SPAD. To compare the results with PKI SPCM, it is important that the output light power from the fiber going into both the detectors be same. Light onto the SiPM is focused using a fiber (core diameter of $62.5\mu\text{m}$) that has GRIN lens assembly on one end as shown in Figure 5.14. Since the same fiber cannot be used for PKI SPCM (requires FC connector), a different fiber with same core diameter and FC connector that had the same output power was used. The power levels were measured using a power meter before and after the experiment. PCR were measured with V_{TH} on Stanford counter set to -6 mV (< 1 p.e.). Figure 5.15 shows the obtained results; it should be noted that DCR has been subtracted from all the plotted PCR. It can be seen that for the same light level, the count rate increases with increasing V_{OV} and the count rate approached that of the PKI SPCM at $10V_{OV}$. Attenuation versus PCR was not measured beyond $10 V_{OV}$ due to the sudden increase of DCR by ~ 10 times as V_{OV} was increased from 10 to 11 V (see Figure 5.12), the reason for which is unknown. Further, it is interesting to note that even after the SPCM count rate saturates, the count rates of the

cooled SiPM keep increasing, suggesting that it has much wider dynamic range than the PKI SPCM.

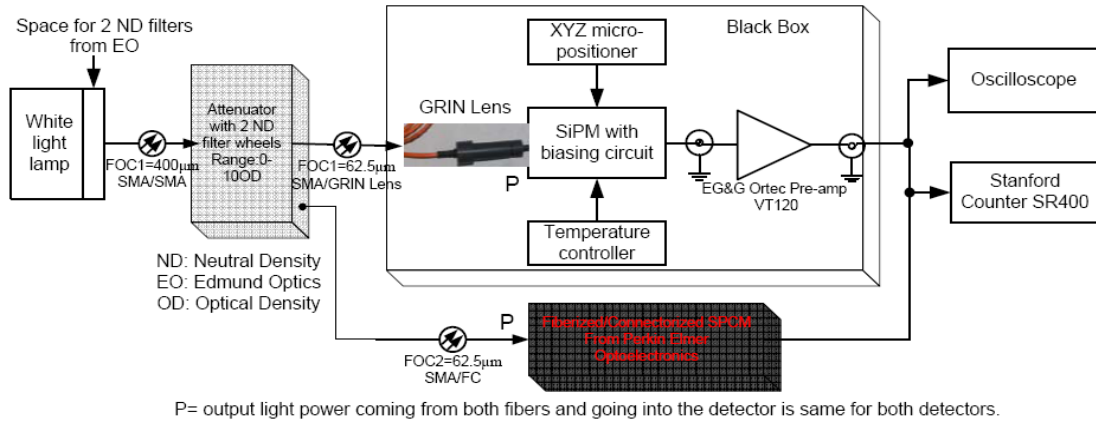


Figure 5.14 Cooled SiPM: Block diagram of the experimental set-up for sensitivity measurement.

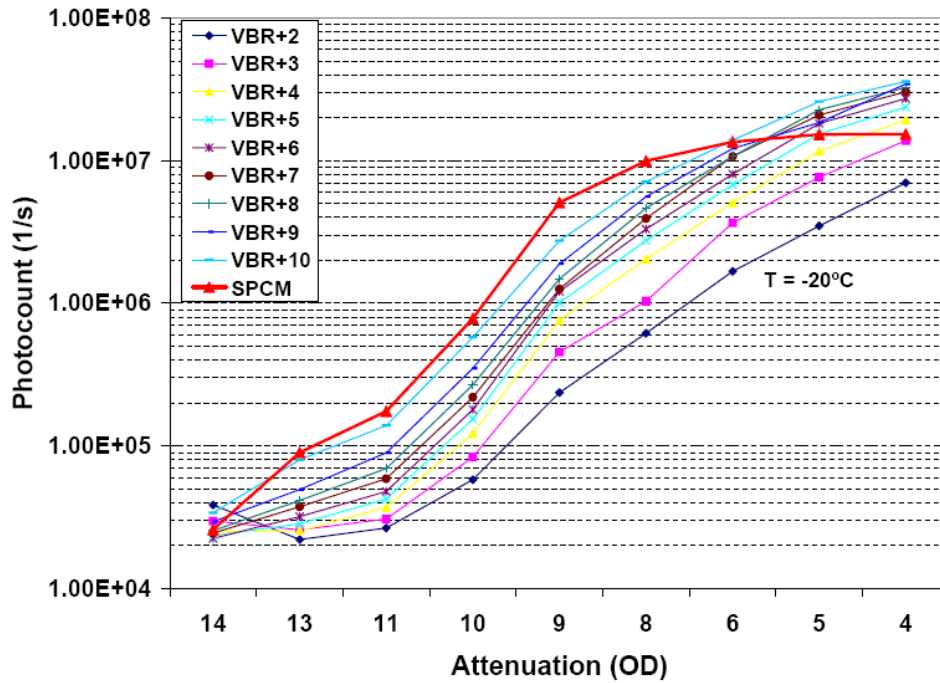


Figure 5.15 Cooled SiPM: Attenuation versus PCR at different V_{OV} .

Figure 5.16 shows the attenuation versus PCR of cooled SiPM plotted against that of PKI SPCM for each V_{OV} to filter effects due to non-calibrated filters as discussed in section 3.6 (refer to sub-topic Sensitivity, optimum operating point and SNR). From Figure 5.16 it can be seen that that cooled SiPM is highly sub-linear at low V_{OV} and becomes more and more linear as V_{OV} is increased. The red-line in Figure 5.16 is the plot of PCR of PKI SPCM plotted against itself representing the ideal linear curve. The cooled SPCM curves increase vertically around $\sim 15\text{MHz}$ (point where the topmost red curve intersects the $V_{BR}+10$ curve in Figure 5.15), since the PKI SPCM reaches saturation, suggesting that the cooled SiPM has more DR and linearity than the PKI SPCM. This is the

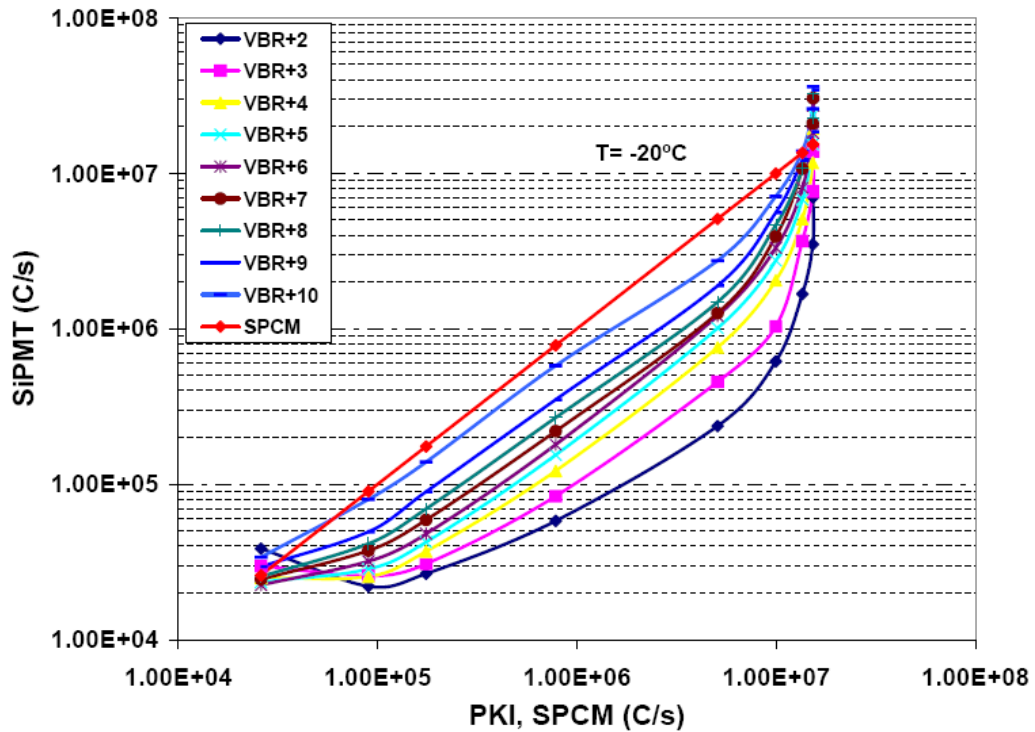


Figure 5.16 Attenuation versus PCR of PKI SPCM versus Cooled SiPM for increasing V_{OV} .

Figures 5.15 and 5.16 suggest that $10V_{OV}$ is the best over-voltage for cooled SiPM in order to obtain similar sensitivity levels as PKI SPCM. Figure 5.17 shows the plot of SNR (calculated using Equation 3.6) at each over-voltage plotted for different light levels and it shows that best SNR is obtained at $10V_{OV}$.

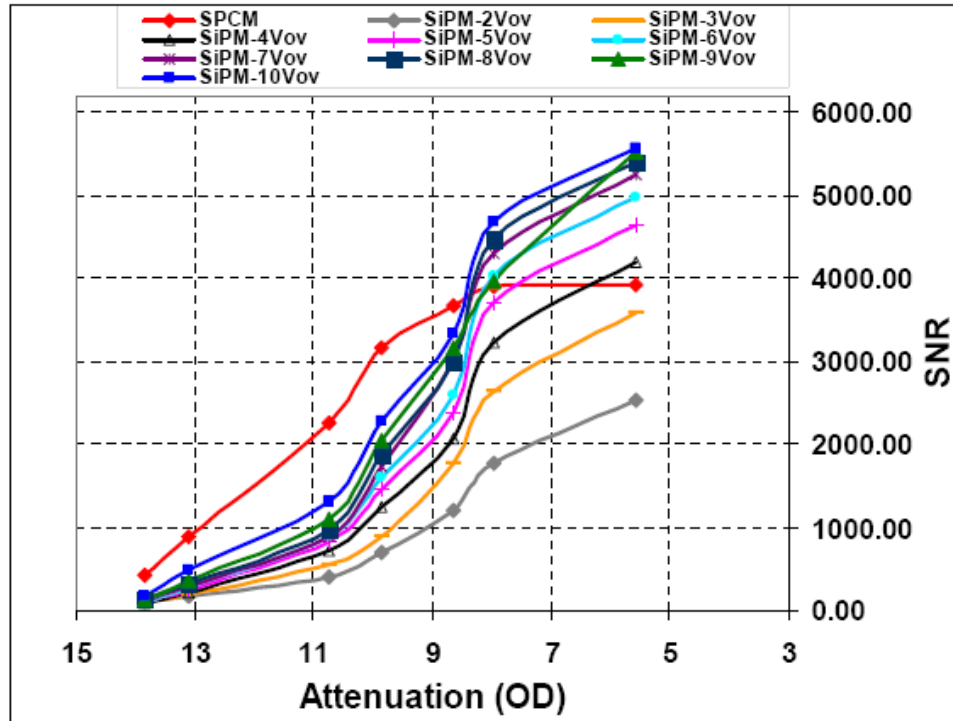


Figure 5.17 Cooled SiPM: Signal-to-Noise ratio.

Linearity and Dynamic Range (DR)

DR and linearity of a SiPM when used as photon counter is different as compared to when it is used as photon number resolver and is discussed in section 1.4. From the above results it was found that the cooled SiPM has the best combination of sensitivity and SNR at $10V_{OV}$. Figure 5.18 shows the comparison of attenuation versus PCR curves of the cooled SiPM and PKI SPCM, both tuned to optimum parameters. The shape of the

curve is due to the non-calibrated filters. The aim of Figure 5.18 is to show that both PKI SPCM and cooled SiPM have similar PCR for same attenuation suggesting that cooled SiPM can match the sensitivity of PKI SPCM when biased appropriately. Further the higher DR of cooled SiPM is clearly visible in this figure. Figure 5.19 shows the attenuation versus PCR of cooled SiPM plotted against attenuation versus PCR of PKI SPCM. It can be seen that the device has good linearity since curve is quite linear on the log-log scale. The DR of the cooled SiPM is $\sim 28\text{MHz}$ which is almost 2 times higher than the DR PKI SPCM (15MHz) and ~ 3 times higher than S-SPCM. The obtained DR is in very good agreement to with the DR predicted on the basis of dead-time from Figure 5.9. It must be noted that maximum count rate measured with this device was $\sim 36\text{MHz}$, but the device started saturating at $\sim 28\text{MHz}$.

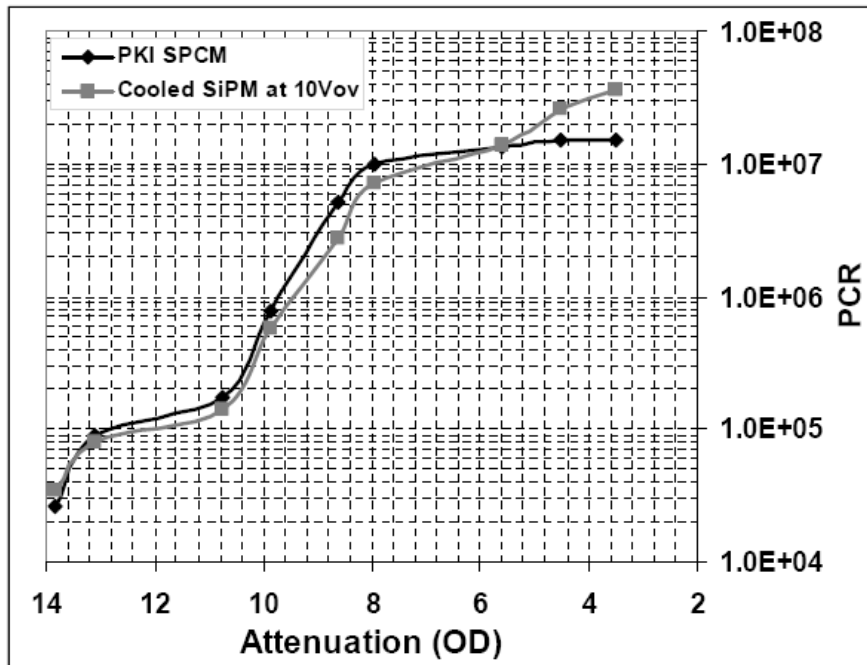


Figure 5.18 Comparison of cooled SiPM at 10Vov with PKI SPCM.

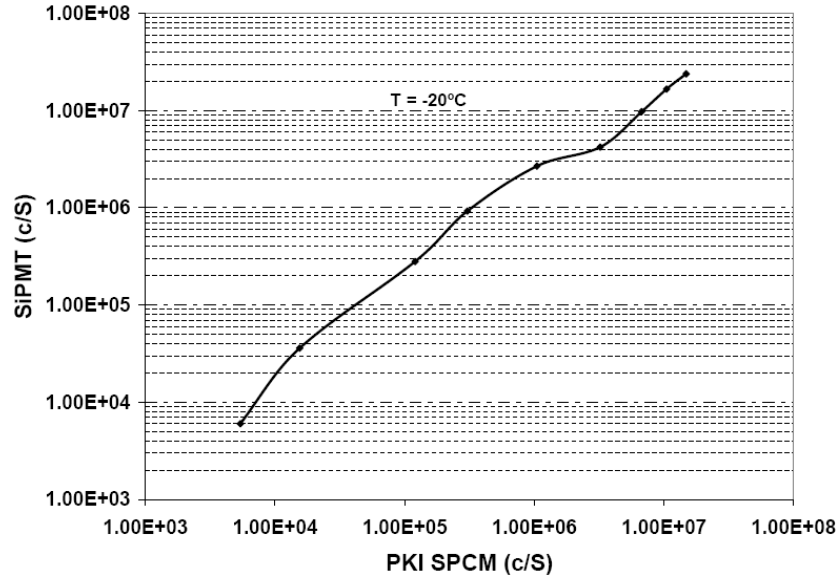


Figure 5.19 Comparison of linearity of cooled SiPM at 10Vov with PKI SPCM.

Sensitivity at different wavelengths

For the cooled SiPM, PDE or QE was not known; hence it was necessary to study its response to different wavelengths of interest. The block diagram of the experimental set-up is shown in figure 5.20. In this set-up the white-light lamp and the attenuator box from the set-up show in Figure 5.14 are replaced with a monochromator. The monochromator has the facility to select different wavelengths (0-1000nm) and the attenuation levels can be changed using a shutter that controls the amount of light that can pass through the window. Since the attenuation levels are un-calibrated, for each light level, count rates are recorded at the output of cooled SiPM and PKI SPCM. It is known that PKI SPCM has very good sensitivity in the visible spectrum and its PDE is known too, hence if similar count rates are obtained with the cooled SiPM, it could be concluded that cooled SiPM has good sensitivity to these wavelengths. Results of last section showed that this SiPM has the best combination of sensitivity and linearity at $V_{OV} = 10V$,

$V_{TH} = -6mV$, hence the SiPM was adjusted to these settings for this experiment. Figure 5.21 show the obtained results. It is clear that this SiPM has good sensitivity in the visible spectrum (count rates similar to SPCM) and that it is more sensitive at shorter wavelengths (400nm) than the SPCM.

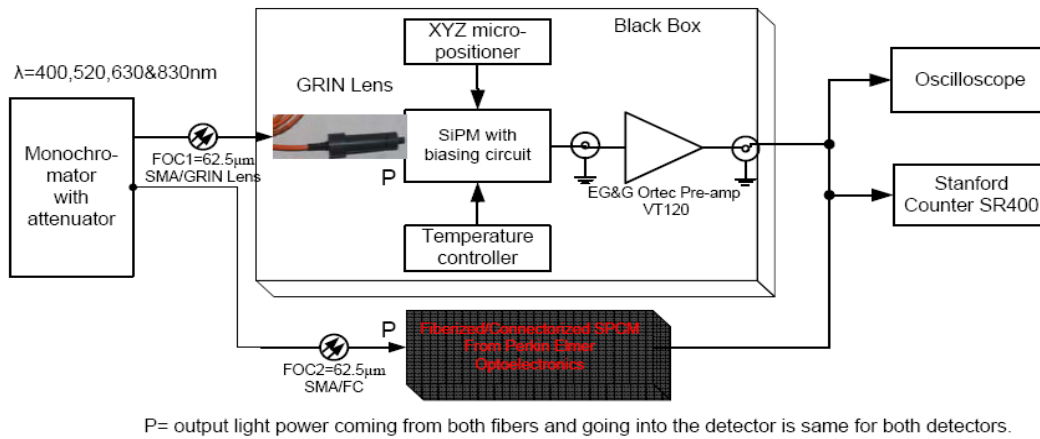


Figure 5.20 Cooled SiPM: Block diagram of the experimental for measuring sensitivity to different wavelengths.

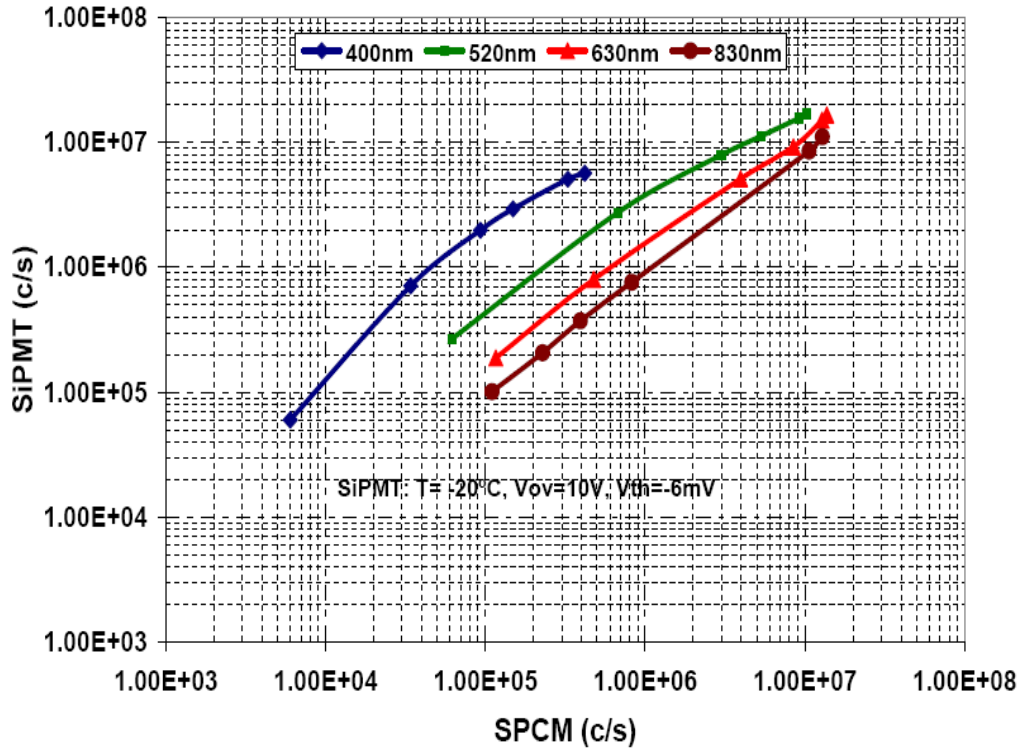


Figure 5.21 Cooled SiPM: Sensitivity at four different wavelengths.

Summary

From the results obtained with this SiPM it can be concluded that:

- DCR can be significantly lowered (~50 times) by operating at lower temperatures.
- Similar (un-cooled) detectors were tested in our lab few years back and it was found that the DCR of those detectors were so high that it practically occupied the whole DR of the device. Hence, although those devices might have been sensitive, the DCR was such that it became impossible to detect any useful signal above noise. This could have been the case with this SiPM too (DCR = 13MHz at +25°C, 10V_{OV}), *but cooling the detector made it practically usable.*

- Maximum SNR is achieved by operating the detector at high V_{OV} and low V_{TH} . Although it has the effect of increasing the DCR, it increases the signal much more than the noise.
- If DCR is not a problem for a particular application, sensitivity levels similar to that of PKI SPCM can be achieved by operating this detector at voltages much higher than V_{BR} . Although, MDS^1 is affected by the increased DCR (section 3.6). It is important to note that all the recorded PCR include contribution of noise whose contribution is unknown and needs to be studied. Noise in SiPM is discussed in detail in section 5.4.

¹ MDS (Minimum Detectable Signal) is the minimum signal that can be detected by a single photon detector. For SPAD and SiPM, Absolute value of DCR can be counted as background since it is known and can be subtracted. But, fluctuation of the DCR represents the noise due to DCR; hence, assuming poisson statistics, square root of DCR can be defined as the MDS.

5.3 Hamamatsu MPPCs: Experimental Results and Discussion

This section presents the electrical characterization of two SiPMs (MPPCs) from Hamamatsu photonics [6] as high-speed photon-counters and investigates their feasibility for DNA-sequencing application. The two devices were introduced in section 1.6 and their important specifications are shown in table 5.4; more information can be obtained from [6]. MPPC1 and MPPC in Table 5.4 are referred to as 100-pixel device and 1600-pixel device respectively.

Table 5.4 Specifications of the characterized Hamamatsu MPPCs [6].

Specification	MPPC 1	MPPC 2
Type/Model	S10362-11-100U	S10362-11-25U
Chip Size (mm)	1.5 x 1.5	1.5 x 1.5
Size of 1 pixel (μm)	100 x 100	25 x 25
Effective Active Area (mm)	1 x 1	1 x 1
Fill Factor*¹ (%)	78.5	30.8
No of pixels/mm²	100	1600
Operating Voltage, V_{OP} (V)	69.72	70.89
DCR		
0.5 p.e. thr	716K	438K
1.5. p.e. thr	125K	12.5K
Gain (M)	2.4E+06	2.74E+05
Temp ($^{\circ}\text{C}$)	+25 $^{\circ}\text{C}$	+25 $^{\circ}\text{C}$
Wavelength (λ) (nm)	655	655

*1: Ratio of active area of the pixel to the entire area of the pixel.

5.3.1 Experimental Set-up

Figure 5.22 shows the optical set-up used for characterizing the devices. Since the gain of one amplifier was not enough for this device, two amplifiers (EG&G Ortec

VT120C) each with a gain of 20 were used as shown in Figure 5.22. Unlike cooled SiPM (was not fiberized for electrical characterization), these devices were already fiberized using the same fiberization system described in section 1.7. The fiberization system for SPAD was permanent and adjusted for maximum light coupling efficiency. For these SiPMs the assembled fiberization system was temporary, hence a XYZ micro-positioner was used to focus the light with maximum efficiency. The detector (not visible in photo) is mounted on the heat-sink and the light is focused from the fiberized connector as shown in Figure 5.23. A fiber with core diameter of $200\mu\text{m}$ is used for all the experiments. The optical set-up was placed in a black-box (similar to Figure 5.7) for isolating the detector from ambient light. Similar to cooled SiPM, the output from the amplifier is connected simultaneously to oscilloscope and Stanford counter SR400.

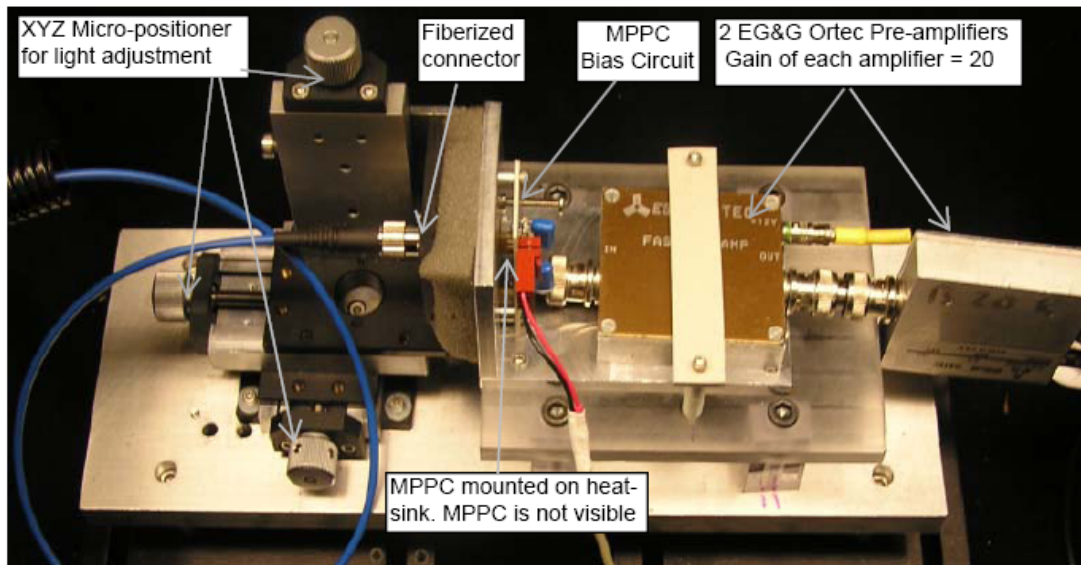


Figure 5.22 Optical set-up for characterizing 100-pixel and 1600-pixel MPPCs.

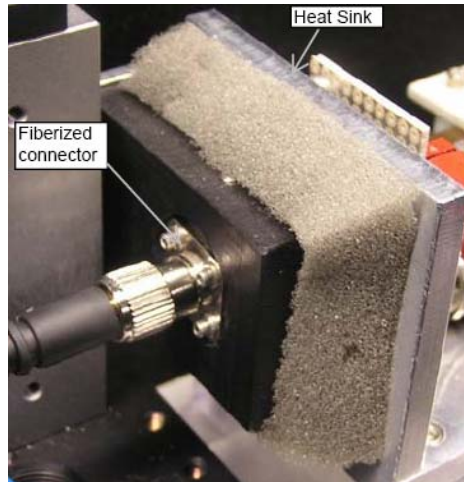


Figure 5.23 Fiberized connector used for focusing light on MPPCs.

5.3.2 Electrical Characterization

Same experimental methods as cooled SiPM (section 5.2.3) were used for characterizing these devices. The devices were biased using the circuit shown in the datasheet [6].

Breakdown voltage (V_{BR})

Usually, manufacturers provide V_{BR} specification of a device, but instead of V_{BR} , operating voltage (V_{OP}) along with the gain at this operating voltage is specified with each MPPC. Table 5.4 shows the specifications in which V_{OP} , DCR and Gain at V_{OP} are specific for our device and may vary for different devices of the same type. Since the gain is already high at V_{OP} , it implies that V_{OP} is already a few volts above the V_{BR} . V_{BR} for these devices was measured and found to be 68.92V and 69.29V for the 100-pixel and

1600 pixel device respectively, which means that the 100-pixel device is biased $\sim 0.8V$ above V_{BR} and the later device is biased $\sim 1.6V$ above V_{BR} . It must be noted that V_{BR} varies with temperature and hence depending on the experimental conditions and method of measurement, these numbers may vary.

Dead time

Dead-time is determined as described in section 5.2.4 (see Dead Time). Figure 5.24 shows the output pulses for 100-pixel (a, b) and 1600-pixel (c, d) device respectively. The FWHM for 100-pixel and 1600-pixel device is approximately 20ns and 18ns respectively, but it must be noted that the 100-pixel device has a longer tail as compared to the 1600-pixel device and this difference is noticed in the maximum pulse width. Maximum pulse width for 100 and 1600-pixel device is 35-40ns and 25-30 ns respectively. Therefore the expected maximum achievable count rate should be in the range of 25-30 MHz for 100-pixel device and 33-40 MHz for the 1600-pixel device. Pulses due to 1p.e. 2p.e. etc. are distinctly visible with these devices as shown in Figure 5.24a and 5.24d, which was not the case with the cooled SiPM (see Figure 5.9).

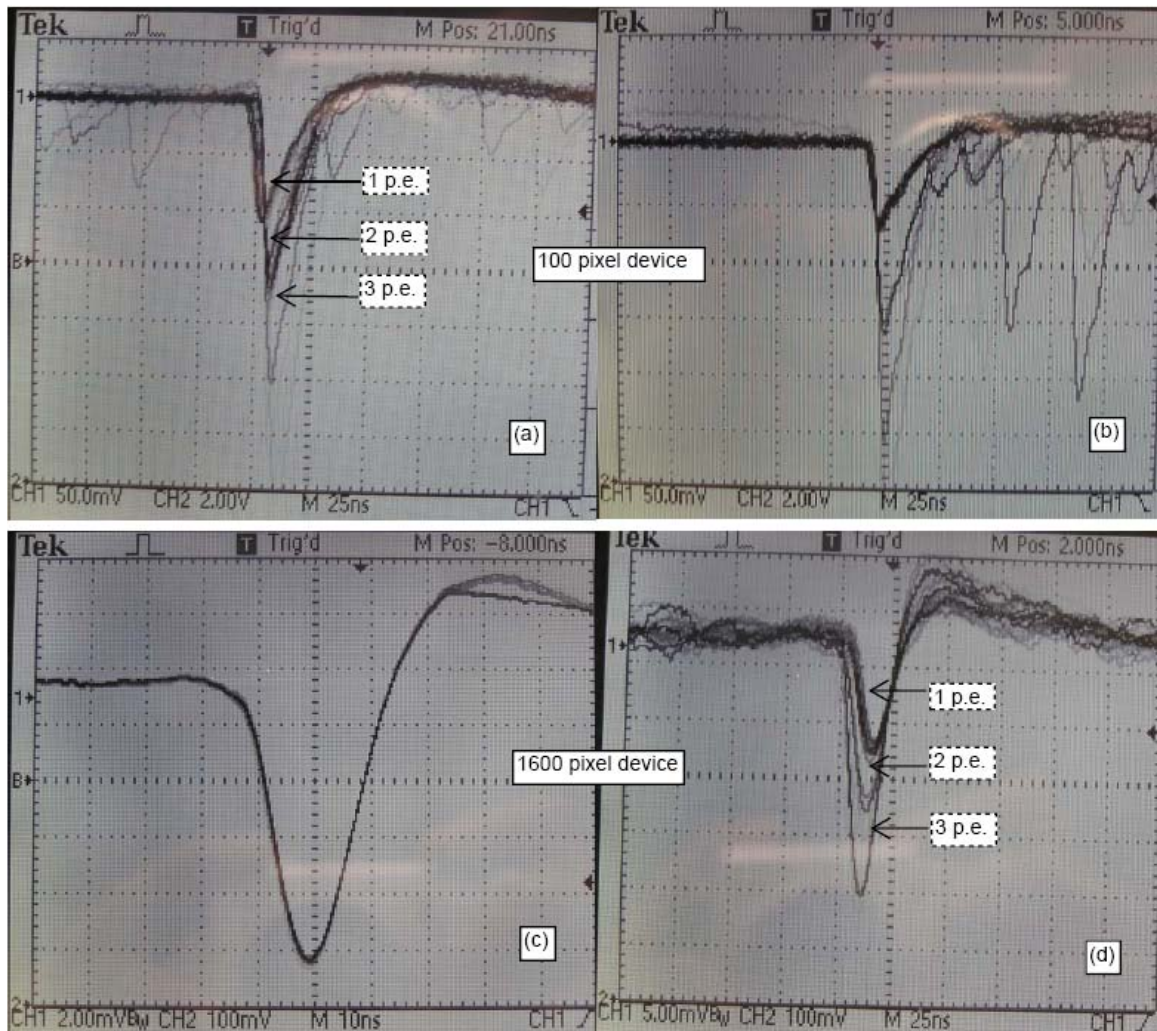


Figure 5.24 Output pulses, (a, b) 100-pixel device, (c, d) 1600-pixel device at low (left) and high (right) V_{OV} . Note: (c) was recorded in the averaging mode.

Dark Count Rate (DCR)

(a) Variation of DCR with V_{OV}

Figure 5.25 shows the variation of DCR with V_{Bias} for 100-pixel (top) and 1600-pixel (bottom) device respectively. Instead of V_{BR} , DCR was measured starting with minimum bias set at V_{OP} . V_{TH} was set at ~ 0.5 p.e which is approximately -20 mV as seen

in Figure 5.26. The recorded values of DCRs are comparable with the values specified in Table 5.4 for these particular devices at 0.5p.e, which means that the selected V_{TH} (-20mV) actually corresponds to 0.5p.e. These results also confirm that it was necessary to provide more gain (2 output amplifiers) for these devices, since the count rates matched the count rate provided in the passport for these specific devices only after providing more gain. It can be seen that the DCR for 100-pixel device is much higher than the DCR for 1600-pixel device and it was observed that the increase in DCR when the bias is changed from V_{OP} to $V_{OP}+1V$ is much higher (6.9 times) for 100-pixel device as compared to 1600-pixel device (1.68 times). This implies that the increase in gain with V_{OV} is higher for 100-pixel device as compared to 1600-pixel device. Since the gain at V_{OP} for these devices is already high (Table 5.4), they can be expected to achieve high sensitivity at comparatively lower V_{OV} . Hence the DCR was not measured at higher over-voltages. Other reason for not measuring DCR at high V_{OV} was the fear of damaging the device since it was not known if they could be biased to high V_{OV} .

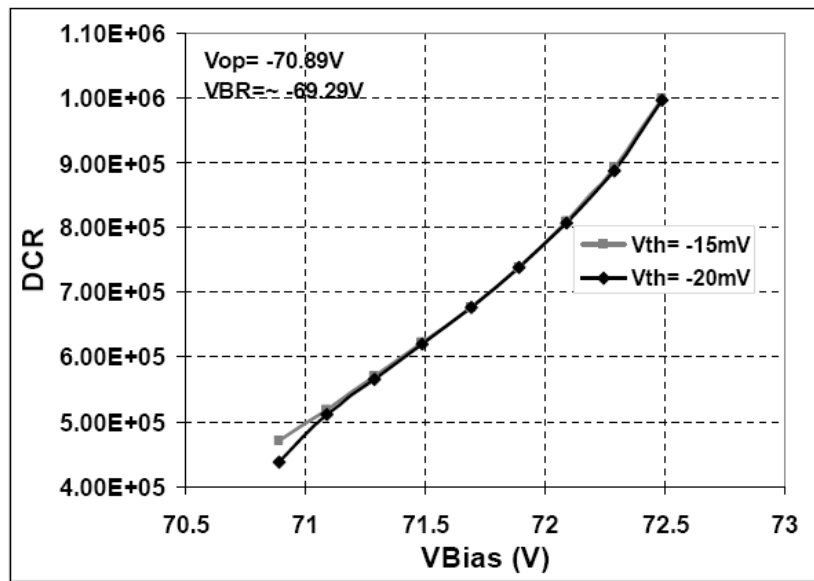
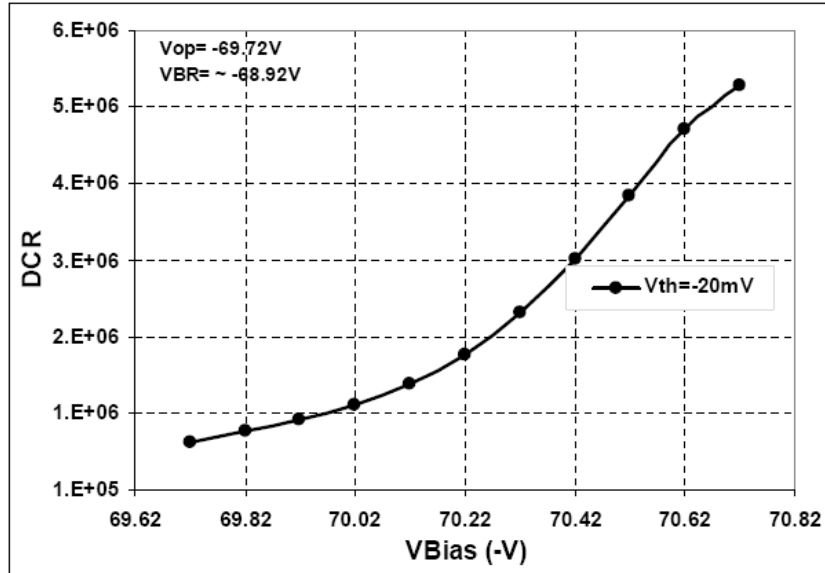


Figure 5.25 Variation of DCR with V_{Bias} for 100-pixel and 1600-pixel device.

(b) Variation of DCR and PCR with comparator threshold (V_{TH})

Figure 5.26 shows the variation of DCR with V_{TH} at $V_{Bias} = V_{OP}$ for both devices. Step like characteristics were observed for both the devices. The meaning of these characteristics are explained in detail in section 5.2.4 (refer to Variation of DCR with

comparator threshold). From Figure 5.26 it can be seen that the steps in both the devices are much more distinct as compared to the cooled SiPM (see Figure 5.13) which implies that these devices have uniform gain across the active-area of the pixel as compared to the cooled SiPM. It can be seen that the number of steps in 100-pixel device are much more distinct and larger in number as compared to the 1600-pixel device. It was speculated in the DCR section of section 5.2.4 that 3p.e, 4p.e, etc. pulses is mainly due to cross-talk. Since the 100-pixel device has large number of steps as compared to the 1600-pixel device, it implies that it has higher cross-talk as compared to the 1600-pixel device. This can also be confirmed from the fact that the fill factor of 100-pixel device (78.5) is much greater than that of 1600-pixel device (30.8) (see Table 5.4). Further, for the 100-pixel device, the ratio of counts from the first step to the second, second to the third and so on is approximately constant which is not true in case of 1600-pixel device. This means that for the 100-pixel device the percentage of pulses corresponding to 1p.e, 2p.e, 3p.e. and so on is approximately constant (at $V_{Bias}=V_{OP}$).

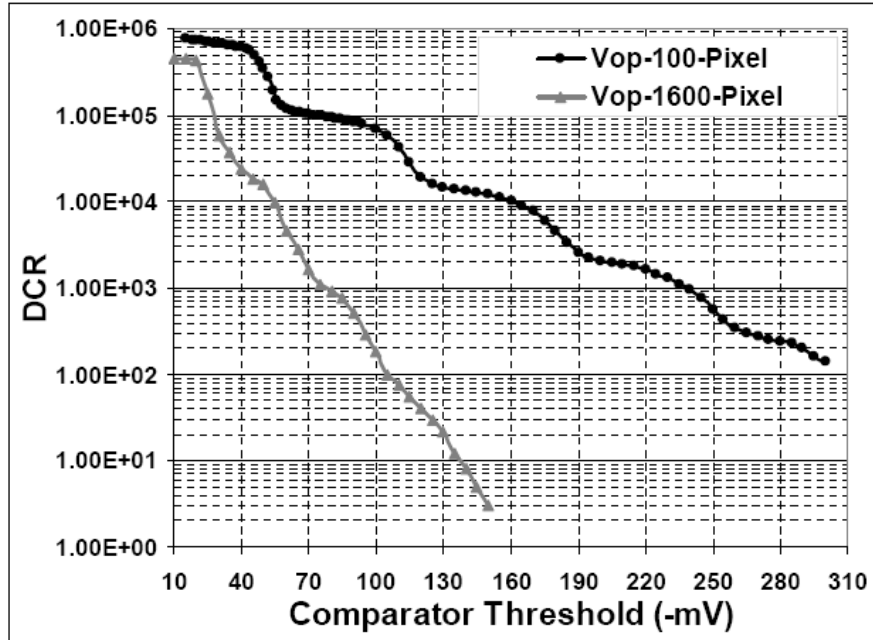


Figure 5.26 Variation of DCR with comparator threshold for 100-pixel and 1600-pixel device ($V_{Bias} = V_{OP}$).

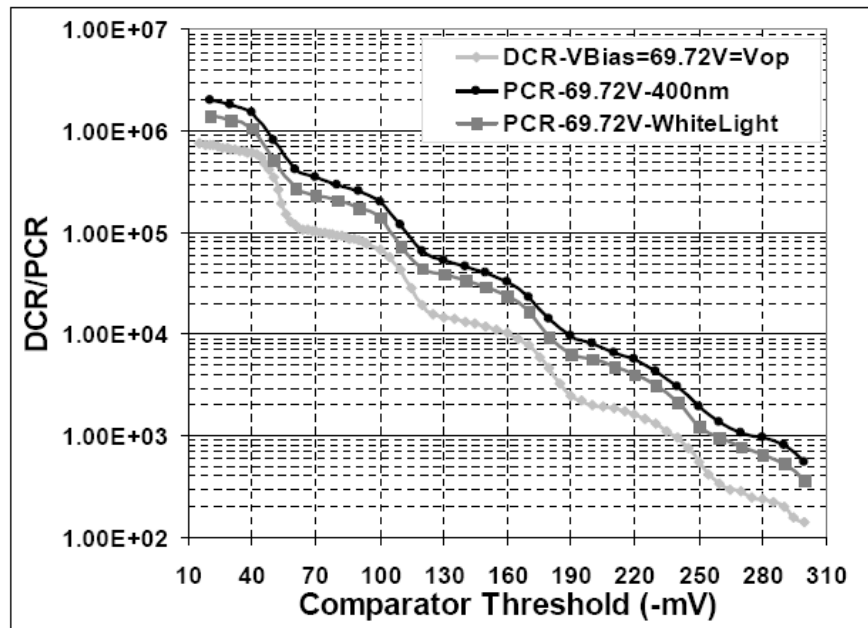


Figure 5.27 100-pixel device: Variation of DCR and PCR with comparator threshold ($V_{Bias}=V_{OP}$).

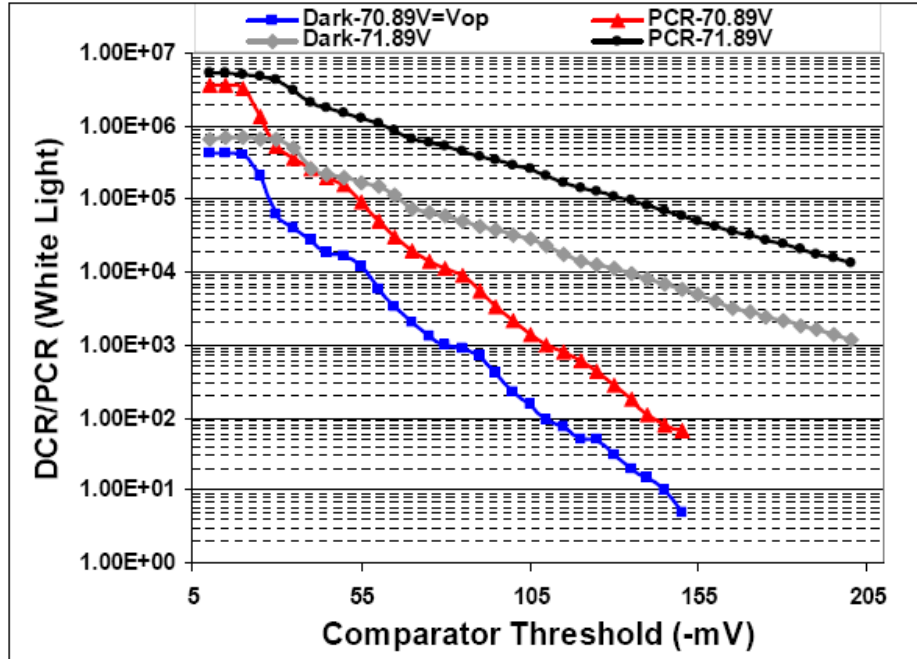


Figure 5.28 1600-pixel device: Variation of DCR and PCR with comparator threshold at $V_{Bias} = V_{OP}$ and $V_{OP}+1V$.

For 1600-pixel device, the ratio of drop in count rate from step1 to step 2 is also approximately constant for both DCR and PCR for same V_{Bias} (Figure 5.28). For this device, the same curves were also measured at higher bias voltages and it was observed that the rate of drop in count rate is different (smaller) at higher V_{Bias} . For example, from step1 to step2, the count rate decreased by ~ 20 times at $V_{Bias}=V_{OP}$ and only 3.5 times at $V_{Bias}=V_{OP}+1V$. Also, for $V_{Bias}>V_{OP}$, the behavior of the steps changed. It can be seen that the over-all count rate drops much more slowly as compared to when $V_{Bias}=V_{OP}$ curve and the number of visible steps almost decreases by half (Figure 5.28, Dark-70.89V= V_{OP} & Dark-71.89V). This means that the percentage of pulses due to 2p.e. increases significantly at $V_{Bias}=V_{OP}+1V$. Further, the number of distinctly visible steps almost decreased by half at $V_{Bias}=V_{OP}+1V$ (Figure 5.28, PCR-71.89V curve). Similar behavior

was observed with the cooled SiPM in the dark (Figure 5.13). *It was found that the behavior of these steps is related to the noise of the SiPM and is discussed in section 5.4.*

Sensitivity, Operating Point, Linearity and DR

Sensitivity measurements for this device were performed similar to the cooled SiPM and the results are shown in Figure 5.29 and Figure 5.30 for 100-pixel and 1600-pixel device respectively. The minimum bias voltage was selected to be V_{OP} and was increased in steps of 0.5V, until improvement in sensitivity levels were observed. The black line in each figure represents the most linear curve.

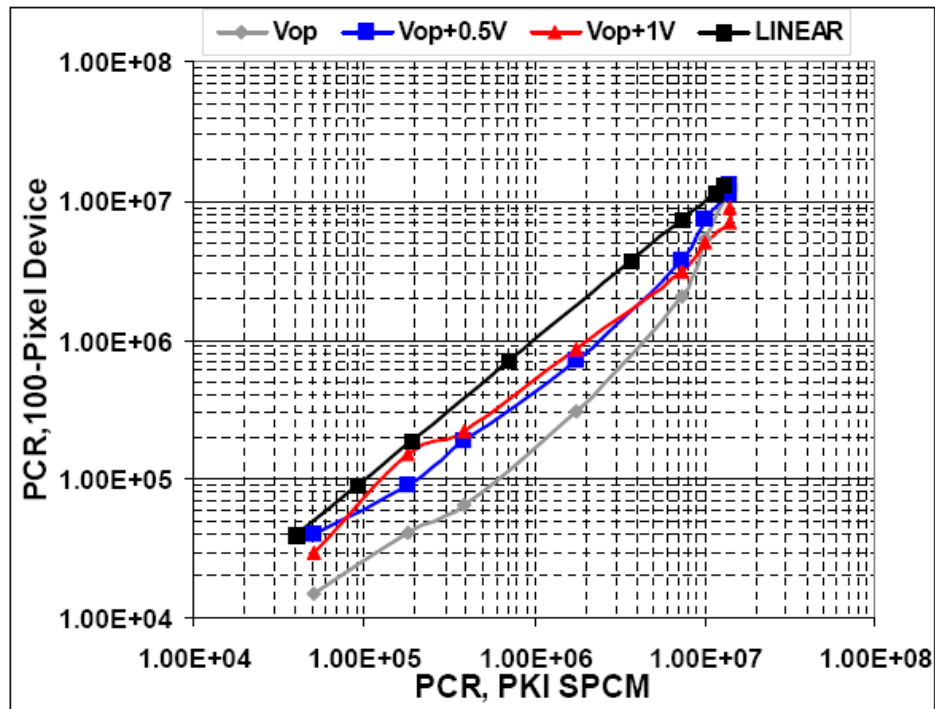


Figure 5.29 100-pixel device: Sensitivity, DR and linearity.

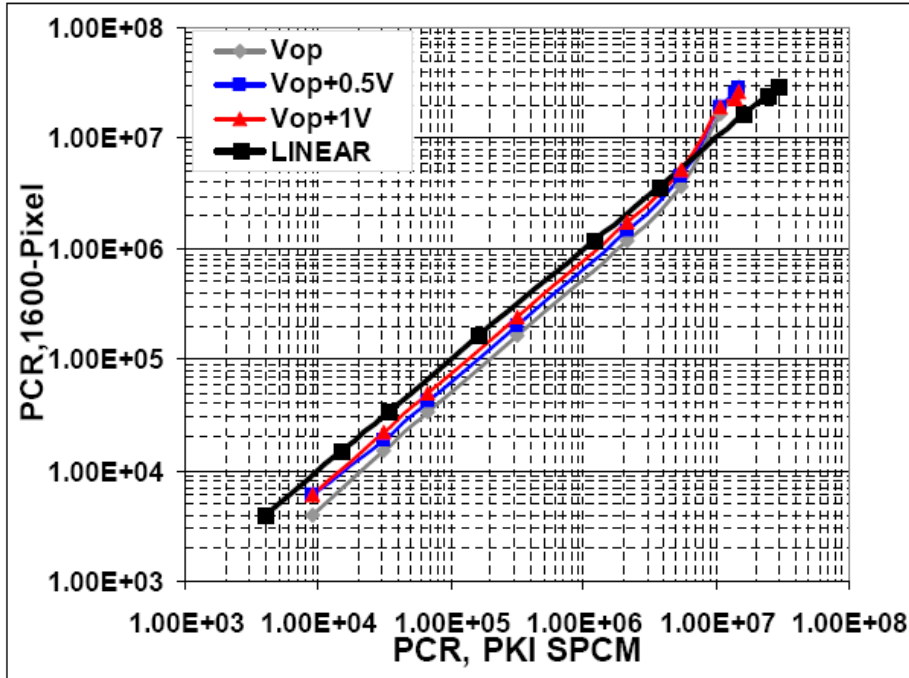


Figure 5.30 1600-pixel device: Sensitivity, DR and linearity.

Based on the obtained results, following conclusions can be made:

- PCR are sub-linear and much less sensitive at V_{OP} for both devices and become more and more linear and sensitive as the V_{Bias} is increased beyond V_{OP} .
- For 100-pixel device, good improvement can be seen at $V_{Bias} = V_{OP} + 0.5V$, but not much improvement is seen when V_{Bias} is increased further to $V_{OP} + 1V$ (Figure 5.29). The reason for this is that the DCR of this device increases much faster when V_{Bias} is increased from $V_{OP} + 0.5V$ to $V_{OP} + 1V$ (Figure 5.25 (top)).
- For the 1600-pixel device, similar level of improvement is observed for every 0.5V increase from V_{OP} to $V_{OP} + 1V$ (Figure 5.30) and it is also consistent with the linear increase in DCR curve from V_{OP} to $V_{OP} + 1V$ (Figure 5.25 (bottom)).

- For the best V_{OV} , the DR for 100-pixel device is ~ 14 MHz and ~ 28 MHz for the 1600-pixel device. This large difference is because the area of one pixel in the 100-pixel device is 16 times larger than the area of one pixel in the 1600-pixel device. Further, the measured DR for 100-pixel is much lower than the value estimated on the basis of output pulse widths (25-30 MHz) from Figure 5.24. This implies that the actual time it takes for the pixel to recover is longer than the output pulse width or since the DCR of this device is rather large at $V_{OP}+1V$ (5.4MHz), the output count rate saturates much faster.
- Figure 5.31 compares the 100-pixel and 1600-pixel device at best V_{OV} . It shows that the 1600-pixel device is more linear than the 100-pixel device. The reason for this should be the small dead-time because of much smaller size of the pixel.

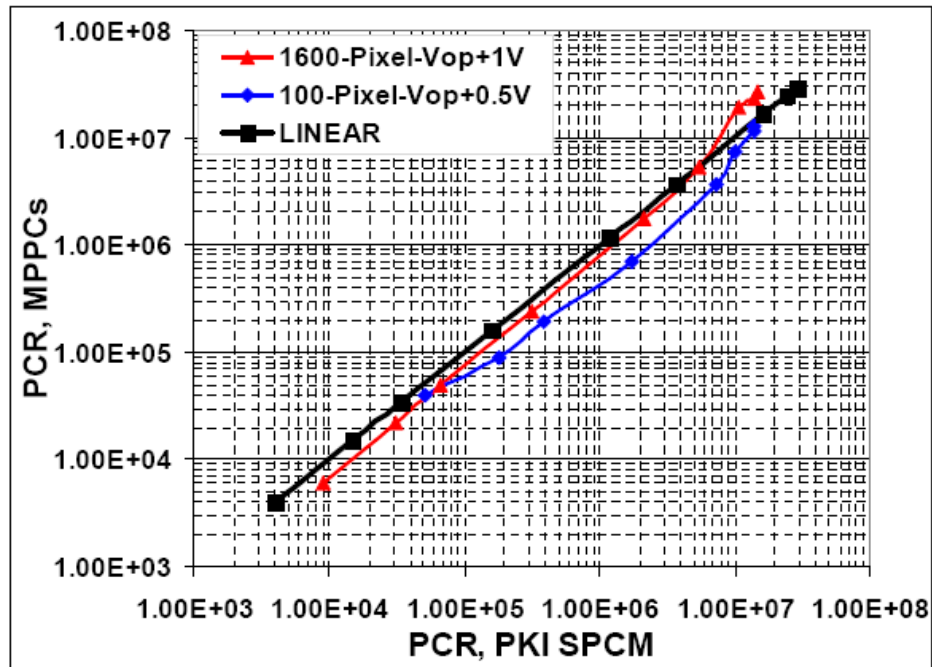


Figure 5.31 Comparison of sensitivity, DR and linearity for 100-pixel and 1600-pixel device.

As was the case with cooled SiPM and S-SPCM, above results show that highest sensitivity is achieved by operating a detector at highest feasible over-voltage and minimum feasible threshold. This was also confirmed using the SNR results described in next section. It is very important to note that although these devices are operated at room temperature and have much higher DCR as compared to the cooled SiPM, they are very sensitive since their PCR is comparable with that of PKI SPCM at much lower over-voltage. More importantly, even with such high DCR they are able to measure actual signal above the DCR. Further, the DR of 100-pixel device (14 MHz) is comparable with that of PKI SPCM, whereas DR of 1600-pixel device (28MHz) is ~ 2 times greater as that of PKI SPCM and two ~ 3 times greater than S-SPCM (10MHz). Next section analyzes the after-pulsing and cross-talk in all three SiPM from the point of view of their use as photon counter.

Signal to Noise Ratio

SNR for the 100-pixel and the 1600-pixel device was calculated using Equation 3.6 and the results are shown in Figure 5.32 and Figure 5.33 respectively. SNR was calculated using the calculated mean for DCR and PCR for different conditions from the results described in section 5.4. For the 100-pixel device, it can be seen that the SNR is the best for $V_{\text{Bias}} = 70.22\text{V}$ and does not improve when the bias is further increased. For 1600-pixel device, similar SNR improvement is seen for each 0.5V increase in V_{Bias} from $V_{\text{Bias}} = 70.89\text{V}$ (V_{OP}) to $V_{\text{Bias}} = 71.89\text{V}$ ($V_{\text{OP}}+1\text{V}$). These results are in very good agreement with the sensitivity results obtained for 100-pixel (Figure 5.29) and 1600-pixel

(Figure 5.30) device respectively, where similar trend was observed for increase in sensitivity.

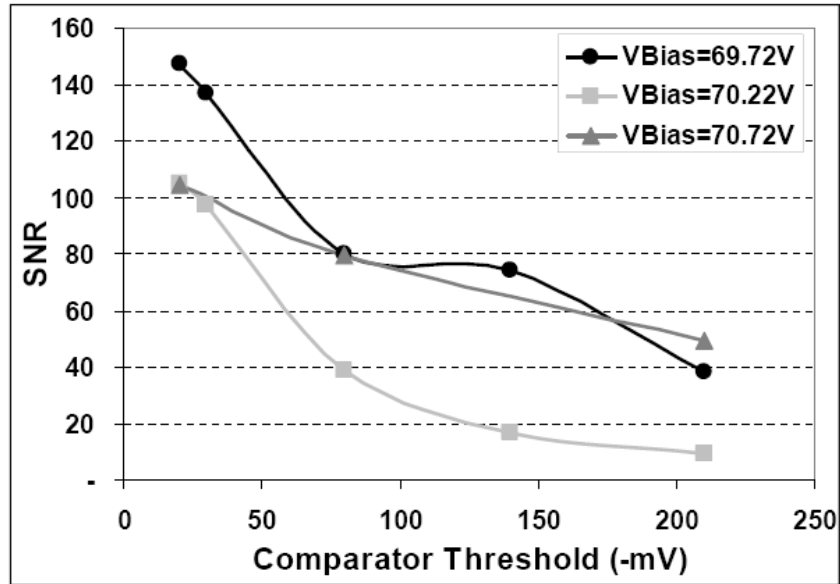


Figure 5.32 100-pixel device: Signal-to-Noise ratio.

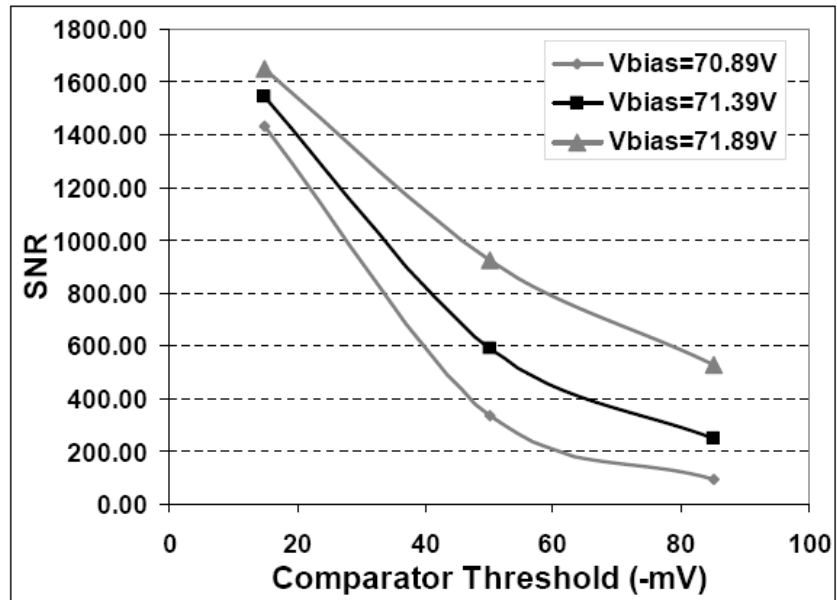


Figure 5.33 1600-pixel device: Signal-to-Noise ratio.

Further, for the 100-pixel device it can be seen that the SNR is better at 70.22V as compared to 70.72V; the reason for this is the small dynamic range (14MHz) and very high DCR of this device at these bias voltages. Basically, the DCR of this device is so high (5.4 MHz) at $V_{Bias}=70.72V$ that it occupies significant portion of the dynamic range (14 MHz) of this SiPM, therefore as soon as the light level is increased a little, the count rate already approaches saturation, thus limiting the SNR. This (very high DCR) was one of the prime reasons that SiPM were practically un-usable up to few years back. The DCR practically occupied whole DR making it impossible to detect any signal above noise, especially in photon counting applications. But it can be seen that these devices have progressed fast as the technology progressed and have become practically usable in photon counting applications.

5.4. After-pulsing and Cross-talk in SiPM (Noise Analysis)

This section studies the noise in SiPMs from the point of view of its application to photon counting. It was mentioned and discussed in section 5.2.4 (see variation of DCR with comparator threshold) that after-pulsing and cross-talk in SiPMs are referred to as noise in this thesis. Being analog in nature, SiPMs have only been used in photon number resolving applications where the incoming signals are rare and where a bunch of photons are expected to be received simultaneously. Some of these applications include PET scanning in nuclear medicine [29], scintillating fiber readout in high energy physics [29] and imaging atmospheric Cherenkov telescope (IACT) in Astroparticle Physics [30]. In these applications, the signals to be detected are very strong; hence the threshold (comparator threshold) of the read-out electronics is set above the noise level, thus eliminating most of the contribution of DCR and noise and still is able to detect the actual signal. Hence, although the effects of noise have been studied, they are not studied in great detail.

On the other hand, when SiPM is used as a photon counter, it cannot be biased at high V_{TH} ; hence effects of noise and DCR cannot be bypassed by setting high thresholds of read-out electronics¹. Further, SiPM is essentially used as a digital detector; hence the effects of after-pulsing and cross-talk will be different since pulses of all amplitudes (1p.e, 2p.e, 3p.e, etc.) are registered as one pulse.

¹ In photon number resolving applications, the expected incoming signal is very strong, i.e. a bunch (few tens-few thousands) of photons are expected to be received simultaneously. Therefore the comparator threshold of the readout electronics is usually set very high, thus high DCR, afterpulsing and cross-talk effects are usually bypassed.

Noise in a photon counting system is determined by the distribution of photo counts. A correctly operating photon counting system follows a Poisson distribution where the variance of the photo counts (the number of photons counted over the given time interval) is equal to its mean value. In this case, match between the measured photon count distribution and the Poisson distribution determines the quality of the counting circuit. In order to characterize the noise, output counts from all the three SiPMs were recorded for approximately 10mins with an integration time of 10ms. For each SiPM, counts were recorded at 2-4 different over-voltages and for each over-voltage; counts were recorded at 2-4 different comparator thresholds. These threshold values were set somewhere near the center of each plateau (steps) observed in Figure 5.13 (cooled SiPM), Figure 5.27 (100-pixel device) and Figure 5.28 (1600-pixel device). It was thought that in the centre of the step (plateau), the SiPM counts all the pulses due to 1p.e, 2p.e etc depending on the step the threshold is set at, and hence it was selected as the measurement point. The Stanford counter was used for measurement and it was controlled using Lab View through GPIB interface. The counts were recorded onto a text file and then processed in excel. Histograms of all the recordings for all the devices were plotted. Figure 5.34 shows the plot of one such recorded points and Figure 5.35 shows the obtained histogram. Similar processing was done and plotted for all the SiPMs. Finally, the mean and variance of the recorded counts were calculated and plotted and are discussed below for each SiPM.

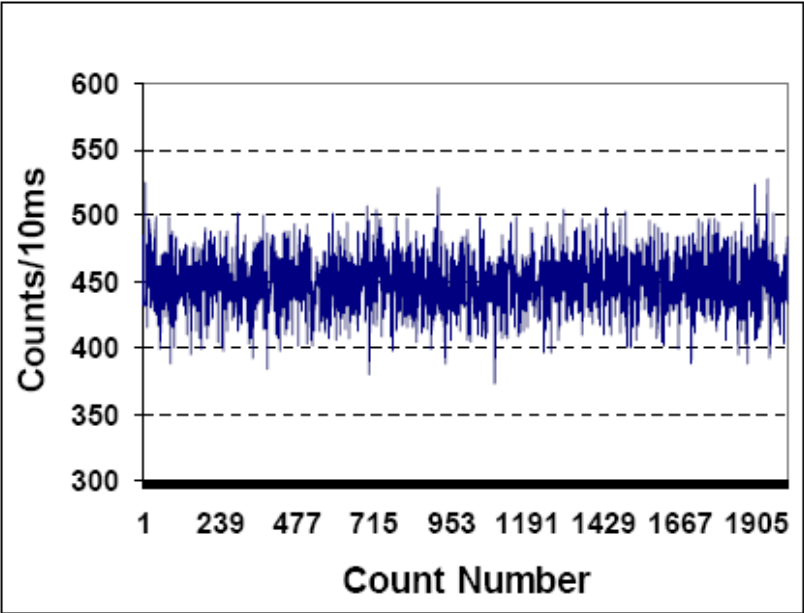


Figure 5.34 Recording of counts for noise analysis (integration time is 10ms).

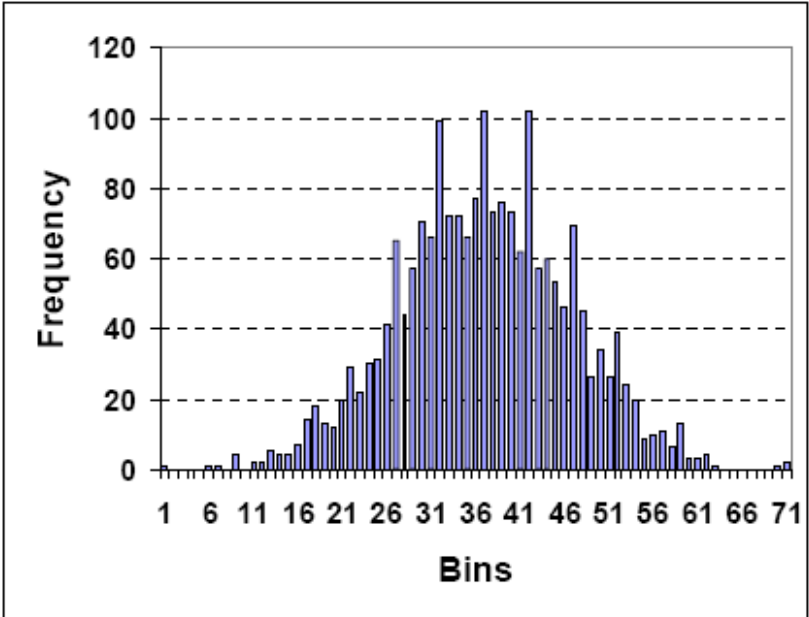


Figure 5.35 Histogram of the recorded counts shown in Figure 5.32.

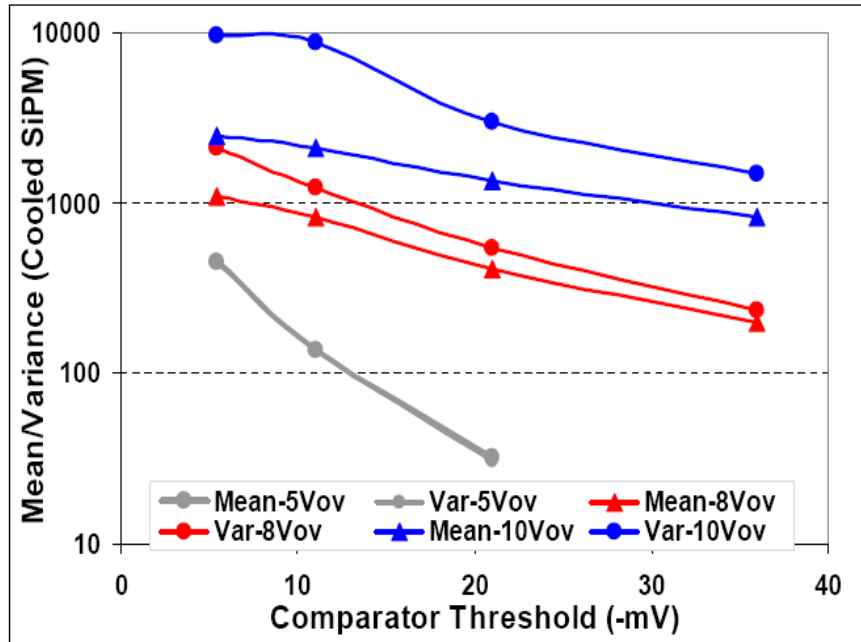


Figure 5.36 Cooled SiPM: Variation of mean and variance with V_{OV} and V_{TH} .

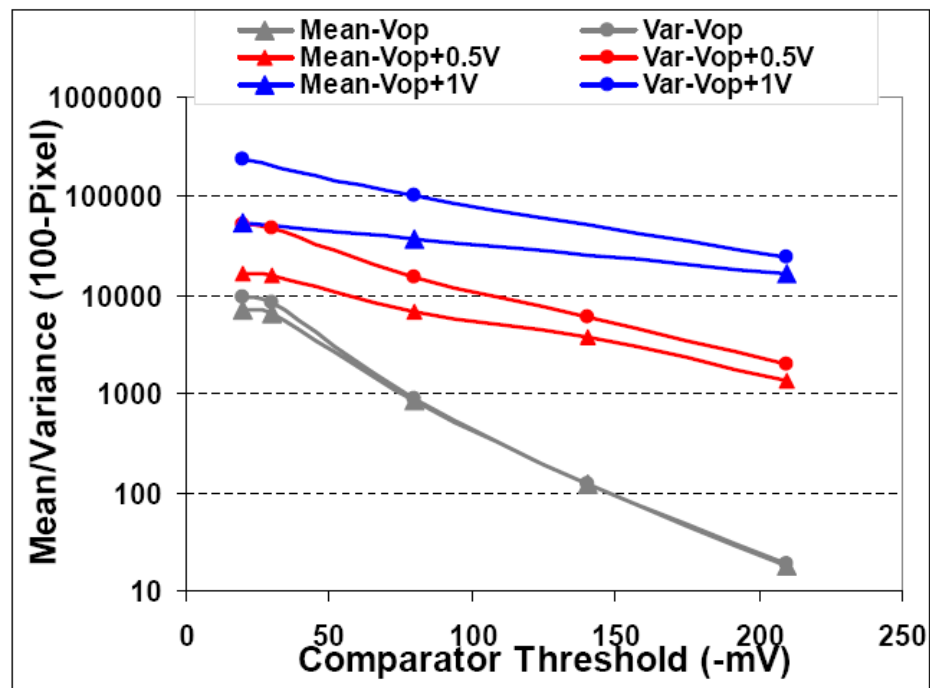


Figure 5.37 100-pixel device: Variation of Mean and Variance with V_{OV} and V_{TH} .

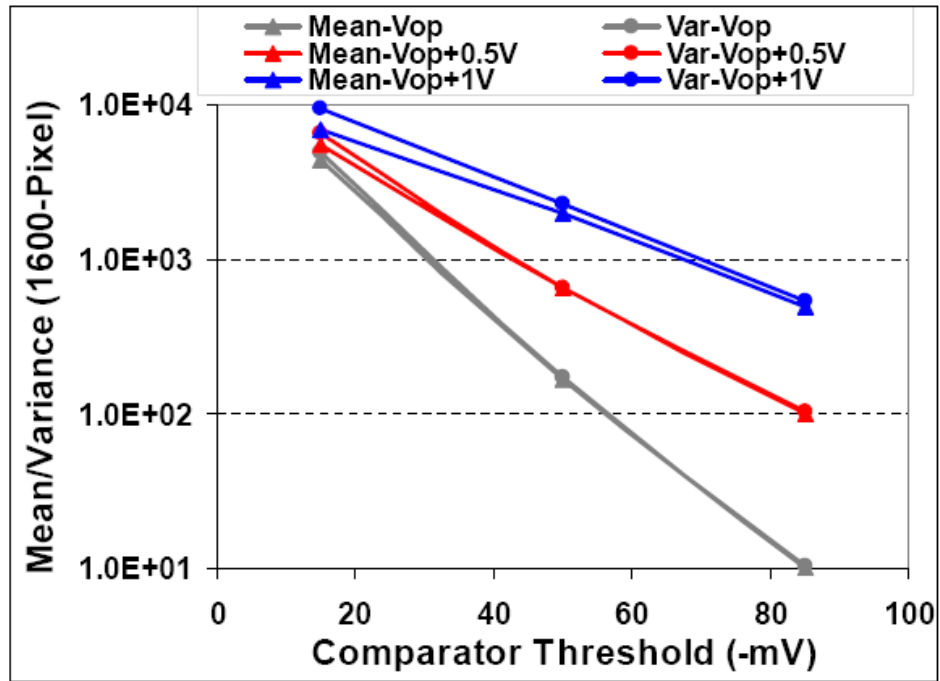


Figure 5.38 1600-pixel device: Variation of Mean and Variance with V_{OV} and V_{TH} .

Figure 5.36, Figure 5.37 and Figure 5.38 show variation of mean and variance of the registered dark counts at the output of cooled SiPM, 100-pixel device and 1600-pixel device respectively. Following observations and conclusions are made based on the obtained results:

- For all three SiPMs, it was observed that the mean and variance converge with increasing comparator threshold and decreasing over-voltage and they become equal for some optimum combinations of V_{OV} and V_{TH} . This implies that under certain conditions SiPM follows a poisson distribution and hence acts as a noiseless photon counter.

- For all the three SiPMs, it was observed that the difference between mean and variance is much higher when V_{TH} is below 1p.e. and decreases much more at $V_{TH} > 1p.e$ as compared to the drop from 2p.e to 3p.e and so on. This implies that the contribution of noise is maximum when $V_{TH} < 1p.e$ and this is expected. Further, this also suggests that after-pulsing contributes very high percentage of 1p.e pulses as compared to pulses greater than 2p.e.
- From Figure 5.36 it can be seen that mean and variance of cooled SiPM at $5V_{OV}$ is the same for all thresholds suggesting that it follows Poisson distribution. This implies that there is no after-pulsing and cross-talk in the cooled SiPM at $5V_{OV}$. Further it is known and discussed in section 5.2.4 (see variation of DCR with V_{TH} section) that the number of steps basically represents the number of simultaneous pulses that a SiPM is able to resolve. For cooled SiPM, 3 steps were observed at $5V_{OV}$ (see $V_{BR}+5$ curve in Figure 5.13) suggesting that the SiPM registered up to 3p.e pulses in dark. Since, due to the nature of generation of after-pulsing 2 or more counts are registered for one photon and hence it would definitely affect the Poisson distribution (Variance > Mean). *But the fact that 3 pulses were observed by the SiPM at $5V_{OV}$ (Figure 5.13) and Poisson distribution is observed for all thresholds at the same V_{OV} suggests that these steps are only due to cross-talk and more importantly it implies that cross-talk does not affect Poisson distribution and hence does not contribute additional noise when SiPM is used as a photon counter. Further this result implies that there is a relation between the step-like behavior of SiPM and its noise.* The same behavior was observed in all three SiPMs; see Figure 5.37 (noise) and Figure 5.26 (DCR steps) for 100-pixel device

and Figure 5.38 (noise) and Figure 5.26 or Figure 5.28 for 1600-pixel device. *From these results a very important conclusion can be made, i.e. cross-talk does not affect the Poisson distribution when used as a photon counter i.e. cross-talk does not add any additional noise in photon counting mode.*

- The mean and variance of 1600-pixel device (Figure 5.38) is same for most of the conditions, suggesting that it has much less noise as compared to the 100-pixel device (Figure 5.37). This is confirmed by the fact that in 1600-pixel significant drop in DCR was observed when V_{TH} was increased from less than 1p.e to greater than 1p.e (Figure 5.26).
- The relation between number of steps and cross-talk is also confirmed by the fact that 1600-pixel device has almost half the number of steps (2-3) as compared to the 100-pixel device (5) (see Figure 5.26). Further, according to the data sheet [6], the fill-factor of the 1600-pixel device (30.8%) is significantly smaller (>50%) as compared to the 100-pixel device (78.5%), therefore it is expected that the 1600-pixel device will have much smaller cross-talk. This further confirms the assumption. Based on aforementioned discussion, it can be speculated that the cross-talk happens only due to optical photons and is explained in section 5.4.1
- The nature and shape of the steps is same in the dark and light (see Figure 5.27 and 5.28), suggesting that the physical phenomena responsible for avalanche generation is the same in the dark and light and that the percentage of noise contribution is also the same in both conditions. Hence same, noise performance can be expected from the SiPMs in the light. Similar recordings as DCR were

made for the 100-pixel and the 1600-pixel device in light and the recorded values are summarized in Figure 5.39 and Figure 5.40 respectively.

Vbias=69.72V										
Vth(-mV)	20	20	30	30	80	80	140	140	210	210
	Dark	Light	Dark	Light	Dark	Light	Dark	Light	Dark	Light
Mean	6983	8843	6437	8100	845	1084	122	162	18	27
VARIANCE	9674	14215	8198	10490	897	1217	123	166	18	28
Var/Mean	1.39	1.61	1.27	1.30	1.06	1.12	1.01	1.03	1.01	1.04
Vbias = 70.22V										
Mean	16761	20790	15891	19522	6777	8161	3699	4654	1352	1651
VARIANCE	52627	60628	46519	54328	14829	17376	6064	7233	1951	2252
Var/Mean	3.14	2.92	2.93	2.78	2.19	2.13	1.64	1.55	1.44	1.36
Vbias = 70.72V										
Mean	53511	58458			37115	40247			16236	17523
VARIANCE	241379	200767			103195	86163			24315	21778
Var/Mean	4.51	3.43			2.78	2.14			1.50	1.24

Figure 5.39 Mean and variance of 100-pixel device in dark and light.

Vbias=70.89V						
Vth(-mV)	15	15	50	50	85	85
	Dark	Light	Dark	Light	Dark	Light
Mean	4329.99	43638.04	166.73	2184.19	10.07	158.84
VARIANCE	4968.14	45300.62	171.43	2334.28	10.39	171.57
Var/Mean	1.15	1.04	1.03	1.07	1.03	1.08
Vbias=71.39V						
Mean	5528.51	52524.2	651.52	7142.1	98.73	1221.22
VARIANCE	6507.27	55412.6	659.29	7612.7	103.60	1264.5
Var/Mean	1.18	1.05	1.01	1.07	1.05	1.04
Vbias=71.89V						
Mean	6980.09	61874.8	1993.73	18817	496.97	5612.29
VARIANCE	9495.75	64607.3	2281.27	19010	533.72	5646.96
Var/Mean	1.36	1.04	1.14	1.01	1.07	1.01

Figure 5.40 Mean and variance of 1600-pixel device in dark and light.

5.4.1 Cross-talk Mechanism and its Effect on Photon Counting Performance of SiPM

From the results and discussion in the previous sections (section 5.2.4 and 5.4) it was established that cross-talk does not affect photon counting performance of SiPM. It was also mentioned that cross-talk affects photon-number resolving and photon counting performance of SiPM in different ways since in photon counting applications 1p.e, 2p.e, 3p.e.etc pulses are just counted as one pulse. The results suggest that cross-talk in these SiPMs mainly happens due to optical photons. Reverse biased silicon diodes emit photons at the rate of $\sim 10^{-5}$ photons per electron crossing the p-n junction when they are operated in geiger mode [52]. These photons may or may not initiate an avalanche in the neighboring pixels depending on where they are absorbed as shown in Figure 5.41. Since the travel time of these photons is much faster (speed of light) than the dead time (pulse width) of the already fired pixel, even if they initiate a discharge, this discharge probably takes place in the same time frame as the original fired pixel (pulse width 20-30ns). As a result, the fired pixel (due to cross-talk) will generate a pulse slightly shifted in time, but the time is so small that charge generated by both the pulses is summed up in the same cycle, thus generating an output pulse with output charge (amplitude) equal to the sum of all the fired pixels. The amplitude of the output pulse is proportional to the number of fired pixel, but, since the V_{TH} of SiPM is fixed and is $<1p.e$, it registers this pulse as just one pulse, i.e. effectively only one pulse is registered for one originally fired pixel as well as other pixels that fired due to cross-talk, thus no additional counts (noise) are generated due to cross-talk. Hence Poisson distribution is not affected by the cross-talk. But, in

photon number resolving applications, cross-talk will affect the dynamic range of the SiPM, since dynamic range in this case is equal to the number of pixels of the SiPM.

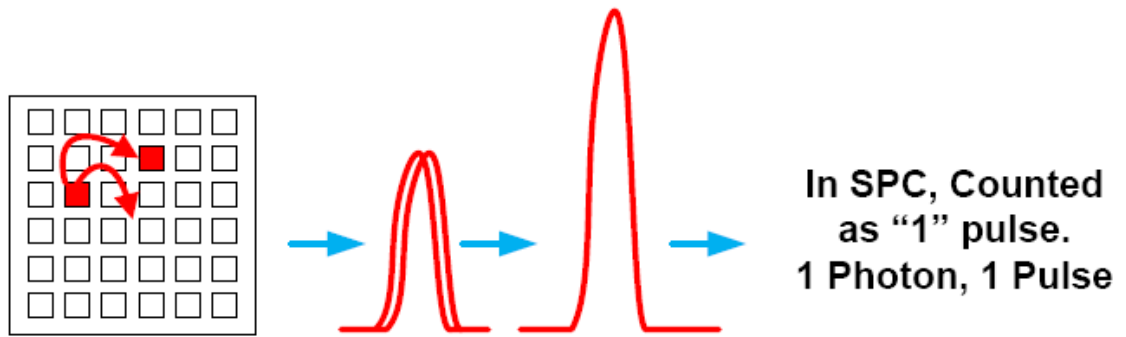


Figure 5.41 Effect of cross-talk on photon counting performance of SiPM.

5.5 Summary

So far, SiPMs were used only as photon-number resolving devices and in very limited applications due to their rather high dark count. Up to few years back, DCR of SiPM made them practically unusable in many applications, especially photon counting applications. DCR of SiPM practically occupied the complete dynamic range of the SiPM making it practically impossible to detect any photons above the DCR. SiPM is based on CMOS technology and technology and use of pure silicon is considered to be the main reason behind the high DCRs. As the technology progressed, these devices also progressed and a significant improvement in DCR of SiPMs has been achieved. This led to the recent commercialization of the SiPMs and devices with relatively low DCRs at room temperature became commercially available [6]. This chapter presented the need for investigating SiPMs as detectors for high-speed photon counting applications as opposed to photon number resolving applications and characterized the photon-counting performance of three different SiPMs from two different manufacturers. Conditions for using SiPM as high-speed photon counter were studied and are summarized in Table 5.5. The results show that these devices have single photon sensitivity and can match the performance of best commercially available large-area SPCM.

Table 5.5 Comparison and summary of important performance parameters of all the three characterized SiPMs.

Parameter	Cooled SiPM	100-Pixel Device	1600-Pixel Device	Units
Min amplification required (Gain)	20	40	40	Av
V_{TH} on Photon Counter (-mV) ^{*1}	- 4 to 6	-20	-15	mV
Optimum operating voltage for highest sensitivity ^{*2}	$V_{BR}+10$	$V_{OP}+0.5$	$V_{OP}+1$	volts
DCR for above conditions	200	1870	737	KHz
Dynamic Range (DR)	~30	~14	~28	MHz
Minimum Detectable Signal (MDS)for above conditions ^{*3}	450	1367	858	Photons/sec
Max SNR for above conditions	6000	279	2200	

*1: This value is usually around 0.5 p.e. since it is important to count all the photons.

*2: Optimum operating voltage may vary for different devices if the gain of the devices of same type varies a lot.

*3: MDS of SPCM module is 22 photons/sec.

It was also shown that the SiPM needs to be operated at highest feasible over-voltage and lowest possible comparator threshold for counting all the pulses and achieving maximum sensitivity. Although increasing over-voltage has the effect of increasing DCR, it was shown that the over-all SNR is increased much more than the DCR. SiPMs reported in literatures so far can be broadly categorized into two categories viz. the SiPM from Hamamatsu (MPPC) and all the other reported SiPMs. The Hamamatsu SiPMs have significantly lower DCR even at room temperature whereas the other SiPMs have much higher DCR. This thesis investigated both types of SiPMs and it

showed that if the SiPM with high DCR (cooled SiPM in this thesis) is cooled to lower temperature, it can count photons with high sensitivity.

Further these results also show that SiPMs can definitely be used as detectors for sequencing the DNA and potentially other applications, for e.g. spectroscopy. Current SiPMs have a minimum active area of 1mm^2 which is not needed for many photon counting applications. Hence, even if the area of SiPM is reduced by half, DCR of SiPM will significantly reduce, facilitating their use in many more applications. Noise of SiPMs was characterized in detail and it was found that cross-talk in SiPMs does not add noise when used as a photon counter. This is a very important result, since a lot of efforts are directed towards optimizing the SiPM structures to minimize the cross-talk. Non-availability of large area SPADs and large area SPAD-arrays is a known problem, but this research shows that SiPMs have the potential to replace large area SPADs as high-speed photon counters without the need for quenching circuits. Since SiPMs are based on standard CMOS technologies, it makes them much more attractive for design and development of integrated arrays at very low cost.

SiPM based photon counting set-ups were integrated into our single lane DNA-sequencing set-up and excellent DNA-sequencing results were obtained. The results are discussed in next chapter.

CHAPTER 6

DNA SEQUENCING WITH SOLID-STATE SINGLE PHOTON DETECTORS

This chapter presents and the results of DNA-sequencing performed with four different detectors that were characterized in this thesis viz. the SPAD model C30902S-DTC, cooled SiPM from Voxel-Inc (MAPD), 100-pixel device and 1600-pixel device, both from Hamamatsu Photonics.

6.1 Experimental Set-up

Single-lane DNA-sequencing machine described in section 1.1 and shown in Figure 1.1 was used for these experiments. Detailed description of this DNA-sequencer can be found in [7]. Figure 6.1 shows the block-diagram of the DNA-sequencing experiment whose operation is similar to Figure 1.1B explained in section 1.1. The cooled SiPM was not fiberized during the electrical characterization (Figure 5.5) and hence it was fiberized for performing DNA-sequencing whereas all the other detectors were already fiberized.

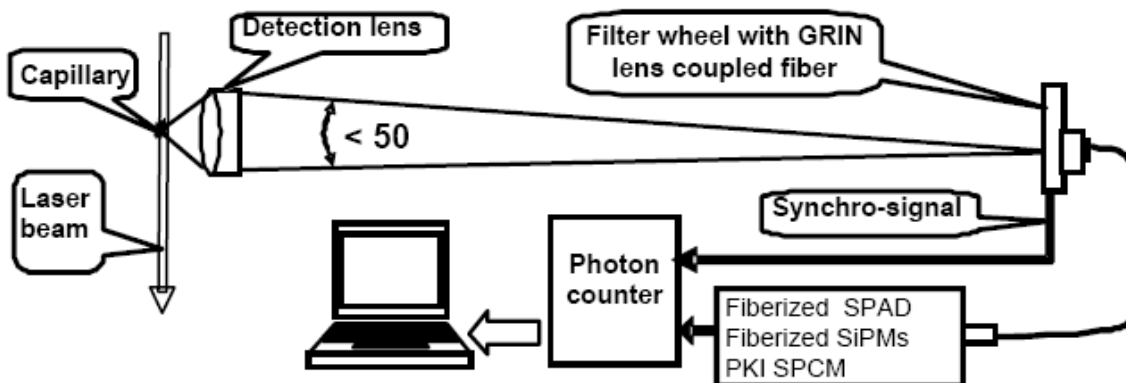


Figure 6.1 Typical set-up for DNA-sequencing experiment.

6.2 Integration of Detector Modules into Single-lane DNA-sequencer

In order to perform DNA-sequencing, it is necessary to use the counter circuit designed in our lab, since this counter circuit board has a parallel port connection to transfer the data on to a PC that consists of software that can access, record and process this data. Either the histogram of the output counts or the real-time DNA-sequencing traces can be viewed on the computer using the designed software.

Single Channel Photon Counting Module (S-SPCM)

Since the output pulses from the S-SPCM are compatible with the counter circuit, the output from the S-SPCM could be directly connected to the counter input, thus making the integration an easy task. The sequencing traces can be viewed in real-time

through our base calling software. Since the S-SPCM is already fiberized, focusing of light was not a problem at all. The M-SPCMs are also integrated in the same way, except that they are connected to a 16 or 32-channel amplifier and counter circuit respectively.

SiPMs

As mentioned earlier, to perform DNA-sequencing it is necessary to connect the output from the photon counting circuit to the specially designed high-speed counter that is connected to computer and the designed software. The negative going output pulses from the SiPMs (Figure 5.8 and 5.25) were not compatible with the counter circuit designed in our lab, hence, like S-SPCM the output from SiPMs could not be passed directly to the counter. We have a 32-channel amplifier whose output is connected to a 32-channel counter that also can be connected to the computer via the parallel port. Further, the counter circuit is synchronized with the filter wheel that determines the integration time. Hence this circuit board was utilized. Since, we wanted to perform single-lane sequencing, only one channel out of the 32-channels was utilized; Figure 6.2 shows the photo of the set-up. In order to make the output signal from the Ortec amplifier (output of SiPM is connected to Ortec amplifier VT120C as shown in Figure 5.5 and 5.22) compatible with the input of the 32-channel amplifier, it was passed through a variable signal attenuator. Different attenuation was required for different SiPM and is discussed later. Figure 6.3 shows the output pulse from the 32-channel amplifier that was passed on to the counter for further processing. Figure 6.4 shows the block diagram and Figure 6.5 shows the photo of the complete experimental set-up that was used to perform DNA-sequencing with SiPMs.

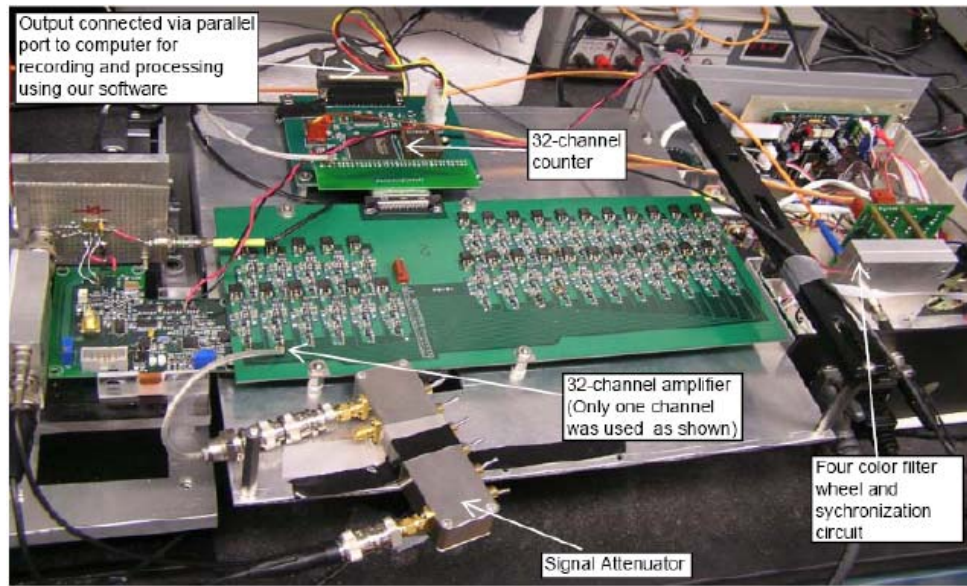


Figure 6.2 Electrical set-up for performing DNA sequencing with SiPMs.

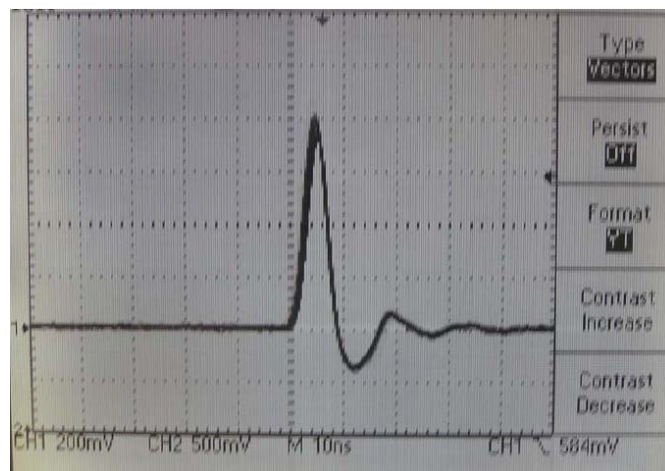


Figure 6.3 Output pulse from the 32-channel amplifier circuit.

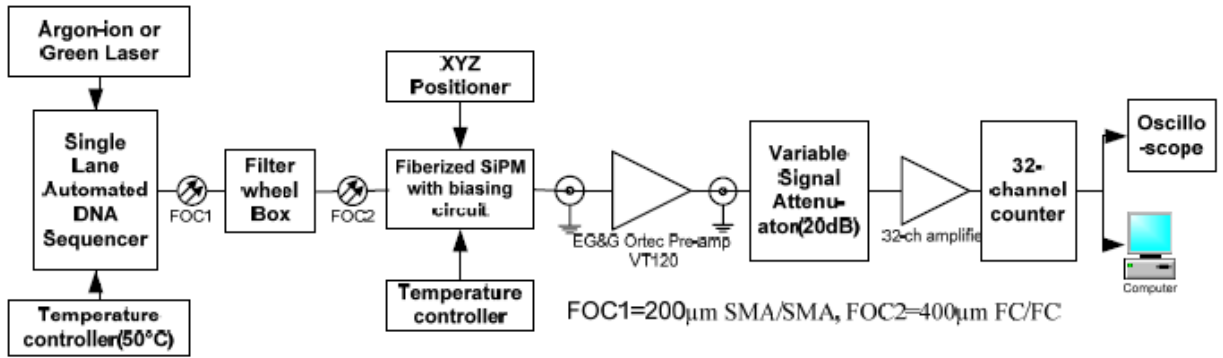


Figure 6.4 Block diagram of the complete DNA-sequencing set-up used for SiPMs.

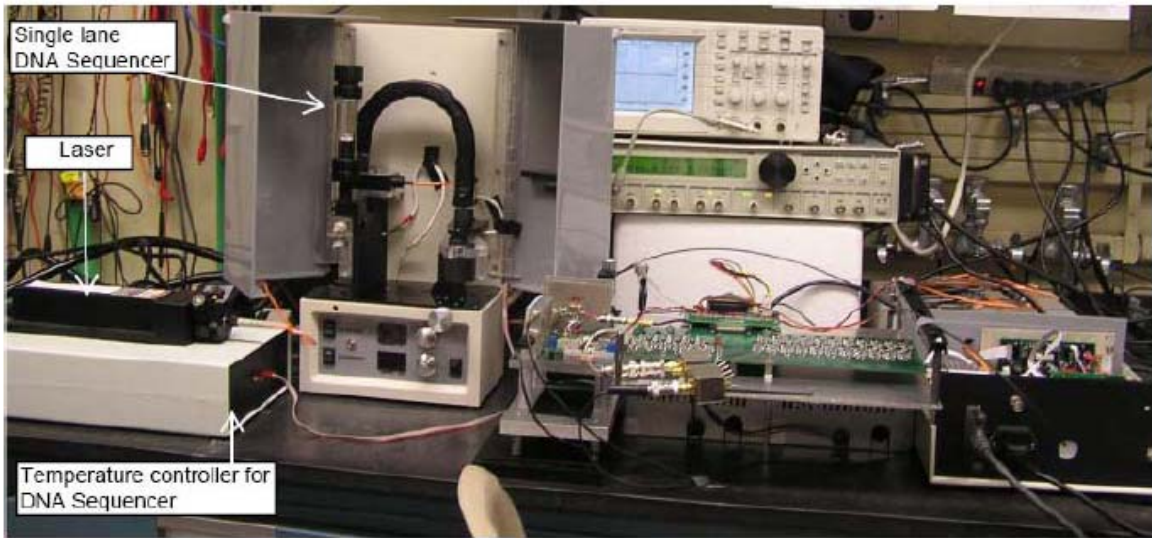


Figure 6.5 Photo of the complete DNA-sequencing set-up used for SiPMs.

6.4 Sequencing Results

6.4.1 Sequencing with individual detectors (S-SPCM and SiPMs)

Sequencing reagents and conditions

Industry standard DNA sample described here was used for all experiments: 100-bp Fluorescein Ruler (100-1000bp range in 100bp increments, Bio-Rad, CA, USA), Internal Lane Standard 600 (ILS-600, 60-600bp range in variable 20-25-50bp increments, Promega, WI, USA) and four-color sequencing standard labeled with BigDye (BigDye Terminator v1.1 Sequencing Standard Kit, ABI, CA, USA). To prepare 100-bp Fluorescein Ruler for loading, 18 μ l Hi-Di Formamide (ABI, CA, USA) were added to 2 μ l sample, denatured at 95°C for 3min and then chilled on ice. ILS-600 and Big Dye Sequencing Standard were prepared according to the corresponding manufacturers' protocols. In some experiments ILS-600 and 100bp ruler were combined together to form a “mixed” ladder. All samples were electro-kinetically injected into uncoated fused silica capillaries (56cm total length, 50cm detection length L_{DET} , 50 μ m ID, 365 μ m OD from PolyMicro Tech., AZ, USA) filled with POP-7 separation polymer (ABI, CA). Buffer vessels were filled with ABI 310 running buffer with EDTA. The sequencing runs were carried out at running voltage of 6.8-11.2kV (120-200 V/cm) at 50°C.

Sequencing traces and quality factors

DNA-sequencing traces for three types of detector viz. SPAD, cooled SiPM and MPPC are shown in Figure 6.6, Figure 6.7 and Figure 6.8 respectively. Figure 6.9 shows

the quality factor curves of all the four detectors. A green laser (NdYAG laser) was used for all the experiments. It must be noted that quality of DNA-sequencing depends on a lot of factors such as quality of the separation medium quality of the polymer etc. The primary goal of this research was to investigate if these detectors are feasible for performing DNA-sequencing at all. Further, DNA-sequencing with each detector was performed at different times under different conditions; hence DNA-sequencing performance such as QF cannot be accurately compared on the basis of these results. Although, similar results were obtained with all the detectors (SPAD and SiPMs) and these results are comparable to the standard QF results obtained with this dye which proves that all the detectors are suitable for DNA-sequencing application.



Figure 6.6 S-SPCM (C30902S-DTC): DNA-Sequencing traces (Laser power = 18mW).

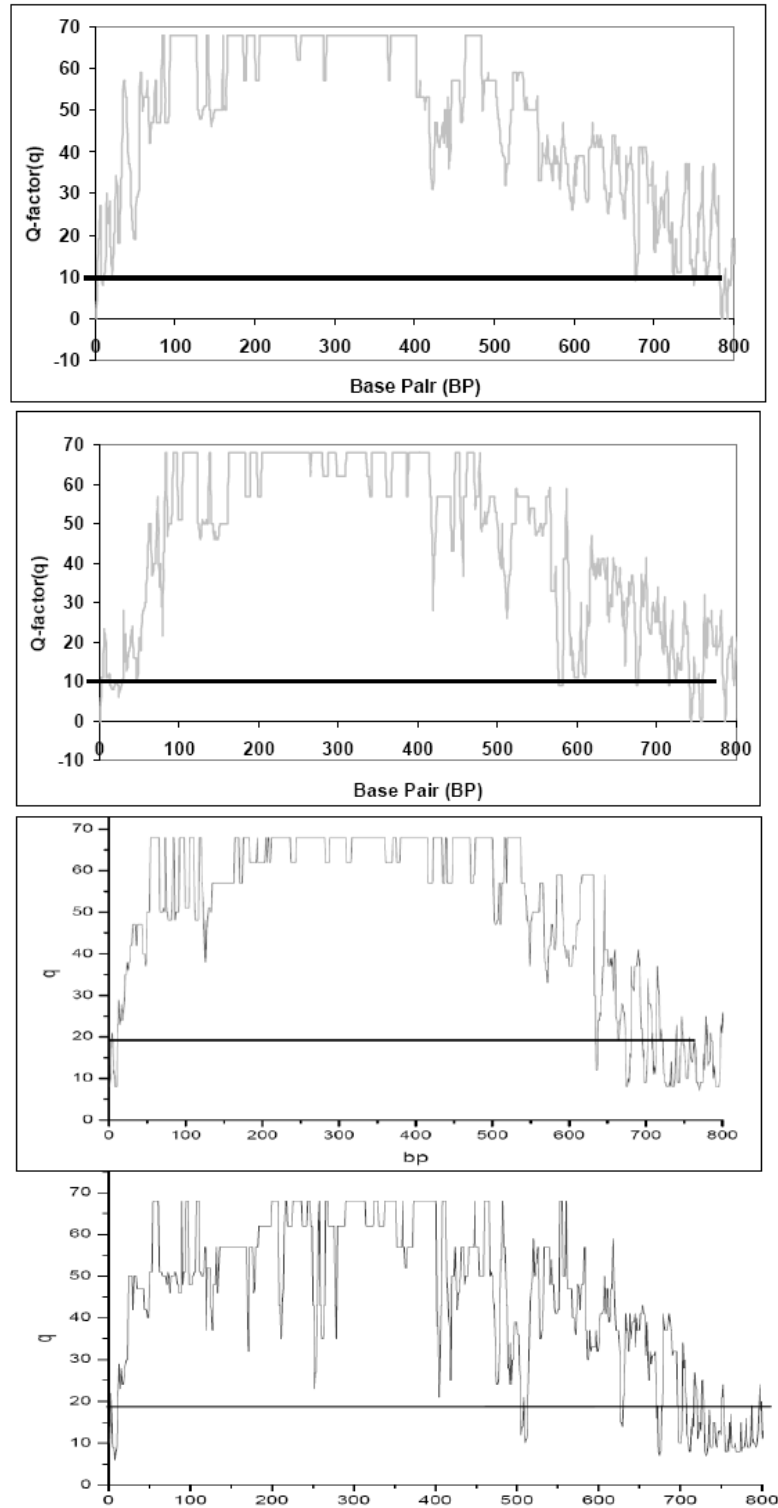


Figure 6.9 Quality factor curves for all four SiPMs obtained using universal Phred software; (a) S-SPCM (SPAD), (b) 100-pixel SiPM, (c) 400-pixel SiPM, (d) 1600-pixel SiPM.

Following conclusions are made based on the obtained DNA-sequencing results:

- Obtained Q-20 read lengths obtained with all the devices are comparable with the results obtained with commercial DNA-machines for the same DNA-sample.
- Dynamic range and linearity of the designed S-SPCM and all the three SiPMs is sufficient for this application.
- Due to the much smaller DCR of the SPAD (500 Hz) and the Cooled SiPM (200 KHz) as compared to the 100-pixel device (1.87 MHz) and 1600-pixel device (600 KHz) at the optimum operating point, the cooled SPAD and Cooled SiPM are able to resolve the smaller peaks much better (better read length) than the 100-pixel and 1600-pixel device. This basically means that the cooling the detector (lowering DCR) improves the SNR of the sequence detection.
- Read length largely depends on the quality of the polymer. If the quality of the polymer is not good, the resolution of the peak degrades i.e. they become wider. In case of cooled SiPM, we can see that the peak heights are still good near the 570 bp, but the peak resolution degrades, which means that the quality of the polymer was not as good as other detectors and hence the resolved base pair number is smaller.
- These results prove that noise in SiPMs does not affect the quality of sequencing. It was shown that cross-talk does not add additional counts, but due to the nature of after-pulsing it cannot be avoided and the noise results show that SiPMs do have after-pulsing. In simple terms, afterpulsing basically generates extra count for one photon and distorts the one-to-one ration between the received and registered photons. For example, let's assume that for each detected photon, on an

average 1.1 or 1.2 counts are registered. In this case if the DNA-sequencer generates on an average 1 million counts/s, instead of 1 million counts/sec, 1.2 million counts/s will be registered. If similar increase in counts is registered for all the wavelengths, it can be thought that the extra counts provide added gain to the sequencer, thus enhancing the sequencing performance.

- To achieve the best sensitivity and linearity results, detectors must be biased at the highest over-voltage and lowest comparable threshold. Although the DCR increases, but the effective SNR increases even more.

6.4.2 Multi-lane DNA-sequencing

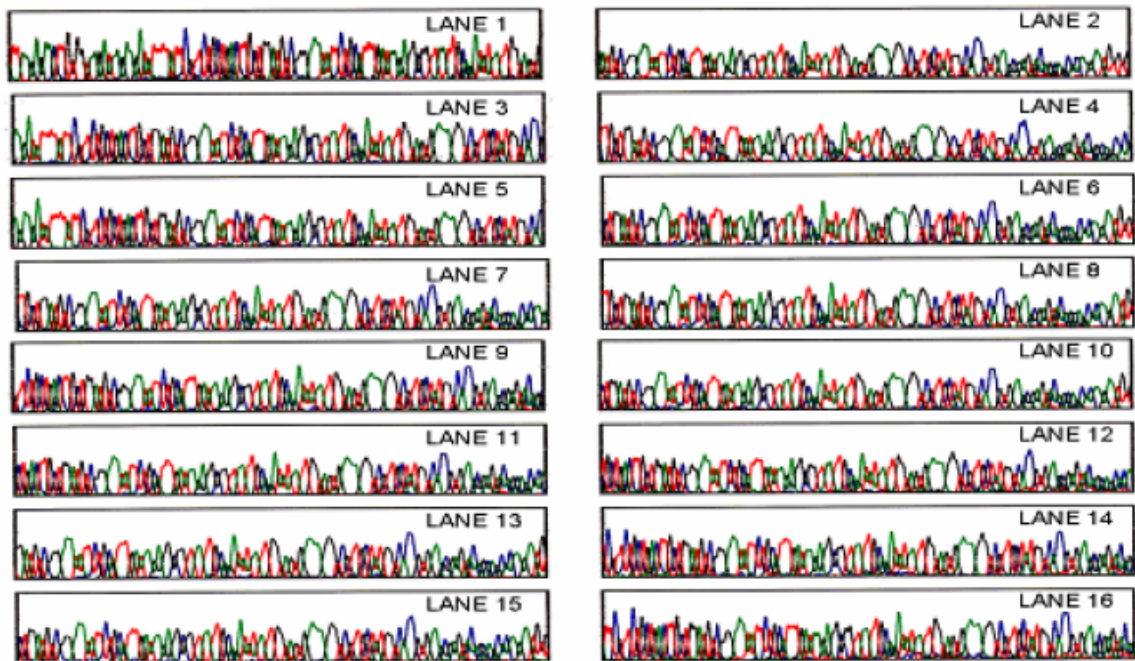


Figure 6.10 Fragment of the sequencing trace between 600 and 700 bases obtained with the 16-channel photon counting module. BigDye™ Sequencing Standard (ABI, CA, USA) diluted to 1: 64 in formamide.

The sequence detection sensitivity obtained with the 16-channel single photon counting module was more than 4 times higher than the sensitivity of the best commercial DNA sequencer ABI-3730.

6.5 Summary

The primary goal of this research was to investigate the feasibility of solid-state detectors for DNA-sequencing applications. The results of this chapter showed that all the characterized detectors (SPAD and SiPMs) can be used as highly sensitive detectors for DNA-sequencing. Hence, these results provide, *for the first time, experimental demonstration of the application of large-area SPAD and SiPMs to DNA-sequencing, and opening up a new field of application for SiPMs.* Until recently, there was limited choice of available detectors for DNA-sequencing (PMT and CCD), but this research opens up many more choices. Approximately 10-fold improvement in sensitivity was obtained as compared to PMT based systems. Since the cost of consumables is the highest in DNA-sequencing, the sensitivity improvement of photon detection systems will facilitate the use of much lesser sequencing reagents (more resolved base pairs for same amount of DNA-sample). Further more diluted DNA-samples can be used and still be able to resolve same base-pairs. Both, less re-agents and use of diluted sample will provide significant cost reduction.

Out of the four detectors that were used to perform DNA-sequencing two were cooled detectors (SPAD from PKI and cooled SiPM from Voxel-Inc) and two were uncooled (100-pixel and 1600-pixel device from Hamamatsu). As expected, better results were obtained with the cooled devices due to much lower DCR and hence better SNR and the ability to detect smaller peaks towards the end of sequencing. The fact that it is possible to perform DNA-sequencing at room temperature with relatively low-cost devices and obtain comparable results implies that the cost of photon detection systems can be significantly reduced. This will enable the design of low-cost DNA-sequencers that will be affordable by the university labs. Further, unavailability of arrays of large-area SPADs is a known problem. Since, SiPM is based on standard fabrication technology; arrays of SiPMs can be easily designed and fabricated, thus providing an excellent solution to unavailability of large area SPAD arrays for DNA-sequencing and some other applications at a significantly lower cost.

CHAPTER 7

CONCLUSION AND FUTURE WORK

Detection of ultra-weak fluorescent signals is required in wide range of applications today and many new applications are still being realized. With the advent of Single photon counting technology, the way in which different problems are addressed in wide range of fields has changed dramatically. This technology has gained wide spread importance in fields such as molecular biology, medical diagnosis and forensic analysis etc. to name a few. Until a decade ago, PMT was the only choice of detector for more than 50 years and is now being replaced by solid-state single photon detectors due to the numerous advantages offered by the new solid-state devices. These new detectors are progressing fast with technology and will potentially replace PMTs in most applications. DNA-sequencing is one such application that requires detection of ultra-weak fluorescent signals. Hence, progress in DNA-sequencing technologies depends a lot on the progress in photon detection technologies. This thesis investigated the commercially available solid-state single photon detectors and their application to DNA-sequencing. Two types of solid-state detectors having single photon sensitivity available are SPADs and SiPMs; both the detectors were investigated. This work presented, for the first time, experimental evidence of the application of large-area solid-state single photon detectors to DNA-sequencing. Thus large number of detectors can now be used for DNA-sequencing as compared to only two choices (PMT and CCD) that were available until recently. 10-fold

increase in sensitivity was achieved, thus facilitating significant cost reduction in DNA-sequencing.

7.1 Conclusions

Characterization of SiPMs a high-speed photon counters and application of large-area SPADs and SiPMs to DNA-sequencing are the main contributions of this thesis. In order to accomplish these tasks, design, development, prototyping, testing and characterization of various modules was involved. Outcomes of this research are listed as follows:

1. Feasibility of large-area SPAD for highly sensitive detection of DNA-sequences.

SPAD is the best choice of detector for detecting ultra-weak fluorescent signals and a good choice of detector for DNA-sequencing. Still, it was not used due to the complexity of the involved optics. A stand-alone, compact, general purpose, portable, high-performance photon counting module was designed based on large-area (0.5mm diameter) SPAD model C30902S-DTC from PKI. All aspects of the designed module such as temperature, stability, noise, speed were characterized. A dynamic range of 10MHz and a linear range of ~2MHz were demonstrated, which is the best possible result achievable with this SPAD and sufficient for DNA-sequencing. It was demonstrated that in order to achieve highest possible sensitivity, the SPAD needs to be operated at highest feasible over-voltage and

smallest feasible comparator threshold. Method of characterizing the sensitivity of a detector was shown. Sensitivity comparable with that of the best commercially available large-area SPCM module from PKI (costs USD 4500) was achieved at an over-voltage of 10V. Thus a high-performance photon counting module comparable with the best was designed at much lower cost. The designed module was successfully integrated into a single lane DNA sequencing instrument. Single fluorescent molecule sensitivity and excellent DNA sequencing results (~10 fold sensitivity improvement as compared to PMT) were obtained, experimentally demonstrating the feasibility of large-area SPAD to DNA-sequencing for the first time.

2. Unique multi-channel photon counting systems for high-throughput DNA-sequencing. It was found that the un-cooled SPAD model C30902S could not be used for DNA-sequencing even when sufficient heat sink was provided. Multi-channel systems based on the same cooled SPAD (model C30902S-DTC) were designed. A dead-time range of 50-60ns was found to be sufficient for the cooled SPADs. For cooled SPADs (C30902S-DTC), it was found that the SPADs with unusually high dark counts also exhibited bad over-all performance. Tuning of SPADs to obtain consistent performance from all the channels was shown.
3. Investigation and characterization of SiPMs for high-speed photon counting applications and its application to DNA-sequencing. So far, SiPMs have only been reported to have been used in high energy physics, nuclear medicine, astrophysics etc. applications, but in principle they can be used as high-speed photon counters. This work shows the advantages, detailed characterization in

particular noise analysis of SiPMs, when used as photon counters. The results show that, like SPAD, high sensitivity, linearity and dynamic range can be achieved when optimum operating conditions are set (see Table 5.5). All the three SiPMs have comparable or much higher dynamic (14-28 MHz for different SiPMs) and linear range as compared to PKI SPCM and S-SPCM. Once again it was shown that best photon counting results are obtained when the detector is biased at lowest feasible comparator threshold and highest feasible over-voltage. It was also found that cross-talk of the SiPM does not add noise to the photon-counting performance of SiPM. Based on these results, optimum configuration of SiPMs for photon-counting applications can be formulated. DNA-sequencing was performed with all the SiPM and excellent results were obtained, which opens up a completely new field and application for this device. Further, since they are CMOS based devices, they offer all the advantages of CMOS technology. This research shows that they can definitely replace SPADs in DNA-sequencing applications, thus providing two important solutions to (i) un-availability of low cost large-area SPADs for DNA-sequencing and many other applications and (ii) extremely low-cost solution to un-availability of large-area SPAD arrays for many applications since arrays of SiPMs can be easily designed at low cost (based on CMOS).

7.2 Recommendations for Future Work

Solid-state single photon detectors have the potential and will replace tradition PMTs in most applications that require detection of ultra-weak fluorescence signals. SPADs have been available for a few years, but SiPMs were commercialized only recently. Although in principle, SiPMs can be used a photon counters, they have only been used as photon-number resolver in limited applications in high energy physics, nuclear medicine, astrophysics etc. to name a few. This thesis, characterizes the SiPMs for the first time. The results show that SiPM can be used as high-speed photon counters and further they have wide dynamic range, good linearity and simple requirements of associated circuits. Further, this thesis also provides a proof of the use of SiPM as high-speed photon counter by experimentally demonstrating its application to DNA-sequencing. Based on this research, future work can be listed as follows:

1. Most of the research, design and development effort of SiPMs concentrates on the use of SiPM in photon-number resolving applications. This work showed the SiPM can be used as a high-speed photon counter. It was also found that cross-talk in SiPM does not contribute to noise when used as a photon counter. Therefore, SiPMs can now be optimized and designed specifically for photon counting applications. Currently available SiPMs have a minimum active area of 1mm^2 , which is not necessarily required in many photon counting applications. If SiPMs with smaller active area are designed, the dark count rate of such devices

will reduce significantly facilitating their use in many more photon counting applications.

2. Application of SiPM for detecting weak fluorescence signals in DNA-sequencing was investigated for the first time in this thesis. These devices have the potential to be used in other bio-medical applications, one such application is spectrography. Hence, use of SiPMs in other photon counting applications need to be investigated.
3. Arrays of large area SPADs are needed in many applications, but are not available. Since SiPM is based on CMOS technology, design of SiPM arrays should be relatively easy and very cost-effective. Therefore arrays of SiPM optimized for photon counting applications need to be investigated.
4. Design of fully integrated, stand-alone single and multi-channel SiPM-based photon detection systems (SiPM + amplifier + counter).

BIBLIOGRAPHY

- [1] Human Genome Project (HGP) [Online]. Available: <http://www.genome.gov/10001772>
- [2] Human Genome Project (HGP) [Online]. Available: http://www.ornl.gov/sci/techresources/Human_Genome/home.shtml
- [3] SPCM-AQ Single-Photon Counting Module, Vaudreuil, QC, Canada, PerkinElmer Optoelectronics, 1993, [Online]. Available: <http://optoelectronics.perkinelmer.com>
- [4] Silicon avalanche photodiode series C30902E, C30902S, C309021E and C309021S datasheet [Online]. Available: <http://optoelectronics.perkinelmer.com>
- [5] Solid State Silicon Multi-pixel Avalanche Photodiode datasheet [Online]. Available: http://www.voxtel-inc.com/datasheets/SiPMT08_datasheet.pdf
- [6] Multi pixel photon counter catalogue, Hamamatsu Photonics, Japan, [Online]. Available: http://jp.hamamatsu.com/resources/products/ssd/pdf/mppc_kapd0002e02.pdf
- [7] L. Alaverdian, S. Alaverdian, O. Bilenko, I. Bogdanov, E. Filippova, D. Gavrilov, B. Gorbovitski, M. Gouzman, G. Gudkov, S. Domratchev, O. Kosobokova, N. Lifshitz, S. Luryi, V. Ruskovoloshin, A. Stepukhovich, M. Tcherevishnick, G. Tyshko, V. Gorfinkel, "A family of novel DNA sequencing instruments based on single photon detection" *Electrophoresis* 23, pp. 2804-2817, 2002.
- [8] C. Trottier, M. Davies, H. Dautet, M. Wabuye, S A. Soper, A. Kapanidis, T. Lacoste and S. Weiss, "Single Photo-Counting Technology for Single-Molecule Detection Applications in Biotechnology", *PharmaGenomics*, pp 25-34, Feb. 2004, [Online]. Available: <http://optoelectronics.perkinelmer.com>
- [9] Applied Biosystems, CA [Online]. Available: <https://www2.appliedbiosystems.com/>

- [10] A Luckey, T. Norris, L. Smith, "Analysis of resolution in DNA sequencing by capillary gel electrophoresis", *J. Phys. Chem.*, 97, pp. 3067-3075, 1993.
- [11] Heller, C, "Influence of electric field strength and capillary dimensions on the separation of DNA", *Electrophoresis*, vol. 21, no. 3, pp. 593-602, 2000.
- [12] Heller, C, "Separation of double-stranded and single-stranded DNA in polymer solutions: I. Mobility and separation mechanism", *Electrophoresis*, vol. 20, no. 10, pp. 1962-1977, 1999.
- [13] L-Q. Li and L. M. Davis, "Single photon avalanche diode for single molecule detection," *Rev. Sci. Instrum.* 64, pp. 1524–1529, 1993.
- [14] S. A. Soper, Q. L. Mattingly, and P. Vegunta, "Photon burst detection of single near-infrared fluorescent molecules," *Anal.Chem.* 65, pp. 740–747, 1993.
- [15] N. S. Nightingale, "A new silicon avalanche photodiode photon counting detector module for astronomy," *Exp. Astron.*1, pp. 407–422, 1991.
- [16] P. D. Townsend, J. G. Rarity, and P. R. Tapster, "Single photon interference in 10 km long optical fiber interferometer", *Electron. Lett.* 29, pp. 634–635, 1993.
- [17] B. F. Levine and C. G. Bethea, "Room-temperature optical time domain reflectometer using a photon counting InGaAs/InP avalanche detector," *Appl. Phys. Lett.* 46, pp. 333–335, 1985.
- [18] G. Ripamonti and S. Cova, "Optical time-domain reflectometry with centimeter resolution at 10215 W sensitivity," *Electron.Lett.* 22, pp. 818–819, 1986.
- [19] A. Lacaíta, P. A. Francese, S. Cova, and G. Ripamonti, "Single-photon optical time-domain reflectometer at 1.3 μ m with 5-cm resolution and high sensitivity," *Opt. Lett.* 18, pp. 1110–1112, 1993.

- [20] G. Ripamonti and A. Lacaita, "Single-photon semiconductor photodiodes for distributed optical fiber sensors: state of the art and perspectives," in *Distributed and Multiplexed Fiber Optic Sensors II*, J. P. Dakin and A. D. Kersey, eds., Proc. SPIE 1797, pp. 38–49, 1993.
- [21] I. Prochazka, K. Hamal, and B. Sopko, "Photodiode based detector package for centimeter satellite laser ranging," in *Proceedings of the Seventh International Workshop on Laser Ranging Instrumentation*, C. Veillet, ed. IOCA-CERGA, Grasse, France, pp. 219–221, 1990.
- [22] F. Zappa, G. Ripamonti, A. Lacaita, S. Cova, and C. Samori, "Tracking capabilities of SPADs for laser ranging," in *Proceedings of the Eighth International Workshop on Laser Ranging Instrumentation*, J. J. Degnan, ed., NASA Conf. Publ. 32141 NASA, Greenbelt, Md., pp. 5, 25–30, 1992.
- [23] F. Stellari, F. Zappa, S. Cova, and L. Vendrame, "Tools for Non-Invasive Optical Characterization of CMOS Circuits," *Proceedings of International Electron Device Meeting IEDM '99*, pp. 5-8, Dec. 1999.
- [24] V. O'Connor and D. Phillips, *Time-Correlated Single Photon Counting*. New York: Academic, 1984.
- [25] H. Dautet, P. Deschamps, B. Dion, A. D. MacGregor, D. MacSween, R. J. McIntyre, C. Trottier, and P. P. Webb, "Photon counting techniques with silicon avalanche photodiodes," *Appl. Opt.* 32, pp. 3894–3900, 1993.
- [26] S. Cova, M. Ghioni, A. Lotito, I. Rech, and F. Zappa, "Evolution and prospects for single-photon avalanche diodes and quenching circuits," *J. Mod. Opt.*, vol. 51, no. 9/10, pp. 1267–1288, Jun/Jul. 2004.
- [27] Silicon Photomultipliers datasheet, SensL, Cork, Ireland, [Online]. Available: http://www.sensl.com/Products/02Silicon_Photomultipliers_-_High_Gain_APDs.html
- [28] Solidstate Photomultipliers (SSPM) datasheet, Photonique SA, Geneva, Switzerland, [Online]. Available: http://www.photonique.ch/Products_SSPM_main.html#1.0SSPMs

- [29] P. Buzhan, B. Dolgoshein, L. Filatov, A. Ilyin, V. Kantzerov, V. Kaplin, A. Karakash, F. Kayumov, S. Klemin, E. Popova, S. Smirnov "Silicon photomultiplier and its possible applications" Nucl. Instr. and Meth. A 504, pp. 48–52, 1992.
- [30] A. N. Otte, B. Dolgoshein, H. G. Moser, R. Mirzoyan, and M. Teshima, "Status of Silicon Photomultiplier Developments as optical Sensors for MAGIC/EUSO-like Detectors", 29th International Cosmic Ray Conference, 00, 101–106, 2005.
- [31] M. Shur, Physics of Semiconductor Devices, Prentice Hall, 1990.
- [32] D. Neamen, Semiconductor Physics and Devices, McGraw-Hill, 2002.
- [33] S.M. Sze, Physics of semiconductor devices, John Wiley & Sons Inc, 1969.
- [34] R. J. McIntyre, "The distribution of gains in uniformly multiplying avalanche photodiodes: Theory," IEEE Trans. Electron Devices, vol. ED-19, pp. 703–713, June 1973.
- [35] P. P. Webb, R. J. McIntyre, and J. Conradi, "Properties of avalanche photodiodes," RCA Rev. 35, pp. 235-278, 1974.
- [36] Avalanche Photodiodes: A User's Guide by EG&G Optoelectronics, Canada, [Online]. Available: http://optoelectronics.perkinelmer.com/content/ApplicationNotes/APP_APDUUsersGuide.pdf
- [37] Phred-Quality Base Calling [Online]. Available: <http://www.phrap.com/phred/>
- [38] P. Pakhlov, "SiPM: Development and Applications," Power point Presentation, [Online]. Available: rd.kek.jp/slides/20051214/SiPM.ppt
- [39] S. Cova, M. Ghioni, A. Lacaita, C. Samori, and F. Zappa, "Avalanche photodiodes and quenching circuits for single-photon detection," Appl. Opt. 35, pp.1956-1963, 1996.
- [40] A. Tsupryk, "Opto-mechanical system for high throughput ultra sensitive DNA sequencing instrumentation," PhD Dissertation, Stony Brook University, 2005.

- [41] R. H. Haitz, "Mechanisms contributing to the noise pulse rate of avalanche diodes," *J. Appl. Phys.* 36, 3123–3131, 1965.
- [42] S. Cova, A. Lacaita, and G. Ripamonti, "Trapping phenomena in avalanche photodiodes on nanosecond scale," *IEEE Electron. Devices Lett.* 12, 685–687, 1991.
- [43] Maxim, DS-1100, 5-Tap Economy Timing Element (Delay Line), [Online]. Available: <http://www.maxim-ic.com>
- [44] M. Ghioni, A. Gulinatti, I. Rech, F. Zappa and Sergio Cova, "Progress in Silicon Single-Photon Avalanche Diodes," *IEEE J. Select. Topics Quantum. Electron.*, Vol. 13, no. 4, pp. 852-862, July/Aug., 2007.
- [45] W. O. Oldham, R. R. Samuelson, and P. Antognetti, "Triggering phenomena in avalanche diodes," *IEEE Trans. Electron Devices*, vol. ED-19, no. 9, pp. 1056–1060, Sep. 1972.
- [46] A. Lacaita, M. Ghioni, F. Zappa, G. Ripamonti, and S. Cova, "Recent advances in the detection of optical photons with silicon photodiodes," *Nucl. Instrum. Methods A* 326, pp. 290–294, 1993.
- [47] R. Rigler and E. S. Elson, *Fluorescence Correlation Spectroscopy: Theory and Applications*, Chemical Physics. Berlin, Germany: Springer-Verlag, 2001.
- [48] W. Becker, *Advanced Time-Correlated Single Photon Counting Techniques*. Berlin, Germany: Springer-Verlag, 2005.
- [49] B. Dolgosheina, V. Balagura, P. Buzhan, M. Danilov, L. Filatov, E. Garutti, M. Groll, A. Ilyin, V. Kantserov, V. Kaplin, A. Karakash, F. Kayumov, S. Klemin, V. Korbel, H. Meyer, R. Mizuk, V. Morgunov, E. Novikov, P. Pakhlov, E. Popova, V. Rusinov, F. Sefkow, E. Tarkovsky, I. Tikhomirov, Calice/SiPM Collaboration, "Status Report on Silicon Photomultiplier Development and its Applications", *Nucl. Instr. and Meth. A* 563, pp. 368-376, 2006.
- [50] M. Taguchi, "Development of Multi-pixel Photon Counters," Master's Thesis, Kyoto University, Feb. 2007.

- [51] A.Goetzberger, B.McDonald,R.H.Haitz, andR.M. Scarlett, “Avalanche effects in silicon p-n junctions. II. Structurally perfect junctions,” J. Appl. Phys., vol. 34, pp. 1591–1600, 1963.
- [52] P. Lacaita, F. Zappa, S. Bigliardi, M. Manfredi, “On the bremsstrahlung origin of hot-carrier-induced photons in silicon devices”, IEEE Trans. Electron Dev., vol. 40, no. 3, pp. 577-582, 1993.
- [53] A. Rochas, M. Gani, B. Furrer, P. A. Besse, R. S. Popovic, G. Ribordy, and N. Gisin, “Single photon detector fabricated in a complementary metal–oxide–semiconductor high-voltage technology,” Rev. Sci. Instrum., vol. 74, pp. 3263–3270, 2003.
- [54] E. Sciacca, A. C. Giudice, D. Sanfilippo, F. Zappa, S. Lombardo, R. Consentino, C. Di Franco, M. Ghioni, G. Fallica, G. Bonanno, S. Cova, and E. Rimini, “Silicon planar technology for single-photon optical detectors,” IEEE Trans. Electron Devices, vol. 50, no. 4, pp. 918–925, Apr. 2003.
- [55] M. J. Binns, S. Bertolini, R. Wise, D. J. Myers, and T. A. McKenna, “Effective intrinsic gettering for 200 mm and 300 mm P/P-wafers in a low thermal budget 0.13 μm advanced CMOS logic process,” in Semiconductor Silicon 2002 (Electrochem. Soc. Proc. S.), H. R. Huff, L. Fabry, and S. Kishino, Eds., Pennington, NJ, PV 2002-2, pp. 647–657.
- [56] A. Rochas, M. Gosch, A. Serov, P. A. Besse, R. S. Popovic, T. Lasser, and R. Rigler, “First fully integrated 2-D array of single-photon detectors in standard CMOS technology,” IEEE Photon. Techno. Lett., vol. 15, no. 7, pp. 963–965, Jul. 2003.
- [57] C. Jackson, A. Morrison, D. Phelan, and A. Mathewson, “A Novel Silicon Geiger-Mode Avalanche Photodiode,” IEEE-International Electron Devices Meeting (IEDM), vol. 32.2, 2002.
- [58] P. Antognetti, S. Cova, and A. Longoni, “A study of the operation and performances of an avalanche diode as a single photon detector,” in Proceedings of the Second Ispra Nuclear Electronics Symposium, EURATOM Publ. EUR 537e (Office for Official Publications of the European Communities, Luxembourg, Belgium, 1975), pp. 453–456.

- [59] S. Cova, A. Longoni, and A. Andreoni, "Towards picosecond resolution with single-photon avalanche diodes," *Rev. Sci.Instrum.* 52, pp. 408–412, 1981.
- [60] R. G. Brown, K. D. Ridley, and J. G. Rarity, "Characterization of silicon avalanche photodiodes for photon correlation measurements.1: Passive quenching," *Appl. Opt.* 25, pp. 4122– 4126, 1986.
- [61] S. Cova, A. Lacaita, M. Ghioni, G. Ripamonti, and T. A. Louis, "20 ps timing resolution with single-photon avalanche diodes," *Rev. Sci. Instrum.* 60, pp. 1104–1110, 1989.
- [62] A. Lacaita, S. Cova, M. Ghioni, and F. Zappa, "Single photon avalanche diodes with ultra fast pulse response free from slow tails," *IEEE Electron. Devices Lett.* 14172, pp. 360–362, 1993.
- [63] R. J. McIntyre and P. Webb, "Low-noise, reach-through avalanche photodiodes," U.S. Patent 5 583 352, 1996.
- [64] F. Zappa, M. Ghioni, S. Cova, L. Varisco, B.S. Sinnis, A. Morrison, and A. Mathewson, "Integrated array of avalanche photodiodes for single-photon counting," *Proc. European Solid-State Device Research Conference ESSDERC '97*, pp. 600-603, 1997.
- [65] C. Jackson, D. Phelan, A. Morrison, M. Redfern, A. Mathewson, "Toward integrated single-photon-counting micro-arrays", *Opt. Eng.* 42(1), pp. 112–118, Jan. 2003.
- [65] Franco Zappa, Angelo Gulinatti, Piera Maccagnani, Simone Tisa, and Sergio Cova, "SPADA: Single-Photon Avalanche Diode Arrays," *IEEE Photon. Techno. Lett.*, vol. 17, no. 3, pp. 657–659, Mar. 2005.
- [67] W.J. Kindt, H.W. van Zeijl, S. Middelhoek, "Optical Cross Talk in Geiger Mode Avalanche Photodiode Arrays: Modeling, Prevention and Measurement", *Proc. of the 28th European Solid-State Device Research Conference, ESSDERC'98*, pp.192-195, Sept.1998.
- [68] D. M. Taylor, J. C. Jackson, A. P. Morrison, A. Mathewson, J. G. Rarity, "Characterization of novel active area silicon avalanche photodiodes operating in the geiger mode," *Journal of Modern Optics*, 51:9, pp. 1323 -1332, 2004.

[69] A. Gulinatti, P. Maccagnani, I. Rech, M. Ghioni, and S. Cova, “35 ps time resolution at room temperature with large area single photon avalanche diodes,” *Electron. Lett.*, vol. 41, pp. 272–273, 2005.

[69] A. Restelli, I. Rech, P. Maccagnani, M. Ghioni, and S. Cova, “Monolithic silicon matrix detector with 50 μ m photon counting pixels,” *J. Modern Opt.*, vol. 54, pp. 213–223, 2007.

[70] id Quantique, <http://www.idquantique.com/>

[71] Micro Photon Devices (MPD), <http://www.microphotondevices.com/>

[72] Voxtel-Inc, <http://www.voxtel-inc.com/>

[73] SensL, <http://www.sensl.com/>

[74] Photonique SA, <http://www.photonique.ch/>

[75] A. Gasanov, V. Golovin, Z. Sadygov, N. Yusipov. – *Technical Physics Letters*, v.14, No.8, pp.706, 1998.

[76] A. Gasanov, V. Golovin, Z. Sadygov, N. Yusipov. – *Microelectronics*, v.18, No.1, p.88, 1989.

[77] A. Gasanov, V. Golovin, Z. Sadygov, N. Yusipov Avalanche photodetector, Russian patent #1702831, application from 10.11.1989.

[78] Z. Sadygov, I.M. Zheleznykh et al., “Microchannel avalanche semiconductor photodetectors: status and perspectives”, *Proc. SPIE*, v.3516, pp.167-175, 1999.

[79] G. Bondarenko, P. Buzhan, B. Dolgoshein, V. Golovin, E. Guschin, A. Ilyin, V. Kaplin, A. Karakash, R. Klanner, V. Pokachalov, E. Popova, K. Smirnov, “Limited Geiger-mode microcell silicon photodiode: new results” *Nucl. Instr. and Meth. A* 442, Issues 1-3, pp 187-192, 2000.

[80] N. Anfimov, I. Chirikov-Zorin, Z. Krumshteyn, R. Leitner, A. Olchevski, "Test of micropixel avalanche photodiodes", Nucl. Instr. and Meth. A 572, pp. 413-415, 2000.

[81] Saveliev and V. Golovin, "Silicon avalanche photodiodes on the base of metal resistor-semiconductor (MRS) structures," Nucl. Instr. Meth. A 442, pp 223-229, 2000.

[82] J. C. Jackson, A. P. Morrison, D. Phelan and A. Mathewson, "A Novel Silicon Geiger-Mode Avalanche Photodiode", IEEE-International Electron Devices Meeting (IEDM), vol. 32.2, December, 2002.

[83] D. Beznosko, G. Blazey, D. Chakraborty, A. Dyshkant, K. Francis, D. Kubic, J. G. Lima, V. Rykalin, V. Zutshi, "Investigation of a solid-state photodetector", Nucl. Instr. and Meth. A 504, pp. 48-52, 2003.

[84] P. Buzhan, B. Dolgoshein, L. Filatov, A. Ilyin, V. Kantzerov, V. Kaplin, A. Karakash, F. Kayumov, S. Klemin, E. Popova, S. Smirnov "Silicon photomultiplier and its possible applications" Nucl. Instr. and Meth. A 504, pp. 48-52, 2003.

[85] Golovin and V. Saveliev, "Novel type of avalanche photodetector with Geiger mode operation," Nucl. Instr. MethA 518, pp 560-565, 2004.

[86] Z. Sadygov, et al., Three advanced designs of avalanche micropixel photodiodes, in: Proceedings of the Fourth International Conference on New Developments in Photodetection, Beaune (France), June 19-24, 2005, Nucl. Instr. and Meth. A 567 (1), pp. 70-73, 2005.

[87] C. Piemonte, "A new silicon photomultiplier structure for blue light detection", Nucl. Instr. and Meth. A, 568, pp. 224-232, 2006.

[88] C. Piemonte, R. Battiston, M. Boscardin, G. Dalla Betta, A. Guerra, N. Dinu, A. Pozza, and N. Zorzi, "Characterization of the First Prototypes of Silicon Photomultiplier Fabricated at ITC-irst", IEEE Transactions on Nuclear Science, Vol. 54, No. 1, Feb 2007.

[89] D. Renker, "New trends on photodetectors" Nucl. Instr. and Meth. A 571, pp. 1-6, 2007.

[90] V D Kovaltchouk, GJ Lolos, Z Papandreou and K Wolbaum “Comparison of a silicon photomultiplier to a traditional vacuum photomultiplier”, Nucl. Instr. and Meth. A, vol. 538, pp. 408-415, 2005.

[91]Dubna APD-group publications, [Online]. Available: <http://sunhe.jinr.ru/struct/neo/apd/publications.html>

[92] I. Britvich, Y. Musienko and D. Renker, “Investigation of a photon counting avalanche photodiode from Hamamatsu photonics” Nucl. Instr. and Meth. A 567, pp. 276–280, 2006.

[93] S. Cova, “Active quenching circuit for avalanche photodiodes,” U.S. patent 4,963,727 (20 October 1990) (Italian patent 22367A/88); licensed for industrial production to Silena SpA, Milano, Italy.

[94] C J. Trottier, P. Deschamps, B. Dion, A R. Comeau, “Active quench circuit and reset circuit for avalanche photo diode”, U.S. patent 5532474, Aug.1999.

[95] H. Dautet, P. Deschamps “Active quench circuit for an avalanche current device”, U.S. patent 5933042, July 1996.

[96] F. Zappa, M. Ghioni, S. Cova, C. Samori, and A. C. Giudice, “An integrated active-quenching circuit for single-photon avalanche diodes,” IEEE Trans. Instrum. Measurements, vol. 49, pp. 1167–1175, Dec. 2000.

[97] F. Zappa, S. Cova, and M. Ghioni, “Monolithic circuit of active quenching and active reset for avalanche photodiodes,” U.S. Patent 6 541 752, Apr. 1, 2003. Eur. Patent Appl. 01200851.2-2217, Mar. 6, 2001; Italian Patent MI2000 A000467, Mar. 6, 2000.

[98] M. Ghioni, S. Cova, F. Zappa, and C. Samori, “Compact active quenching circuit for fast photon counting with avalanche photodiodes,” Rev. Sci. Instrum., vol. 67, pp. 3440–3448, 1996.

[99] Linear Integrated Systems, SST-215, High Speed N-Channel Lateral DMOS FET Switch with Zener Diode Protection (SMT), [Online]. Available: <http://www.linearsystems.com>

- [100] W. Nicholson, Nuclear Electronics, Wiley, New York, 1974.
- [101] D. Gavrilov, B. Gorbovitski, M. Gouzman, G. Gudkov, A. Stepukhovich, V. Ruskovoloshin, A. Tsuprik, G. Tyshko, O. Bilenko, O. Kosobokova, S. Luryi, V. Gorfinkel, "Dynamic range of fluorescence detection and base-calling accuracy in DNA sequencer based on single-photon counting," Electrophoresis, vol.24, No 7-8, pp.1184-1192, 2003.
- [102] V. Dhulla, G. Gudkov, D. Gavrilov, A. Stepukhovich, A. Tsupryk, O. Kosobokova, A. Borodin, B. Gorbovitski and V. Gorfinkel, "Single Photon Counting Module Based on Large-area APD and Novel Logic Circuit for Quench and Reset Pulse Generation," IEEE J. Select. Topics Quantum. Electron., Vol. 13, no. 4, pp. 926-933, , July/August 2007.
- [44] M. Ghioni, A.Gulinatti, I. Rech, F. Zappa and Sergio Cova, "Progress in Silicon Single-Photon Avalanche Diodes," IEEE J. Select. Topics Quantum. Electron., Vol. 13, no. 4, pp. 852-862, , July/August 2007.
- [103] Integrated temperature controllers for peltier modules IC Max 1978 datasheet [Online]. Available: <http://www.maxim-ic.com/>
- [102] Max 1978 evaluation kit datasheet [Online]. Available: <http://www.maxim-ic.com/>
- [103] SchmartBoard, <http://www.schmartboard.com/>
- [104] R. G. Brown, R. Jones, J. G. Rarity, and K. D. Ridley, "Characterization of silicon avalanche photodiodes for photon correlation measurements. 2: Active quenching," Appl. Opt. 26, pp. 2383–2389, 1987.
- [105] A. Rochas, "Single Photon Avalanche Diodes in CMOS Technology", Ph.D. Thesis, Lausanne, 2003.
- [106] id150 series Miniature 8-channel photon counter for OEM applications [Online]. Available <http://www.idquantique.com/>

- [107] C. Niclass, M. Sergio, and E. Charbon, "A Single Photon Avalanche Diode Array Fabricated in Deep-Submicron CMOS Technology", [Online]. Available: http://aqua.epfl.ch/PDF/01D_3_926_v1.1.pdf
- [108] V. Dhulla, G. Gudkov, A. Stepukhovich, A. Tsupryk, O. Kosobokova, D. Gavrilo, V. Gorfinkel, "Single photon detection module for multi-channel detection of weak fluorescence signals", conference on Smart Medical and Biomedical Sensor Technology III, Proc.of SPIE Vol.6007 600719-1, pp. 1-9, 2005.
- [109] G. Gudkov, V. Dhulla, A. Borodin, D. Gavrilo, A. Stepukhovich, A. Tsupryk, B. Gorbovitski, V. Gorfinkel, "32-channel single-photon counting module for ultra-sensitive detection of DNA sequences", conference on Advanced Photon Counting Techniques, Proc.of SPIE vol.6372, 63720C, Boston, Massachusetts, USA Oct 1-4, 2006.
- [110] S.Tudisco, L.Cosentino, G.Fallica, P.Finocchiaro, F.Musumeci, A.Scordino, D.Sanfilippo, G.Privitera, S.Privitera, H.Thienpont, M.Vervaeke, B.Volckaerts, P.Vynck, "SINPHOS - SINGLE PHOTON Spectrometer for Biomedical Application" Nuclear Physics B (Proc. Suppl.) 150, pp. 317-320, 2006.
- [111] P.Finocchiaro, A.Campisi, L.Cosentino, A.Pappalardo, F.Musumeci, S.Privitera, A.Scordino, S.Tudisco, G.Fallica, D.Sanfilippo, M.Mazzillo, A.Piazza, J.Van Erps, M.Vervaeke, B.Volckaerts, P.Vynck, A.Hermanne, H.Thienpont, S.Lombardo, E.Sciacca, "A New Generation of Low-voltage Single Photon Micro-sensors with Timing Capability", Nucl. Instr. and Meth. A 567, Issue 1, pp. 83-88, 2006.
- [112] A. Rochas, P. Besse, R. Popovic, "Actively recharged single photon counting avalanche photodiode integrated in an industrial CMOS process," Sens. Actuators A pp. 110, 124-129, 2004.
- [113] B. F. Aull, A. H. Loomis, J.A. Gregory, D..J. Young, "Geiger-mode Avalanche Photodiode Arrays Integrated with CMOS Timing Circuits," in Proceedings of the 56th Annual Device Research Conference Digest, 22-24, 58-59, June 1998.
- [114] Photon Counting Detector Module, PDM Series, 2003, Bolzano, Italy: Micro Photon Devices, [Online]. Available: www.micro-photondevices.com
- [115] VT120 Fast Timing Preamplifier datasheet, [Online]. Available: <http://www.ortec-online.com/electronics/preamp/vt120.htm>

[116] I. Britvitch, I. Johnson, D. Renker, A Stoykov and E. Lorenz, “Characterisation of Geiger-mode avalanche photodiodes for medical imaging applications”, Nucl. Instr. and Meth. A, 571, pp. 308–311, 2007.

LIST OF ABBREVIATIONS

Abbreviation or Symbol	Term
APD	Avalanche Photodiode
AQC	Active Quenching Circuit
BP	Base pair
CE	Capillary Electrophoresis
DC	Dark Counts
DCR	Dark Count Rate
DL	Delayed Luminescence
EO	Edmund Optics
<i>F</i>	Electric Field
GM	Geiger Mode
HGP	Human Genome Project
MDS	Minimum Detectable Signal
MQC	Mixed Passive-active Quenching Circuit
MRS	Metal Resistive Semiconductor
M-SPCM	Multi-channel single photon counting module
ND	Neutral Density
OD	Optical Density

PCB	Printed Circuit Board
PCR	Photon/Photo-Count Rate
P_{de}	Photoelectron Detection Probability
PDE	Photon Detection Efficiency
p.e	Photoelectron
PMT	Photomultiplier Tube
PKI	Perkin Elmer Optoelectronics
PKI SPCM	Single Photon Counting Module, SPCM AQ-1X from PKI
PQC	Passive Quenching Circuit
QC	Quenching Circuit
QE	Quantum Efficiency
SiPM	Silicon Photomultiplier
SNR	Signal-to-Noise Ratio
SPAD	Single Photon Avalanche Diode
SPC	Single Photon Counting
SPCM	Single Photon Counting Module
SPCS	Single Photon Counting System
SPCT	Single Photon Counting Technology
V_{Bias}	Bias Voltage
V_{BR}	Breakdown Voltage
V_{OV}	Over Voltage ($V_{Bias} - V_{BR}$)

APPENDIX A

DETAILED CIRCUIT DIAGRAM AND LAYOUT FILES OF THE DESIGNED PCB

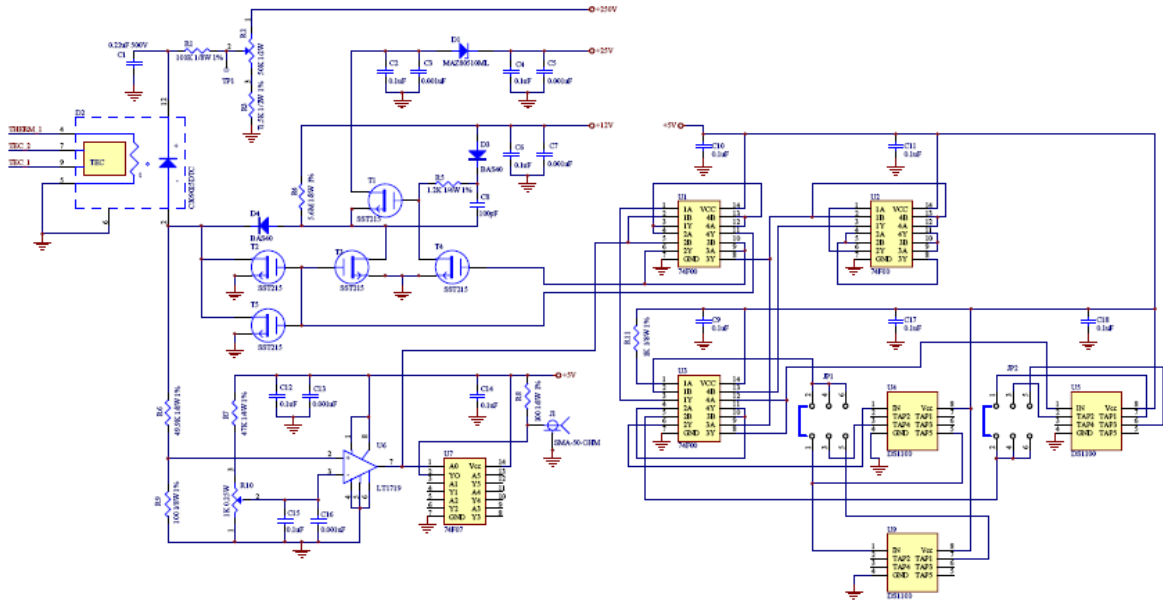


Figure A.1 Detailed circuit diagram of the quenching circuit shown in Figure 3.2. S-SPCM and 16-channel M-SPCM are based on this circuit.

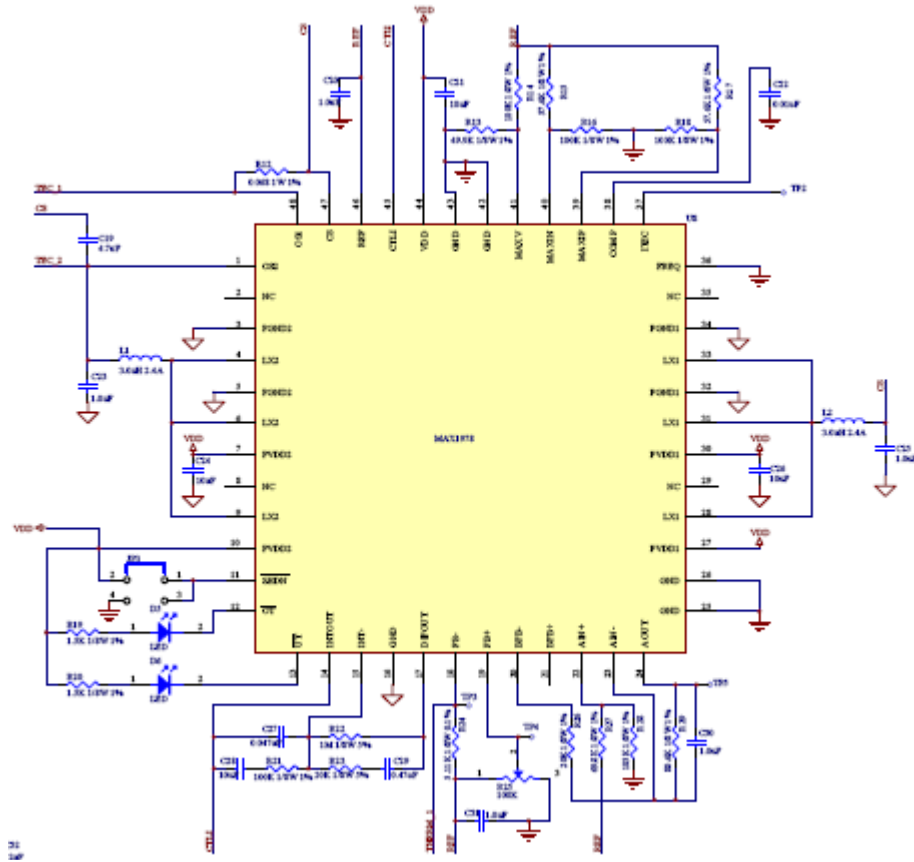


Figure A.2 Detailed circuit diagram of the temperature controller circuit for SPAD model C30902S-DTC.

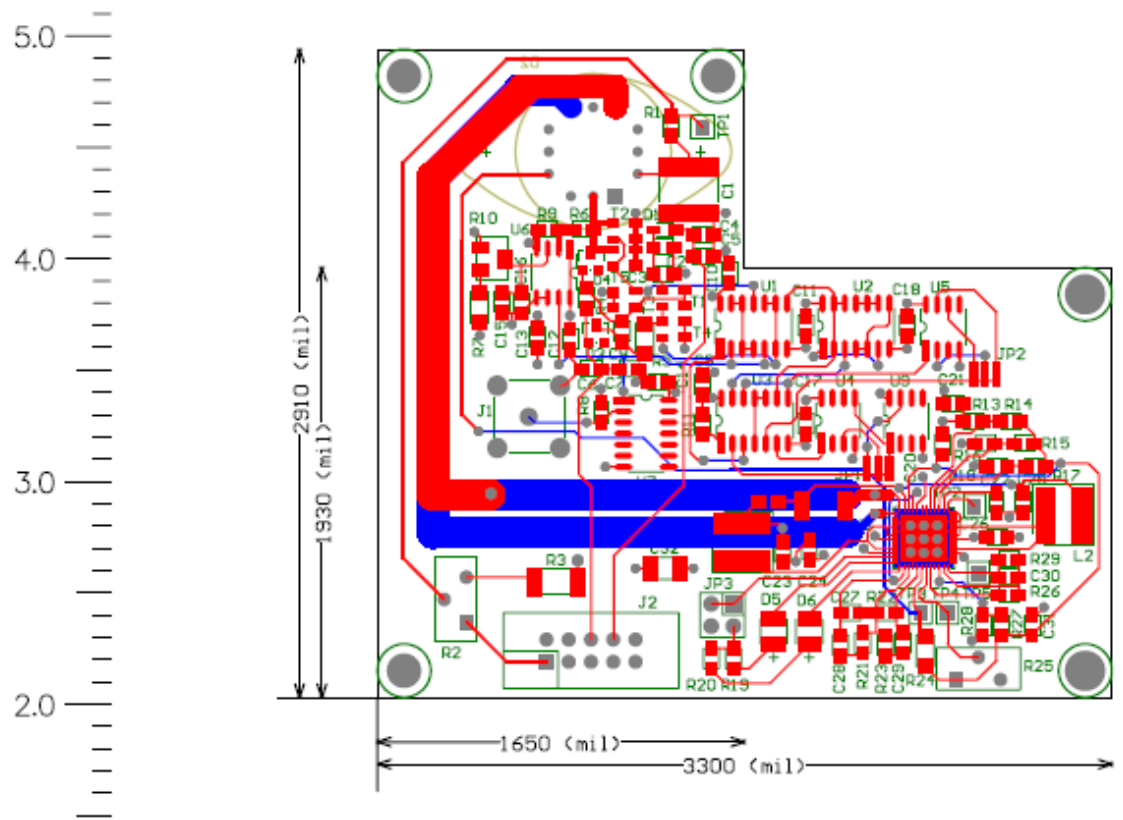


Figure A.3 Layout of the implemented circuits. PCB consists of quenching circuit and temperature controller circuit. The thick blue and red tracks are for supporting the high current switching in temperature controller circuit. Photo of fabricated PCB is shown in Figure 3.17.

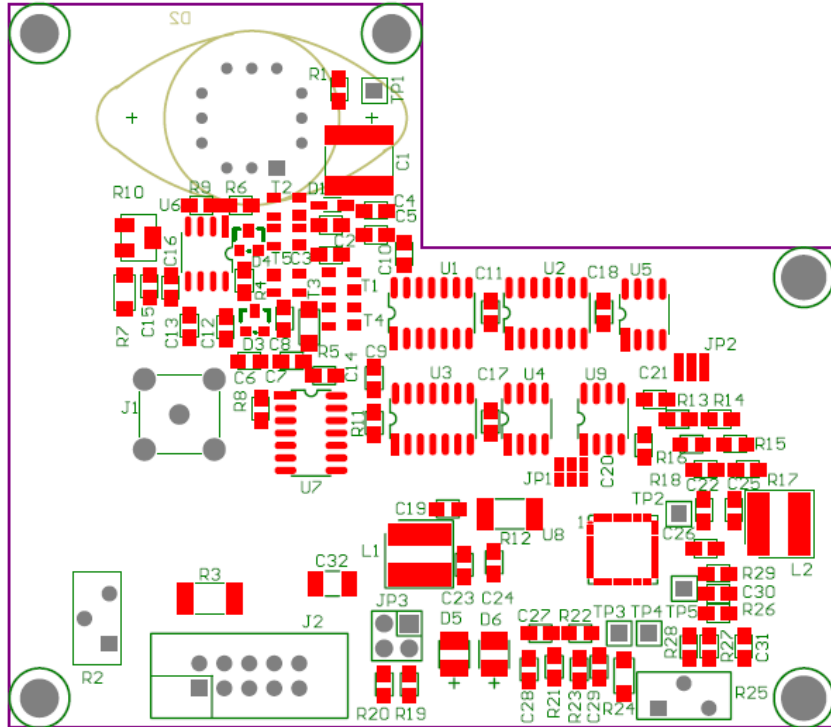


Figure A.4 Layout view showing component placements

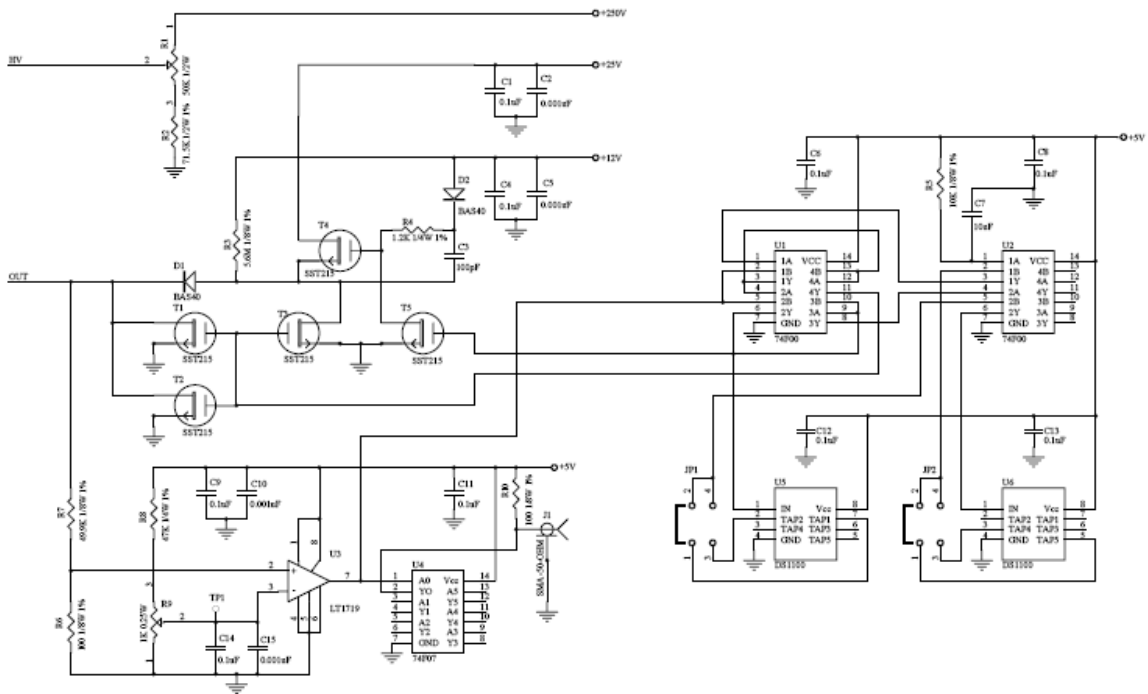


Figure A.5 Detailed circuit diagram of the Improved quenching circuit shown in Figure 3.10; 32-channel M-SPCM is based on this circuit.

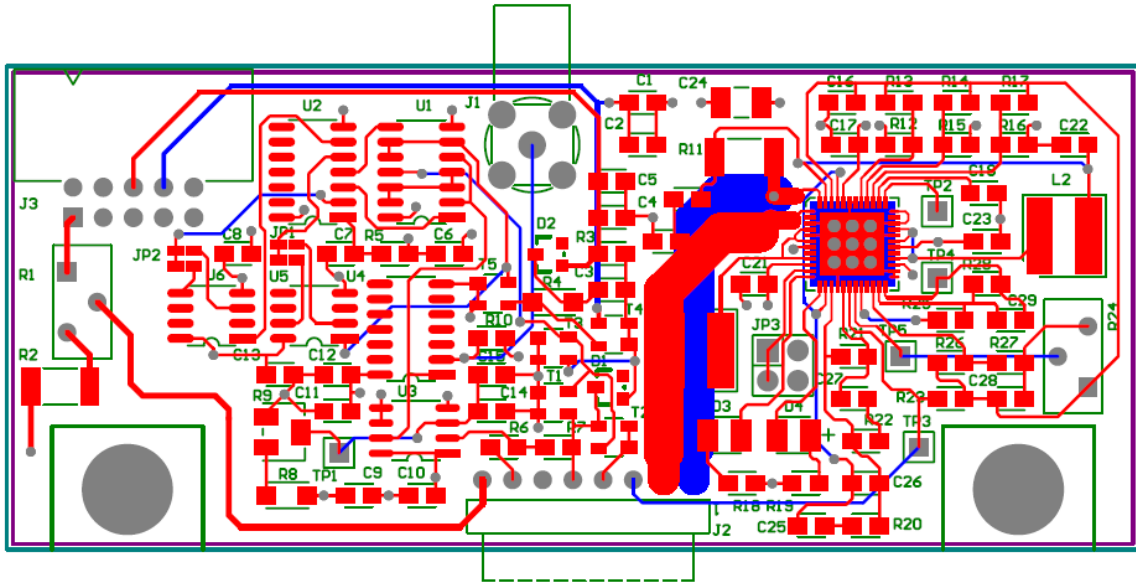


Figure A.6 PCB layout consisting of improved quenching circuit and temperature controller.



Figure A.7 Photo of fabricated PCB. 32-channel photon detection module is based on this PCB.